Hristo IVANOV MSc

Investigations on long range FSO (Free Space Optics) links (including Deep Space Communication), effected mainly by fog and cloud conditions and influenced by atmospheric turbulences

DOCTORAL THESIS

to achieve university degree of

Doktor der technischen Wissenschaften

submitted to

Graz University of Technology

Supervisor

Ao.Univ.-Prof. Dipl.-Ing. Dr.techn. Erich Leitgeb

Institut für Hochfrequenztechnik

Graz, May 2020

EIDESSTATTLICHE ERKLÄRUNG

Ich erkläre an Eides statt, dass ich die vorliegende Arbeit selbstständig verfasst, andere als die angegebenen Quellen/Hilfsmittel nicht benutzt, und die den benutzten Quellen wörtlich und inhaltlich entnommene Stellen als solche kenntlich gemacht habe.

Graz, am 14.05.2020 .....

(Unterschrift)

Englische Fassung:

STATUTORY DECLARATION

I declare that I have authored this thesis independently, that I have not used other than the declared sources / resources, and that I have explicitly marked all material which has been quoted either literally or by content from the used sources.

14.05.2020 .....

date

(signature)

Abstract

The current thesis considers a full-scale high-end analysis of Free Space Optical (FSO) atmospheric channel that comprises the main tropospheric weather effects deteriorating significantly the optical wireless communication links. Although the primary investigated atmospheric influence is Mie scattering due to fog and clouds, the atmospheric turbulence-induced fading is also taken into account. Both effects lead to significant impairments for all types of FSO scenarios considering short as well as very long FSO communication links. Apart from the various carried out analyses including empirical as well as theoretical models, in frame of the current work pioneering VOA-based (Variable Optical Attenuator) hardware channel emulator was implemented and evaluated. In order to address the listed tasks, attenuation data, acquired during real measurements in Graz, Austria as well as using high quality and proven European Centre for Medium-Range Weather Forecasts (ECMWF) and Radiosonde Observation (RAOB) databases, are processed and analysed. In particular, both long-distance conventional terrestrial as well as space-to-ground FSO links are handled in respect to Mie scattering (fog and clouds) as well as turbulence-induced scintillations. The MATLAB simulated and measured atmospheric attenuation values highly contribute to experimental evaluation of long-distance deep space FSO communication downlinks, which are of decisive importance for the already started technological revolution in near and outer space. In order to verify their operation in respect to adverse atmospheric turbulence and Mie scattering, FSO communication downlink is studied by means of simulations involving high photon efficiency SNSPD-based (Superconducting Nanowire Single Photon Detector) Poisson link, which is standardized by Consultative Committee for Space Data Systems (CCSDS) and modelled in MATLAB development environment. The findings well support the pioneering high-end breadboard for testing deep space FSO downlinks in laboratory conditions, which is developed within the current work with the partial support of European Space Agency (ESA). Even though the breadboard, which implements real state-of-the-art SNSPD, is evaluated based on FSO channel with static atmospheric attenuation, the VOA-based channel emulator is solely tested in terms of dynamic optical fluctuations with frequency up to 1 kHz.

Kurzfassung

Die vorliegende Arbeit beschäftigt sich mit einer vollständigen Analyse des atmosphärischen Free-Space-Optics (FSO) Kanals, einschließlich der troposphärischen Wetter Effekte, welche die optische Freiraumkommunikation erheblich beeinflussen. Berücksichtigt werden neben dem primären atmosphärischen Einfluss - der Mie-Streuung aufgrund von Nebel und Wolken - auch das durch atmosphärische Turbulenzen induzierte Fading. Beide Effekte führen zu erheblichen atmosphärischen Störungen für alle Arten von FSO-Szenarien, wenn sowohl kurze als auch sehr lange FSO Kanäle berücksichtigt werden. Zu den verschiedenen durchgeführten Analysen, einschließlich empirischer und theoretischer Modelle, wurde im Rahmen der laufenden Arbeit ein innovativer Hardware-Kanalemulator basierend auf einem Variable Optical Attenuator (VOA) implementiert und evaluiert. Um die aufgelisteten Aufgaben zu bewältigen, werden Dämpfungsdaten verarbeitet und analysiert, die bei realen Messungen in Graz (Österreich) sowie unter Verwendung hochwertiger und bewährter Datenbanken (European Centre for Medium-Range Weather Forecasts (ECMWF) und Radiosonde Observation (RAOB)) akquiriert wurden. Es werden sowohl konventionelle terrestrische FSO Verbindungen über größere Distanzen, als auch Weltraum – Erde Verbindungen in Bezug auf die Mie-Streuung (Nebel und Wolken) sowie turbulenzinduzierte Szintillationen behandelt. Die mit Hilfe von MATLAB ermittelten atmosphärischen Dämpfungswerte tragen in hohem Maße zur experimentellen Evaluierung von FSO Kommunikations-verbindungen über große Entfernungen im Weltraum bei, die für die bereits begonnene technologische Revolution im Weltraum von entscheidender Bedeutung sind. Um den Betrieb von FSO Systemen unter Bedingungen wie atmosphärische Turbulenzen und Mie-Streuung zu verifizieren, werden Simulationen der FSO Strecke durchgeführt. Hierbei wird ein SNSPD-basiertes (Superconducting Nanowire Single Photon Detector) Poisson-Modell mit hoher Photoneneffizienz verwendet, welches durch die Consultative Committee for Space Data Systems (CCSDS) standardisiert ist und in der MATLAB-Entwicklungsumgebung modelliert wird. Die Ergebnisse verifizieren den High-End Prototypen zum Testen von FSO-Downlinks im Weltraum unter Laborbedingungen, der im Rahmen der vorliegenden Arbeit mit teilweiser Unterstützung der Europäischen Weltraumorganisation (ESA) entwickelt wurde. Obwohl der Prototyp unter Verwendung eines hochmodernen SNSPDs auf der Grundlage eines FSO Kanals mit statischer atmosphärischer Dämpfung bewertet wird, wird der VOA-basierte Kanalemulator ausschließlich auf dynamische optische Leistungsschwankungen mit einer Frequenz von bis zu 1 kHz getestet.

Table of Contents

Table of Contents

Table of Contents

List of Figures

List of Figures

List of Figures

List of Tables

Abbreviations

AM	Air Mass
AMOFSG	Aerodrome Meteorological Observation and Forecast Study Group
APD	Avalanche Photodiode
ASTM	American Society for Testing and Materials
BERT	BER Tester
CCSDS	Consultative Committee for Space Data Systems
CFLOS	Cloud Free Line of Site
CU	Control Unit
CW	Continuous-wave
DAC	Digital to Analog Converter
DCR	Dark Count Rate
DFB	Distributed Feedback Laser
DLR	German Aerospace Center
DSOC	Deep Space Optical Communication
DT	Dead Time
EDFA	Erbium-Doped Fiber Amplifier
ECMWF	European Centre for Medium-Range Weather Forecasts
EIRP	Effective Isotropic Radiated Power
ER	Extinction Ratio
ESA	European Space Agency
FoV	Field of View
FSO	Free Space Optics
GEO	Geostationary Equatorial Orbit
HAP	High Altitude Platform
HG	Henyey – Greenstein
HPE	High Photon Efficiency
HV	Hufnagel – Valley
IM/DD	Intensity Modulation/Direct Detection
IoT	Internet of Things
I^2C	Inter – Integrated Circuit
LCT	Laser Communication Terminal
LDPC	Low Density Parity Check
LDS	Laser Diffraction System
LEO	Low Earth orbit
LIDAR	Light Detection and Ranging
$LiNbO_3$	Lithium Niobat
LLCD	Lunar Laser Communication Demonstrator
LoS	Line-of-Sight
MEMs	Micro Electro-Mechanical Systems
MEO	Medium Earth Orbit
MFD	Mode Field Dimeter
MISO	Multiple Input Single Output
MM	Multi Mode
M2M	Machine to Machine
MOPA	Master Oscillator Power Amplifier

Abbreviations

MZM	Mach-Zehnder Modulator
NASA	National Aeronautics and Space Administration
NICT	National Institute of Information and Communications Technology
NIR	Near Infrared
NRZ	Non-Return to Zero
OGS	Optical Ground Station
OICETS	Optical Inter-orbit Communications Engineering Test Satellite
OOK	On-Off Keying
PAR	Peak to Average Ratio
PAT	Pointing, Acquisition and Tracking
PDF	Probability Density Function
PIN	Positive-Intrinsic-Negative
PPB	Photons per Bit
PPM	Pulse Position Modulation
PPP	Poisson Point Process
PRBS	Pseudo Random Binary Sequence
PSD	Particle Size Distribution
PSDen	Power Spectral Density
RAOB	Radiosonde Observation
RF	Radio Frequency
SCPPM	Serially Concatenated Pulse Position Modulation
SFP	Small Form-factor Pluggable
SIMO	Single Input Multiple Output
SM	Single Mode
SMF	Single Mode Fibre
SNSPD	Superconducting Nanowire Single Photon Detector
STD	Standard Deviation
TRL	Technology Readiness Level
VCSEL	Vertical-Cavity Surface-Emitting Laser
VenSAR	Venus uses Venus Synthetic Aperture Radar
VOA	Variable Optical Attenuator

Chapter 1

1. Introduction

The proposed various analyses and results accompanied with self-developed evaluation breadboard provides novel approaches for evaluation of very long-distance terrestrial as well as space-to-ground Free Space Optical (FSO) downlinks under precisely controlled conditions. In order to reach the objectives, a comprehensive overview considering long-distance FSO channel characterization is carried out beforehand. The defined goals in the introduction part are accomplished through the thesis based on interdisciplinary approach considering optical communication theory and design, probability and statistical analyses as well as atmospheric physics and electrical engineering.

1.1 Overview of FSO communication technology

The idea of transmitting information based on light is available since ancient times when fires were extensively used for communication in terms of defence. Few millenniums later, this concept was continued with invention of the light telegraph and Graham Bell's Photophone. However, the tremendous advances in Radio Frequency (RF) communication systems did not allowed wireless optical data transmission to be really considered as a reliable communication way until the invention of Laser in the 1960. The first FSO duplex link for commercial needs, operating over distance of 14 km, was built between two Japanese cities in 1970 ***[1]***. Since then, contemporary FSO communication systems characterized with a carrier frequency between 20 – 375 THz underwent significant improvements. Recently, German Aerospace Center (DLR) demonstrated a long-distance 10.45 km terrestrial FSO link distinguished with 1.72 Tbps, which by itself is a new world record for data transmission ***[2]***. In general, contemporary FSO systems are characterized with enormous information capacity, high beam directivity with small divergence angle, no susceptibility to jamming, insignificant weight and size, absence of electromagnetic interferences and free of licenses unregulated spectrum, which means frequency planning is not required. Regarding system architecture, a conventional FSO has two transceivers each containing transmitter and receiver. On the one hand, the design and the selected components are organized in terms of the chosen detection scheme, which can be either Intensity Modulation/Direct Detection (IM/DD), or Coherent one. On the other hand, a certain architecture is dependent on the desired system parameters and system performance. The most notable and general FSO parameters, which are related to: 1) transmitter unit are: operational wavelength, transmitted optical power, and divergence angle; 2) free-space communication link are: FSO link

distance, orientation of optical channel and propagation medium 3) receiver unit are: aperture diameter, receiver sensitivity as well as receiver's field of view (FoV). Moreover, the overall system performance is evaluated based on well-known quality of service parameters such as SNR, BER, etc. FSO technology experiences major restrictions in terms of link distances due to operation at wavelengths within visible as well as Near Infrared (NIR) part of the optical spectrum. Apart from the Line-of-Sight (LoS) requirements, the most significant challenge for FSO communication is because of transmitting medium (in the most cases free-space atmosphere) causing various optical signal impairments including extinction, fading and phase-front distortions ***[3]***. Especially this is a crucial issue for long-distance terrestrial (> 0.5 km) as well as ultra-long ground-to-space/space-to-ground (> 500 km) links, which are the core topic of the thesis ***[4]***. Nevertheless, FSO technology with its tremendous performance (bandwidth) is applied in variety of conventional as well as emerging scenarios. The implementation of FSO technology in long backhaul networks as well as 'Last Mile' communication successfully compete with RF bands ***[3]***, ***[4]***. Addressing the higher information capacity demands of the next generation 5G networks, FSO technology offers 100 Gbps backhaul links over distances of several kilometres, which surpasses more than 10 – 100 times the performance of the RF available solutions ***[5]***. This is still not comparable with optical fiber backbone networks having 1 Tbps data rates combined with elastic allocation of resources ***[6]***. Furthermore, last mile FSO approach easily allows reaching 1 Gbps data throughput based on cheap and commercially available systems [7]. In addition, FSO is applied in variety of emerging ultra-long-distance scenarios including Low Earth orbit (LEO), Medium Earth Orbit (MEO) and Geostationary Equatorial Orbit (GEO) satellites as well as High Altitude Platform (HAP) systems. Currently, the implementation of FSO communication approach between those space borne units aims to overcome bandwidth limitations in RF part of the spectrum ***[8]***, ***[9]***. In addition, optical wireless technology is considered as the major candidate for establishing ultra-long-distance communication links for interplanetary missions to Moon, Mars, Venus, etc. ***[10]***. Similar to conventional terrestrial links, FSO communication in deep space surpasses RF capacity in a range of 10 – 100 times ***[11]***. Especially this is true for FSO downlinks incorporating Superconducting Nanowire Single Photon Detectors (SNSPD) which for the case of Mars – Earth channel support even > 130 times higher data throughput than RF ***[10]***, ***[12]***. Without an exception, long-distance terrestrial as well as deep space FSO links communicating through Earth's atmosphere experience significant performance issues due to Mie scattering (fog and Cirrus clouds) as well as atmospheric turbulence-induced fading for which investigation the current thesis provides highly sophisticated approaches.

1.2 Research objectives and literature review

The limitations of RF spectrum in terms of channel capacity, leads to significant congestions and restrictions in transmitted data rates. According to Cisco Systems, the IP traffic is going to grow up to 4.8 Zettabytes per year by 2022, which is more than three times in comparison with 2017. Apart from video streaming, considerable amount of the future traffic will be dedicated to Machine-to-Machine (M2M) and Internet of Things (IoT) applications. The most significant part of mobile traffic will be devoted to smartphones. In particular, Ericsson

Company reports that transmitted data with smartphones will increase 10 times until 2022 in comparison with 2016. In other words, each month will be generated 60 Exabyte data traffic, which additionally applies more stringent requirements to the next generation 5G and 6G networks. FSO technology is a major candidate to support the foreseen tremendous data traffic *[4]*. The same is valid for ultra-long ground-to-space/space-to-ground links. According to National Aeronautics and Space Administration (NASA), the future interplanetary-channel distances should be increased up to 40 AU (1 AU = 149.6 million kilometres) with transmission rates reaching around 1 Gbps *[13]*. During last decades, optical wireless terrestrial technology underwent significant evolution from the proof-of-concept architecture with ~200 Mbps (*[14]*) to commercially available solutions with 10 Gbps data rates *[3]*. As it is stated in *[15]*, this tremendous performance is due to various novel advances in FSO technology including coding-, modulation-, diversity-, hybrid FSO/RF-techniques, which significantly boost the FSO system capabilities. In addition to data rates, the distances of FSO links significantly increases reaching near and outer (deep) spaces with space borne units located at millions of kilometres from Earth. More specifically, FSO systems are considered as an optimal solution for the revolutionary high-speed data rate connections in space. The future communication links between GEO's/LEO's orbit to ground should exploit fully the available channel information capacity with data rates more than 1 Tbps (*[16]*) in comparison to the mentioned 1Gbps in terms of deep space *[13]*. Both ESA and NASA organizations have worked over technology for development of fast FSO communication links in space during last decades *[10]*, *[17]*. Currently, in frame of EDRS program, which is a successor of the GEO satellite Alphasat that allows 1.8 Gbps FSO-based transmission over 45000 km, two GEO satellites relaying on the TESAT Laser Communication Terminal (LCT) are lunched *[18]*, *[19]*, *[20]*. In accordance with *[18]*, their architecture is based on coherent modulation scheme implementing homodyne BPSK at 1064 nm. On the other hand, NASA also plans to develop GEO optical relay terminals of first generation.

Having in mind these demands and achievements, FSO systems with their tremendous bandwidth are considered as a very practical solution is respect to variety of long-haul terrestrial and space applications. However, those ground-to-space/space-to-ground and ground-to-ground FSO links are highly vulnerable to tropospheric influences comprising mainly Mie scattering (fog and clouds) as well as atmospheric turbulences *[21]*. Those effects normally lead to considerably high attenuation easily violating the LoS requirement and partly or completely blockage of FSO communication links, which raise the always-important topic for reliability and availability of FSO systems in the presence of adverse weather conditions. The accomplished thesis work in terms of long-haul (terrestrial and interplanetary) links is considered as an important contribution to the atmospheric channel characterization of long-distance FSO, which is not easily accessible for experimental campaigns. Considering atmospheric physics including extinction processes as well as atmospheric turbulence-induced fading, the presented approach is extremely helpful for validation of significantly longer links, barely demonstrated in reality. Similar to the already accomplished ESA's FSO experimental campaign with ARTEMIS GEO satellite *[22]*, the current work mainly intends to support long–haul channel characterization possibly applied

in future interplanetary missions to Mars, Venus, etc. Having motivated by the faced challenges in FSO communication, due to physical processes in the Earth's atmosphere, the thesis at first offers a state-of-the-art analysis regarding the significant achievements in FSO link characterization as well as previous and future near and deep space missions.

1.2.1 Estimation of atmospheric FSO channel

The main issue in realization of long-distance wireless optical links is due to atmospheric effects including Mie scattering and atmospheric turbulence *[21]*, *[23]*. In particular, Mie scattering comprising fog and clouds is well investigated in the literature. The theoretical approach developed by Mie, which is based on Maxwell`s equations investigates in detail the interaction between water particles and the applied optical communication wavelength *[24]*, *[25]*, *[26]*. To address the atmospheric fog and clouds attenuation, in addition to Mie theory, the microphysics of both phenomena is further investigated. More specifically, models for Liquid Water Content (LWC) and Particle Size Distribution (PSD) are under scrutiny in the context of theory and empirical measurements *[27]*, *[28]*, *[29]*. Due to high complexity of merging together Mie theory and particles' microphysics, a few empirical approaches considering atmospheric meteorological optical range measurements are applied, including Kim, Kruse and Al Naboulsi models *[30]*, *[31]*, *[32]*. Furthermore, various studies and measurements performed in different locations support the analytically developed theoretical and empirical models *[33]*, *[34]*. Comparison between measurements of continental fog in Graz, Austria and maritime fog in La Turbie, France is performed in *[23]*, *[35]*. In addition, channel characterization considering fog attenuation in Graz, Milano and Nice is provided in *[36]*. Cloud events are rarely considered in the literate due to their too high attenuation, normally fully terminating the ground-to-space/space-to-ground FSO links. In *[38]* authors proposed several possible approaches for evaluation of clouds' optical attenuation involving Mie theory, cloud microphysics as well as Kim, Kruse empirical models. Moreover, a maximum-likelihood sequential detection together with equalization is considered in *[39]*, which is performed in time, in order to fight the outages regarding various types of clouds. Even in this arrangement, only clouds characterized with negligible optical thickness (optical attenuation) are able to be faced, which is again a challenge for the low amount of optical received power regarding deep space FSO communication.

Atmospheric turbulence-induced fading is of decisive importance in terms of long-distance FSO communication links. Turbulence theory is mainly based on Kolmogorov spectrum, which provides information regarding the changes in the atmospheric refractive index causing optical power penalties due to fluctuations in the received signal *[40]*, *[41]*, *[43]*. The three most applied and well-built atmospheric turbulence models available in *[43]*, *[44]* are Gamma – Gamma, Log – Normal and Negative Exponential ones, which estimate the Probability Density Function (PDF) in respect to received irradiance changes due to weak, medium and strong turbulence-induced fading. Atmospheric turbulence is a major problem regarding deep space FSO communication between Earth and outer space. Since the very first conducted analytical study of scintillation influences over FSO space communication link done in *[45]* by Fried, various experiments were performed. Significant part of them were accomplished until 2012 by National Institute of Information and Communications

Technology (NICT) in collaboration with European Space Agency (ESA) ***[46]***. The first GEO to ground bidirectional data optical link extensively used for characterization of the atmospheric turbulence channel is established between Artemis satellite and La Teide Observatory at Tenerife, Spain ***[22]***. Apart from the provided BER performance regarding the considered FSO communication uplink (average BER = 10^{-3}) and downlink (average BER = 10^{-7}) in ***[22]***, the applied data analysis shows that atmospheric turbulence is charterized with typical refractive index structure parameter C_n^2 within the range of 10^{-15} – 10^{-22}. In ***[47]***, two measurement campaigns involving Artemis satellite are presented, which goal is to mitigate atmospheric uplink induce fading considering transmitter diversity technique with only one laser source. Experimental data regarding famous Kiodo campaign between Japanese LEO OICETS (Optical Inter-orbit Communications Engineering Test Satellite) and the DLR's Optical Ground Station (OGS) in Oberpfaffenhofen, which are provided in ***[48]***, show the fluctuations of received optical downlink power obtained by means of pupil plane and differential image motion monitoring cameras. Moreover, detailed atmospheric turbulence-induced fading measurements in respect to Kiodo campaign are given in ***[49]***. Another new initiative of NICT provided in ***[50]***, is the SOCRATES satellite having laser transmitter terminal on board used for investigation of the scintillation effect based on a transmitter with four lasers and error correcting codes. The findings within both campaigns including OICETS and SOCRATES satellites are well compared in ***[51]*** and the results are processed in terms of estimating a good enough approximation model, which represent the deviation of the received optical downlink power. In parallel with those initiatives involving tremendous resources, a vertical profile of refractive index structure parameter used for investigations of clear-air scintillations in terms of space-to-ground downlinks is well approximated based on Radiosonde Observation (RAOB) data ***[52]***, ***[53]***. In particular, the impairments of terrestrial as well as near and deep space optical communication downlinks due to atmospheric turbulence-induced fading are examined by means of RAOB in ***[54]***. Moreover, the first try for comparison between RAOB and Kiodo measurement campaign is proposed in ***[54]***.

In comparison with the easier accessible terrestrial long-distance FSO communication links, the evaluation of deep space wireless optical commination channels need to be preliminary addressed in controlled laboratory environment before to be tested within a real scenario. For this purpose, NASA created an advance Technology Readiness Level (TRL) scale, which indicates the maturity of the examined technologies ***[55]***.

The FSO propagation path though free-space atmosphere is emulated based on a few hardware and software approaches. One approach for testing the performance of wireless optical systems in various tropospheric conditions is based on artificial laboratory chambers ***[56]***, ***[57]***. Although those arrangements are claimed to offer a satisfactory fog- and atmospheric turbulence-testing environment, their tiny proportions cannot fully emulate a FSO channel. Another unconventional method for simulation of a real link is proposed in ***[58]***. In this work, authors use the 50 m Koruza indoor corridor (**Chapter 5.3**) together with a few artificial fog and smoke sources, which are capable to address a minimum Mie scattering visibility of 0.02 km, namely maximum 150 – 230 dB/km measured optical

attenuation. Since building one the first well-documented porotypes relying on mechanical system with rotating phase screens given in ***[59]***, atmospheric turbulence fading was further represented by a few more compact designs considering external optical intensity modulators. Furthermore, the clear-air atmospheric scintillation influences are introduced in ***[60]*** based on self-made (Variable Optical Attenuator) VOA-based fading emulators operating independently from each other and supporting response time up to 2 μs. Moreover, DLR built the testbed TRUST aiming to evaluate FSO feeder link communication between ground and a GEO satellite. The two terrestrial FSO transceivers are installed at 26 km distance from each other and ~800 m difference in respect to their elevation, which allows the worst outer space FSO scenario with 2° elevation angle and 125 mm receiver aperture in the presence of strong atmospheric turbulence ($C_n^2 = 10^{-12}$) to be evaluated ***[16]***. Along with the offered hardware, a software tool for characterization of a FSO deep space communication link based on Serially Concatenated Pulse Position Modulation (SCPPM) encoder and Additive White Gaussian Noise (AWGN) channel operating in the presence of atmospheric turbulence with 0.05 – 0.3 scintillation index is proposed in [61], which provides 3 – 4 dB gain. Contrary to those vague simulations, emulating AWGN link, a high-accurate FSO Poisson channel modelling is offered in ***[62]***. The simulated results in support to the Deep Space Optical Communication (DSOC) mission initiated by NASA, proved that Mars – Earth deep space FSO communication downlink can operate up to 256 Mbps and ~2 dB away from the given non-fading information capacity. While atmospheric turbulence scintillations and Mie scattering (clouds) are not taken into account in ***[62]***, there are specifically developed software tools including the work in ***[63]***, where Mie scattering (clouds) attenuation is introduced based on European Centre for Medium-Range Weather Forecasts (ECMWF) data. In addition, sensors for temperature, density and humidity are used in ***[64]*** to characterize the continental fog impairments.

1.2.2 Long-distance (deep space) FSO communication

The most high demanding telecommunication scenarios involve ultra-long deep space-to-ground distances. Currently, wireless data transmission technology relies on RF spectrum to relay data over long-haul 10^5 – 10^9 km links, which is mandatory for near-Earth planet's observation including Moon, Venus, Mars, Saturn, Jupiter, etc. ***[66]***. The missions to Mars involving Mars 2020, InSight, MAVEN, ExoMars, etc., are realized within UHF/X band limiting the data rates up to 2 Mbps ***[67]***. Another utilized option, which significantly boost the data throughput, is communication link within Ka-band RF spectrum. While Ka-band provides ~4 times the information capacity of X-band, this option leads to an additional challenge due to larger antenna's apertures, namely greater weight as well as higher power consummation demands. Even though, this technology progress is evaluated as a significant accomplishment, the all advances in the area of measurement equipment and sensors development impose new demands in respect to data throughput. The Venus Synthetic Aperture Radar (VenSAR), which is built in the frame of the planned Envision mission to Venus, delivers up to 1.25 Terabits per day ***[68]***. In other words, if Ka-band featured with maximum 10 Mbps data throughput is the technology of choice, again a bottleneck challenge will be introduced. Having in mind these restrictions, deep space FSO communication

emerged as the best option to support this high-demanding data transfer. In particular, the new information capacity requirements due to more sophisticated remote sensing technologies such as Light Detection and Ranging (LIDAR) and RADAR as well as future goals for full High Definition (HD) video transmission involves state-of-the-art optical communication links based on single-photon detection *[12]*. This type of High Photon Efficiency (HPE) FSO communication was already envisaged back in 1981, when J. Pierce published one of his famous works *[69]*, modelling a photon-counting channel obeying Poisson distribution. With the substantial technological advances and appearing of pioneering SNSPDs, deep space single-photon communication is already subject to standardization by Consultative Committee for Space Data Systems (CCSDS) described in details in **Chapter 7** *[70]*, *[71]*. The previously accomplished Lunar Laser Communication Demonstrator (LLCD) by NASA, which implements 16 SNSPD's array, allows the tremendous 38 – 622 Mbps FSO communication downlink between Moon and Earth *[13]*, *[72]*. The success of LLCD leads to preparing and lunching soon a similar mission to Mars/Venus, namely Deep Space Optical Communication (DSOC) demonstration involving revolutionary 64 SNSPD's array at distance up to 2.7 AU and data rate of 267 Mbps *[12]*. Both missions are based on IM/DD modulation schemes implementing Pulse Position Modulation (PPM) at 1550 nm wavelength, which is the most appropriate design in respect to ultra-long-distance deep space FSO links. The capabilities of SNSPD raise a possibility for implementation of deep space FSO links in other high-demanding scenarios part of future planned ESA missions. In particular, the Envision mission to Venus, planned for 2032, is considered as a challenge with its 1.25 Tb/day *[68]*. Similar to LLCD and DSOC, in order to cope with the large amount of collected VenSAR data equivalent to ~15 Mbps throughput, the RF link should be accompanied by FSO communication (Hybrid RF/FSO) *[73]*.

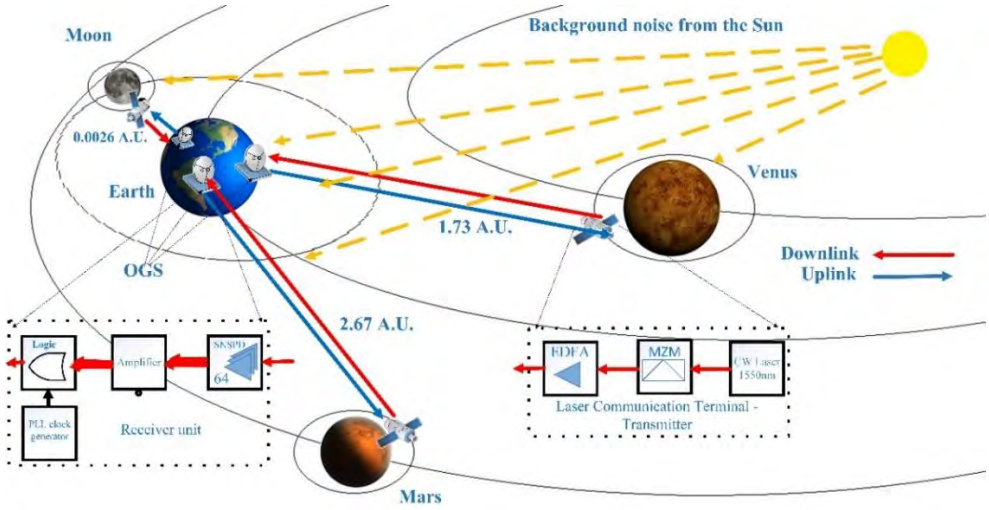

Figure 1.1: Deep space FSO communication scenario based on TESAT and LLCD laser communication terminals

In general, deep space FSO data transmission link are asymmetric that results in mainly downlink FSO data transmission. This is especially true for the listed above deep space

missions where high amount of telemetry data are send back to Earth, which fact is well considered in the provided design by CCSDS standards *[70]*. Consequently, only downlink FSO architecture case is implemented in the current work, while uplink with its different specifics is subject to further work. Taking into account *[18]*, *[74]* and *[75]*, TESAT LCT with which Alphasat and EDRS GEO satellites are equipped on board as well as the architecture of the space borne FSO transmitter used in LLCD and DSOC missions result in a common design regarding FSO transmitter part. While the TESAT LCT module is based on coherent scheme with external phase modulator, the current design is adhered to IM/DD scheme with external intensity Mach-Zehnder Modulator (MZM) used in deep space (LLCD mission, etc.) In particular, the transmitter unit given in the self-drawn ***Figure 1.1*** is based on Master Oscillator Power Amplifier (MOPA) technology, which incorporates continuous-wave (CW) laser at 1550 nm, MZM and Erbium-Doped Fiber Amplifier (EDFA).

	TESAT LCT *[18]*	LLCD *[74]*	Artemis *[22]*
Communication wavelength	1064 nm	1550 nm	819 nm
Modulation	BPSK	16-PPM	2-PPM
Beam divergence	10 µrad	16.2 µrad*	20.8 µrad
Transmitted optical power	2.2 W	0.5 W	10 mW
Telescope diameter	0.135 m Duplex	0.107 m Duplex	0.25 m
Downlink data rate	1.8 Gbps	620 – 38 Mbps	2 Gbps
Distance	45000 km	400000 km	35787 km
Total power	160 W	90 W	-
Total mass	53 kg	30 kg	-

Table 1.1: Comparison between LCT operational parameters of the three most prominent TESAT, LLCD and Artemis downlinks' optical transmitters

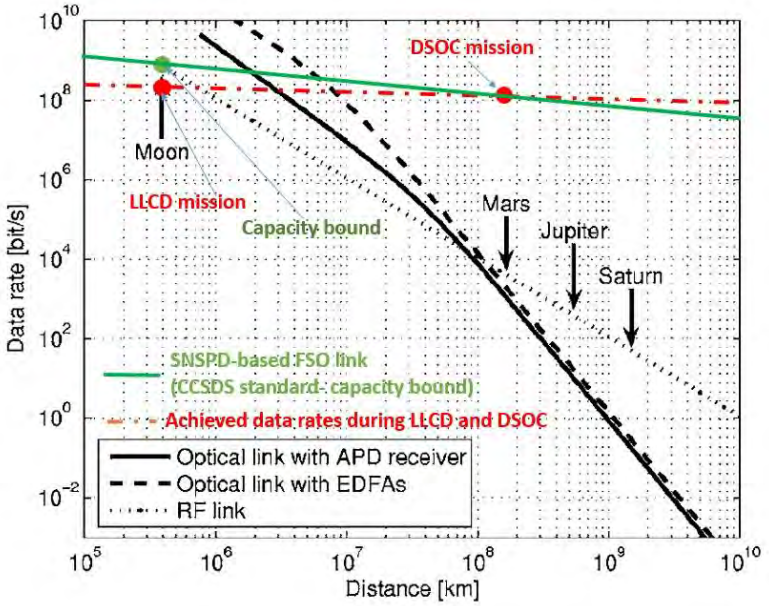

Figure 1.2: Comparison of deep space communication data rates in respect to RF, conventional FSO with APD receiver (with/without EDFAs) and SNSPD-based FSO systems (Modified figure taken from [66])

Apart from the outstanding output beam quality and appropriate power consummation, this configuration delivers the required flexibility in respect to tuning the output optical power, peak-to-average optical power ratio, laser linewidth as well as pulse shape and width ***[76]***. In particular, based on last technological advances, the average transmitted optical power at output of MOPA reaches ≤ 10 W, while the peak power is in the range of 0.1 – 1 kW ***[11]***. Moreover, in accordance with ***[11]***, the beam width for typical deep space downlink is 2 – 8 μrad. In comparison to the high similarity in respect to the transmitter part, the receiver part installed in OGS, which is located on ground, is completely different. While for TESAT LEO/GEO LCT-to-Earth link, the receiver utilizes a Positive-Intrinsic-Negative (PIN)/Avalanche Photodiode Diodes (APD) ***[20],*** the breakthrough deep space missions to Mars, Venus and Moon implements SNSPD-based receiver architecture whose draft design is also offered in ***Figure 1.1***. Furthermore, a comparison between TESAT LCT and LLCD LCT together with the already considered Artemis LCT is provided in ***Table 1.1***.

Having addressed the different technological approaches to design a deep space-to-ground communication system, a comparison between data throughput for the case of a RF link, a conventional FSO (with/without EDFAs) based on APD as well as a SNSPD-based FSO channel is given in ***Figure 1.2***. While the figure is obtained from ***[66]***, here a self-modified version is applied, which includes the outstanding results during LLCD and DSOC missions as well as the recommendations of CCSDS in respect to maximum information capacity (the minimum 0.125 ns slot width of the considered PPM modulation) ***[70]***. It is evident that there is not currently another alternative to single-photon-based FSO communication downlinks, which reach data rates of ~ 300 Mbps at Earth-Mars distance and beyond.

1.3 Thesis organization and contribution

Vulnerability of FSO technology to atmospheric conditions, leads to significant performance issues. While short terrestrial links for commercial needs, which do not exceed 1 km distance, are still in position to mitigate those problems, this is not the case for longer and especially ultra-long (space-to-ground) links. Since the current thesis deals with long-distance FSO communication, the tropospheric effects including Mie scattering as well as atmospheric turbulence-induced fading are of decisive importance. Regarding terrestrial FSO links, the influence of atmospheric conditions is evaluated by means of theory, real measurements as well as experimental demonstrations. In general, long-haul space-to-ground downlinks implementing state-of-the-art mitigation techniques require enormous resources for real measurement campaigns. Therefore, the two main persuaded approaches within current work are breadboarding and simulations that profitable combination converge to development of custom-made laboratory testbed incorporating a pioneering VOA-based channel emulator. Furthermore, the developed and the adapted simulations based on MATLAB programming environment merge theoretical models as well as atmospheric characterization in terms of real measurements. To the best of authors' knowledge, the concept for an alternative approach to real tests and measurements in respect to VOA-based channel emulator accompanied by SNSPD-based testbed was officially offered for first time

in media within two high-quality published documents (*[77]*, *[78]*), which are part of the current work.

From architecture point of view, FSO systems are subject to strong parameterization, which serves as useful tool for achieving the performance goals. Moreover, they are influenced by considerable amount of probabilistically defined factors, which include mainly atmospheric effects, but also misalignments caused by vibration as well as background noise due to artificial and real light sources. Given this fact, **Chapter 2** offers a state-of-the-art link budget analysis that integrates in a new way the available approaches with their similarities and differences in contrast to RF communication. Contrary to the most link budget characterizations offering only a solution in terms of simple uniform beam wave (*[42]*), the used approach also favours the employment of TEM_{00} Gaussian intensity profile describing precisely the behaviour of a real scenario. Besides, a new solution for dealing with vibration losses in terms of optimization regarding the divergence angle of an optical source and its contribution to full link budget equation is given in *[79]*. In order to align with the main objectives, once the free-space atmospheric impairments are introduced, **Chapter 3** offers complete FSO channel characterization. Although other atmospheric effects such as snow and rain are examined, the main emphasis is placed on Mie scattering – fog attenuation < 450 dB/km and cloud attenuation values between 0.37 dB/km and ~600 dB/km – as well as atmospheric turbulence with an average optical power penalties < ~10 dB. In particular, the carried out analyses involve and unite various theoretical and empirical models, which are implemented based on applied mathematics' approaches with accent on special functions, statistics and probabilities. Nevertheless, they cannot substitute a real evaluation for which the current work proposes a futuristic solution in respect to implementing and testing a pioneering VOA-based channel emulator given in **Chapter 4**. With its compact size, the hardware emulator is used for verification of long and ultra-long FSO link distances. Relying on specially developed GUI application, two types of VOAs – 850 nm (MM) Multi Mode – VOA and 1550 nm (SM) Single Mode – VOA – are integrated that offer controlled attenuation up to max 60 dB, while the fading frequency can be raised up to 200 Hz (absolute maximum 1 kHz) *[80]*, *[81]*. Moreover, BER performance analysis of the developed unit is conducted with a high-end Small Form-factor Pluggable (SFP) transmitter solution allowing representation of a real terrestrial 850 nm FSO communication link.

By means of theoretical and empirical models which merge into various simulated results, both ECMWF and RAOB databases are tested and applied in **Chapter 5** and **6** *[80]*, *[82]*. In particular, state-of-the-art solutions for determining fog and cloud optical attenuation involve Mie theory, measurements and VOA-based hardware channel emulator, all serving as evaluation techniques in **Chapter 5**. The findings show that the only manageable disruptions for a space-to-ground FSO downlink operating in clouds is caused by Cirrus (up to 12 dB optical attenuation) with ~22 % coverage in respect to the estimated time, while nearly all other clouds lead to full LoS FSO blockage. In order to have an alternative to the developed VOA-based FSO link emulator, the 50 m Koruza fog channel developed by IRNAS Institute involving two artificial fog and haze sources is charterized by means of Laser Diffraction System (LDS) and post data processing with Mie theory analysis *[83]*.

Regarding atmospheric fog, a measurement campaign's database from Graz, Austria is post-processed in respect to its light and thick continental fog records. For the measured 2.7 km terrestrial FSO link, also the clear-air atmospheric turbulence is introduced in **Chapter 6** employing RAOB data from Vienna, Austria. Moreover, the impact of atmospheric scintillations in respect to a space-to-ground downlink for three aperture diameter sizes (1 m, 1.5 m, 8 m) and two elevation angles (20° and 30°) is introduced ***[82]***, ***[84]***.

Chapter 7 is considered as the most significant contribution of the current work to the area of FSO technology, which can find application in various emerging space-to-ground communication scenarios. In particular, it investigates in detail still state-of-the-art deep space wireless optical links, which are the most critical long-distance FSO channels in terms of range and atmospheric effects. The HPE FSO link is realized with a single-photon detector implementing cutting-edge SNSPD technology, which is subject to real conducted measurements showing ~40 % quantum efficiency, ~300 Hz Dark Count Rate (DCR), ~20 ns dead time (DT) ***[84]***, ***[85]***. Moreover, the developed MATLAB simulations investigated fully the BER performance of deep space FSO links in the presence of atmospheric scintillation effects with 0.55 – 5.2 dB optical power penalties simulated in **Chapter 6** ***[82]***, ***[86]***. For this purpose, Poisson channel modelling with emphasis on Poisson Point Processes (PPPs) is applied. In order to support the analyses in **Chapter 5** and **6** as well as the aforementioned performed MATLAB modelling, a self-developed breadboard for investigation of ultra-long-distance FSO communication links is presented in **Chapter 7**. The self-designed testbed architecture in ***[77]***, which is partly developed within ESA's Hybridised Optical/RF Payload Data Transmitter study (***[73]***), implements the already built channel emulator (***[78]***) as well as the futuristic SNSPD receiver unit, which is one of the most crucial components regarding a space borne FSO communication links. The assessments of SNSPD as well as VOA-based channel emulator in respect to highly mitigated atmospheric turbulence scintillations with < 0.55 dB attenuation, shows a decent performance at the maximum 1 kHz fading frequency ***[85]***, ***[87]***.

During the process of preparing the current work, the author published subnational part of his state-of-the-art contributions in well-referred conference proceedings, journal papers, book chapters and a project report. The aforementioned documents, which proved the originality of the solved problems and results are listed in the **Own publication** section. Moreover, their contribution is well presented in the written thesis.

Chapter 2

2. Link budget analysis

FSO systems offer very high performance in terms of bandwidth and data throughput respectively. However, various factors need to be taken into account during manufacturing process in terms of achieving desired system characteristics and more specifically supporting high enough reliability and availability levels. In general, the availability is considered to be satisfactory when the implemented FSO technology complies with the five nines agreement ***[88]***. Nevertheless, this goal is difficult to be attained due to atmospheric effects such as Mie scattering and atmospheric turbulence leading to optical signal impairments. Furthermore, the used laser technology operating within NIR spectrum require LoS propagation accompanied with very precise alignment while the divergence angle is kept to a minimum. Consequently, the transmitted optical power and receiver sensitivity should be very carefully selected by means of accurate link budget calculations that is an important step for achieving the set goals within the current thesis.

2.1 Unified RF/FSO link budget calculations

To address the main parameters as well as constrains of FSO systems, a link budget analysis valid for all types of wireless optical communication links is provided. By analogy with the RF communications, the link budget of a FSO system could be calculated based on concept involving directivity of the transmitter and receiver antennas. In general, the definition for Effective Isotropic Radiated Power (EIRP) is introduced in terms of measuring the antenna's possibility to concentrate the RF signal in one direction. Although FSO systems are characterized with high-directivity LoS transmission and consequently it is not necessary to be considered the antenna gain, this model allows unification of the applied theory regarding evaluation of RF and optical communication technologies. When the transmitted FSO beam has uniform radial irradiance profile with transmitted optical power P_{tn} [mW] in direction of the receiver, the obtained optical power P_r [mW] is calculated with Eq. (2.1) ***[89]***.

$$P_r = P_{tn} \frac{S_t S_r}{z_d^2 {\lambda_0}^2} \quad [mW] \qquad (2.1)$$

Where S_t and S_r are the areas of the transmitter and receiver antennas, z_d is the distance of FSO link and λ_0 is the operational wavelength. Nevertheless, FSO system generally transmits optical beam characterized with transverse Gaussian profile, which is explained by the fact that the majority of laser sources operates at TEM_{00} mode. Although the propagation through

the free space partly influences the optical field due to various possible atmospheric effects, it is well assumed that the fundamental mode is preserved. Assuming perfectly aligned FSO channel and applying a Gaussian instead of uniform beam profile leads to doubling the transmitted optical power in the direction of the FSO receiver, namely $P_t = 2P_{tn}$ ***[89]***. Nevertheless, uniform distribution is still well-accepted approximation for some long-distance space-to-ground FSO links for which the Gaussian beam profile is already considered as enough flat. Taking into account the Eq. (2.1) as well as the introduced RF concept considering receiver and transmitter antenna's gains, the equation for the received optical power P_r regarding FSO communication channels operating based on Gaussian distribution ($P_t = 2P_{tn}$) is provided in (2.2) ***[42]***.

$$P_r = P_t G_t G_r z_l \ [mW] \quad (2.2)$$

Where G_t is the gain of the transmitter antenna, G_r is the gain of the receiver antenna and z_l is the loss due to free space, all of which are provided in Eq. (2.3), Eq. (2.4) and Eq. (2.5). Moreover, considering EIRP definition given in ***[90]***, the EIRP = $P_t G_t$.

$$z_l = \left(\frac{\lambda_0}{4\pi z_d}\right)^2 \quad (2.3) \qquad G_t = \frac{4\pi}{\Omega_t} \quad (2.4) \qquad G_r = \frac{4\pi S_r}{\lambda_0^2} \quad (2.5)$$

The solid angle Ω_t, which depends on divergence angle of the emitted laser beam θ_t, describes the directivity of transmitter optics antenna. In particular, the divergence of the transmitted optical beam is due to diffraction effect determined by initial Gaussian beam radius r_0 as well as λ_0. More specifically $\theta_t = \lambda_0/\pi r_0$. Having in mind that FSO systems are featured with very small divergence angles between 1 – 8 mrad, which lead to applying the following approximation regarding solid radiation angle.

$$\Omega_t = 2\pi(1 - cos\theta_t) \approx \pi\theta_t^2 \quad (2.6)$$

In general, instead of using optical power in [mW], the link budget involves logarithmic scale, which allows representation of all values in a short range. Consequently, the optical power is calculated in [dBm] and the optical attenuation in [dB] (Eq. (2.7) and Eq. (2.8)).

$$P_{dBm} = 10log_{10}\frac{P_{mW}}{1mW} \ [dBm] \quad (2.7) \qquad A_{dB} = 10log_{10}\frac{P_{1\_mW}}{P_{2\_mW}} \ [\text{dBm}] \quad (2.8)$$

Where P_{1_mW} and P_{2_mW} are two exemplar power levels. Considering the introduced logarithmic scale, the Eq. (2.2) can be presented in logarithmic form provided in (2.9).

$$P_r[dBm] = P_t[dBm] + G_t[dB] + G_r[dB] + z_l[dB] \quad (2.9)$$

The provided FSO link analysis can be used to express various system properties of the considered FSO communication link. In particular, the system power figure, which corresponds to system power margin, is calculated based only on the internal properties of FSO transceiver units. Where a_{sys} represents all system losses related to selected components ***[35]***.

$$P_{sys}[\text{dBm}] = P_t[dBm] + G_t[dB] + 20\log(S_r)\,[dB] - \sum a_{sys}\,[dB] \quad (2.10)$$

When the link distance (path losses A_p) is introduced, the amount of the received power P_r is defined. It should be noted that P_r is calculated without deteriorating atmospheric influences to be considered ***[35]***.

$$A_p = 20\log(2z_d)\,[dB] \qquad P_r[\text{dBm}] = P_{sys}[\text{dBm}] - A_p[dB] \quad (2.11)$$

2.2 Link budget analysis based on FSO specifics

In general the transmitted optical power from the laser source P_t [dBm] is attenuated due to several important factors including losses in the transmitter and receiver antenna's optics $A_{tr,opt}$ [dB], $A_{r,opt}$ [dB], geometrical losses A_{geo} [dB], misalignment losses A_{mis} and atmospheric attenuation A_{atm} [dB], which is the major problem and the core topic of the current thesis work. The received optical power P_r [dBm] is calculated based on Eq. (2.12) ***[79]***.

$$P_r = P_t - A_{tr,opt} - A_{geo} - A_{atm} - A_{r,opt} - A_{mis} \ [\text{dBm}] \quad (2.12)$$

Each selected optical receiver is characterized with sensitivity P_{r_min} [dBm], which corresponds to the minimum received optical power necessary to attain a certain BER (SNR) value. FSO systems usually have satisfactory performance when the BER has values between 10^{-6} and 10^{-12} ***[89]***. Once the sensitivity P_{r_min} is introduced the link margin M [dB] is calculated in (2.13).

$$M = P_t - P_{r,min} - A_{tr,opt} - A_{geo} - A_{atm} - A_{r,opt} - A_{mis} \ [\text{dB}] \quad (2.13)$$

Larger link margins allow FSO system to tackle with more severe atmospheric attenuation, which is important in terms of the constantly changing weather conditions. In particular, M [dB] can be increased in case either transmitted laser power in increased or receiver sensitivity is decreased. In addition, M can be improved in terms of applying mitigation technique. The first considered attenuation is due to non-ideal transparency of the implemented lenses in FSO transmitters and receivers ***[79]***.

$$A_{tr,opt} = A_{r,opt} = -10log_{10}(\tau) \ [\text{dB}] \quad (2.14)$$

Where τ is the transparency factor, which obtains values within the range of 0 and 1. The second significant issue is regarding the geometrical losses, which are explained with diffraction theory and are solely related to FSO system design. In other words atmospheric propagation link does not contribute to this problem. In general, transmitted optical beams have a Gaussian intensity profile, which is true for most offered laser sources and corresponds to TEM_{00} mode. The geometrical losses and the initial Gaussian beam radius are given in Eq. (2.15) and Eq. (2.16).

$$A_{geo} = 20lg\left[\frac{\sqrt{r_0{}^2 + (\theta_t z_d)^2}}{\sqrt{2}R_r}\right] [dB] \quad (2.15) \qquad r_0 = \frac{\lambda_0}{\pi\theta_t} \quad (2.16)$$

where z_d is the distance of FSO link, λ_0 is the operation wavelength, R_r is the radius of the optical antenna and θ_t is the divergence angle of the transmitted laser beam. The next losses are due to misalignments, which are caused by mechanical movements, building sway and mounting inaccuracies during the installation phase ***[89]***. The Eq. (2.17) provides the relation between the undesired deviations θ_d and divergence angle θ_t of the transmitted beam ***[79]***.

$$A_{mis} = 8.686 \left[\frac{\theta_d}{\theta_t}\right]^2 [dB] \quad (2.17)$$

In the ideal case, the deviation angle $\theta_d = 0°$ which leads to FSO system without misalignment losses. Finally, atmospheric attenuation mostly due to Mie scattering A_{tt} and atmospheric turbulence A_{tur} impairments, which are fully investigated in the current thesis, are introduced (Eq. (2.18)).

$$A_{atm} = A_{tt} + A_{tur} \ [\text{dB}] \quad (2.18)$$

An example for link budget calculations regarding terrestrial long-distance FSO system is considered based on following system parameters: laser beam with Gaussian intensity profile; $P_t = 10$ dBm; $\theta_t = 1.3$ mrad; $z_d = 2$ km; $\tau = 0.85$; $\lambda_0 = 850$ nm; $P_{r,min} = -28$ dBm (BER = 10^{-8}); $R_r = 0.1$ m; $V = 10$ km. The Mie scattering attenuation A_{tt} is simulated based on Kruse fog model and the given visibility $V = 10$ km for which calculations Eq. (3.21) and Eq. (3.22) are applied (**Chapter 3)**. The corresponding power level diagram is provided in ***Figure 2.1***.

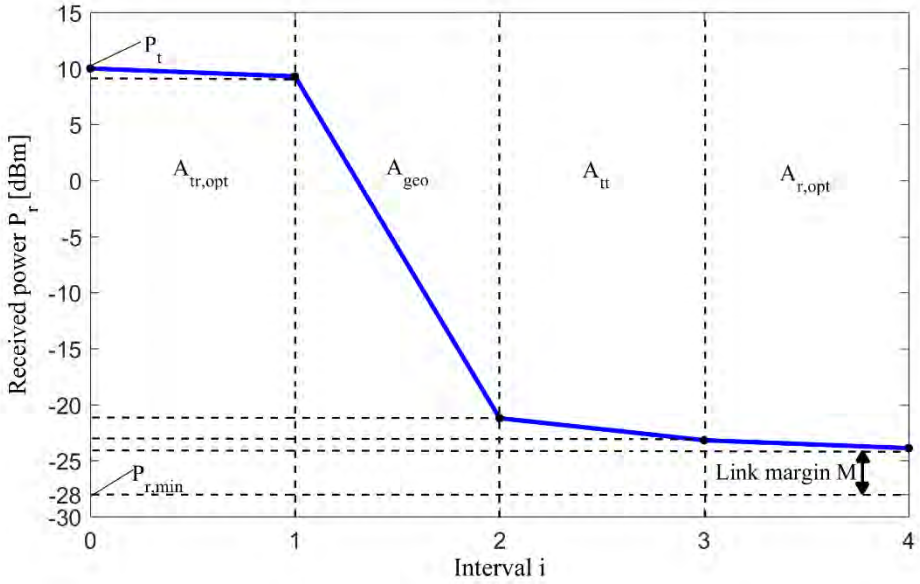

Figure 2.1: Power level diagram (The figure is obtained from own publication [79])

Where the interval i corresponds to: losses in the transmitter antenna's optics $A_{t,opt}$ i(0-1); geometrical losses A_{geo} i(1-2); Mie scattering attenuation A_{tt} i(2-3); losses in the receiver antenna's optics $A_{r,opt.}$ i(3-4). Due to the importance of misalignment losses A_{mis} and their

mitigation based on selection of an optimum divergence angle, an additional analysis is provided in ***Figure 2.2***. More specifically, θ_d versus available link margin M in dependence on θ_t is simulated based on Eq. (2.13) and Eq. (2.17).

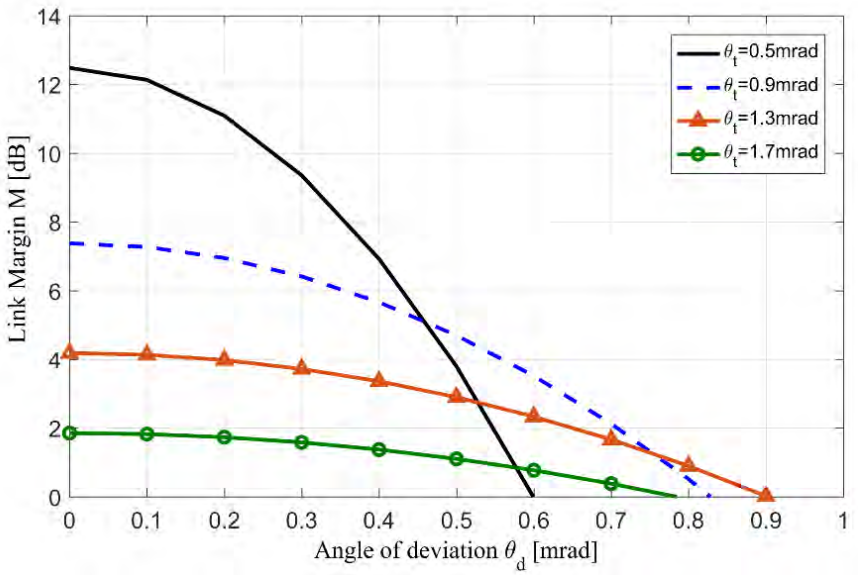

Figure 2.2: Link margin M versus θ_d for 4 different divergence angles θ_t (The figure is obtained from own publication [79])

When the divergence angle θ_t is increased up to one optimum value, due to Gaussian intensity profile, the FSO system is able to cope with larger deviation angles θ_d (≤ 0.9 mrad), while it operates with the same detector sensitivity ($P_{r,min} = -28$ dBm) corresponding to BER $= 10^{-8}$ ***[79]***.

Chapter 3

3. FSO atmospheric channel

The main atmospheric influences, which lead to significant deterioration of a FSO communication channel, are absorption, scattering as well as changes in temperature and pressure parameters. The optical attenuation properties of nearly all weather conditions comprising fog, clouds, rain, snow, scintillations and beam wandering are direct consequence of them. Usually their impact over wirelesses optical channel lead to substantial power losses and in some cases, complete blockage of the LoS link.

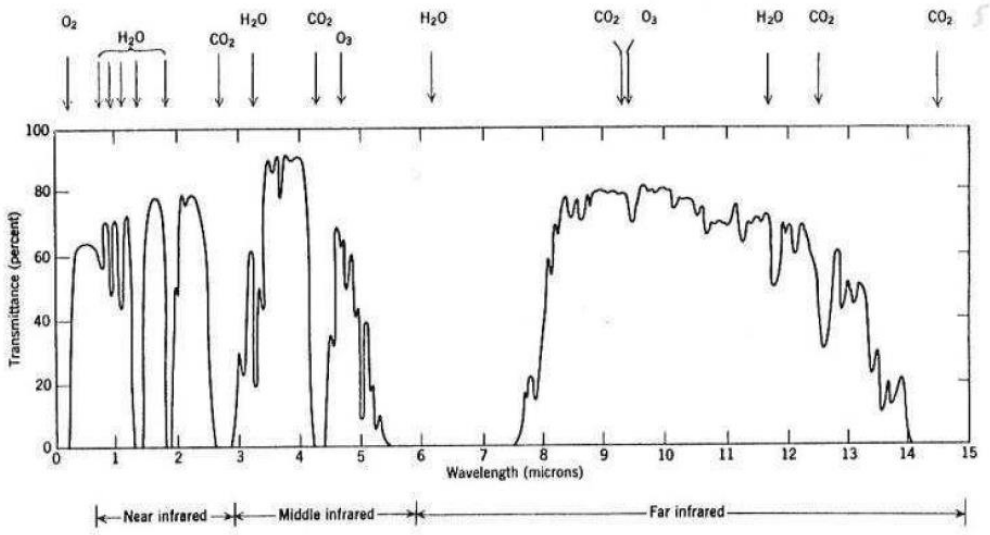

Figure 3.1: Transmittance of the atmosphere in terms of molecular absorption for 1.82 km horizontal channel at sea level (The figure is obtained from [91])

While absorption process is not observed in case of larger suspended particles (fog, clouds, rain, snow, etc.), it should be still taken into account in terms of air molecules. Absorption losses are explained by loss of photons' energy due to thermal processes. For each molecule, there is a specific absorption spectral line, which normally is additionally widen because of the Doppler effect. The transmittance of the atmosphere in terms of molecular absorption is provided in ***Figure 3.1 [91]***. The measurements are accomplished based on 1.82 km horizontal channel at sea level in a wavelength range of 0.1 – 14 μm. In particular, the

atmospheric gasses, which have impact over NIR part of the spectrum are N_2, O_2, H_2, H_2O, O_3 and CO_2. Where the highest optical attenuation is caused by H_2O, CO_2, O_2 and O_3 ***[92]***.

In general, for most FSO communication scenarios, the selected operation wavelength is in one of the special transmission windows. Considering NIR FSO communication, the two most often applied free of absorption windows are in the range of 780 – 850 nm and 1520 – 1600 nm. In some cases, also FSO communication at 1064 nm is used. Consequently, the utilized wavelengths also in terms of the current work are 780 nm, 850 nm and 1550 nm for which the attenuation due to absorption is lower than 0.2 dB/km and thus is neglected ***[92]***.

In addition to the absorption effect, FSO beam is influenced by scattering effect caused by various aerosols (mainly fog and clouds). In particular, the attenuation due to scattering process is explained by angular redistribution of the optical power, caused by molecules, water droplets or other suspended particles in the atmosphere. According to the theory, there are three main scattering regimes including Rayleigh, Geometrical and Mie scattering. Rayleigh scattering is observed mainly in case of air molecules and particles with radius < 0.1 μm, which corresponds to more than 10 times lower dimensions than the used wavelength ***[93]***. Having in mind the insignificant Rayleigh cross section of the air molecules, its effect over the transmitted optical beam is neglected. However, in case of larger suspend particles in the air, which have sizes comparable with the selected NIR wavelength, the optical attenuation is already substantial. In other words, this is the case of Mie scattering phenomenon, which happens when the radii of water droplets are larger than ~1 μm, namely between ~1 – 20 μm ***[94]***, ***[95]***. Consequently, the harshest atmospheric conditions in terms of wireless optical communication are due to fog and clouds causing optical attenuation up hundreds of decibels. Together with the atmospheric turbulence-induced fading with fluctuation frequency within 0.1 Hz – 1 kHz, which in practice is reduced to 0.1 – 200 Hz and reaches < 10 dB (**Chapter 6**), the availability of long-distance FSO is significantly affected ***[15]***.

3.1 Mie scattering effect: Fog and Clouds attenuation

In accordance with the International visibility code table, the most severe Mie scattering in respect to fog is attained during dense fog events having attenuation of 339.6 dB/km @778 nm wavelength for 50 m visibility ***[88]***. In the case of long-distance space-to-ground FSO links, the scattering is mainly caused by various cloud types, where the most problematic one are Cumulus clouds with vertical development leading to attenuation of ~600 dB/km ***[95]***. In both cases, a high concentration of water particles with radii, which are comparable with the selected communication wavelength, is observed. Furthermore, the fog effect can be divided into two types, namely maritime and continental fog that differ in the amount of imposed attenuation. The maritime fog is similar to clouds and according to ***[94]*** results in optical power penalties up to ~450 dB/km, which even exceeds the maximum optical attenuation provided in International visibility code table in ***[88]***. Moreover, this event is very unstable and can be characterized with large differences of the imposed attenuation for a 1-second period. In case of continental fog, the attenuation is substantially lower with a maximum peak approximately equal to ~120 dB/km ***[63]***. Furthermore, the fluctuations of the attenuation are significantly weaker or in other words, the continental fog is more stable.

In order to estimate the fog induced-attenuation in a FSO communication channels, two main approaches are applied. While the first method utilizes microphysical fog parameters and Mie scattering theory, the second approach applies empirically derived models. Regarding the first aforementioned method, the Particle Size Distribution (PSD) of the considered fog event should be measured.

3.1.1 Evaluation of Mie scattering attenuation in terms of Mie theory

The Mie theory is defined based on Maxwell`s equations, as it describes the interrelation between a random sphere and electromagnetism. Although Mie theory is an excellent tool for parametrizing various mediums, it is limited due to requiring the medium to be populated with particles having a spherical shape with negligible absorption. Nonetheless, the main atmospheric effects and especially fog and clouds events are extremely accurately represented by the theory, which allows sophisticated evaluation of their influence over a FSO transmitted beam. In the specific case, fog and cloud medium is built by suspended in the air spherical homogeneous drops of water characterized with a refractive index and diameter. Mie theory is a complex and effective method for computation of the optical properties of water particles ***[83]***. In particular, Mie theory is used to model extinction and more specifically scattering processes due to interaction of optical signal with the suspended water droplets, namely the scattering C_s and the extinction C_e cross sections. In respect to fog and cloud atmospheric conditions, the cross sections are the effective areas of interaction between a transmitted optical beam and a water droplet. Nevertheless, instead of an effective cross section, in general it is well accepted to be used scattering Q_s and extinction Q_e efficiencies. In addition, due to knowledge of the extinction and scattering cross selections, the Mie theory can be used for indirect approximated calculations of the average absorption efficiency $Q_a = Q_e - Q_s$. The three of them are provided in Eq. (3.1), Eq. (3.2) and Eq. (3.3) ***[24]***, ***[25]***.

$$Q_s(n_m, r, \lambda_0) = \frac{C_s(n_m, r, \lambda_0)}{G} \quad (3.1) \qquad Q_a(n_m, r, \lambda_0) = \frac{C_a(n_m, r, \lambda_0)}{G} \quad (3.2)$$

$$Q_e(n_m, r, \lambda_0) = \frac{C_e(n_m, r, \lambda_0)}{G} \quad (3.3)$$

Where G is the real cross section area of a particle corresponding to a projection onto a perpendicular plane and n_m is the complex refractive index ***[83]***. In other words, G is equal to πr^2. Due to small particle sizes, the rules of geometric optics cannot be applied and consequently the effective area C_s can be larger than the real cross section. Mie efficiency is not limited up to one and can obtain variety of different values, which is clearly showed in the forward calculations of Mie scattering efficiency. Nevertheless, before considering the listed efficiency parameters, the scattering and extinction cross sections should be defined. To address the Mie theory, specific knowledge regarding the propagating medium are required, namely the value of complex refractive index. While this could be not an easily feasible task for some atmospheric aerosols, the n_m is very well defined in terms of water particles. Considering the wavelength dependence of n_m, the water refractive index has values between $1.33 + i1.96\ 10^{-9}$ for 550 nm up to $1.21 + i0.05$ for 10 μm ***[26]***. Once n_m is known for the applied FSO wavelength, scattering and extinction cross sections, which are basically effective areas of interaction between the transmitted optical beam and a water droplet, are determined. In particular, the extinction cross section of a particle is equal to the

equivalent area, which suspends the same amount of energy, lost through scattering as well as absorption processes. Having in mind the negligible complex part of the refractive index for NIR wavelengths in respect to water, absorption influence is negligible and omitted. In accordance with Mie theory, the calculations of scattering and extinction cross sections in case of homogeneous sphere are accomplished with Eq. (3.4) and Eq. (3.5) ***[24]***, ***[25]***.

$$C_s(n_m, r, \lambda_0) = \frac{\lambda_0^2 e^{-\frac{4\pi r Im(n_m)}{\lambda}}}{2\pi\gamma_g |n_m|^2} \sum_{n=1}^{\infty} (2n+1)(|a_n|^2 + |b_n|^2) \qquad (3.4)$$

$$C_e(n_m, r, \lambda_0) = \frac{\lambda_0^2}{2\pi} \sum_{n=1}^{\infty} (2n+1) Re\left(\frac{a_n + b_n}{n_m^2}\right) \qquad (3.5)$$

Where a_n and b_n are Mie scattering coefficients, which depend on the medium refractive index n_m, water droplet radius r as well as the applied FSO wavelength λ_0. Moreover, the parameter γ_g is a geometrical term, which takes into account the change of the transmitted wavelength due to the absorption factor. The derived coefficients a_n and b_n given in Eq. (3.6) and (3.7) are defined based on Ricatti – Bessel functions based on well accepted assumption that refractive index of a single particle is equal to 1 ***[96]***. They undergo several accomplished transformations before to be found a possible solvable solution (Eq. (3.6) and Eq. (3.7)) which algorithm is used in the carried out simulations ***[96]***, ***[24]***, ***[25]***.

$$a_n = \frac{n_m \psi_n'(x)\psi_n(n_m x) - \psi_n'(n_m x)\psi_n(x)}{n_m \psi_n'(x)\xi_n(n_m x) - \psi_n(x)\xi_n'(n_m x)} \qquad (3.6)$$

$$b_n = \frac{\psi_n'(x)\psi_n(n_m x) - n_m \psi_n'(n_m x)\psi_n(x)}{\psi_n'(x)\xi_n(n_m x) - n_m \psi_n(x)\xi_n'(n_m x)} \qquad (3.7)$$

Here $x = 2\pi r/\lambda_0$ is the size parameter, which includes the inherent dependence on the wavelength and it is discussed later in the chapter. If it is considered the wave number $k = 2\pi/\lambda_0$, the size parameter is $x = kr$. Furthermore, the absorption cross section is calculated based on scattering and extinction cross sections, namely $C_a = C_e - C_s$. As mentioned, the absorption losses in a medium depends mainly on imaginary part of the refractive index which in terms of water droplets (fog and clouds) is negligibly small ($10^{-3} - 10^{-7}$) and it is omitted. However, this is not valid for other aerosols such as carbon suspended particles (smoke), which mainly attenuate the FSO signal due to absorption. Based on the described parameter C_s, the scattering coefficient β_s is given in the derived Eq. (3.8) ***[83]***.

$$\beta_s(n_m, r, \lambda_0) = \int_{r_{min}}^{r_{max}} C_s(n_m, r, \lambda_0)\, n(r)\, dr \qquad (3.8)$$

According to Eq. (3.8), the scattering coefficient is determined by multiplication of C_s and particle concentration $n(r)$ for all different radii. More specifically $n(r)$ is the Particle Size Distribution (PSD) of the water droplets in the troposphere, which is described based on experimentally proved modified Gamma function ***[97]***. Once the scattering coefficient β_s is introduced based on Mie theory, the optical attenuation is calculated by means of well-known logarithmic form of Lambert – Beer law (Eq. (3.9)) in [dB] which is valid only for single scattering events. Moreover, the propagation medium should be light monochromatic and homogenous. In other words, the Eq. (3.9) is allowed to be applied only in medium

characterized with low enough optical thickness and large enough average distance between two scattering events respectively.

$$A_{tt}(n_m, r, \lambda_0) = 4.34\beta_s z_d \quad (3.9)$$

The current thesis applied formula (3.9) based on the assumption that only single-scattering fog and cloud events are taken into account. While fog with its low water particles per unit volume concentration N_c < 100 cm^{-3} favours the usage of Eq. (3.9), cloud events normally are considered as a multiple scattering medium easily reaching values of N_c up to 400 cm^{-3} (rarely up to 1300 cm^{-3} ***[26]***) with length of several kilometres ***[28]***. Nonetheless, the most often occurred clouds regarding deep space communication are the high altitude (5 – 14 km) Cirrus clouds with approximated global average equal to 22.8 % ***[98]***. Moreover, they are characterized with very low concentration per unit volume and an average physical range. Hence, the assumption that Cirrus clouds are described as homogeneous single-scattering medium is still completely relevant ***[28]***, ***[95]***. Taking into account Eq. (3.8) and Eq. (3.9), the self-derived equation for the specific Mie scattering attenuation is Eq. (3.10) ***[83]***.

$$A_{tt}(n_m, r, \lambda_0) = 4.34\ 10^{-3} \int_{r_{min}}^{r_{max}} Q_s\,(r, \lambda, n_e) n(r) \pi r^2 dr\ [dB/km] \quad (3.10)$$

Where instead of scattering coefficient, a scattering efficiency Q_s is applied. Furthermore, the Eq. (3.10) includes integration over all radius spectrum of the water droplets suspended in the air during a typical fog (clouds) event for 1 km FSO link length.

As was noted above, clouds are generally described as a multiple scattering medium and since transmitted photons are characterized with their own paths, each of them should be separately tracked. This multipath propagation leads not only to spatial and angular, but also to temporal dispersion, which substantially affects the data rates ***[99]***. Mie theory, applied mainly for single scattering events (fog), cannot offer by itself a full solution to this problem. In addition, Lambert – Beer for calculation is valid for ballistic photons undergoing only single scattering ***[39]***. Consequently, Monte Carlo Raytracing algorithm should be normally applied to examine the propagation of a FSO pulse through a cloud medium. Apart from the derived optical thickness and scattering coefficient, the applied model required also knowledge for the scattering angle. In other words, due to multiple scattering effect, Mie theory is applied also in terms of deriving the angular distribution function of the transmitted optical power. Usually due to complexity in terms of deriving the phase function based on Mie theory, an approximated one is applied (Eq. (3.11)) ***[39]***.

$$P(\theta) = \frac{(1 - g^2)}{2\pi(1 - 2gcos\theta + g^2)^{3/2}} \quad (3.11)$$

The Henyey – Greenstein (HG) function is depended on parameter g, which directly corresponds to the physical distance at which the transmitted optical pulse is already spatially defused. Parameter g normally obtaines values between 0.85 – 0.995. In order to derive the PDF of the zenith scattering angle θ, the cover area by the phase function should be normalized to 1. The PDF of zenith angle θ is derived and given in Eq. (3.12) based on ***[39]***.

$$PDF(\theta) = P(\theta)\frac{\sin(\theta)}{2} = \frac{(1 - g^2)}{2\pi(1 - 2gcos\theta + g^2)^{3/2}} \frac{\sin(\theta)}{2} \quad (3.12)$$

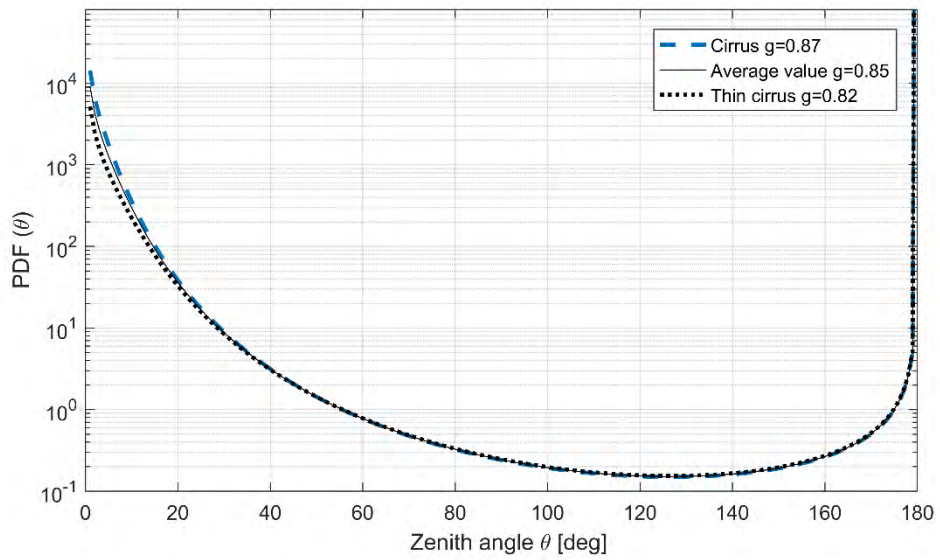

Figure 3.2: PDF of zenith Mie scattering angle θ for Cirrus clouds

In ***Figure 3.2***, the PDF versus zenith scattering angle is self-simulated for an average value of g as well as for the evaluated in the current work Cirrus and thin Cirrus clouds. Having implemented the phase function in Monte Carlo Raytracing algorithm, this would allow sophisticated channel modelling which determines fully the considered space-to-ground FSO performance. However, the complexity of this model to reproduce the transmitted optical pulse through a cloud requires an additional improvements. In ***[39]*** together with Monte Carlo Raytracing algorithm also Markov Chain is used, which provides easier way for numerical computations.

3.1.2 Fog and clouds microphysics analysis: PSD and LWC

In general, the microphysics of fog and cloud phenomena is characterized by a few parameters, as the most significant ones are the Liquid Water Content (LWC) and Particle Size Distribution (PSD). Both parameters can obtain a wide range of values in dependence on the specific type of Mie scattering conditions. While for the continental fog the amount of water is normally below 0.2 g/m^3 ***[34]***, the maritime fog is categorized with values up to 0.4 g/m^3 and clouds up 1 g/m^3 ***[28]***. In addition, fog particles, namely the water droplets, are normally with radius between minimum 1 µm for radiation fog and maximum 20 µm for maritime fog ***[28]***, ***[34]***. Similar to fog effect and according to ***[28]***, ***[97]***, clouds are formed based on condensation process containing mainly water droplets with radii from 0.1 µm up to 20 µm. However, they can still reach values more than 100 µm.

Due to fact that water droplets' size distribution provides the highest amount of information including the range of different particle sizes as well as their specific concentration, this will be the most important and the first considered parameter. It can be concluded from the various available experimental results given in ***[26]***, ***[27]***, ***[28]*** that the average particle radius of radiation fog is between 2 – 12 µm, while the particle radius for maritime fog is similar to clouds and normally between 6 – 20 µm. In order to obtain PSD from real carried out fog

and cloud observation, numerous atmospheric and medium parameters should be considered. Another possibility is to be utilized sophisticated Laser Diffraction System (LDS) for PSD analysation, which is used in **Subchapter 5.2**. Consequently, an analytical approach is nearly used which is highly beneficial in terms of Mie scattering evaluation (fog and clouds). The modified Gamma PDF, which provides the distribution of water droplets in accordance with their dimensions (radii) is given in Eq. (3.13) ***[97]***.

$$p(r) = ar^{\alpha} \exp\left[-\frac{\alpha}{\gamma}\left(\frac{r}{r_p}\right)^{\gamma}\right] \qquad (3.13)$$

While a, α and γ are positive constants that values depend on the specific fog conditions, r_p is the particle radius which corresponds to the maximum of the considered modified Gamma PDF. When the total particle's concentration N_c is also considered, the frequency distribution, namely PSD of all particles is given in Eq. (3.14).

$$n(r) = N_c p(r) \qquad (3.14)$$

Based on Eq. (3.13) and Eq. (3.14), the following analytical expression in terms of fog PSD is derived and shown in Eq. (3.15) ***[27]***.

$$n(r) = ar^{\alpha} \exp(-br^{\gamma}) \qquad (3.15)$$

Similar to the modified Gamma PDF, modified Gamma PSD is characterized with the positive constants a, α, b and γ ($\gamma = 0$), which values depend on the specific fog and cloud conditions. Their values for 4 types of different fog effects are provided in ***Table 3.1*** together with information regarding the total concentration of water droplets and the peak distribution radius r_p ***[27]***. Moreover, the modified Gamma PSD for the 4 cases are depicted in ***Figure 3.3***. Similar to fog, the modified Gamma PSD data for clouds is given in ***Table 3.2*** and ***Figure 3.4 [28]***.

Fog type		$n(r)$ [np/cm^3]	a	α	b	r_p [µm]
Maritime fog	Dense	20	0.027	3	0.3	10
	Moderate	20	0.066	3	0.38	8
Continental fog	Dense	100	2.37	6	1.5	4
	Moderate	200	607	6	3.0	2

Table 3.1: Modified Gamma PSD parameters for maritime and continental fog (The parameter values are obtained from [27])

Cloud type	$n(r)$ [np/cm^3]	a	α	b	r_p [µm]
Cumulus	250	2.6	3	0.5	12
Stratus	250	27	2	0.6	8
Stratus/Stratocumulus	250	52.7	2	0.75	6
Altostratus	400	6.26	5	1.11	7
Nimbostratus	200	7.67	2	0.42	11
Cirrus	0.025	$2.21\ 10^{-12}$	6	0.09	96
Thin Cirrus	0.5	0.011	6	1.5	6

Table 3.2: Modified Gamma PSD parameters for various clouds (The parameter values are obtained from [28])

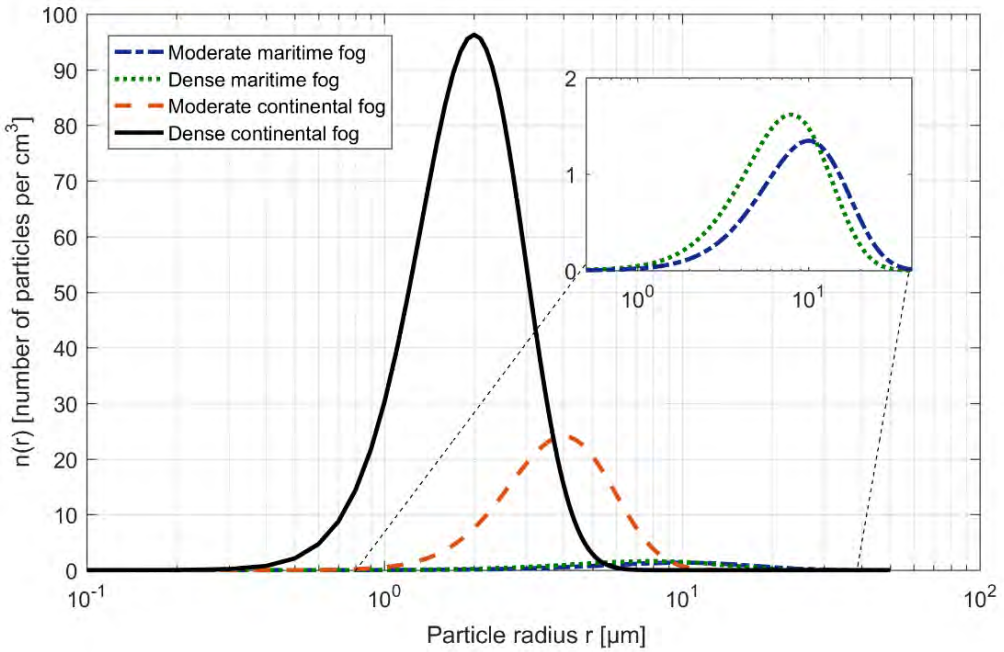

Figure 3.3: Modified Gamma PSDs for maritime and continental fog

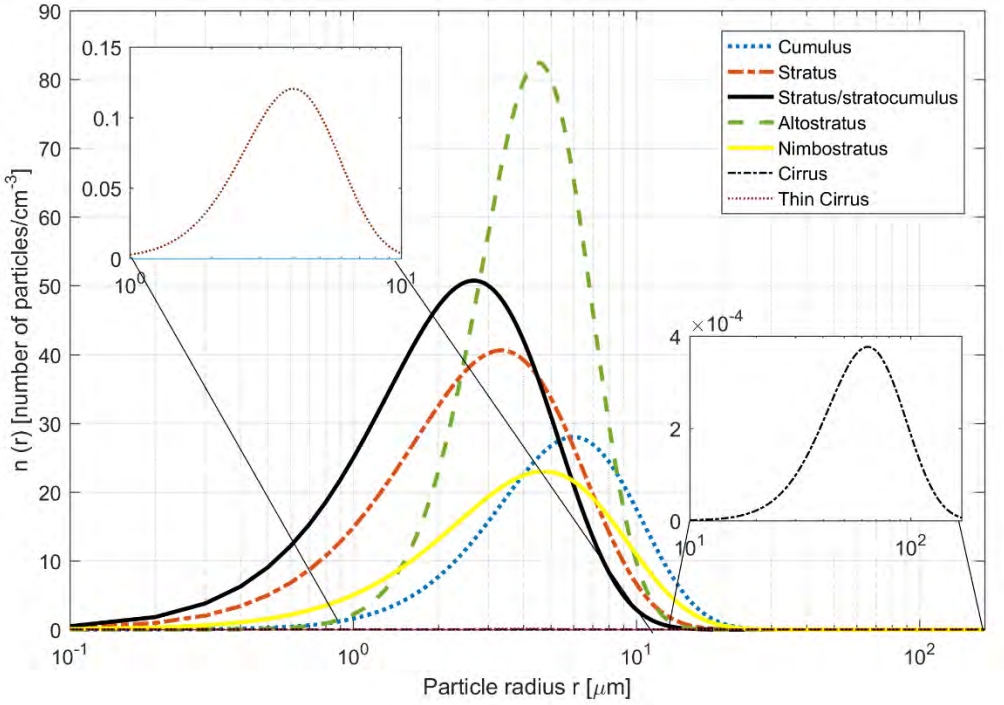

Figure 3.4: Modified Gamma PSDs for 7 types of clouds

Along with PSD parameter, the second important feature regarding microphysics of fog and cloud droplets is the LWC, which is subject to profound investigation and it is well presented in the literature. Due to well-proven interrelation between the microphysical characteristics,

the LWC is calculated based on the modified Gamma distribution, namely the empirically defined PSD in Eq. (3.15). Similar to ***[100]*** and ***[101]***, considering the density of water ρ_w, which is between 0.91 g/cm^3 for ice and ~1 g/cm^3 for pure water, together with the derived Eq. (3.8), the expression for LWC is given in Eq. (3.16).

$$LWC = \frac{4}{3}\pi\rho_w \int_{r_{min}}^{r_{max}} r^3\, n(r) dr \qquad (3.16)$$

The LWC is dependent on the fog type (radiation or maritime one), which is subject to the specifics of the region as well as the current climate conditions. Alike PSD parameter, LWC is featured with broad diversity of values which spectrum is approximately between 0.01 – 0.4 g/m^3 for fog (***[102]***) and can reach up to 1 g/m^3 in terms of Cumulus clouds ***[28]***. While for light continental fog, the amount of water per cubic meter is ~0.01 g/m^3, for heavy one is already ~0.2 g/m^3 ***[26]***, ***[34]***. Moreover, the LWC of the maritime fog is 0.2 – 0.4 g/m^3 and for clouds the LWC spectrum is already extended 3.1*10^{-4} – 1 g/m^3, where the lowest values of 3.1*10^{-4} – 0.064 g/m^3 are for thin Cirrus and Cirrus clouds respectively ***[28]***, ***[34]***. In accordance with ***[103]*** the empirically derived relation between visibility V [km] and LWC is a curved described based on Eq. (3.17) ***[101]***.

$$V = b(LWC)^{-a} \qquad (3.17)$$

The parameters a=0.66 and b strictly depend on the specifics of the evaluated fog type. In particular, b can obtain a value in the interval between 0.01 for light fog up to around 0.06 for dense maritime fog. Although the introduced meteorological visibility V allows calculation of the Mie scattering attenuation, the Eq. (3.17) does not include by itself the influence of the selected operation wavelength. In other words, it provides information only in terms of the applied central wavelength, namely 550 nm. Nevertheless, the authors in ***[101]*** introduced a relationship between b, a and the wave-dependent β_s parameters. Taking into account that a =0.66, coefficient b is investigated in terms of the normalized Mie scattering R = β_s (3.725 nm) / β_s (550 nm). Depending on the selected modified gamma distribution the change of b is between 0.01 – 0.09. This vague interrelation between the parameters is not easily and practically applicable. Consequently, a direct experimentally proved relation between Mie scattering coefficient β_s and LWC would be a better approach. More specifically, with exceptions of the different coefficients, the link between them follows the same curve type described with Eq. (3.17).

$$\beta_s = b_s(LWC)^{-a_s} \qquad (3.18)$$

In comparison with Eq. (3.17), b_s and a_s do not only depend on observed fog conditions but also on the selected operational wavelength. Having in mind the accomplished research in ***[29]***, which proposes more direct link between b_s and β_s in terms of Eq. (3.18), Mie scattering β_s versus LWC for the region of 65 <= a_s <= 178 and 0.63 <= b_s <= 0.96 is partly considered. Nevertheless, the very recent results in ***[100]*** offer the full solution to the problem. In particular, Monte Carlo algorithm combined with power low regression model allows enough accurate derivation of a_s and b_s for different fog events as well as wavelengths. The values of a_s and b_s obtained from Mori et al. ***[100]*** are given in ***Table 3.3***.

Fog type / λ_0 [nm]	Maritime fog		Radiation fog	
	a_s	b_s	a_s	b_s
785	156	1.01	1130	1.01
850	154	1	767	0.956
1064	155	1	695	0.976
1550	154	1	758	0.897
10000	114	1	104	0.994

Table 3.3: a_s and b_s fog parameters applied in Eq. (3.18) for λ_0= 785 nm; 850 nm; 1064 nm; 1550 nm and 10 μm (The parameter values are obtained from Mori et al. [100])

Taking into account the assumption that only single Mie scattering process occurs in the presence of fog and clouds, the phase function (***Figure 3.2***) is not introduced. Consequently, the Beer – Lambert low is still observed and in order to express the optical attenuation, β_s (Eq. (3.18)) is directly substituted in Eq. (3.9).

3.1.3 Kim, Kruse and Al Naboulsi empirical fog models

Although the used modelling in the current work merging together Mie theory and fog microphysics is highly accurate, enabling full control over fog and clouds representation, the requirements for preliminary knowledge of PSD makes it difficult to be applied in all cases. To address this issue, several well-established empirical approaches have been developed over the years. The most prominent models are the Mie, Kruse and Al Naboulsi, which are extensively described in ***[31]***. All of them are based on the easily applicable atmospheric visibility parameter V. The visibility distance is defined at 2 % or 5 % atmospheric transmittance, where only black objects in front of the horizon can be detected ***[34]***. In other words, the visibility parameter is calculated regarding contrast ratio between the aforementioned black object and the surrounding background environment. Similar to optical propagation, the decreasing behaviour of visual contrast with enlarging the visibility range obeys Lambert – Beer law (Eq. (3.9)).

$$C_v = e^{(-V\alpha_e)} \qquad (3.19)$$

Where α_e is the extinction coefficient in [1/km], which in the case of the selected FSO wavelengths is equal to Mie scattering coefficient β_s (the absorption is neglected), and V is the visibility parameter in [km]. There are two above-mentioned visual contrast thresholds T_c, which are empirically proved and used in case of visibility range calculations. While the most used value is T_c = 2 %, in several special cases (e.g. aviation) 5 % is more appropriate. The T_c = 2 % is applied for first time in the famous Koschmieder's law (Eq. (3.20)), which is a special case of Lambert – Beer equation regarding visibility range V for 550 nm ***[21]***.

$$V\,[km] = \frac{\ln(1/T_c)}{\beta_s[1/km]} = \frac{3.912}{\beta_s[1/km]} \qquad (3.20)$$

Addressing that the FSO system operates in the NIR spectrum, the wavelength should be also taken into account. This is accomplished by famous empirical Kruse equation, which provides combination of all parameters above considering again T_c = 2 %. In addition to it,

also logarithmic scale is applied that is useful and convenient in terms of further link budget calculations. In other words, the specific attenuation γ [dB/km] considering visibility V [km] is provided in Eq. (3.21) ***[21]***.

$$\gamma\,[dB/km] = \frac{10log_{10}(1/T_c)}{V[km]}\left(\frac{\lambda_0}{\lambda_{550}}\right)^{\delta} = \frac{17}{V[km]}\left(\frac{\lambda_0}{\lambda_{550}}\right)^{\delta} \qquad (3.21)$$

In addition, the operation wavelength λ_0 of the FSO system is normalized based on λ_{550} = 550 nm corresponding to the maximum sensitivity of a human eye as well as solar spectrum irradiance. In order to represent the attenuation regarding the different types of fog, Kruse provides a few values for parameter δ (Eq. (3.22)) ***[92]***.

$$\delta = \begin{cases} 1.6 & V > 50\ km \\ 1.3 & 6 < V < 50\ km \\ 0.585V^{1/3} & 0 < V < 6\ km \end{cases} \qquad (3.22)$$

This parameter is empirically derived based on data for the PSD in terms of different fog types and it is related to visibility V. However, the Kruse model does not provide enough accuracy regarding visibility range lower than 1 km. Therefore Kim model is created in ***[30]***, which clearly separates the visibility range under 1 km. According to it, when V< 0.5 km, the wavelength is not anymore of importance and it is ignored.

$$\delta = \begin{cases} 1.6 & V > 50\ km \\ 1.3 & 6 < V < 50\ km \\ 0.16V + 0.34 & 1 < V < 6\ km \\ V - 0.5 & 0.5 < V < 1\ km \\ 0 & V < 0.5\ km \end{cases} \qquad (3.23)$$

In addition to Kim and Kruse models, Al Naboulsi also developed its own model separating continental and maritime fog events. This model approximates the attenuation due to dense, moderate and light fog events (50 m until 1 km) for wavelengths λ_0 between 0.69 – 1.55 nm. In other words, an assumption that the majority of continental and maritime fog events, which lead to weather-based disruptions, are characterized with a visibility between 50 m up to 1 km is made. The Al Naboulsi empirical equations taking into account continental and maritime fog are provided in Eq. (3.24) and Eq. (3.25) ***[32]***.

$$\beta_{s\_con} = \frac{0.11478\lambda_0 + 3.8367}{V} \qquad (3.24)$$

$$\beta_{s\_mar} = \frac{0.18126\lambda_0^2 + 0.13709\lambda_0 + 3.7502}{V} \qquad (3.25)$$

In general, Al Naboulsi fog model is well accepted in case of terrestrial links with several kilometres distance, where the attenuation due to fog events characterized with visibility range of more than 1 km is not of significant importance. Similar to Kim and Kruse model, the found attenuation is calculated based on Lambert – Beer law provided in Eq. (3.9).
The comparison of all four described models is simulated in ***Figure 3.5 a)*** where the link distance in accordance with Al Naboulsi model is selected to be up to 1 km. The wavelength is 850 nm and transmittance is 2 %. It is evident that the Kruse model is the only one, which

has a major difference in its behaviour than the other two ones, which are later developed in time and are considered as more accurate. In order to observed the influence of the wavelength over the FSO performance, in ***Figure 3.5*** b) a self-built comparison between Kim and Kruse model for 850 nm and 1550 nm is given. Due to fact that Kim model is non-dependent on the wavelength for V < 0.5 km a difference is noticed only when Kruse model is applied. In particular, for 1550 nm the atmospheric attenuation decreases, which is an expected result in terms of the presented Mie theory and fog microphysical analysis.

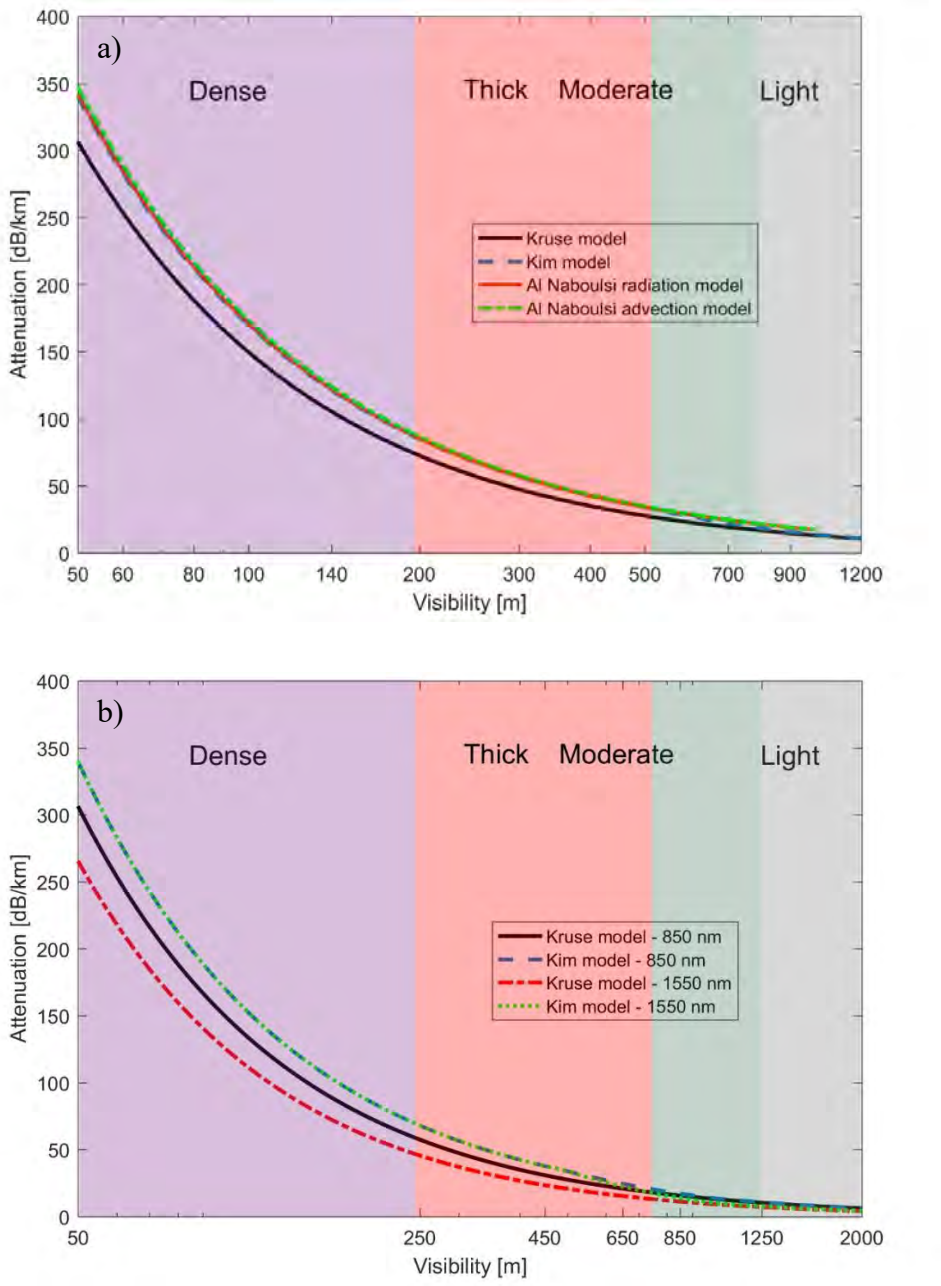

Figure 3.5: Comparison between Kim, Kruse and Al Naboulsi Mie scattering fog models regarding a) λ_0 = 850 nm and T_c = 2 % (Modified figure based on own publication [31]); b) two different wavelengths λ_0 = 850, 1550 nm and for T_c = 2 %

3.2 Atmospheric turbulence-induced FSO fading

The atmospheric turbulence effect is based on the energy redistribution process. During this process, eddies are produced, which are characterized by various sizes and refractive indices. Depending on the size of air pockets, the turbulence can lead to several different issues in terms of beam propagation through the free-space medium. In case eddies are smaller in comparison to FSO beam, the transmitted laser wave front is distorted. This causes irradiance fluctuations, namely scintillations. If the air pockets are larger than the beam diameter, the laser beam is deviated and beam wandering occurs.

3.2.1 Refractive index structure parameter based on RAOB

Fluctuations of the refractive indices causing significant optical power losses are dependent on the main atmospheric characteristics including temperature, humidity, pressure as well as wind velocity. The structure parameter of the index of refraction C_n^2 describes the explained variations as various models are developed considering different possible communication scenarios ***[104]***. A typical value for C_n^2 lies between 10^{-17} for weak turbulence and 10^{-12} in case of strong turbulence. Although the commonly applied and empirically validated turbulence models provide rough values regarding C_n^2, in most of the cases a higher accuracy is required. In general, Gurvich, SLC-day and Hufnagel – Valley (HV) models mainly depend on altitude to provide data regarding C_n^2. An exception is only partly made by the Pamela model, which requires information regarding the average atmospheric parameters as well as HV model demanding knowledge for the wind speed, which is well approximated with Buffon model ***[21]***. However, these methods cannot still delivery satisfactory results, which to be comparable to real space-to-ground FSO link measurements. In order to address this issue, a sophisticated approach processing telemetry data from Radiosonde Observation (RAOB) atmospheric measurements is considered ***[52]***, ***[54]***. In parallel with the work in ***[54]***, a RAOB database containing meteorological information for various geographical locations is used. The radio sounding data includes atmospheric vertical profile up to 30 km of various atmospheric parameters such as pressure, geopotential height, temperature, dew point temperature, relative humidity, mixing ratio, wind orientation, wind velocity, potential temperature, equivalent potential temperature and virtual potential temperature. The proposed model is presented for first time from Van Zandt and it is based on Tatarski energy spectrum ***[105]***. More specifically, it applies the Tatarski solution for C_n^2, which is provided in ***[106]***.

$$C_n^2 = 3.78\, M^2 L_0^{\frac{4}{3}} \qquad (3.26)$$

Where M provides information for the changes of index of refraction in terms of height and L is the turbulence outer scale parameter. M is calculated based on Eq. (3.27) provided in ***[106]*** and L_0 versus altitude h is expressed with an experimentally validated Eq. (3.28) ***[54]***.

$$M = \frac{-79\ 10^{-6} P}{T^2} \frac{dT}{dh} \qquad (3.27) \qquad L_0 = \frac{5}{\left(1 + \left(\frac{h - 7500}{2500}\right)^2\right)} \qquad (3.28)$$

In other words, C_n^2 is expressed with Eq. (3.29), which allows the using of ROAB data for precise investigation of atmospheric turbulence-induced fading.

$$C_n^2 = 3.78\left(\frac{-79\ 10^{-6}P}{T^2}\right)^2\left(5/\left(1+\left(\frac{h-7500}{2500}\right)^2\right)\right)^{4/3}\left(\frac{dT}{dh}\right)^2 \quad (3.29)$$

The used absolute temperature in [K] in Eq. (3.29) is dependent on the atmospheric pressure, which change with altitude. Consequently, this leads to inaccuracy in terms of calculated C_n^2. This is the reason that in ***[107]***, the potential temperature is proposed to be applied. The potential temperature is invariant in terms of atmospheric pressure changes, which leads to higher precision. Furthermore, the potential temperature is calculated with Eq. (3.30) (***[107]***) in terms of reference pressure that is equal to 1000 hPa. The newly derived formula considering C_n^2 calculated based on Eq. (3.30) is provided in Eq. (3.31) ***[54]***.

$$\theta = T\left(\frac{P}{P_0}\right)^{R/c_p} \quad (3.30)$$

$$C_n^2 = 3.78\left(\frac{-79\ 10^{-6}P}{T\theta}\right)^2\left(5/\left(1+\left(\frac{h-7500}{2500}\right)^2\right)\right)^{4/3}\left(\frac{d\theta}{dh}\right)^2 \quad (3.31)$$

3.2.2 Log – Normal and Gamma – Gamma optical intensity distributions

Once the C_n^2 is calculated, the investigation of atmospheric turbulence influence over transmitted FSO beam is based on probability theory and statistics. Depending on the strength of the atmospheric turbulence-induced fading the fluctuations of the optical intensity follows a few different PDFs. In accordance with Rytov theory, the fundamental Log – Normal distribution is applied in case of weak turbulence conditions ***[40]***.

$$P(I_r^2) = \frac{1}{\sqrt{2\pi\sigma_r^2 I_r^2}}exp\left\{-\frac{(\delta - E[\delta])^2}{2\sigma_r^2}\right\} \quad (3.32)$$

Here the σ_r^2 is the Rytov variance, which is also known as scintillation index for the case of weak atmospheric turbulence. It is defined in terms of log-normalized intensity (log-intensity fluctuations) $\delta = ln(I_r/I_0)$ of the transmitted optical beam, where I_0 is the statistical average equal to $\langle I_r \rangle$ and I_r is the received intensity. In particular, applying a logarithmic function over turbulence-induced intensity fluctuations, which are log-normally distributed leads to Gaussian distribution. In other words, log-intensity Rytov variance σ_r^2 is defined based on Gaussian statistics. Consequently the mean value of log-intensity fluctuations is $E[\delta] = \sigma_r^2/2$. Considering an ordinary plane wave, Rytov variance of Log – Normal intensity distribution, namely scintillation index in terms of weak turbulence for horizontal and for the case of vertical FSO downlink is provided in Eq. (3.33) and Eq. (3.34) (Eq. (3.34) is self-modified in terms of elevation angle γ) ***[40]***.

$$\sigma_r^2 = 1.23C_n^2k^{7/6}z_d^{11/6} \quad (3.33)$$

$$\sigma_R^2 = 2.25k^{\frac{7}{6}}\frac{1}{\sin^{11/6}(\gamma)}\int_{h_0}^{H} C(h)_n^2\,(H-h_0)^{5/6}dh \quad (3.34)$$

Where z_d is the link distance, γ is the elevation angle, h_0 is the height of the ground station and H is the maximum height of the troposphere corresponding to approximately 12 km. Due to the large fluctuations of C_n^2 near the ground and longer atmospheric path, the elevation angle should be ≥ 20°. Consequently, for or the further simulations, the elevation angle is taken to be at minimum 20°, which corresponds to the worst possible zenith angle equal to 70° ***[108]***, ***[109]***. Considering, atmospheric weak turbulence, the log-intensity Rytov variance is equal to the normalized irradiance variance of Log – Normal distribution, namely scintillation index. This approximation is valid when $\sigma_r^2 < 1$ ***[43]***. Addressing again the fact that Gaussian statistics is applied in terms of the log-normally distributed normalized irradiance, a natural logarithmic scale is used for the log-intensity variable. Consequently, by considering a simple mathematical transformation $x = 10\ln(x)/\ln(10)$ [dB], the log-intensity variable is expressed in [dB]. In other words, the scintillation Rytov variance in dB scale in provided in Eq. (3.35).

$$\sigma_r^2 = 23.17C_n^2k^{7/6}z_d^{11/6}\ [dB^2] \quad (3.35)$$

Considering that the mean value of log-irradiance fluctuations is equal to approximately two times the deviation (rms of Rytov irradiance variance) ***[110]***, the mean optical attenuation value for weak turbulence is calculated based on the Eq. (3.36).

$$A_{tur} = 2\sqrt{23.17C_n^2k^{7/6}z_d^{11/6}}\ [dB] \quad (3.36)$$

In accordance with Eq. (3.33) and Eq. (3.36), the analysis for a long-distance terrestrial FSO link operating in the presence of weak atmospheric turbulence-induced fading is accomplished. ***Figure 3.6***. depicts the dependence of log-intensity variance in terms of FSO link distance z_d and refractive index structure parameter C_n^2.

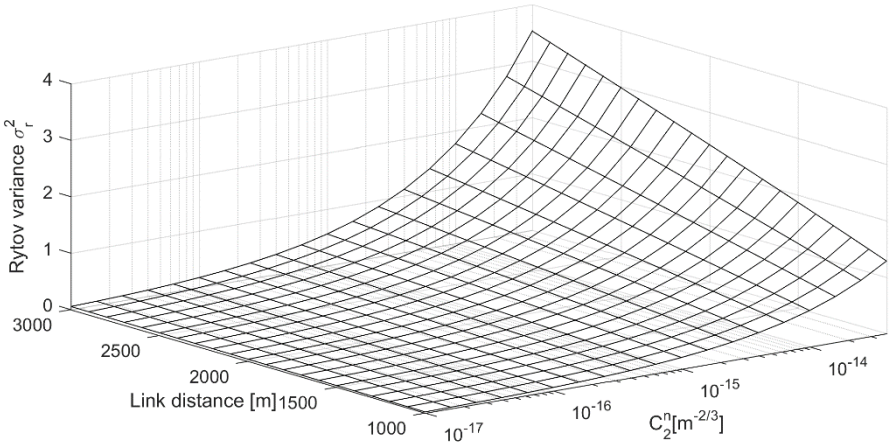

Figure 3.6: Rytov variance versus FSO link distance and C_n^2

With increasing the link distance, the weak turbulence theory ($\sigma_r^2 < 1$) allows to be handled only decreased values of C_n^2, which leads to a Rytov variance lower than one. In addition,

the mean optical attenuation due to weak turbulence, namely the mean value of the normalized log-irradiance fluctuations in [dB] is depicted in ***Figure 3.7***.

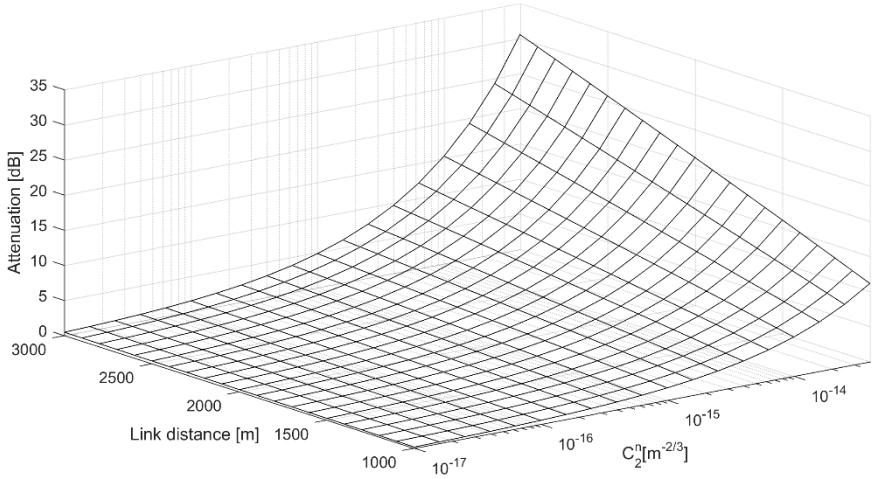

Figure 3.7: Mean value of clear-air weak atmospheric turbulence attenuation versus FSO link distance and C_n^2 valid for the case of $\sigma_r^2 < 1$

Similar to ***Figure 3.6***, its value depends on the link distance as well as C_n^2. Considering Eq. (3.36) and the requirements for $\sigma_r^2 < 1$, the attenuation due to weak turbulence cannot exceed more than 8.5 dB. Otherwise, the FSO link cannot be handled with the introduced Log – Normal irradiance distribution and scintillation index, namely Rytov variance.

In case of stronger clear-air atmospheric turbulence, the Rytov parameter linearly increases with decreasing of refractive index structure parameter and normally reaches value (e.g. 10) which already does not characterized accurately FSO channel. Therefore, Gamma – Gamma distribution is used. This distribution cover all regimes including weak, moderate and strong atmospheric turbulence-induced fading. The irradiance flux variance of Gamma – Gamma distribution, namely scintillation index is based on recalculation of the Rytov variance. While it coincides with the behaviour of Rytov parameter during weak atmospheric turbulences, scintillation index line is getting steeper, saturated and curved if Log – Normal variance is increased more. In other words, the scintillation index of Gamma – Gamma distribution reaches values which does not exceed 6 ***[43]***. Apparently, this parameter is again directly dependent on the structure parameter of index of refraction obtained based on the meteorological RAOB data. The general closed-form expression of Gamma – Gamma distributed and received irradiance I_r is provided in Eq. (3.37) ***[40]***.

$$f(I_r) = \frac{2(\alpha\beta)^{\frac{\alpha+\beta}{2}-1}}{\Gamma(\alpha)\Gamma(\beta)\Omega^{\frac{\alpha+\beta}{2}}} I_r^{\frac{\alpha+\beta}{2}-1} K_{\alpha-\beta}\left(2\sqrt{\frac{\alpha\beta I_r}{\Omega}}\right) \qquad (3.37)$$

Where Ω is the statistical average of the received intensity $< I_r >$. Having in mind, that it is well accepted Gamma – Gamma distribution to be normalized in terms of $< I_r > = 1$, the final expression, which is applied in the current work is given in Eq. (3.38).

$$f(I_r) = \frac{2(\alpha\beta)^{\frac{\alpha+\beta}{2}-1}}{\Gamma(\alpha)\Gamma(\beta)} I_r^{\frac{\alpha+\beta}{2}-1} K_{\alpha-\beta}\left(2\sqrt{\alpha\beta I_r}\right) \quad (3.38)$$

Furthermore, α and β are two parameters, which specify the Gamma – Gamma distribution, that are within the range: 1 – 39 for α and 4 – 43 for β ***[42]***. While α parameter is related to the large-scale air pockets, β parameter corresponds to small-scale air pockets. Considering an ordinary plane wave they are calculated based on Eq. (3.39) ***[111]***.

$$\alpha = \left[\exp\left(\frac{0.49\sigma_r^2}{\left(1+1.11\sigma_r^{12/5}\right)^{7/6}}\right) - 1\right]^{-1} \quad \beta = \left[\exp\left(\frac{0.51\sigma_r^2}{\left(1+0.69\sigma_r^{12/5}\right)^{5/6}}\right) - 1\right]^{-1} \quad (3.39)$$

Here the σ_r^2 is the already investigated Rytov parameter, which is provided for both horizontal as well as vertical long-distance FSO links. Similar to α and β parameters, the variance of Gamma – Gamma distribution σ_I is parametrized in terms of Rytov variance. In other words, Gamma – Gamma variance, namely scintillation index is the recalculated Rytov Log – Normal variance ***[42]***.

$$\sigma_I^2 = \exp\left[\frac{0.49\sigma_r^2}{\left(1+1.11\sigma_r^{12/5}\right)^{7/6}} + \frac{0.51\sigma_r^2}{\left(1+0.69\sigma_r^{12/5}\right)^{5/6}}\right] - 1 \quad (3.40)$$

The Gamma – Gamma distribution variance similar to Log – Normal variance is valid only in case of point receiver. Nevertheless, in reality, the receiver aperture is parameterized with a finite length and power averaging needs to be taken into account. In order to take the aperture diameter into account, the power scintillation index σ_p^2 is introduced. In accordance with ***[84]***, the σ_p^2 is calculated in terms of aperture averaging factor F_a and can obtain values from 0 to 1 (Eq. (3.41)).

$$F_a = \frac{\sigma_p^2}{\sigma_I^2} = \frac{\sigma_I^2(R_d)}{\sigma_I^2(0)} \quad (3.41)$$

In particular, the recalculated decreased power scintillation index σ_p^2 is provided in Eq. (3.42) ***[43]***. The parameter d is calculated with equation $d = \sqrt{(2\pi R_d^2)/4z_d\lambda_0}$.

$$\sigma_p^2 = \exp\left[\frac{0.49\sigma_r^2}{\left(1+0.65d^2+1.11\sigma_r^{12/5}\right)^{7/6}} + \frac{0.51\sigma_r^2(1+0.69\sigma_r^{12/5})^{-5/6}}{1+0.90d^2+0.69d^2\sigma_r^{12/5}}\right] - 1 \quad (3.42)$$

3.2.3 FSO outage probability and optical attenuation

The closed-form expression for the outage probability in terms of Gamma – Gamma turbulence (Eq. (3.38)) is self-derived with a new approach applying special Meijer-G functions and normalized *SNR* denoted with γ_n. The full self-derivation of Eq. (3.43) is given in **Appendix A**.

$$\mathrm{P_{out}}(\gamma_n) = \frac{1}{\Gamma(\alpha)\Gamma(\beta)} \mathrm{G}_{1,3}^{2,1}\left(\alpha\beta \frac{1}{\sqrt{\gamma_n}} \middle| \begin{matrix} 1 \\ \alpha\ \beta\ 0 \end{matrix}\right) \quad (3.43)$$

Having derived Eq. (3.43) and using RAOB data, the relevant simulated results in respect to outage probability of 2.7 km terrestrial FSO link versus atmospheric turbulence strength for different normalized SNR is given in **Chapter 6**.

Once the problem regarding outage probability is solved, the second task includes derivation of FSO optical attenuation due to atmospheric turbulence. The aperture averaging mitigation technique significantly decreases the strength of atmospheric turbulence, which directly corresponds to reduction of the scintillations and more specifically $\sigma_p^2 << 1$. Consequently, in accordance with ***[49]***, the atmospheric turbulence-induced fading is again well described with Log – Normal distribution or it well accepted that $\sigma_r^2 = \ln(\sigma_p^2 + 1) \sim \sigma_p^2$ ***[40]***. This means that atmospheric turbulence-induced attenuation is derived based on Log – Normal distribution, instead of complicated Meijer-G functions, which is applied in respect to outage probability calculations. Furthermore, the outage probability of Log – Normal weak atmospheric function is calculated based on well-known *erf* function ***[49]***.

$$\mathrm{P_{out}}(\mathrm{I_{th}}) = \frac{1}{2}\left(1 + erf\left(\frac{ln\frac{I_{th}}{<I_r>} - \frac{\sigma_r^2}{2}}{\sqrt{2}\sigma_r}\right)\right) \quad (3.44)$$

In accordance with the applied approach in ***[112]***, the $I_{th}/<I_r>$ and more specifically – $10\log_{10}(I_{th}/<I_r>)$ [dB] is the attenuation due to clear-air atmospheric turbulence, corresponding to the required additional link margin necessary to cover the adverse atmospheric turbulence fading. Although representing the receiver based on its required threshold irradiance I_{th} (threshold sensitivity S_{th}) is insufficient to include additional information about applied modulation techniques and receiver performance, it is fully appropriate to describe the FSO link margin requirements in terms of clear-air atmospheric turbulence attenuation ***[112]***. In particular, for calculation of the FSO system's link margin in turbulence atmospheric conditions, the $-10\log10(I_{th}/<I_r>)$ is derived based on Eq. (3.44).

$$10log\frac{I_{th}}{<I_r>} = 10\log\left(exp\left(\sqrt{2}\sigma_r erf^{-1}(P_{out} - 1) - \frac{\sigma_r^2}{2}\right)\right) \quad (3.45)$$

Having in mind the previous assumption together with Eq. (3.45), the required FSO link margin in terms of atmospheric turbulence, calculated based on knowledge for power scintillation index and outage probability, is given in Eq. (3.46) ***[112]***.

$$M(\sigma_p^2, \mathrm{P_{out}}) = -4.343\left(\sqrt{2\,ln(\sigma_p{}^2 + 1)}\, erf^{-1}(P_{out} - 1) - \frac{1}{2}ln(\sigma_p{}^2 + 1)\right) \quad (3.46)$$

For the case of a minimalized outage probability parameter $P_{out} = 10^{-7}$ (100 % availability), the maximum atmospheric turbulence attenuation is provided in Eq. (3.47).

$$A_{tur}(\sigma_p^2) = 4.343\left(3.67\sqrt{2\ln(\sigma_p^2+1)} + \frac{1}{2}\ln(\sigma_p^2+1)\right) \quad (3.47)$$

3.3 Geometrical scattering: Snow and Rain attenuation

In case particle dimensions are significantly larger than FSO wavelength, the scattering effect obeys geometric optics' laws. Especially this is valid for atmospheric effects such as snow and rain, for which particles' radii are considerably larger than 10 times the operating wavelength. Being dependent on severity level, both rain and snow normally cause attenuation within range of 3.1 – 18.3 dB/km ***[93]***. Although this is incomparable with Mie scattering impairments, it can still lead to high attenuation in long-distance terrestrial links.

3.3.1 Snow attenuation

In general, snow is forming based on ice crystals, which transform due to the difference in atmospheric parameters near-Earth surface. According to Aerodrome Meteorological Observation and Forecast Study Group (AMOFSG), the newly-formed snowflakes can reach radius up to 15 mm while the snow rate *S* can reach up to ~25 mm/h. However, during normal snowfall weather conditions, the snow rate is within 1 – 5 mm/h ***[88]***, ***[113]***. In comparison with other weather effects including rain, snow can be measured with two types of [mm/h] scales, namely snowfall depth scale or melted snow scale. Regarding the current thesis, the snow depth scale is applied.

There are two major types of snow depending on the water content including dry snow and wet snow. The specific attenuation in [dB/km], which is wavelength dependent, is calculated based on Eq. (3.48) and Eq. (3.49) ***[114]***.

$$\gamma_{s\_wet} = (0.000102\lambda + 3.79)S^{0.72} \quad (3.48)$$

$$\gamma_{s\_dry} = (0.0000542\lambda + 5.59)S^{1.38} \quad (3.49)$$

Considering the λ = 850 nm wavelength, which is an usual value in case of terrestrial links, the attenuation for both equations is simulated and depicted in ***Figure 3.8***.

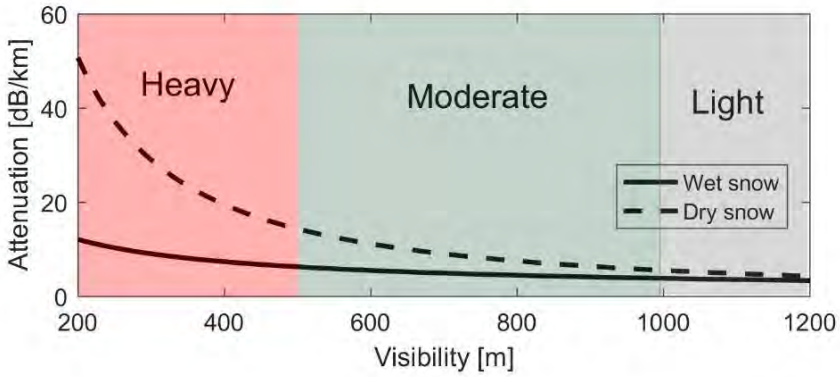

Figure 3.8: FSO attenuation versus visibility for wet and dry snow (Modified figure based on own publication [31])

According to it, there is substantial difference between wet and dry snow in terms of specific attenuation, which can reach up to 50 dB/km for dry and up to 12.2 dB/km for wet one. Moreover, instead of S [mm/h] snow depth scale, the specific attenuation is calculated in terms of meteorological visibility V in [m]. The scale conversion is accomplished based on the following equation: V [m] = 1000 / S [mm/h] ***[113]***. Consequently, the 1 – 5 mm/h snowfall is equal visibility range of 200 m up to 1 km.

3.3.2 Rain attenuation

Apart from snowy weather conditions, the rain can also partly affect FSO transmission. However, due to very short wavelengths in NIR spectrum, its influence is negligible in comparison with RF communication systems. Similar to snow, rainfall R is also measured in [mm/h] scale. According to the classification in ***[88]***, rain precipitation is within the range of ~1 mm/h for a light one and 100 mm/h for a heavy one. The specific attenuation due to rain is calculated based on empirically developed Eq. (3.50) ***[92]***.

$$\gamma_{rain} = 1.29R^{0.64} \qquad (3.50)$$

Having in mind the above equation, the specific attenuation versus rain rate is simulated in ***Figure 3.9***. According to it, even in rare cases of extremely heavy rain, the attenuation does not exceed 25 dB/km. In particular, for an average rainfall of 25 mm/h, the attenuation of the FSO signal is ~10 dB/km.

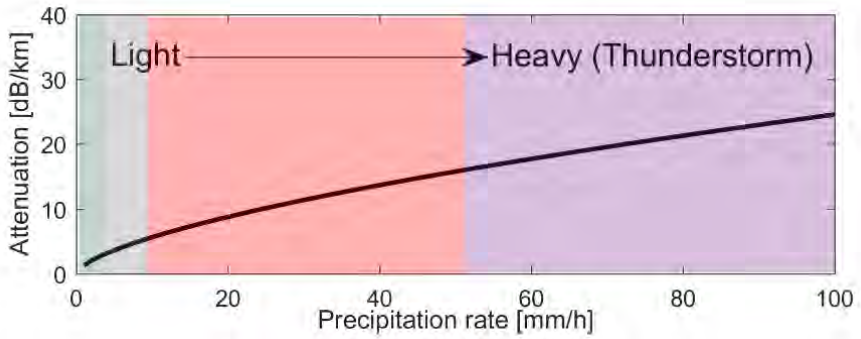

Figure 3.9: FSO attenuation versus precipitation rate in respect to rain (Modified figure based on own publication [31])

Chapter 4

4. FSO channel emulator

The easily accessible evaluation of FSO system's performance regarding its atmospheric free-space propagation channel requires laboratory testbed, that represents various scenarios from medium to ultra-long-distance communication links (> 500 km) operating in Mie scattering and atmospheric turbulence-induced fading as well. While shorter terrestrial links reach not more than 10 km, long-distance space-to-ground channels with their millions of kilometres (10^5 – 10^8 km) length, should be preliminary tested in controlled laboratory environment. In particular, NASA developed TRL scale, which is applied for assessment of maturity regarding variety of space borne technologies. In order to reach the highest 9^{th} level, systems should undergo analytical as well as experimental studies. After the validity of the developed concept is completely proven (1 – 3), the operation of each system component is tested separately (4 – 5). Before final implementation, the technology is evaluated with a self-developed breadboard operating in relevant environment (6 – 9) ***[55]***.

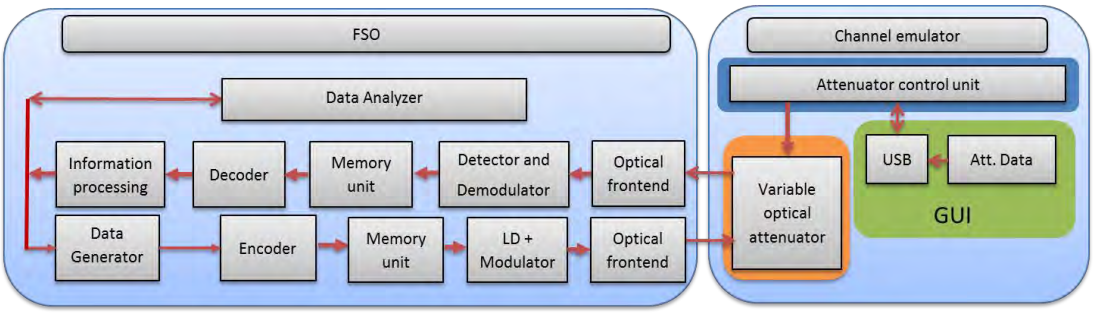

Figure 4.1: Testbed architecture for evaluation of FSO system performance incorporating the developed free-space channel emulator unit based on VOA

Considering the NASA TRL scale as well as previous attempts to reproduce long-distance FSO channel in laboratory conditions, which are well summarized in the introduction, the assessment of wireless optical links in the current thesis is carried out by means of state-of-the-art technique including Variable Optical Attenuator (VOA). Although the concept of a FSO system considers free space as an optical transmission medium, this proposed model is based on fibre optics technology. The approach provides the required compactness, as well as accurate enough results comparable to a real free-space channel case ***[78]***. A basic scheme of the developed channel emulator setup implemented in overall FSO architecture is

provided in ***Figure 4.1***. Apart from the well-known receiving and transmitting parts of a conventional FSO system, the setup includes a developed channel emulator that contains VOA operating at 850 nm/1550 nm, attenuator Control Unit (CU) and software. For the sake of clarity, all channel emulator units are considered and tested separately.

4.1 850 nm and 1550 nm Variable Optical Attenuators (VOAs)

The applied VOAs are commercially produced components from Agiltron Inc (etMEMS^{tm} SM – VOA and MM – VOA), which are based on MEMs (Micro Electro-Mechanical Systems) allowing precise setup of large enough optical attenuation values. The missing wavelength-dependent components in the VOA architecture including filters, lenses and coating ensure the possibility for operation in large wavelength range between 350 nm and 2050 nm as well as handling of high optical power of up to 500 mW. Although, VOA can be controlled based on voltage as well current, during the development phase only voltage was selected to handle the optical power in the fibre-optics channel. Moreover, the VOA is characterized with continuous attenuation resolution and with low input impedance of 100 Ohm. According to the attenuator parameters, the voltage range could be set up between 0 V and 5 V (the absolute maximum is 5.2 V), which corresponds to attenuation values of 0 to 60 dB respectively. The last crucial VOA parameter is the minimum response time, which results in the highest possible imposed fading frequency. While the given minimum response time in the characteristics is 10 ms resulting in 100 Hz fading frequency, the following operation setup allows lowering the response time up to 1 ms (1 kHz). Having in mind that long-distance terrestrial as well as space-to-ground channels are investigated, two VOAs are taken into account. While terrestrial one (etMEMS^{tm} MM – VOA) operates at 850 nm with multimode fibre, the ultra-long-distance space-to-ground High Photon Efficiency (HPE) communication links require 1550 nm VOA with Single Mode Fibre (SMF) (etMEMS^{tm} SM – VOA). Although there is not difference in the specifications, both VOAs are investigated separately.

4.2 Attenuator driver based on internal and external DAC

The VOA unit is controlled with special attenuator driver and computer system. In particular, the attenuator driver plays role of a hardware mediator (interface), which is fed by atmospheric turbulence as well as Mie scattering attenuation data and based on them provides proper voltage levels within the VOA operation range. Moreover, the implemented attenuator driver is utilized together with STM32 Nucleo-F446RE evaluation board, which is well-known platform providing broad spectrum of capabilities. This includes USB communication with computer, which is supported by the available free of charge libraries. In addition, the USB interface also provides the necessary 5 V power supply for the considered driver board.

Considering the performance analysis, two built-up attenuator CUs are utilized with STM32 Nucleo-F446RE evaluation board including STM32F446RE microcontroller and ST-Link/V2-1 debugger. While both CUs (voltage drivers) architectures incorporates a STM32F4 microcontroller ARM Cortex M4 series, which is powered by 3.3 V, the main

difference between them is in terms of the applied Digital to Analog Converter (DAC) module [78]. In particular, the first one whose basic block scheme and wiring diagram are given in ***Figure 4.2*** operates based on an external DAC connected to the microcontroller with an Inter – Integrated Circuit (I²C) serial bus.

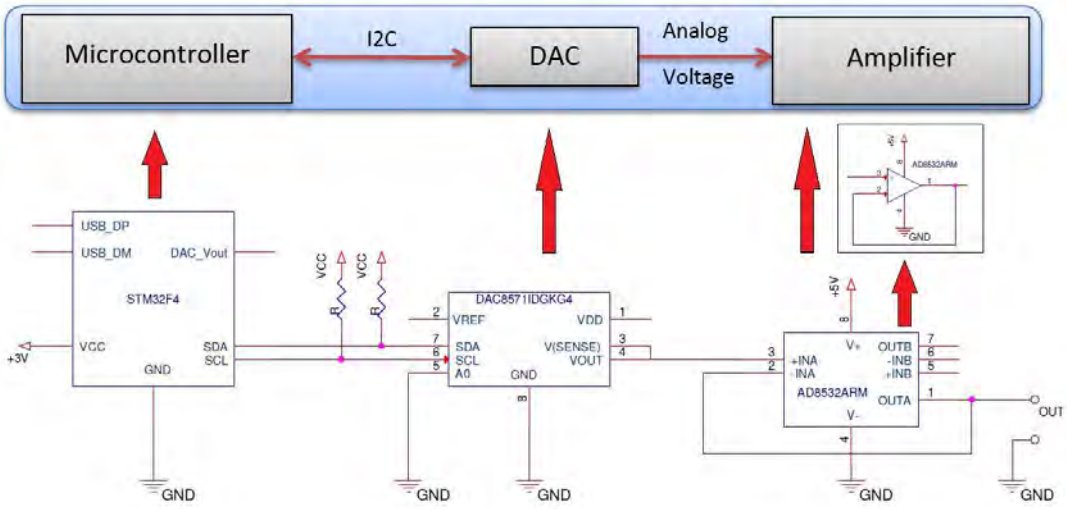

Figure 4.2: Block scheme and wiring diagram of the voltage driver with external DAC unit used for controlling the two VOAs (Modified figure based on own publication [78])

The implemented external DAC is Texas Instruments DAC8571 characterized with following parameters: 16 bit monothonic, settling time in the frame of 10 µs and ± 4 mV accuracy. Moreover, the supported maximum supply voltage of up to 5.5 V as well as the included rail to rail output amplifier leads to exact coverage of the required VOA voltage range (between 0 and 5 V). Nevertheless, since the VOA is characterized with low 100 Ohm impedance, higher amount of output DAC8571 DAC power should be achieved based on increasing the output current. In other words, the output of the DAC is amplified with help of an operational amplifier, which plays role of impedance transformer. Taking into account the already specified control voltage range of the selected VOA as well as the limited USB supply voltage equal to 5 V, a rail to rail amplifier providing output voltage between 0 V and 5 V is needed. Although the selected component AD8532ARM, which is produced by Analog Devices Inc, incorporates two operational rail-to-rail amplifiers, only one of them is implemented in the current control unit while the another is reserved for additional redundancy. In accordance with the specifications, the required supply voltage for each of the amplifiers is in diapason of 3 – 6 V and more specifically their recommended operational voltage regarding the built-up driver is 5.1 V. Moreover, the low supply current of 750 µA @5.1 V for each of the amplifier units results in high output current of 250 mA, which is well suited to the current application. In other words, the small DAC current is used to regulate the VOA, which is considered as a high current load.

Beside the already presented voltage driver architecture, the second proposed attenuator CU described with block and wiring diagram given in ***Figure 4.3*** utilizes the internal DAC of

the microcontroller that generates analogue voltage on the relevant microcontroller pin. The basic parameters of the internal DAC are as follows: 12 bit; sampling rate up to 1 Msps, etc. The main issue here occurs due to low supplied voltage (3.3 V) of the microcontroller. This directly leads to a non-sufficient reference voltage and consequently limited DAC output voltage up to 3.3 V. Having in mind this problem, the two operational amplifiers part of a second obtained AD8532ARM unit are implemented. The first one is used to increase the output voltage up to 5 V. On the other hand, the second operational amplifier operates as an impedance transformer in order to minimize the output impedance in terms of higher output current.

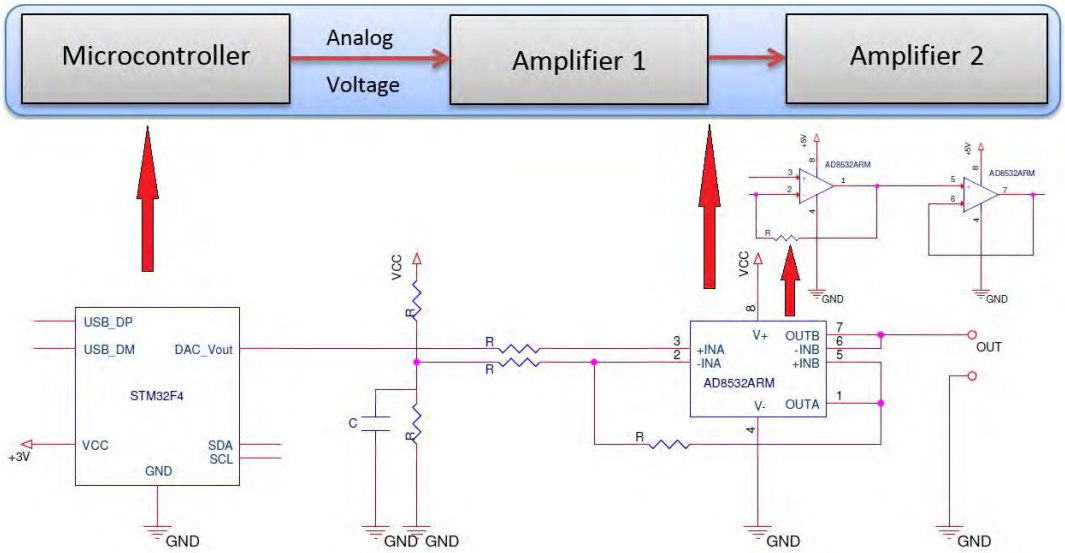

Figure 4.3: Block scheme and wiring diagram of the voltage driver with built-in DAC used for controlling the two VOAs (Modified figure based on own publication [78])

For the purpose of more compact design, the two developed attenuator drivers are implemented in one circuit board, which provides the necessary compactness. The photograph of attenuator CU, involving both drivers relying on external and internal DAC units, is shown in ***Figure 4.4 a)***. Along with this, a photograph of all channel emulator modules incorporating STM32 Nucleo-F446RE evaluation board, attenuator driver board and VOA is provided in ***Figure 4.4 b)***.

The power supply of both electrical circuits is selected based on jumper, which allows switching between evaluation board and external power source. The evaluation board is supplied via mini USB, which delivers +5 V and can be used as a power source for the implemented attenuator driver. In terms of better accuracy, a filter network is integrated into the supply, which means that DAC and amplifier will be run with filtered 5 V voltage. The supply voltage of 3.3 V for the microcontroller is generated with an additionally implemented voltage regulator. In case of problems, also an external power supply can be used with a recommended value of 5.1 V (the minimum voltage should 3.3 V and the maximum 5.5 V). Since the operational amplifiers should be powered with especially stable

power supply, a second jumper allows instead of USB an external supply voltage to be used regarding the two amplifiers. The external source should be specified with voltage range between 3.3 V and 6 V, while the recommend value regarding the implemented VOA is 5.1 V. Moreover, there are three LED indicators, which provides information regarding the selected driver as well as the status of the power supply. While LED 1 indicates that the driver with an external DAC is utilized, LED 3 shows that the driver based on the built-in DAC into the microcontroller is used. Moreover, LED 2 indicates if a proper power supply for the developed driver board is delivered.

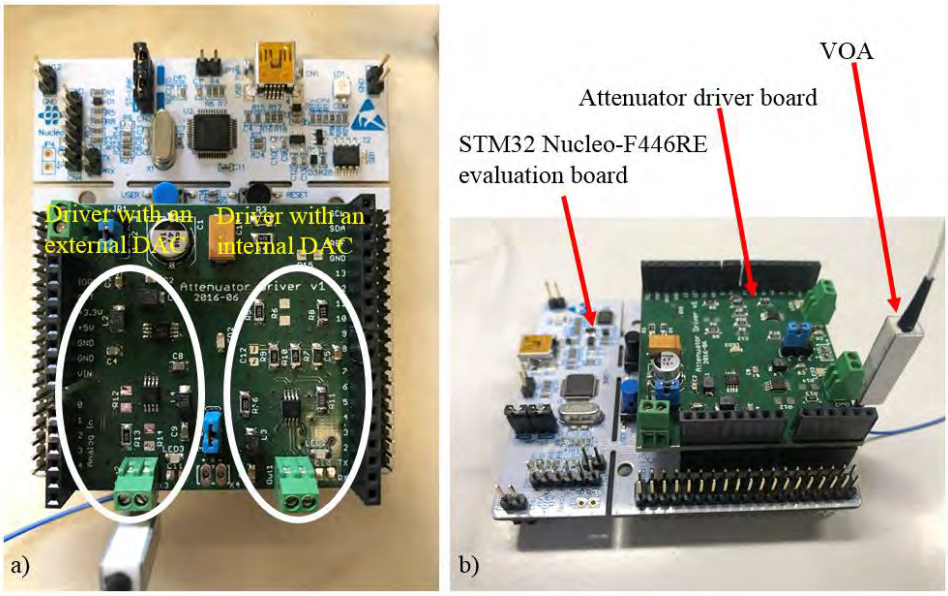

Figure 4.4: Hardware channel emulator: a) Attenuator driver board including voltage drivers with an external DAC and built-in microcontroller's DAC; b) overall system design

The voltage driver based on external DAC with its high accuracy of 16 bits is the most appropriate choice for the required channel emulator design. In comparison, the microcontroller built-in DAC is only 12 bits, which allows not so precise voltage step regulation. In addition, the design with the two operational amplifiers leads to higher instability, which is the second reason to be utilized only the control unit with an external DAC. Moreover, in terms of the following experiments, the developed driver is electrically supplied only via evolution board using mini USB + 5V.

4.3 Graphical user interface controlling the VOA

The utilized STM32 Nucleo-F446RE evaluation board together with the considered attenuator driver is controlled with a developed software, which is based on C Sharp and Windows Presentation Foundation. Its screenshot together with its main provided parameters in terms of representation of FSO channel is shown in Figure 4.5 *[77]*, *[85]*.

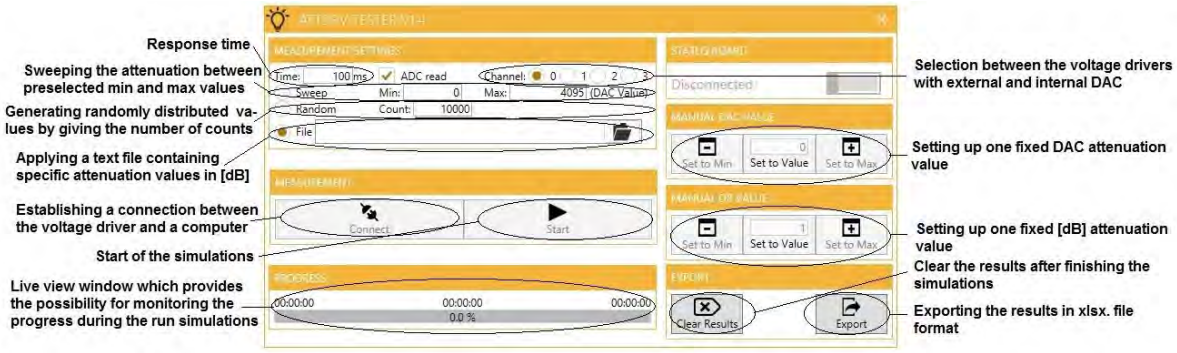

Figure 4.5: Screenshot of the FSO channel emulator's GUI along with short description of its main control functions (Modified figure based on own publications [80], [85])

The main functions are as follows:

- Setting up the time between each of the applied attenuation values in millisecond range (response time).
- Option for sweeping the applied attenuation between specially selected minimum and maximum values.
- Option for generating randomly distributed optical attenuation values by specifying only the number of counts.
- Applying of a text file containing specific attenuation values in [dB].
- One button responsible for initiating a connection between the voltage driver and the computer system and a second button starting the measurements.
- Live view window, which provides the possibility for monitoring the applied attenuation in [dB] as well as DAC values.
- Selection between the two different voltage drivers based on external and internal DAC.
- Setting up one fixed DAC or decibel attenuation value.
- Option for clearing the results as well as possibility for exporting the results into xlsx file format.

4.4 Characterization of the obtained VOA units

In order to address the both kinds of outdoor long-distance FSO links considering terrestrial > 2 km as well as ground-to-deep-space $>10^6$ km ones, two types of channel emulators are implemented and tested. In particular, they are based on two types of VOAs including MM – VOA operating at 850 nm wavelength as well as SM – VOA operating at 1550 nm wavelength.

Having implemented the CU, the main evaluated features of each VOA are electro-optical transfer function, optical attenuation range as well as response times. In order to estimate the performance of the long-distance FSO channel emulator unit and more specifically the applied 850 nm/1550 nm VOA, the arranged measurement setup includes transmitter with

Continuous-Wave (CW) laser source operating at 850 nm/1550 nm wavelength, and receiving part involving commercially available digital optical power meter PM100D from Thorlabs with minimum sensitivity of -43 dBm. The block diagram of the described testbed is given in ***Figure 4.6 [78]***.

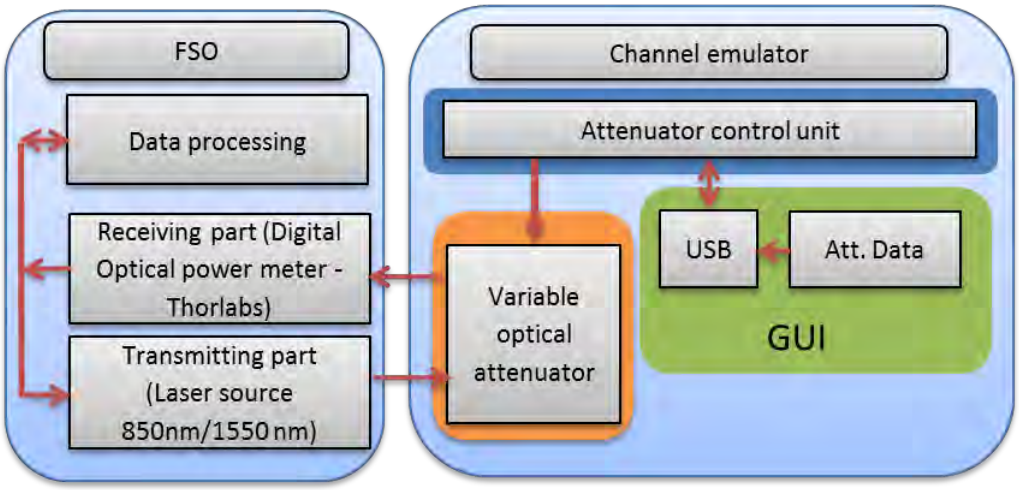

Figure 4.6: Test setup characterizing the VOA-based channel emulator (Modified figure based on own publication [78])

Once the CW laser beam is launched into the optical fibre and its optical power is modified due to channel emulator, the received optical signal is detected based on optical power meter forwarding the collected data to a computer. The carried out tests are performed by means of the internal capabilities of the channel emulator to measure the backward and forward response times as well as electro-optical transfer function based on fine sweeping between minimum and maximum VOA voltage, namely 0 – 5 V (0 – 60 dB attenuation). Moreover, the internal attenuation of VOA unit, which is equal to 1 dB need to be taken into account and the following correction, is implemented in all following simulations, namely 0 – 5 V (1 – 61 dB). Along with this, the estimated VOA performance is additionally verified using a file with randomly distributed attenuation values between preliminary considered voltage (attenuation) limits. The photograph of the described setup is provided in ***Figure 4.7***.

4.4.1 Measurement results in terms of 850 nm MM – VOA

In order to define the electro-optical transfer function of the 850 nm MM – VOA, sweep control voltage within the full range between 0 and 5 V is applied. The resolution depends on the incorporated DAC, part of the provided control block. While the architecture with internal 12 bit DAC integrated into the ARM Cortex M4 microcontroller is limited up to 4096 steps, the second design with an external 16 bit DAC allows up to 16 times higher resolution with 65536 voltage steps ***[80]***. ***Figure 4.8*** shows that the electro-optical transfer function for both cases is characterized with non-linear behaviour. In order to stick to the requirements for linear transfer function, which lowers to a minimum the induced nonlinearities in the emulated long-distance FSO channel, a calibration procedure is applied.

Having analysed ***Figure 4.8***, by increasing the supplied DAC voltage, the VOA-induced optical attenuation over the transmitted CW laser power has a typical exponential growth.

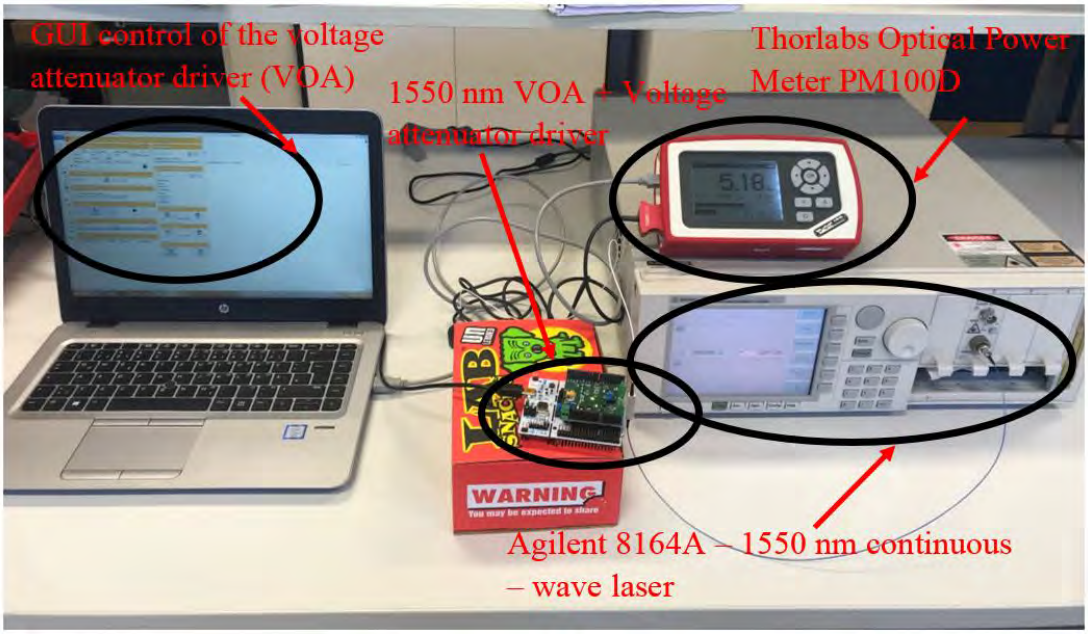

Figure 4.7: Photograph of the testbed architecture shown in Figure 4.6 used for evaluation of the VOA-based FSO channel emulator

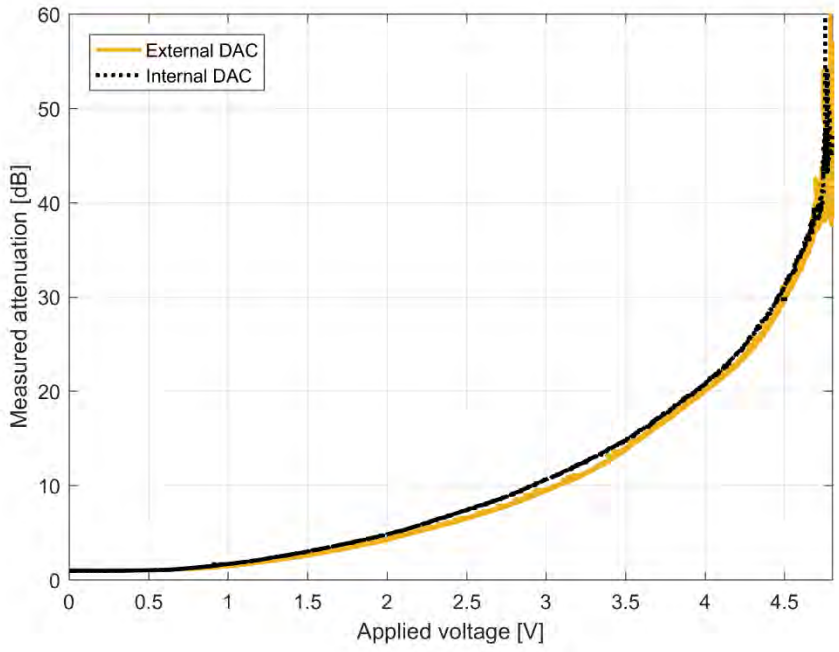

Figure 4.8: Electro-optical transfer function of 850 nm MM – VOA for both voltage drivers with external and built-in DAC (Modified figure based on own publication [80])

Furthermore, the increment of the fluctuations and the line thickness around 4.7 V or 55 dB is sign for system constraints to work nearby and beyond this value. Consequently, the provided VOA setup is restricted to operate within 1 dB @0 V and 55 dB @4.7 V with best performance up to 38 dB. Considering of up to 1 dB losses, the maximum measured enough accurate optical attenuation is exactly 37 dB. On the one hand, there are restrictions into the measurement setup, namely the optical power meter sensitivity is -43 dBm while the 850 nm laser source is 0 dBm. On the other hand after 4.65 V, the transfer function resembling a vertical asymptote, which applies additional difficulties to be setup an accurate and stable attenuation value. In addition, it has to be noted that the attenuation values in respect to individual optical signal measurements are non-linearly distributed in terms of voltage growth. In other words, this non-linear behaviour cannot be applied regarding representation of a real FSO channel. To address this issue, the imported attenuation data has to be processed by a function, which corresponds to the inverse curves in ***Figure 4.8***. The functions for internal and external DAC cases are derived with help of non-linear least squares fitting approach ***[80]***. Unlike the linear case, the non-linear regression is capable to incorporate large range classes of functions with very few restrictions. Moreover, the derived functions could be estimated only based on a small amount of measured values. In combination with the well-built mathematical model, this approximation appeares to be very useful for implementation. Considering those facts and using the non-linear least squares method, the best fitting equation for both cases of external and internal DAC unit is provided in Eq. (4.1) ***[80]***.

$$y = A + Bx + Cx^2 + Dlogx \quad (4.1)$$

Where x is the applied attenuation data in [dB] and y is a DAC value, which corresponds to the desired voltage level. While for the internal DAC, y is between 0 and 4095, the external DAC is characterized with a value between 0 and 65536. Moreover, the parameters A, B, C and D for both cases are provided in ***Table 4.1***.

Parameter	*A*	*B*	*C*	*D*
External DAC [80]	7522.748	745.622	-10.901	11394.194
Internal DAC	561.652	16.622	-0.28766	867.784

Table 4.1: Derived linearization parameters used in Eq. (4.1)

All of them are iteratively found by numerically solved a system of equations where its amount is equal to the total number of the possible DAC voltage values. In accordance with the previous considerations, only the voltage controller with an external DAC will be applied into the further measurements. Consequently, the linearization of the electro-optical transfer function regarding the Internal DAC is only performed in terms of an additional clarification. Once the system configuration based on Eq. (4.1) is accomplished, the attenuation parameter is already linear dependent on the DAC voltage and the applied attenuation respectively. In order directly to measure the induced attenuation in the optical fibre, instead of received optical power, a reference value in respect to the internal link losses due optical fibre, optical connectors, etc. are taken into account ***[80]***. For the current configuration, the corresponding parameter is 1 dB. After this final part of the calibration process, the graph showing the

applied attenuation versus measured attenuation for voltage driver with an external as well as internal DAC is shown in ***Figure 4.9***.

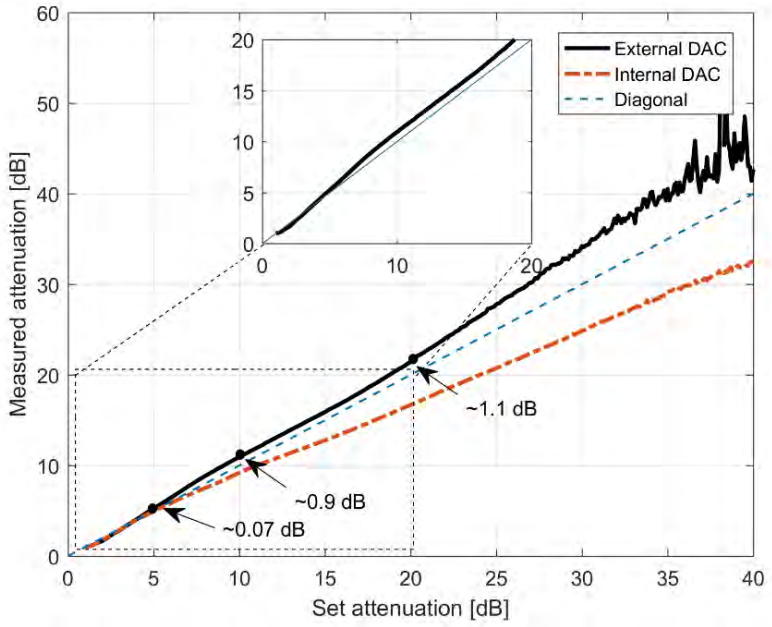

Figure 4.9: Electro-optical transfer function of 850 nm MM – VOA for both control units with external and built-in DAC after the set calibration

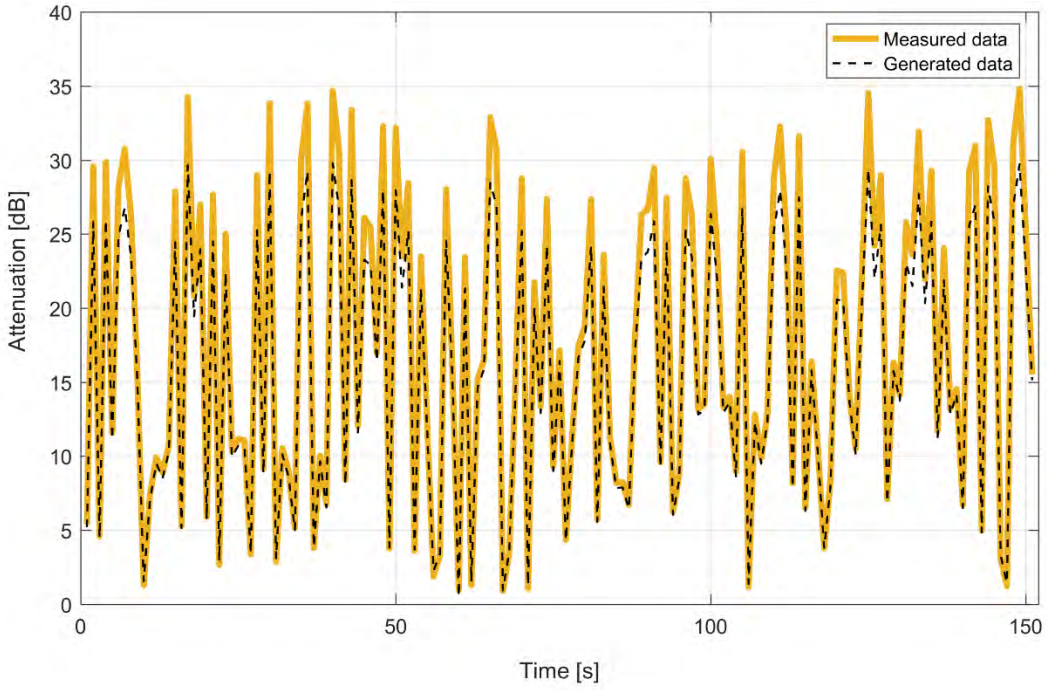

Figure 4.10: Comparison between applied and measured attenuation based on randomly generated data for the case of 850 nm MM – VOA and external DAC (The figure is obtained from own publication [80])

After comparison of ***Figure 4.8*** and ***Figure 4.9***, it is evident that the results are significantly improved. In addition, it is clear that the control unit with an external 16 bit DAC has considerably better performance due to the symmetry properties of the linear electro-optical transfer function. The lower resolution of the internal DAC leads to more problems for finding solution. In other words, as was stated, the VOA will be controlled based only on voltage driver incorporating external 16 bit DAC. Yet some nonlinearities are still present, which leads to a significant error for the higher attenuation levels. So further restrictions are applied to the operation range of the attenuator. According to ***Figure 4.9***, this is between 1 dB and 20 dB where the absolute error does not exceed more than 1.1 dB. Nevertheless, when a simple compensation mechanism is applied, the setup can be used up to nearly maximum range of 55 dB. In addition, the error of 1.1 dB is not stable and can fluctuate in slight amounts in relation to the different operation conditions. An example of randomly distributed samples within 0 – 30 dB range, which are applied to the already calibrated channel emulator, is given in ***Figure 4.10***. It is evident that the absolute error corresponding to the maximum applied attenuation of 30 dB is ~4 dB, while for 20 dB is already ~1.1 dB. These results completely agree with ***Figure 4.9***.

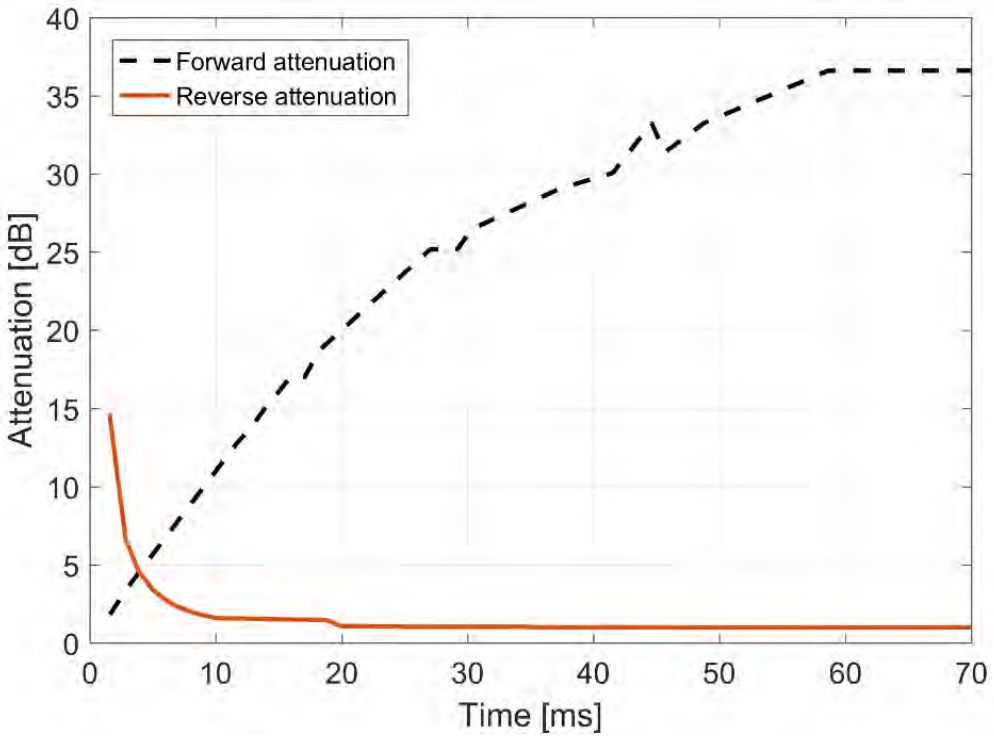

Figure 4.11: Response time measurements regarding 850 nm MM-VOA for external DAC (The figure is obtained from own publication [81])

Contrary to the attenuator specifications, where the response time is 10 ms, for the current setup there is a slight delay. According to the forward attenuation graph in ***Figure 4.11***, the time for reaching the maximum allowed attenuation is 58 ms. On the other hand, for the reverse case, the time to be attained minimum attenuation is 10 ms ***[81]***. Considering a signal attenuation spike due to fading, the total response time is 68 ms, which is a sum of the forward and backword times. Respectively, if the simulated fog or turbulence-induced fading is at minimum 37 dB, the fluctuations should be with frequency ≤ 14.7 Hz (68 ms). Although

this is sufficient for fog-induced fading which is always slower than 1 s (1 Hz), the turbulence scintillations exceed in times the maximum allowed value of 14.7 Hz reaching up to 1 kHz (normally up to 200 Hz). Nevertheless, the changes in the terrestrial turbulence scintillations are characterized with lower attenuation < ~10 dB (**Chapter 6**) compared to the considered 0 ↔ 37 dB case and consequently the VOA operates faster. In particular, the simulations in **Chapter 6** show that the maximum atmospheric turbulence attenuation for a 2.7 km long-distance terrestrial link and R_d = 0.1 m is up to ~8.6 dB, while the mean attenuation value is only ~2.1 dB. Consequently, if a linear region for both forward and backward times within 7 – 15 dB ***Figure 4.11*** is selected, the total response time can be significantly lower and could be between 4 ms and 10 ms corresponding to 250 – 100 Hz.

4.4.2 Measurement results in terms of 1550 nm SM – VOA

In contrast with the 850 nm channel emulator used mainly for representing terrestrial links, the ultra-long-distance deep space FSO downlinks require 1550 nm operating wavelength, which possesses higher resistance to the adverse Mie scattering as well as clear-air atmospheric turbulence ***[70]***. Consequently, the initially incorporated 850 nm MM – VOA is substituted with 1550 nm SM – VOA, which is characterized with another non-linear electro-optical transfer function depicted in ***Figure 4.12***.

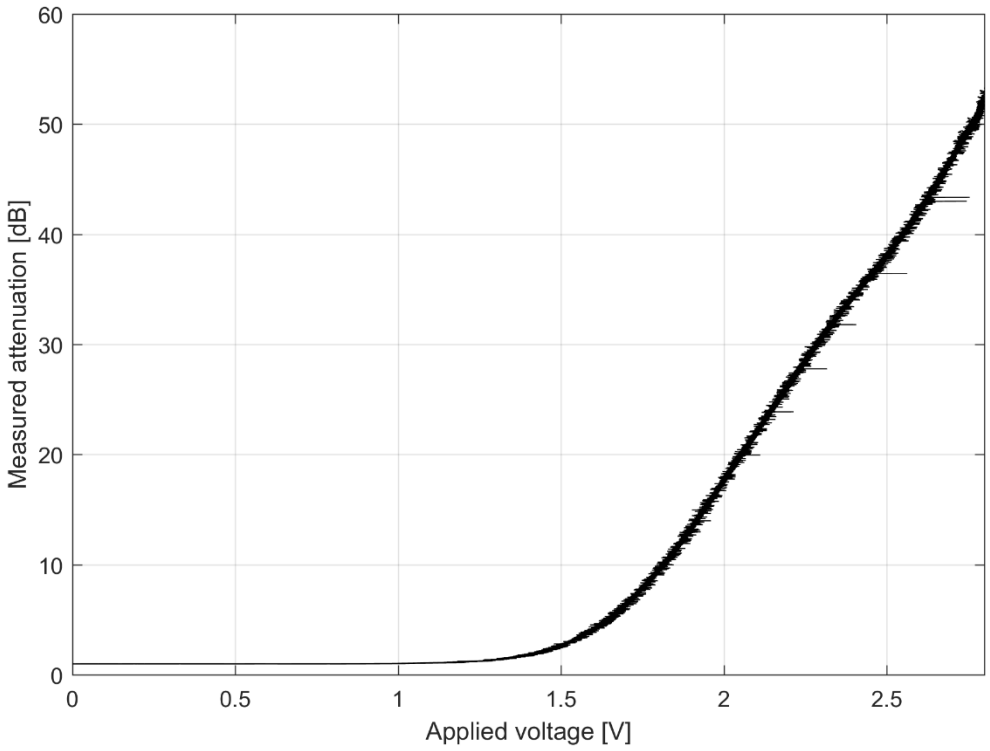

Figure 4.12: Electro-optical transfer function of 1550 nm SM – VOA for the voltage driver with 16 bit external DAC

Having in mind the shown huge impact of the non-linearity over the performance of 850 nm channel emulator, a new improved non-linear curve fitting approach is required regarding the representation of HPE deep space FSO links. In particular, the representation of an authentic deep space FSO channel operating with signal photons demands as low as possible absolute

error. The measured setup includes 1550 nm CW laser @5.6 dBm and digital optical power meter (PM100D) with -43 dBm sensitivity, leading to link margin of 48.6 dB. For achieving electro-optical transfer function with linear behaviour, again the same polynomial regression technique, applied for 850 nm MM – VOA, is used. However, the accuracy is significantly improved by means of splitting the electro-optical transfer function into two parts and applying two higher degree polynomials, each corresponding to a different attenuation range. Respectively, while one polynomial is used for attenuation range between 0 – 5 dB, which according to **Chapter 7**, covers all undesirable atmospheric-induced fading, the second one is within 5 – 55 dB range. The general form of used polynomial is given in Eq. (4.2)

$$y = A + B * x + C * x^2 + D * x^3 + E * x^4 + F * x^5 \qquad (4.2)$$

Similar to Eq. (4.1), while x is the attenuation data in [dB], y is already the DAC value corresponding to the required voltage level by the SM – VOA. Moreover, the coefficients A, B, C, D, E, F for each of the polynomials are provided in ***Table 4.2***.

External DAC	*A*	*B*	*C*	*D*	*E*	*F*
Polynomial 5 – 55 dB	-3324	3.138E4	-1.852E4	5559	819.4	47.13
Polynomial 0 – 5 dB	1.797E4	675.6	24.11	0.6044	0.005228	0

Table 4.2 Derived linearization parameters used in Eq. (4.2)

The measured electro-optical transfer function, after the performed calibration for 1550 nm SM – VOA, is given in ***Figure 4.13***. The applied technique with two polynomials leads to substantial improvement in comparison with results for 850 nm MM – VOA in ***Figure 4.9***.

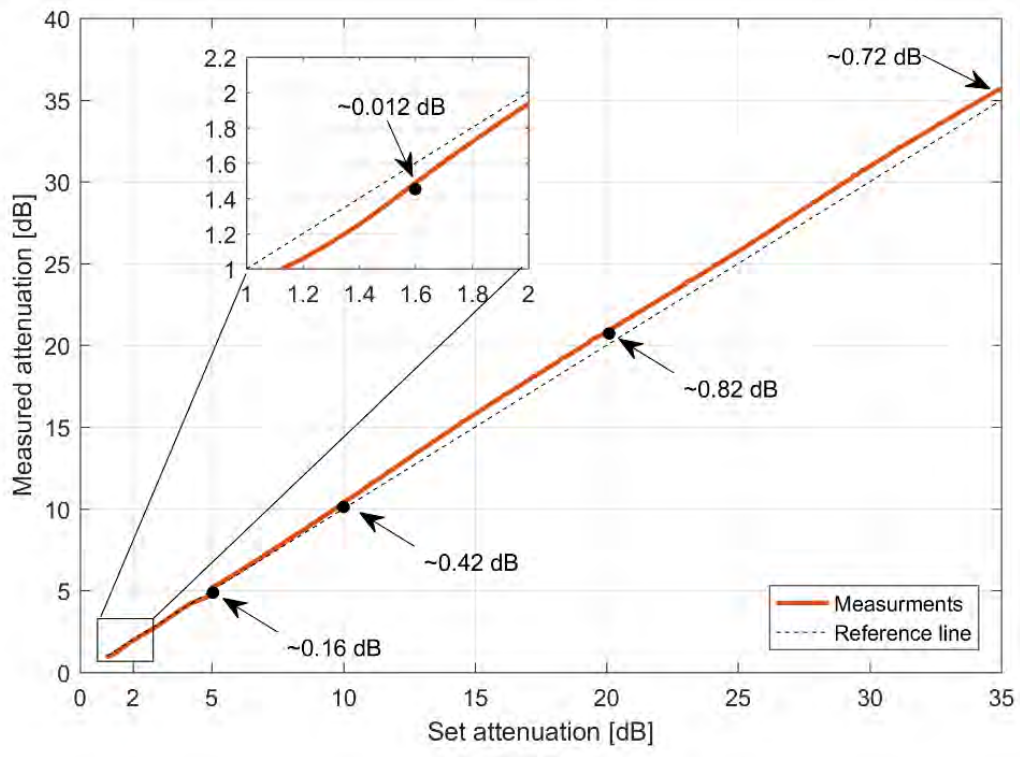

Figure 4.13: Electro-optical transfer function of 1550 nm SM – VOA and the external 16 bit DAC after the set calibration (The figure is obtained from own publication [87])

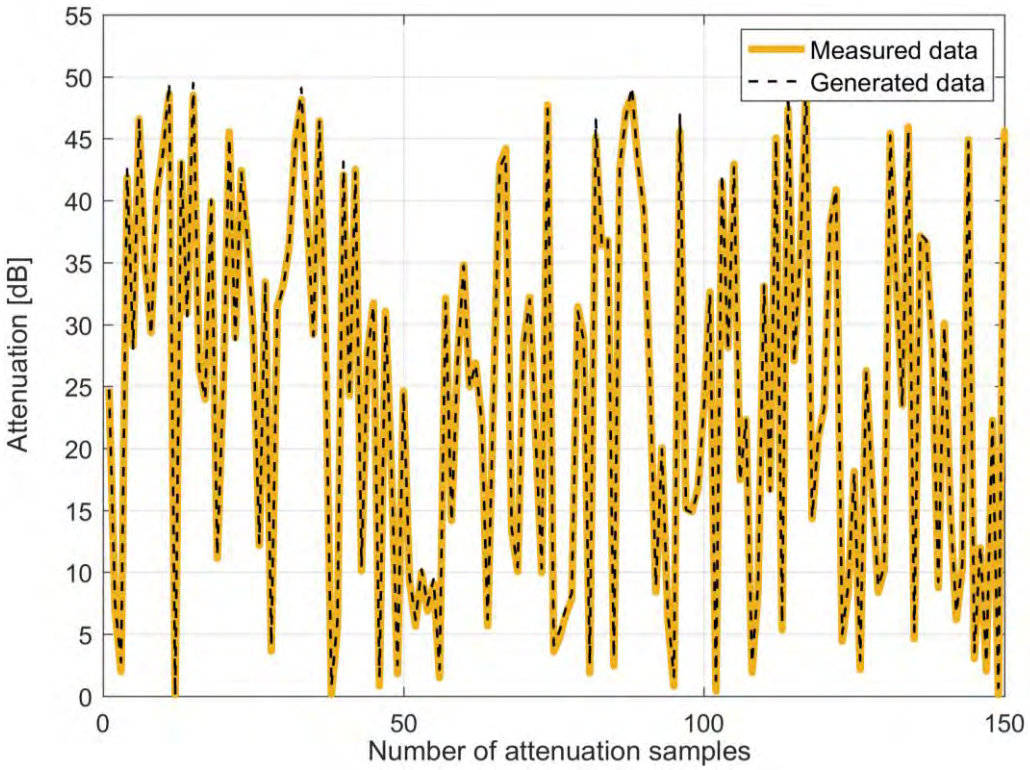

Figure 4.14: Comparison between applied and measured attenuation based on randomly generated data for the case of 1550 nm MM – VOA

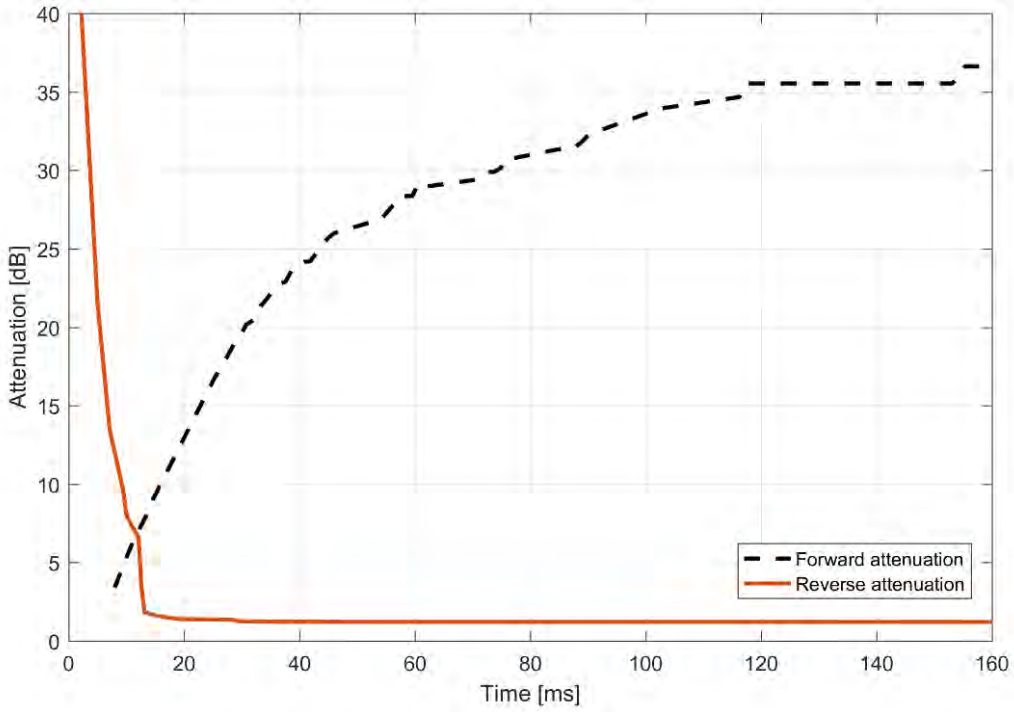

Figure 4.15: Response time measurements regarding 1550 nm SM – VOA (The figure is obtained from own publication [85])

In accordance with **Chapter 6**, the space-to-ground atmospheric turbulence-induced fading normally reaches values from ~0.55 dB @R_d = 8 m up to ~5.2 dB @R_d = 1 m for γ = 20°. Consequently, the 0 – 5 dB polynomial plays the most important role. The performed test with random distributed samples within 0 dB – 50 dB optical power range, which is well aligned with the 48.6 dB link margin of the measurement setup, is shown in ***Figure 4.14***.

Similar to MM – VOA, the given minimum response time in the specifications for SM – VOA is 10 ms. However, according to the forward and reverse attenuation graphs in ***Figure 4.15***, the time for having 0 -> 37dB is 155 ms and 37 dB -> 0 dB is 13 ms respectively ***[85]***. Having summed the two times, the total response time due to an attenuation spike is 168 ms (5.95 Hz). In analogy to terrestrial links the changes in clouds and fog attenuation is slow enough and the main problem is the representation of fast fluctuations related to atmospheric turbulence scintillations. But the results in **Chapter 6** shows that the scintillation range is between minimum 0.55 dB for R_d = 8 m; γ = 20° and maximum 5.2 dB for R_d = 1 m; γ = 20°. Consequently, if the VOA is operated within 1 – 6.5 dB linear region, the fading frequency is 1 kHz (~1 ms) for 0.55 dB and 125 Hz (8 ms) for 5.2 dB. Nevertheless, the operation of channel emulator in the presence of space-to-ground atmospheric turbulence is well investigated in **Chapter 7**.

4.5 Verification of the FSO channel emulator based on SFP

The performance of the hardware channel emulator representing Mie Scattering attenuation as well as atmospheric turbulence-induced fading is tested based on scenario including a SFP module. In particular, these large-scale commercially available transceivers providing interface between electrical and optical technology are implemented in various types of fibre optical networks. Nevertheless, their compactness, low price as well as decent characteristics recently lead to their implementation also in FSO domain. Mainly applied as a last mile solution (up 1 km), various FSO manufactories such as Koruza, Artolink, etc. offer system configurations based on electro-optical SFP transceivers ***[7] [115]***. The most common SFP architecture given in ***[116]*** includes laser transmitter, photodetector, microcontroller, amplifiers as well as control modules, which guarantee the normal system operation. Moreover, their communication wavelength is between 800 nm and 1550 nm with data rates reaching up to 100 Gbps for the most advanced SFP versions ***[5]***. Thought, the main types are SFPs supports 1.25 Gbps, there is an improved SFP+ characterized with 10 Gbps data rates ***[5]***. Having in mind the shown SFP-based FSO system in ***[7]***, the transmitted laser power is <~2 dBm @1550 nm and the photodiode sensitivity is < -23 dBm @1550 nm, which leads to ~25 dB link margin. According to the commercially available systems (e.g. Artolink) as well as ***[5]*** the calculated link margin allows channel losses between 20 – 40 dB with an average value of ~30 dB. Consequently, the link distances that depend on required data rates can reach 1 – 4 km for high 99.9 % availability (three nines). As an example, the 10 Gbps SFP+ solution provided by Artolink with 22 dB link margin supports link distances up to 1.5 km at 1550 nm wavelength. On the contrary, the 1 Gbps FSO system architecture includes an SFP with 40 dB link margin, which can cope with considerably longer distance of up 4 km. After this short introduction to SFP transceivers showing their successful

implementation into wireless optical communication, a low-cost SFP module is introduced regarding an evaluation of the developed channel emulator system with 850 nm SM – VOA. For the purpose of the current scenario, low cost bidirectional TL-SM311LM-GT SFP is considered, which provides 1.25 Gbps throughput. The transmitter is internally modulated using Vertical-Cavity Surface-Emitting Laser (VCSEL), which operates at 850 nm. In order to address the eye safety requirements, the transmitted laser optical power is at maximum -3 dBm, while the sensitivity is at minimum ~ -20 dBm. However, in practice the link margin is roughly estimated to a measured value of ~27 dB for BER = 10^{-12}. The architecture of the developed setup shown in ***Figure 4.16*** evaluates the channel emulator based on unidirectional IM/DD link, which means that only one SFP is implemented. In addition to the SFP module, the current testbed includes the following units: 10 Gbps BER tester (BERT) and SFP evaluation board.

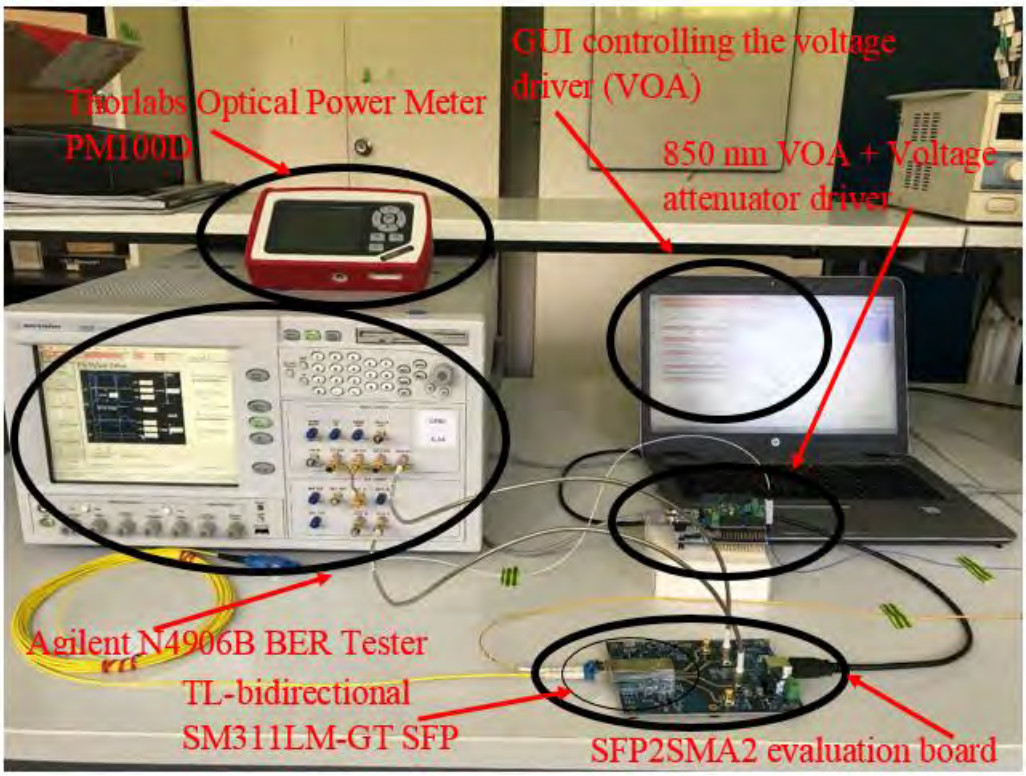

Figure 4.16: Photograph of the self-developed testbed incorporating SFP module used for evaluation of the channel emulator with 850 nm MM – VOA

When the SFP module is applied in a real FSO communication link, the optical fibre could be entirely replaced with a proper beam expander system/receiver lens, which collimates and expands/focus the beam diameter. However, in the case of this setup the MMF is directly coupled into the SFP transmitter and receiver based on LC connectors. In particular, the SFP is connected with VOA via MMF 50/125 μm, which completely satisfies the requirements of both units and additionally allows optimum amount of optical power to be sent and received. Besides the simple representation of a unidirectional FSO link taking into account IM/DD scheme, the testbed includes RF communication part, which takes care of the

electrical signal processing. The SFP module is plugged into SFP2SMA2 evaluation board, which in our case is used as an interface allowing bidirectional SMA connection. The considered board supports both standards including SFP and SFP+ with throughput up to 10 Gbps. The SMA ports are connected to the Agilent N4906B BERT allowing test sequences up to 12.5 Gbps. Consequently, both the evaluation board and BERT fully cover the maximum data rate of SFP module, which is 1.25 Gbps. Considering this target data throughput, the internal BERT clock is setup to 1.25 GHz. In addition, the used pulse pattern for generating Pseudo Random Binary Sequence (PRBS) that internally modulated the SFP laser is 2^{31}-1. After optical pulse detection, the RF signal is send back to BERT for comparison and evaluation of BER.

By itself, the SFP accompanied by evaluation board can be described as a transparent network interface, which in our case is modulated with the already described PRBS of RF pulses. Consequently, our testbed operates based on Non-Return to Zero (NRZ) On-Off Keying (OOK), which is the simplest and the most often applied intensity modulation technique in FSO communications. Similar to FSO systems applying IM/DD scheme with OOK modulation, the SMF module accompanied by evaluation board forward the directly detected optical signal to BERT where the received RF pulses are processed based on maximum likelihood receiver with hard decision decoding. Considering an AWGN channel as well as fixed pulse detection threshold of 0.5, which is shown in ***Figure 4.17***, the BER versus SNR per bit curve for OOK is calculated with Eq. (4.3) ***[42]***.

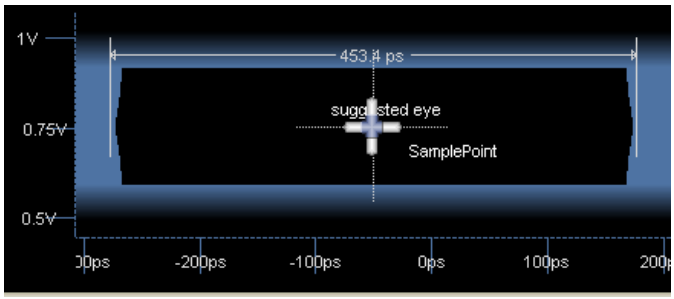

Figure 4.17 BERT setup – sample point

$$BER = Q\left(\sqrt{\frac{E_b}{N_0}}\right) \quad (4.3)$$

Where E_b/N_0 is referred to SNR per bit. Addressing that the maximum likelihood receiver is based on a matched filter, the bandwidth of the AWGN is half of the data throughput. In other words, taking into account Eq. (4.3), BER versus SNR is calculated with Eq. (4.4) ***[117]***.

$$BER = Q\left(\sqrt{SNR/2}\right) \quad (4.4)$$

Once the evaluation testbed architecture is introduced, the performance of the channel emulator module containing VOA is evaluated based on BER parameter. To address this task, the VOA attenuation is changed in the range between 1 – 33 dB while the BER is measured with the considered BERT system. Taking into account ***Figure 4.9*** and more specifically the absolute error between the ideal case and the achieved linear electro-optical transfer function for CU with an external DAC, a correction factor up to 4 dB is applied.

Instead of 1 – 33 dB, a range of 1 – 29 dB is set up. The test-time duration of the each BER measurement is accomplished in terms of the BERT's requirements to be reached 95 % confidence level. The measurements of BER versus applied attenuation are shown in ***Figure 4.18***. According to the measurements, when the optical attenuation does not exceed 27 dB, the optical system based on SFP module operates at very high BER values lower than 10^{-12} (normally up to 10^{-16}). Nevertheless, when the atmospheric attenuation represented with the FSO channel emulator is higher than 27 dB, the BER begin to increase up to 10^{-4}. This behaviour completely corresponds to the link margin of the applied SFP unit, which is ~27 dB (for BER =10^{-12}). In case the attenuation is increased more than 31 dB, the BER rise suddenly and optical link is fully interrupted.

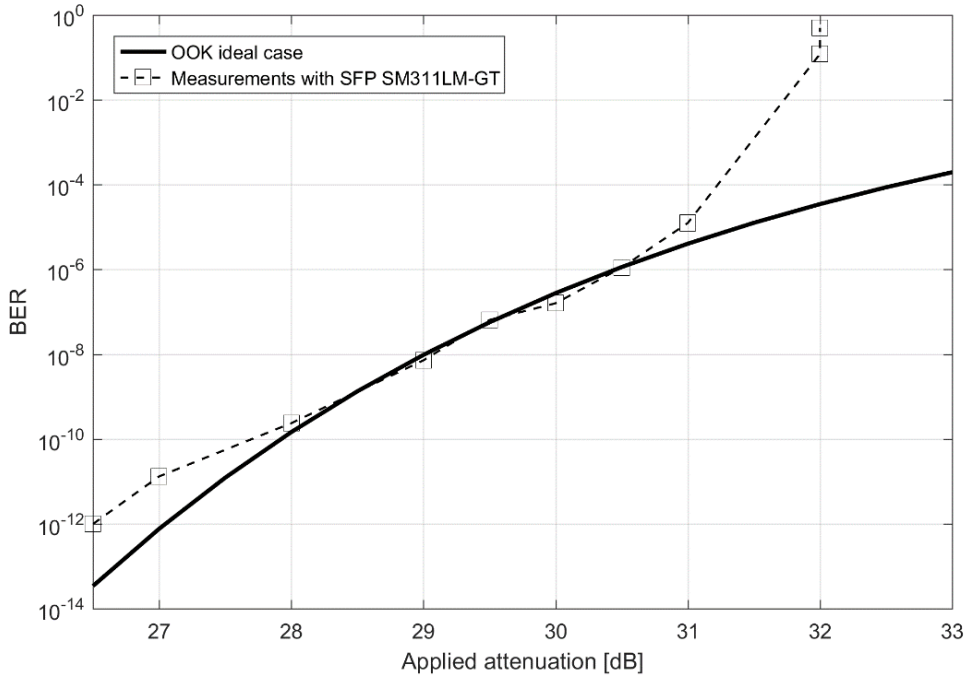

Figure 4.18: Measured BER versus applied attenuation for TL-SM311LM-GT SFP compared to theoretical OOK results

To address the validity of the results, the measured BER values are compared with the ideal system performance case based on Eq. (4.4). In accordance with the outcomes, the theoretically simulated BER curve nearly completely coincides with the real BER measurements. The main difference between the two curves occurs when the attenuation is increased more than 30 dB. The reason for the rapid change in BER leading to immediate optical link interruption is due to applied hard decision decoding with fixed decision threshold. The shown results completely proved the feasibility of the channel emulator in terms of representing a real FSO link. While the current results are for terrestrial links with 850 nm wavelength, similar experiment is possible for the 1550 nm case.

Chapter 5

5. Mie scattering over FSO links

In this chapter, long-distance terrestrial (> 2 km) as well as space-to-ground FSO (> 500 km) links in the presence of Mie scattering (Fog and Clouds) are evaluated by means of simulations, testbeds for FSO channel emulation as well as real measurements (***Figure 5.1***).

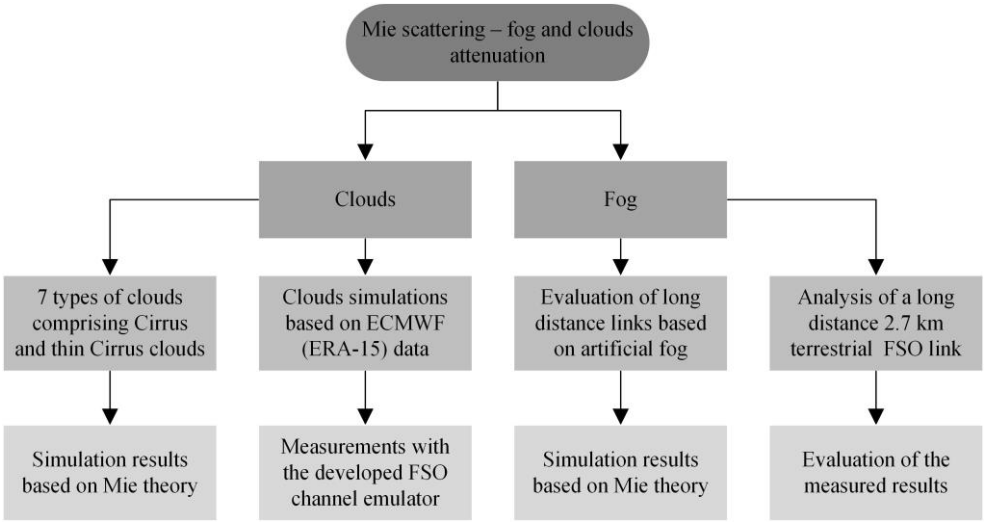

Figure 5.1: Chart of the performed simulations and measurements in Chapter 5

Although Mie theory is used to estimate various clouds-induced optical signal attenuation and its excessively harsh effect over FSO system performance, the main emphasis in **Chapter 5** is placed over high-altitude Cirrus clouds, which are still a substantial problem even for specially located OGSs. Nonetheless, having addressed the available ECMWF data (***[63]***) as well clouds microphysics (**Chapter 3**), a continental space-to-ground FSO link for Graz, Austria regarding various types of clouds is evaluated. Furthermore, the results are utilized to perform tests with the developed FSO channel emulator in **Chapter 4**. Along with clouds, fog is investigated based on Mie theory as well as microphysical parameters derived in **Chapter 3**. In order to observe the FSO performance in a fully controlled environment, which is similar to the developed VOA-based channel emulator, two types of artificial fog sources are compared/investigated based on continental and maritime theoretical fog models. Taking into account real fog measurements, long-distance 2.7 km terrestrial FSO link for the location of Graz, Austria is investigated. Having addressed the introduced Mie theory and

more specifically, the provided Eq. (3.1) and Eq. (3.4) in **Chapter 3** for Mie scattering efficiency, the Q_{sca} is calculated in terms of 785 nm 850 nm and 1550 nm, which are also compared with a laser source operating at 10 µm wavelength. In other words, the water refractive indices that correspond to the provided 4 wavelengths are as follows: $1.32 + i1.38\ 10^{-7}$; $1.32 + i2.93\ 10^{-7}$; $1.31 + i9.86\ 10^{-5}$; $1.21 + i0.05$ ***[26]***. Since the influence of suspended water droplets in the atmosphere over transmitted laser beam depends not only on the radii but also on the wavelengths, the size parameter x is applied (**Chapter 3**) ***[24]***.

r / x	785 nm	850 nm	1550 nm	10 µm
Air molecules – 0.0001 µm	8E-4	7.39E-4	4.05E-4	6.28E-5
Haze – 0.01 – 1 µm	0.08 – 8	0.074 – 7.39	0.0405 – 4.05	0.0063 – 0.63
Fog – 1 – 20 µm	8 – 160.08	7.39 – 147.83	4.05 – 81.07	0.63 – 12.5
Clouds – 0.1 – 100 µm	0.8 – 800	0.74 – 739	0.405 – 405	0.063 – 63
Rain – 100 – 10000 µm	800.41 – 80041	739.2 – 73920	405.37 – 40537	62.83 – 6283.2
Snow – 1000 – 5000 µm	8004.1 – 40020	7392 – 36960	4053.7 – 20268	62.83 – 3141.6

Table 5.1: Calculation of particle size parameter's range for the main atmospheric effects regarding 785 nm, 850 nm, 1550 nm and 10 µm wavelengths

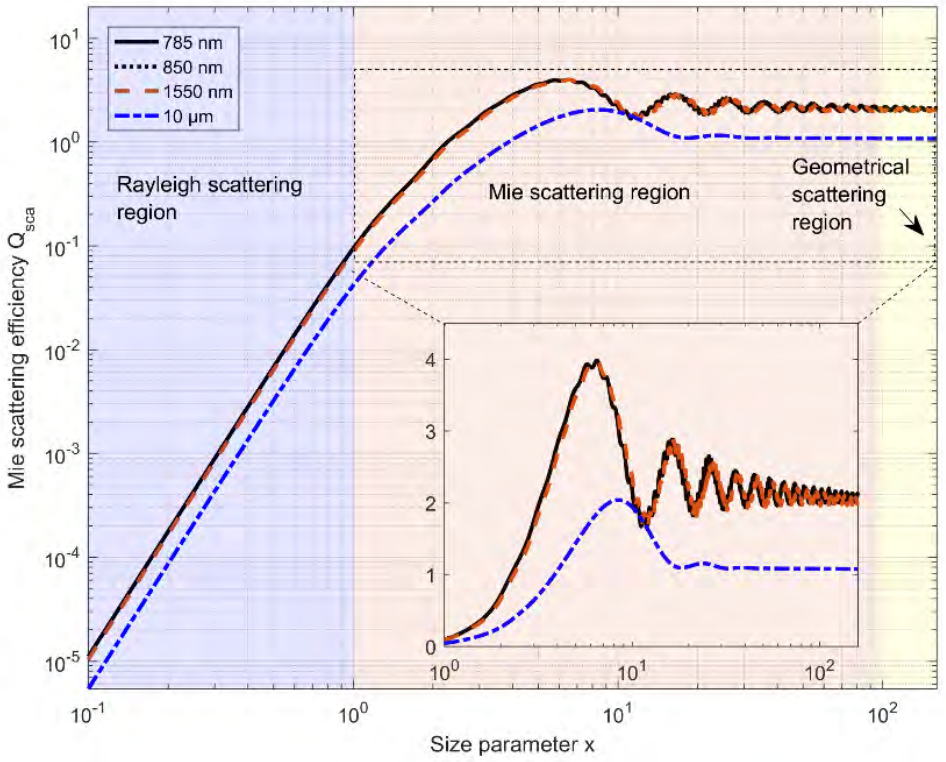

Figure 5.2: Mie scattering efficiency versus size parameter *x* for 785 nm, 850 nm, 1550 nm and 10 µm wavelengths

More specifically, the size parameter concept, which comprises the inherent dependence on the wavelength, allows to be introduced clear differentiation between Mie scattering and the other two scattering regimes including Rayleigh and Geometrical ones. In accordance with

[30], Mie scattering occurs when the size parameter is in the interval ~1 < x < ~100. In other words, when ~1 < x is Rayleigh scattering and when x > ~100 is Geometrical scattering. But normally, Mie theory is considered as a good approximation for particles with x up to 10000 ***[24]***. The size parameters' intervals for the most prominent atmospheric impacts are provided in ***Table 5.1***. The calculations are accomplished based on the provided classification in ***[30]*** regarding different possible particle radii as well as the most utilized 3 wavelengths. In particular, the largest calculated size-parameter interval for the case of fog (8 < x < 160.08) is in respect to the shortest 785 nm wavelength which excludes the results for 10 µm. On the other hand, the calculated Mie scattering efficiency (fog) for all 4 wavelengths involves the range 0.63 < x < 160.08. While clouds are charterized with a similar 0.0063 < x < 160.08 range, it is still possible significantly larger x up to ~800 (λ_0 = 785 nm) to appeared. Based on the applied simulations comprising the theory in **Chapter 3**, the Mie scattering efficiency (fog) versus size parameter x for the 4 wavelengths is depicted in ***Figure 5.2***. Moreover, the three scattering regimes are also shown. Furthermore, in order to address a better scaling of ***Figure 5.2***, clouds with their size parameter reaching x = ~800 are not shown.

5.1 Mie scattering attenuation due to clouds

Similar to fog effect, clouds are formed based on condensation process containing mainly water droplets with radii from 0.1 µm up to ~100 µm (130 µm) ***[28]***, ***[97]***. Nevertheless, the particle concentration N_c of clouds is significantly larger and can exceed 400 cm^{-1} (in rear cases up to 1300 cm^{-1} for Cumulous clouds ***[26]***), which is more than 20 times the particle concentration of heavy advection fog ***[28]***. Consequently, depending on the cloud's type, Mie scattering attenuation can reach up ~600 dB/km leading to full blockade of FSO communication link. This means that clouds considerably decrease the availability and reliability of long-distance space-to-ground links even when the OGS's location is specially selected. Therefore, their investigation is of crucial importance regarding space borne FSO communication channels.

In general, clouds can be observed in the atmosphere up 10 – 13 km, namely up to the end of the Earth's troposphere and they are divided into three categories regarding their height: Low level clouds up to 2 km: Stratus, Stratus/Stratocumulus, Stratocumulus; Middle-level clouds between 2 – 7 km: Altostratus and Nimbostratus; High-level clouds between 3 – 8 km: Cirrus and thin Cirrus. In addition, there are also Cumulus clouds with vertical development between the ground and the top of the troposphere (up to 13 km) ***[118]***. In **Chapter 3**, Mie scattering coefficient due to fog and clouds is calculated based on Mie theory and empirically proved PSDs all implemented in MATLAB simulation environment. Considering the PSD results for each cloud type given in ***Figure 3.4***, the scattering coefficient β_{sca} and the related optical attenuation A_{tt} are calculated with Eq. (3.8) and Eq. (3.9). Instead of particle radius, the used 0.1 resolution in the simulations is in respect to size parameter x, which is applied in Mie theory. Furthermore, the choice of the 1550 nm wavelength adheres with the considered requirements for space-to-ground FSO communication downlink in **Chapter 1**. In order not to duplicate the results, only A_{tt} versus

particle radios r is shown in ***Figure 5.4***, while β_{sca} is characterized with its final simulated values given in ***Table 5.2***. Having addressed the validity of the results, the self-simulated Mie scattering β_{sca} is compared with β_{sca_l} obtained from ***[95]***.

Cloud type	Cumulus	Stratus	Stratus/Strato-cumulus	Stratocumulus[2]
β_{sca_l} [km^{-1}][1]	131.85	56.80	37.45	44.83
β_{sca} [km^{-1}]	130.73	55.9	37.08	44.83
Cloud type	Altostratus	Nimbostratus	Cirrus	Thin Cirrus
β_{sca_l} [km^{-1}][1]	95.02	80.26	0.81	0.086
β_{sca} [km^{-1}]	98.1	79.75	0.92	0.087

[1]Values obtained from [95] [2]The PSD for Stratocumulus is not available and the used β_{sca} is from the literature [95]

Table 5.2: Mie scattering coefficient at 1550 nm for 8 types of clouds

In contrary to fog, the very high concentration of water droplets in clouds leads to significant larger Mie scattering coefficients. This statement is valid for most of clouds including Stratus, Altostratus, Nimbostratus and Cumulus with β_{sca} within 55 km^{-1} and 130 km^{-1}. A major exception is made only by Cirrus clouds, which are very thin, wispy and in comparison with other clouds are formed mainly from ice crystals. In contrast to fog, which is mostly modelled as a single scattering medium, the large Mie scattering coefficients turn the normal clouds into multiple scattering medium. This phenomenon is well defined by optical thickness parameter, which provides information for the number of scattering events regarding a photon that propagates through a cloud with length L_c ***[118]***. The L_c (1 – 3 km) for Cirrus clouds is obtained from the findings in ***[119]***, observing situ data in respect to night (L_c = 1.6 – 3 km) and day (L_c = 1 – 3 km) measurements for equatorial coastal regions. The optical thickness τ_{opt} is calculated by dividing the average range of cloud type by the average distance between two scattering events ***[39]***.

$$\tau_{opt} = \frac{L_c}{d_{sca}} \qquad (5.1)$$

Where according to Mie theory, the distance d_{sca} is the inverse value of the scattering coefficient. Taking into account the already provided Mie scattering coefficients as well as the average cloud dimensions, the optical thickness is calculated and shown in ***Table 5.3***.

Cloud type	Cumu-lus	Stratus	Stratus/ Strato-cumulus	Stratocu-mulus	Alto-stratus	Nimbo-stratus	Cirrus	Thin Cirrus
d_{sca} [m]	7.65	17.88	26.96	22.3	10.19	12.53	1.08E3	11.49E3
L_c [km]	0.5 – 5	0.2 – 0.8			0.2 – 2	2 – 3	1 – 3	
τ_{opt_upper}	653.59	44.74	29.67	35.87	190.27	239.42	2.77	0.261
$\tau_{opt\_lower\_}$	65.35	11.18	7.42	8.96	19.62	159.61	0.92	0.087

Table 5.3: Optical thickness τ_{opt} for upper and lower physical cloud range L_c for 8 types of clouds

Despite the applied computation technique and the accuracy of multiple scattering model, the attenuation due to normal clouds (non-high altitude Cirrus ones) easily exceeds 30 dB,

which means that an observed fragile (deep) space-to-ground FSO link would be completely interrupted ***[118]***. In addition, due to extremely low optical power levels, which reaches the Earth atmosphere in case of space-to-ground FSO communication downlink, the scattered photons are not nearly observed. Consequently, at the receiver mainly ballistic photons are detected without the highly defused ones, which means that the Beer – Lambert low is still valid. This is especially true for the investigated deep space communication downlinks characterized with very low optical power levels (equivalent to single photons) and average aperture diameter of R_d < 1.5 m (max R_d = 8 m) leading to lower aperture averaging coefficient ***[39]***. Nevertheless, in case of shorter near-space satellite feeder links, multiple scattering effect – similar to ***[39]*** – should be considered.

The map provided in ***[98]***, which shows the global amount for Cirrus clouds within period of 25 years, is given in ***Figure 5.3***. Cirrus clouds, covering around 20 – 30 % (22.8%) ***[98]*** of the Earth, have very low average optical thickness $\tau_{opt} < 3$, which is explained by the fact that Mie scattering coefficient is also low (even comparable with atmospheric fog). Consequently, Cirrus clouds can be partly approximated as single scattering medium ***[120]***.

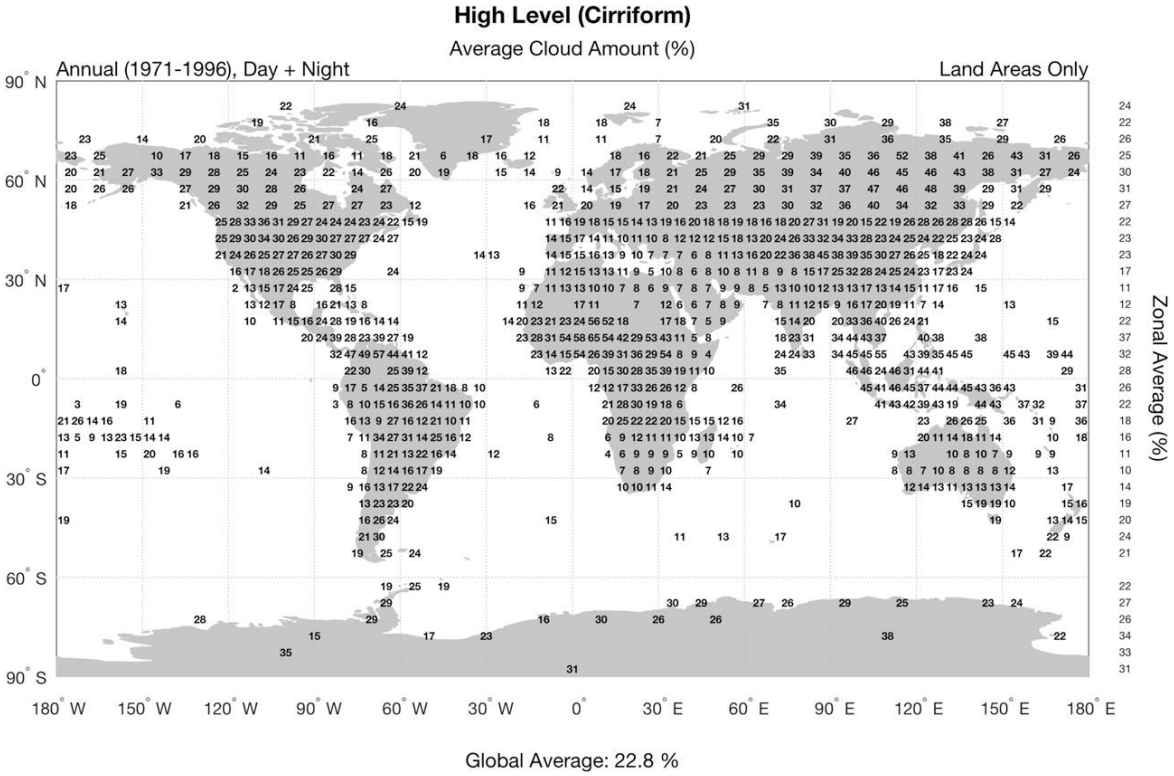

Figure 5.3: Global coverage in respect to Cirrus clouds for period of 25 years (The figure is obtained from publication [96])

Addressing these considerations and similar to accomplished work in ***[118]***, an assumption for single scattering system is introduced. This rough approximation allows to be applied the Beer – Lambert law valid for single scattering medium, namely Eq. (3.9). In contrast to the only given final β_{sca_1} in ***[95]***, the simulated specific attenuation A_{tt} [dB/km] versus particle

radios r for all 7 types of clouds is provided in ***Figure 5.4*** with resolution x = 0.1, corresponding to r = 0.0246 µm (λ_0 = 1550 nm)

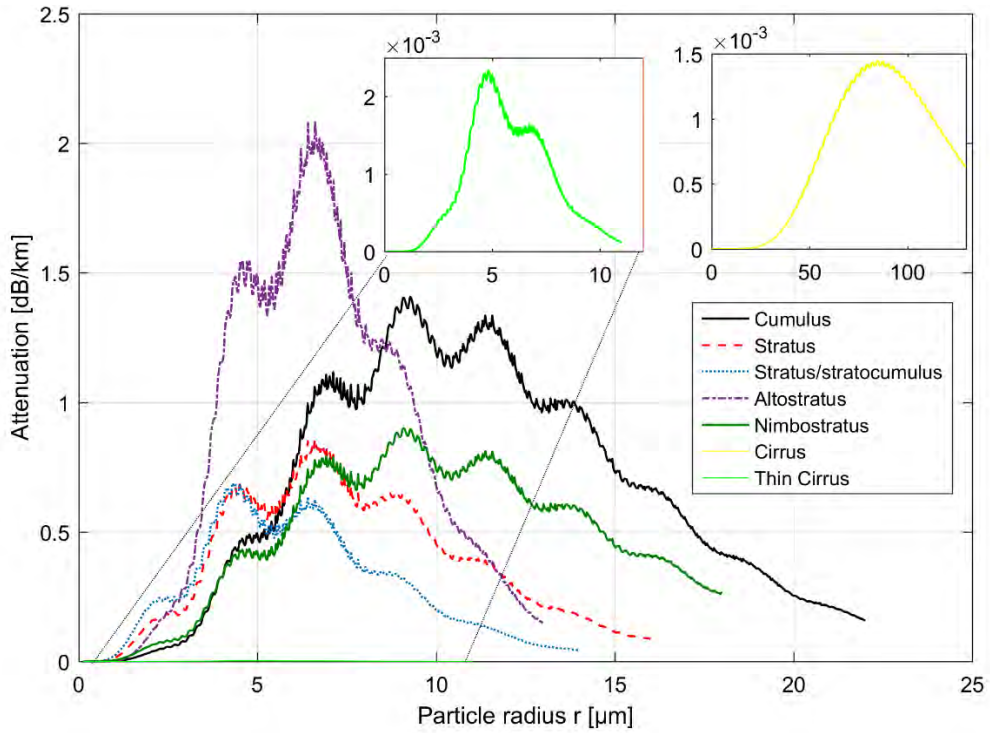

Figure 5.4: Attenuation versus particle radius *r* for 7 types of clouds

Taking into account the minimum and maximum cloud range L_c given in ***Table 5.3***, the total calculated total attenuation values for the all 8 types of clouds (including Stratocumulus) are provided in ***Table 5.4***. The simulation results show that apart from Cirrus clouds as well as thin Stratus – Stratocumulus clouds, the attenuation for the other cases (> 40 dB) cannot be overcome with the available link margin.

Cloud type	Cumu-lus	Stratus	Stratus/ Strato-cumulus	Strato-cumulus	Alto-stratus	Nimbo-stratus	Cirrus	Thin Cirrus
A_{tt_max} [dB]	2.83E3	194.21	128.82	155.75	852.08	1039	11.98	1.13
A_{tt_min} [dB]	283.87	48.55	32.2	38.93	85.2	692.7	3.99	0.37

Table 5.4: Optical attenuation A_{tt} for upper and lower physical cloud range L_c regarding 8 types of clouds

5.1.1 Simulated results for Cirrus clouds at 1550 nm wavelength

The performed analysis in **Subchapter 7.1** shows that each OGS has a very special preselected location where meteorological visibility parameter is maximum, namely V > 20 km ***[30]***. Nevertheless, the Cirrus clouds still appear even when an OGS is located at high altitudes (> 2500 m) in near-equatorial coastal (island) regions. Although the optical attenuation is significantly lower in comparison with other clouds (***Table 5.4***), Cirrus ones

are still unbearable regarding deep space High Photon Efficiency (HPE) FSO downlink communication. The restrictions for a satellite-to-ground FSO link are lower, but still the optical attenuation due to Cirrus atmospheric events should be kept at minimum. While ***Table 5.4*** provides the lower and the upper attenuation limits regarding Cirrus clouds, their full investigation based on the developed MATLAB simulations incorporating the derived theory in **Chapter 3** is given in ***Figure 5.5***. The simulated results, which are aligned with the conclusions in ***[15]***, show that thin Cirrus cause ~1 dB (0.4 – 1.13 dB) optical attenuation while optical power penalties due to Cirrus clouds are in range between 4 – 12 dB. In general, Cirrus clouds does not exceed normally 3 km namely ~12 dB attenuation ***[119]***. Nevertheless, for the following investigation only the average calculated attenuation value of 2.56 dB ((1.13 dB + 4 dB)/2) between the two types of Cirrus clouds is obtained.

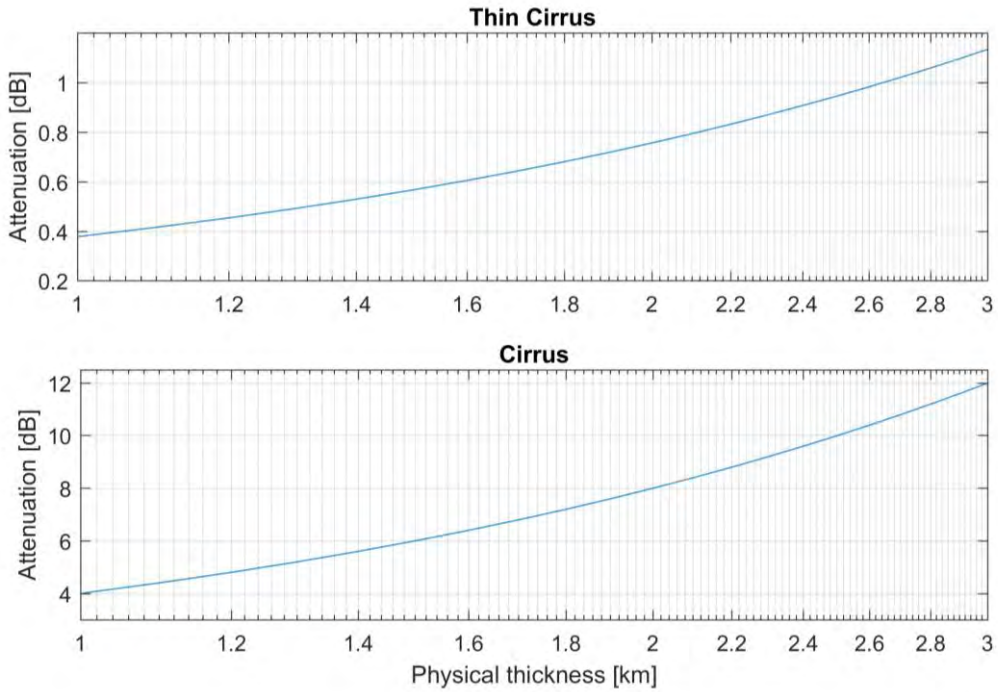

Figure 5.5: Attenuation versus physical cloud thickness for Cirrus and thin Cirrus clouds at 1550 nm wavelength

Bearing in mind ***Figure 3.4***, showing the results from the performed clouds' PSD analysis, the particle sizes for Cirrus (r_p = ~ 96 µm) clouds are significantly larger than thin Cirrus (r_p = ~6 µm) clouds, which is the cause up to 10 times higher optical attenuation.

5.1.2 Estimation of cloud attenuation with ECMWF data for Graz, Austria

In order to evaluate the influence of real clouds-based attenuation over FSO system performance, ERA-15 database developed by ECMWF is used. In particular, the atmospheric data are applied based on an available TU-Graz OPTIKOM group channel model investigating ground-to-space/space-to-ground FSO links provided in ***[63]***. ERA-15 includes 52 parameters characterizing the troposphere, which were measured 3 times per

day, namely every 6 hours. While most of them are related to atmospheric conditions at near ground level, several parameters including LWC are measured in terms of height. Addressing the measured LWC for each separated tropospheric layer and applying Eq. (3.18), allows developing of vertical profile for atmospheric visibility. Consequently, the optical attenuation caused by clouds due to Mie scattering is evaluated. For the purpose of the current carried out investigation, clouds attenuation is evaluated within 1 year period between January and December for the area of Graz, Austria.

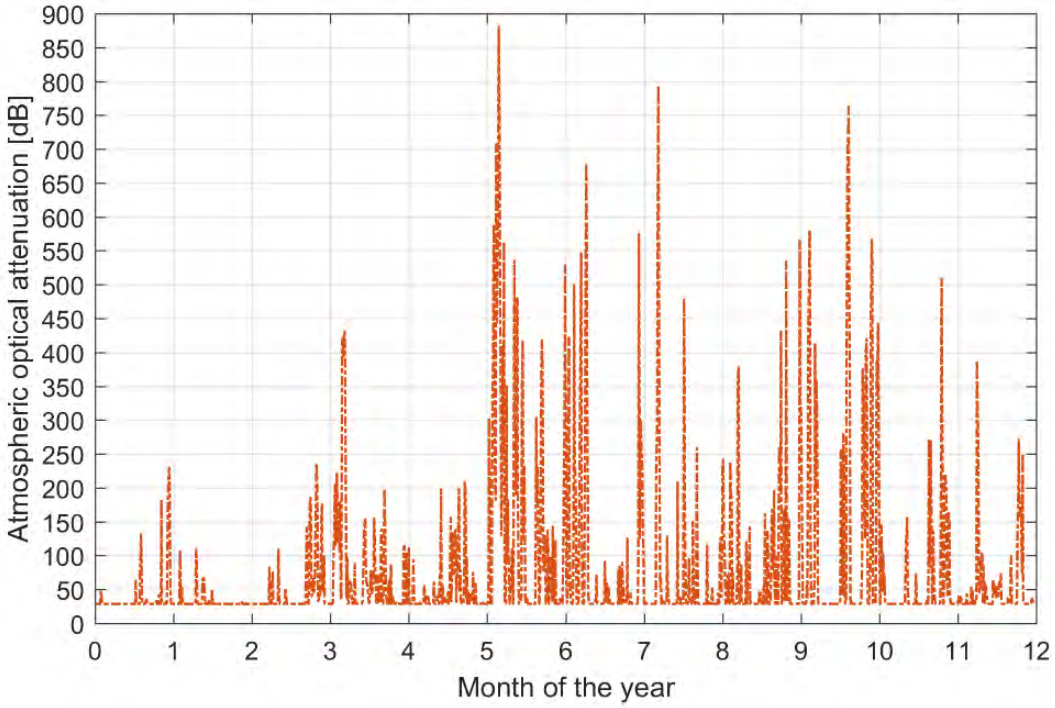

Figure 5.6: Simulation results showing atmospheric optical attenuation due to cloudsat 1550 nm wavelength for Graz, Austria within 1 year period

Figure 5.6 completely complies with the provided results in ***[121]***, which shows that the average cloud coverage (in terms of time) for the longitude and latitude (47.0707° N, 15.4395° E) of Graz Austria is ~50 %. In particular, the value is estimated based on 10 years measurements for 4 months including January, April, July and October, which represent each of the seasons. All 8 types of clouds, namely Cumulus, Stratus, Stratus/Stratocumulus, Stratocumulus, Altostratus, Nimbostratus, thin Cirrus and Cirrus are involved during the observation. According to ***Figure 5.6***, atmospheric attenuation exceeds 600 dB within a number of occasions in the period between October and June. This kind of extremely high fading is characteristic for Cumulus with attenuation between 283.87 – 2.83E3 dB, Altostratus with 85.2 – 852 dB and Nimbostratus with 692.7 – 1039 dB. Although, these simulated values (***Table 5.4***) describe well the channel modelling results shown in ***Figure 5.6*** (A_{tt} > 600 dB), they are an approximation due to limitations in Beer – Lambert law. Nevertheless, these types of clouds, characterized with high optical depth τ_{opt} > 19, completely defuse the optical beam in space, which leads to uniform redistribution of the

optical power and its retransmission of all points of the cloud ***[39]***. Consequently, it occurs extremely high power penalties accompanied with severe temporal dispersion. In other words, during those periods of time the link is considered as blocked with no possibility for LoS FSO communication. Moreover, similar process (but not so severe) is valid for all other clouds for which the optical depth is $\tau_{opt} > 11$ and corresponding optical attenuation is higher than ~40 dB. Cirrus and thin Cirrus and clouds with their low attenuation, which allows still a decent amount of optical power to reach the detector are an exception. In accordance with Table 5.3, they have often optical depth $\tau_{opt} < 1$, which at maximum reaches 2.77. In particular, the estimated Cirrus clouds optical attenuation in **Subchapter 5.1.1** coincide with the given results in ***Figure 5.6*** namely A_{tt} for cirrus is within 4 dB – 11.98 dB and A_{tt} for thin Cirrus is within 0.37 – 1.13 dB. This is an important conclusion due to possibility for establishing space-to-ground FSO communication link. Moreover, ***Figure 5.3*** shows that Cirrus clouds coverage for Vienna and Graz Austria is approximately ~15 %, which well coincides with the provided results in ***Figure 5.6***. The simulated 1-year atmospheric optical attenuation data shown in ***Figure 5.6*** are further applied in terms of investigation of the developed and presented FSO channel emulator in **Chapter 4**.

5.1.3 Measurements with FSO channel emulator based on ECMWF data

The simulated results in ***Figure 5.6*** regarding Mie scattering attenuation due to atmospheric clouds effect are used to validate the terrestrial/space-to-ground FSO channel emulator in **Chapter 4**. In this way, the ability to represent real space-to-ground as well as terrestrial links is confirmed. While terrestrial links are mainly influenced by fog and space-to-ground links by clouds, the current Mie scattering attenuation samples are used to evaluate both. Furthermore, terrestrial as well as near/deep space FSO communication systems are charterized with maximum link margin of 30 dB – 40 dB ***[21]***, which is well supported by the obtained 850 nm MM – VOA as well as 1550 nm SM – VOA units. Once the link margin is spent, the LoS FSO channel is interrupted, namely blocked. In other words, attenuation over 40 dB is not necessary to be considered. Furthermore, fog and clouds attenuation is easily described as a static one due to its slow changes in time in comparison with data throughput. Consequently, the main challenge for the VOA-based channel emulator is due to atmospheric turbulence fading, which does not exceed 10 dB. This topic is investigated in **Chapter 7**.

According to ***Figure 5.6***, the maximum atmospheric attenuation due to Mie scattering (fog and clouds) within 1 year ERA-15 measurements can reach more than 900 dB. Bearing in mind that the incorporated VOA units are limited up to max 60 dB, normalization by scaling has to be accomplished. In particular, the maximum possible attenuation values for both MM – VOA and SM – VOA should not exceed the upper limit defined based on VOAs specifications and calibration accuracy. Although 850 nm MM – VOA can easily cover 40 dB optical attenuation (up to 60 dB), the non-ideal linearization process and used equipment allows link margin up to 20 dB ***[80]***. On the contrary, the improved linearization method used together with 1550 nm SM – VOA proved that the full range between 0 – 60 dB can be exploited. The given limitations up to 50 dB for the SM-VOA in **Chapter 4** (***Figure 4.13***) are due to restrictions in the measurement equipment. After the newly-scaled ERA-15-based

attenuation data for both VOAs are obtained, the measurement setup given in ***Figure 4.7*** is again applied. The results for SM – VOA and MM – VOA are show in ***Figure 5.7 a)*** (***[80]***) and ***b)***.

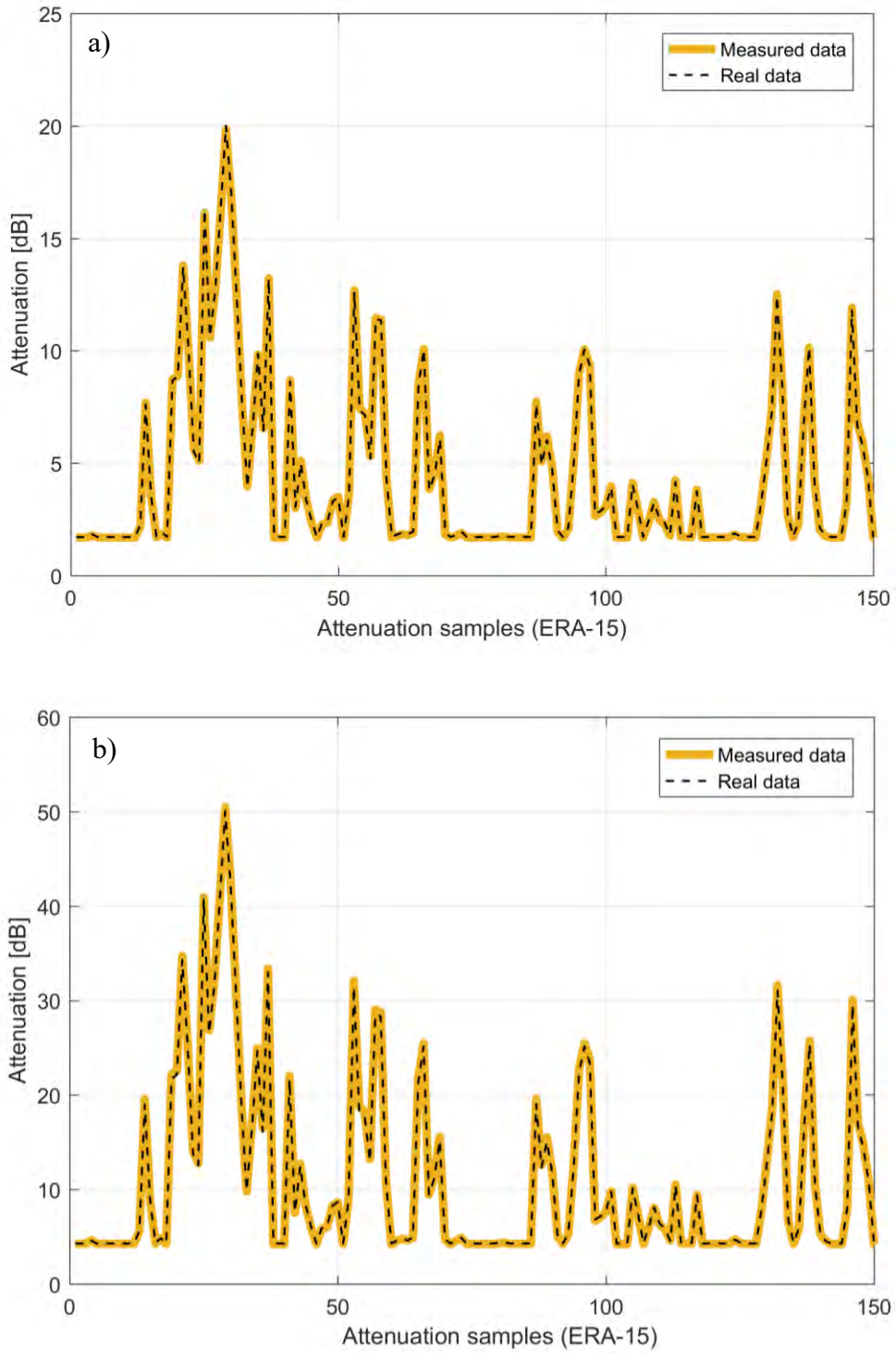

Figure 5.7: Comparison between real ERA-15 data and measured ones in terms of FSO channel emulator incorporating : a) 850 nm MM – VOA (The figure is obatined from own publication [80]); b) 1550 nm SM – VOA

There, the simulated and later scaled optical attenuation data samples from ***Figure 5.6*** are compared with FSO channel emulator measurements using the same data. The atmospheric attenuation data samples are sent each 1 second, which corresponds to fastest maritime fog-induced fading [80]. It is evident that the two graphs showing applied and measured data for each VOA are perfectly matched (~1 dB error for 850 nm MM – VOA (***Figure 4.9***)is not so well visible). Consequently, both selected VOA's ranges (20 dB for the MM – VOA and 50 dB for SM – VOA) precisely represent the real atmospheric conditions. The 1550 nm SM – VOA unit is further investigated in **Chapter 7** based on fast fluctuations caused by atmospheric turbulence-induced fading.

5.2 Experimental FSO test setup based on artificial fog sources

While the developed channel emulator in **Chapter 4** is irreplaceable regarding representation of ultra-long space-to-ground FSO communication links, which are subject to atmospheric turbulence and cloud attenuation, another method for evaluation of long-distance terrestrial links is based on artificial fog sources. In particular, their particle radii between 0.1 μm and 10 μm mainly corresponds to continental fog. The opportunity FSO system to be tested in artificially produced fog environment, where the main fog parameters comprising PSD, LWC and particles concentration are under full control, opens the door for facilitated evaluation of long-distance links (>1 km) in the presence of Mie scattering. In accordance with ***[83]***, the capabilities to represent real fog by means of artificial fog sources is performed in the test facilities of Irnas Institute and more specifically in the 50 m FSO Koruza channel ***[58]***. The measured data are processed with the prepared MATLAB simulations based on Mie theory algorithm and fog microphysics provided in **Chapter 3**. The basic concept of the conducted experiment is depicted in ***Figure 5.8***, where the used Koruza facilities are self-drawn based on information in ***[58]*** and ***[83]***.

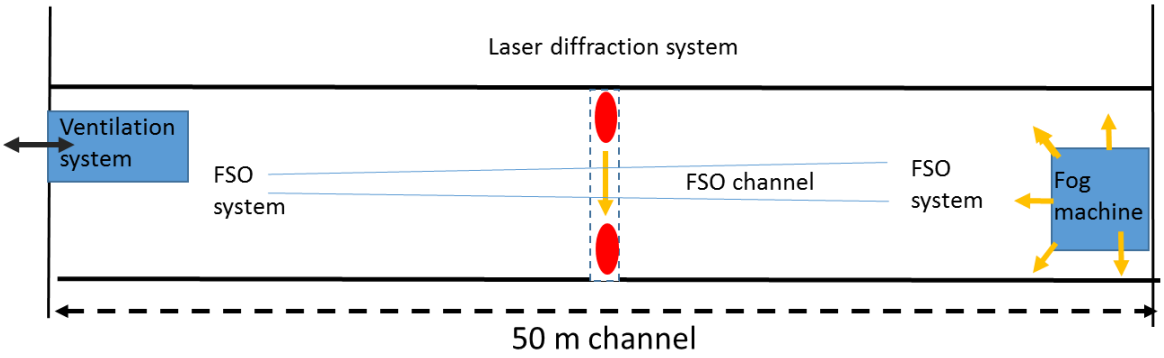

Figure 5.8: Experimental campaign conducted in the 50 m Koruza FSO channel

The used 50 m long channel is a plastic-based corridor, which is well-isolated from the outside environment and comprise an installed FSO link, ventilation system, Laser Diffraction System (LDS) as well as a fog machine. While the fog machines under test including Antari HZ-500 and FAZE-1000 FT ROBE (Show Lighting) are situated in the end of the corridor, an industrial ventilation system with air-flow rate of 3000 m^3/h which ensure the rapid changes of the air inside the tunnel for < 2 min, is installed in the beginning of the corridor [58].

5.2.1 Artificial fog sources: Antari HZ-500; FAZE-1000 FT ROBE

The utilized small-scale chamber in ***[57]*** for generation of an artificial fog operates with evaporated water steam, which creates environment similar to a real fog effect. Nevertheless, due to demands for high temperature and humidity levels, this technique cannot be exploited in the case of larger FSO channel representations including the used plastic-based 50 m long tunnel. Bearing in mind this issue, a well-suited alternative is developed by means of artificial fog machines allowing controlled fog generation ***[83]***. While Antari HZ-500 is a hazer, which produces suspended-in-air particles with size lower than 5 µm, FAZE-1000 FT ROBE is featured with increased size spectrum up to 10 µm, which well emulates real continental fog. Both machines operates based on fog fluid, which is a commercially available mixed of water and Glycol liquid substance in typical proportion of 2:1. In particular, the mixed of 30 % triethylene or propylene Glycol and 70 % water is evaporated by process of heating along with high pressure. Since water has a lower boiling point than Glycol it is easily vaporized, while Glycol is turn into fine vapour with additionally applied high pressure. Once the evaporated substance is dispersed in the cold air, the vapour condensates ***[83]***. For the current purpose, two types of fog juice namely 30 % and 50% Glycol – water solutions are evaluated, where the higher the glycol weight in [%] is, the denser the fog is. According to ***[122]*** and more specifically ***Figure 5.9 a)***, the refractive index has negligible difference within 0 – 50 % Glycol weight for the 3 given different types of Glycol. Having applied the considered simulations based on Mie theory and 850 nm wavelength, the comparison of Mie scattering efficiency in terms of refractive indices for pure water (n_m = 1.33 + 2.93 10^{-7}i) as well as for 30% and 50 % Glycol – water solutions (n_m = 1.395 + 9.8 10^{-8}i; 1.37 + 9.8 10^{-8}i) are assessed (***Figure 5.9 b)***).

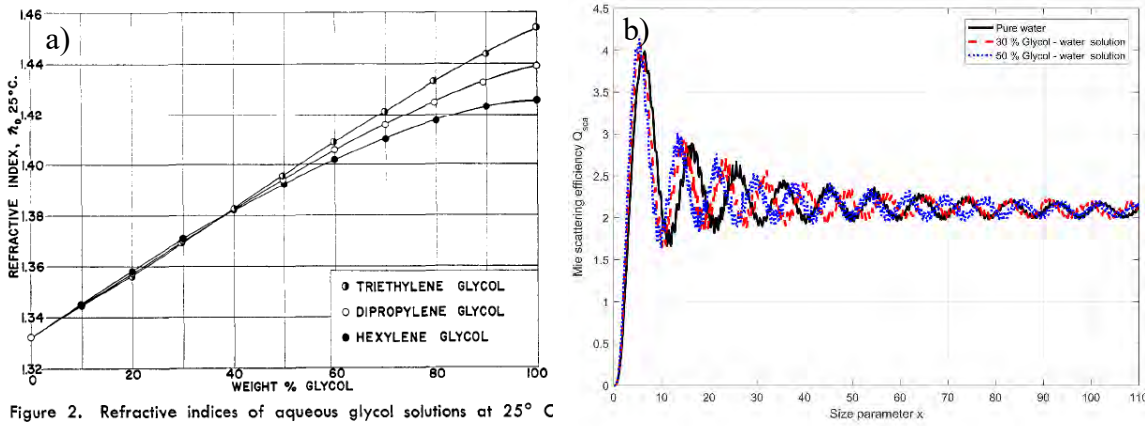

Figure 5.9: Fog fluid based on water and Glycol: a) Refractive index versus different Glycol – water solutions (The figure is obtained from [122]); b) Simulated Mie scattering efficiency for pure water as well as 30 % and 50 % Glycol – water solutions

Although Glycol has slightly larger refractive index than water, which leads to a little bit increased Mie scattering efficiency, the difference is negligible.

5.2.2 PSD characterization of artificial fog sources with laser diffraction system

The measurement of the PSD is accomplished with Spraytech LDS – the photographs of the experiment are provided in ***Figure 5.10*** (One of the photographs is obtained from ***[83]*** and made by Koruza team) – delivered by Malvern Company, which is located in the middle of the 50 m channel, namely 25 m distance from the applied fog machine ***[83]***. This allows the particles to be well-enough dispersed into the air during the measurement. The launched PSD's coherent 5 mW optical beam from a 632.8 nm HE-Ne laser is influenced by suspended particles leading to light scattering in different directions which is recorded based on array of 36 Si detectors.

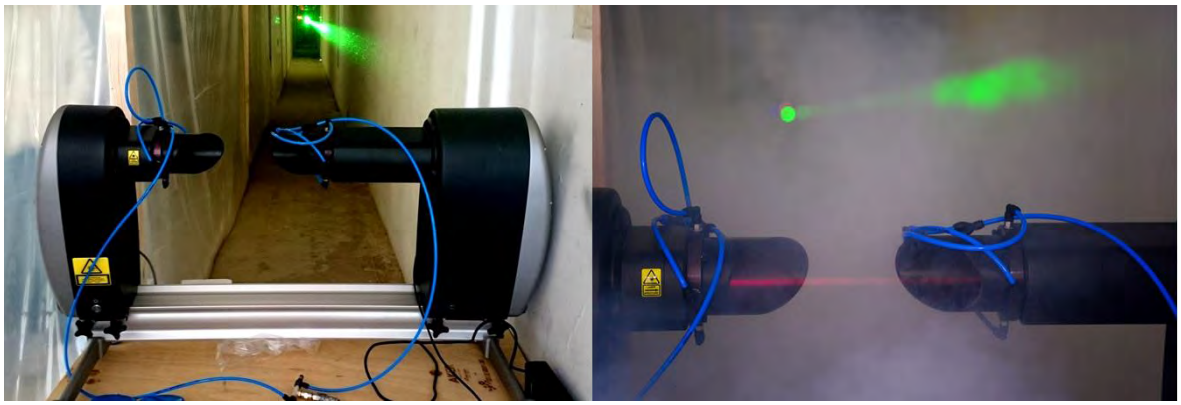

Figure 5.10: Spraytec Malvern device for PSD analysation installed in the middle of 50 m Koruza fog channel (The figure is partly obtained from own publication [83])

In order to recognize different particle sizes, the LDS does a comparison between built-in Mie and Geometrical scattering patterns with the recorded ones during the measurements. The attained operation range is within 0.1 – 2000 µm with an accuracy of 1 %.

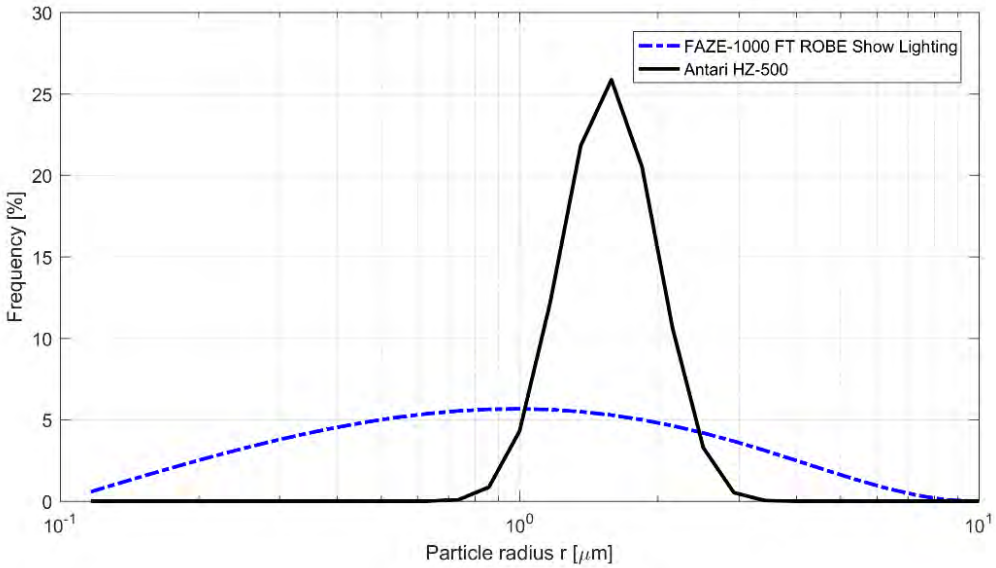

Figure 5.11: Measured frequency distribution of the two artificial fog machines: Antari HZ-500 and FAZE-1000 FT ROBE (The figure is obtained from own publication [83])

The measured frequency distributions, namely PSDs, of the suspended-in-air particles' radii *r* for the two artificial fog sources –FAZE-1000 FT ROBE and Antari HZ-500– are shown in ***Figure 5.11***. Moreover, both measured PSDs are normalized and corresponds to probability density estimates in [%] (i.e. PDF). In order to improve the scaling, a logarithmic graph in terms of x-axis is applied. In accordance with ***Figure 5.11***, the main area of the relative frequency particle-size distribution for Antari HZ-500 haze machine is within 0.8 µm and 3 µm particle radii, which is less than appointed 5 µm for the case of Hazer machine. On the other hand, the measured droplet size spectrum regarding FAZE-1000 FT ROBE fog machine is between 0.1 and 10 µm. Both normalized PSDs are within the specific bounds describing continental fog (1 – 12 µm), which means that maritime fog, featured with particle sizes between 12 – 20 µm, is omitted ***[83]***. In order to carried out the analyses a comparison between analytical PSDs for moderate and dense continental fogs given in ***Figure 3.3*** (***Table 3.1***) and the measured normalized PSDs (PDFs) (***Figure 5.11***) is required. Considering the similarities between moderate continental fog and the measured data (***Figure 5.11***) an equalization in terms of particle concentration for the two PSDs is performed.

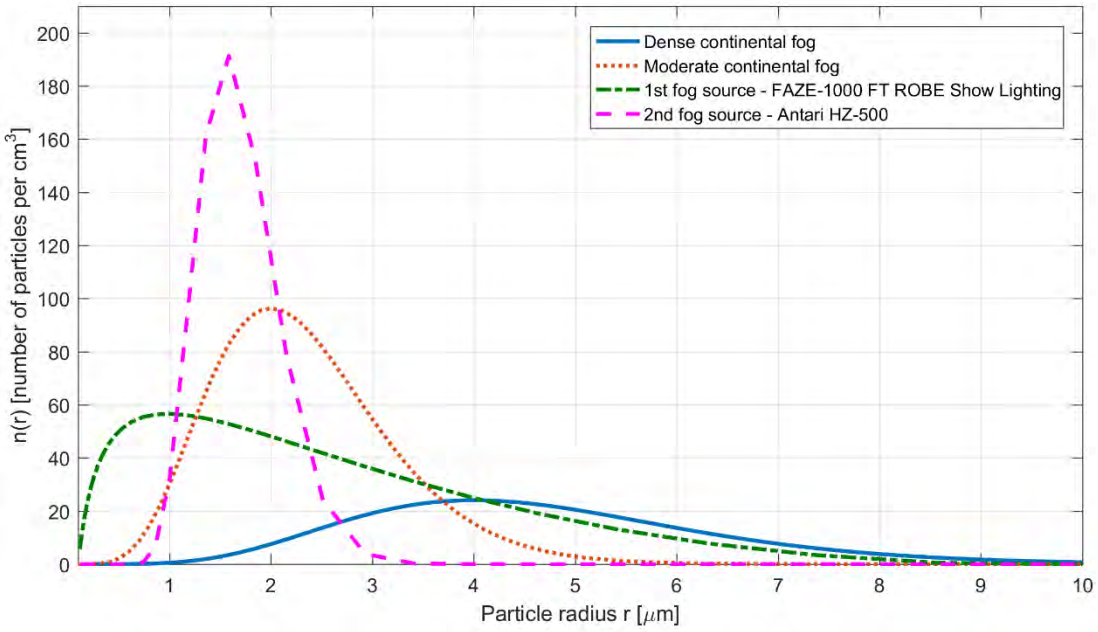

Figure 5.12: Comparison between analytically obtained fog PSDs and measurements of artificial fog with Spraytec LDS (Figure 3.3 and Figure 5.11) (Modified figure based on own publication [83])

Similar to the applied empirically modelled PSD, which is characterized with fog concentration of 200 np/cm^3, the measured probability density estimates (frequency distribution), shown in ***Figure 5.11*** are also scaled up to the same level of concentration. Its value corresponds to very high fog particles' concentration of continental moderate fog provided in ***Table 3.1***, namely 200 np/cm^3. After an assessment in respect to the shown PSDs, it is obvious that FAZE-1000 FT ROBE, is the most appropriate for emulation of continental fog conditions ***[83]***. Its water droplet size distribution partly overlaps with moderate continental fog and nearly fully covers the region of dense continental fog. In

alignment with the developed and the calibrated simulations in terms of clouds' attenuation, the simulated Mie scattering efficiency for 850 nm wavelength in ***Figure 5.9*** and the delivered PSDs in ***Figure 5.12*** are applied together.

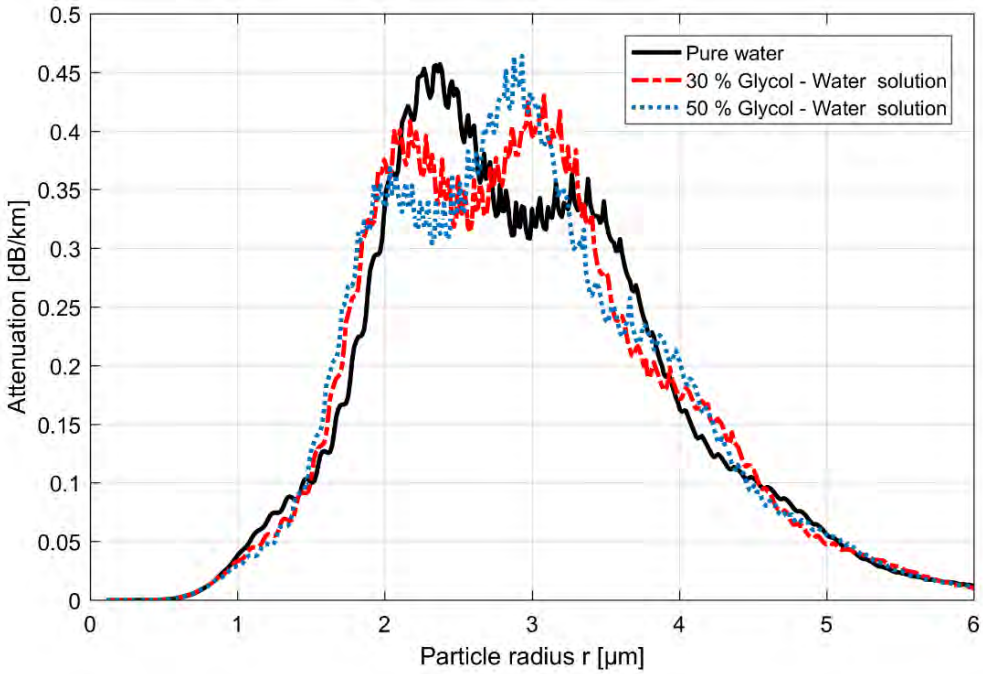

Figure 5.13: Optical attenuation versus particles' radii for moderate continental fog effect regarding pure water, 30 % and 50 % Glycol – water solution

By means of Eq. (3.10), attenuation versus particle radius for the empirically defined moderate continental fog's PSD is simulated in ***Figure 5.13***. The analysis is performed for the three types of Mie scattering efficiency simulated in respect to refractive indices of pure water as well as fog juice with 30 % and 50 % Glycol – water solution. Alike the minimal visual difference, the variation of the specific optical attenuation for the three cases is negligible, namely 69.7 dB/km, 69.7 dB/km and 69.6 dB/km, which corresponds to Mie scattering coefficient ~16 km^{-1}. Having used the Mie theory regarding pure water and 30 % Glycol – water solution, the attenuation for the two types of artificial fog sources defined with their PSDs are given in ***Figure 5.14 a)*** and ***b)***. It is visible from ***Figure 5.14*** that each of the specific attenuation graphs is compared with the relevant measured PSD presented in ***Figure 5.12***. A brief assessment of the ***Figure 5.14*** reveals that both peaks associated to specific attenuation graphs and PSD are displaced. On the one hand, droplets with a radius under 1 μm contribute negligible to the applied attenuation which is visible from the Mie scattering efficiency graph already shown in ***Figure 5.2***. On the other hand, the calculated Mie scattering attenuation with Eq. (3.10) is directly dependent on the radius of the suspended water droplets. Therefore, the peak differences presented in ***Figure 5.14*** is explained by the fact that larger values of Mie scattering coefficient are assigned to larger particle radii ***[83]***. Moreover, due to the specific pattern of Mie scattering efficiency, the specific attenuation is distinguished with numerous minimum and maximum (peaks) values.

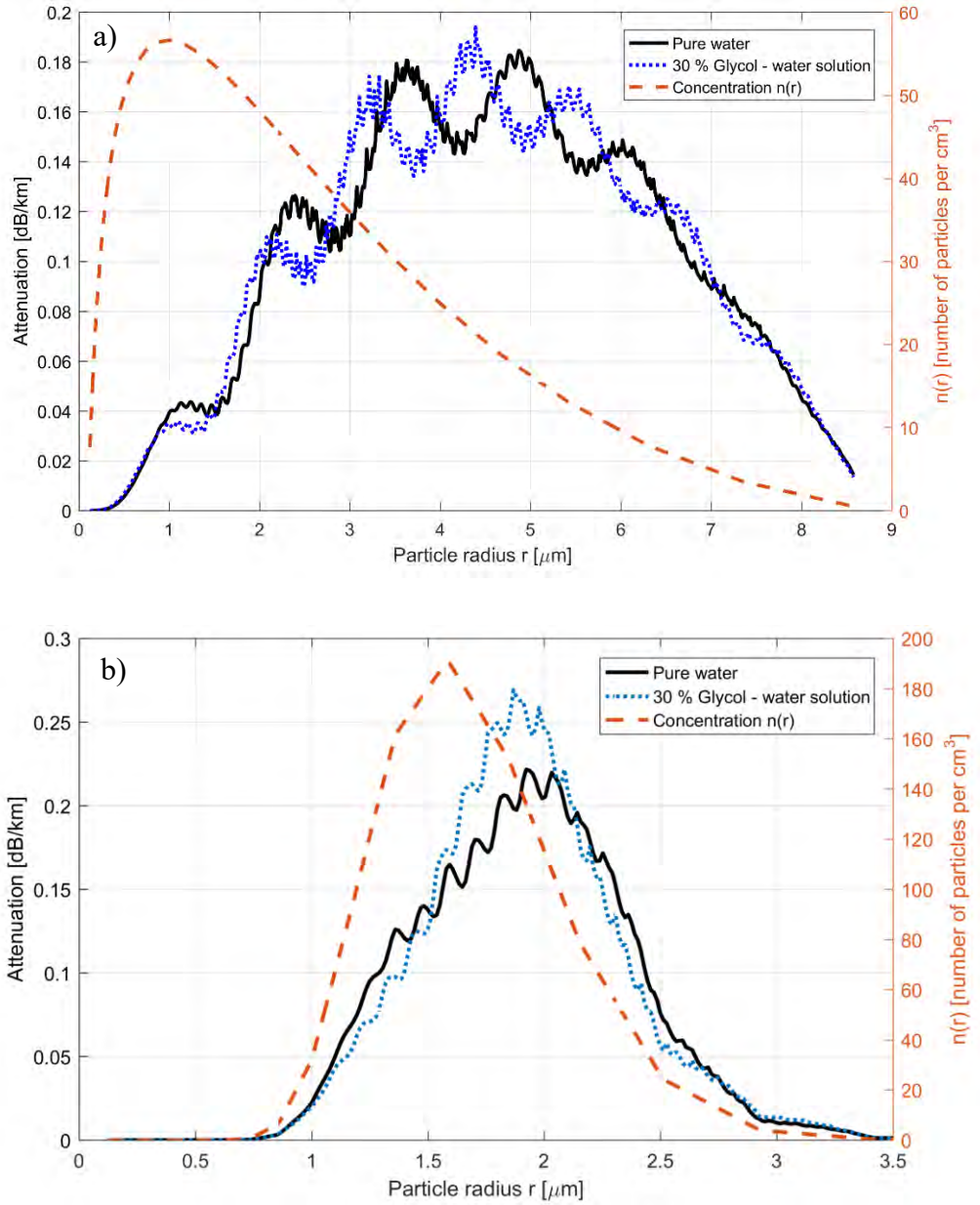

Figure 5.14: Optical attenuation versus fog particles' radii in respect to 3 types of Glycol – water solution for: a) FAZE-1000 FT ROBE; b) Antari HZ-500 (based on [83])

The two specific attenuation graphs compared to the results in respect to moderate continental fog are given in Figure 5.15, which proves the obtained judgement that the FAZE-1000 FT ROBE artificial fog source is the most appropriate source for emulating continental moderate fog conditions, while Antari HZ-500 can be used to generate haze. The two graphs are subject to further assessment in ***Table 5.5***, which offers comparison of the peak distribution radius r_{p_dis}, the peak attenuation radius r_{p_att} and the total imposed specific attenuation A_{tt} calculated with Eq. (3.10). In order to validate the results, again the empirically defined moderate continental fog with total attenuation of 69.7 dB/km is introduced.

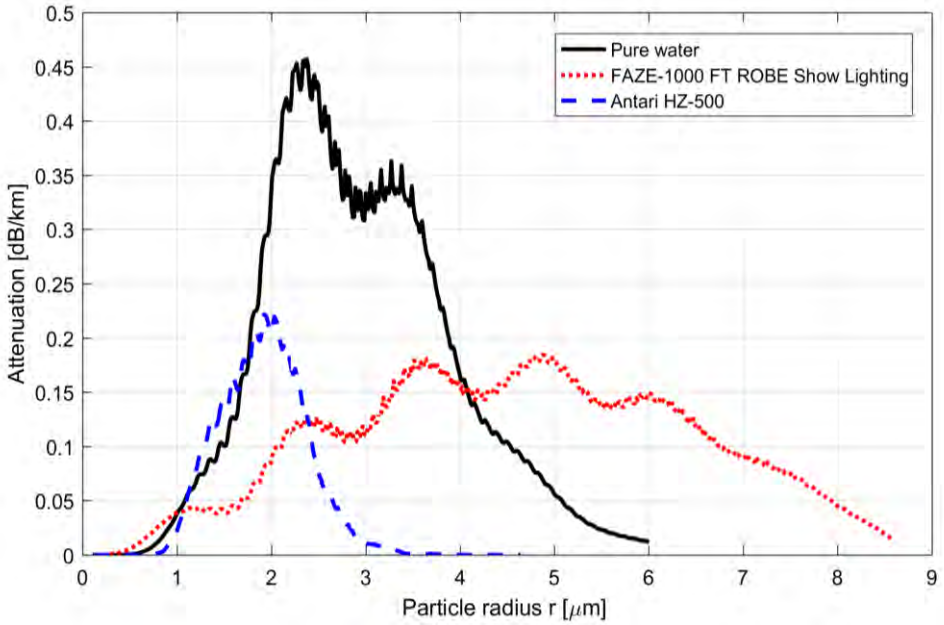

Figure 5.15: Comparison between specific attenuation graphs for moderate continental fog (Figure 5.13) and the two artificial fog sources (Figure 5.14) (based on [83])

Having addressed the shown outcomes in ***Table 5.5***, FAZE-1000 FT ROBE is featured with very similar optical attenuation to moderate continental fog. In particular, the difference in the optical attenuation between emulated fog conditions (62.17 dB/km) and the given moderate continental fog (69.7 dB/km) is 7.53 dB/km. In analogy to ***Figure 5.12***, this discrepancy with the real moderate continental fog happens due to partial redistribution of suspended water droplets in the air ***[83]***. Similar to the total specific optical attenuation, peak distribution radius r_{p_dis} [µm] and peak specific attenuation radius r_{p_att} [µm] are also provided in ***Table 5.5***.

Artificial fog sources	r_{p_dis} (µm)	r_{p_att} (µm)	A_{att_water} (dB/km)	$A_{att\_30\%\_Glycol}$ (dB/km)
Fog machine – FAZE-1000 FT ROBE	1.58	2.1	62.21	62.17
Hazer machine – Antari HZ-500	0.87	4.6	17.72	17.29
Moderate continental fog – Table 3.1	2	2.3	69.7	69.7

Table 5.5: Comparison between both evaluated artificial fogs along with the considered moderate continental fog case (Modified table based on own publication [83])

Hence, both dense and moderate continental fog conditions are represented by FAZE-1000 FT ROBE ***[83]***. Based on previous measurement campaigns and simulations, it can be observed that the total attenuation due to continental fog in Graz, Austria has maximum value around 120 dB/km ***[94]***. After comparison with the calculated results in ***Table 5.5***, it can be concluded that based on the developed setup these tropospheric conditions can be simulated. Nevertheless, this type of emulators are bulky and not easy for control. Moreover, the exact accuracy in respect to real Mie scattering representation is hard to be estimated. Consequently, the developed VOA-based channel emulator has substantial advantage in comparison to this kind of fog representation.

5.3 Fog analysis of long-distance 2.7 km terrestrial FSO link

In accordance with the own publication ***[84]*** (published within the current thesis) an evaluation of a real long-distance terrestrial FSO link for the location of Austria representing typical continental weather conditions is performed. The used measurement data set record is based on ***[33]***. The obtained real measurements regarding Mie scattering attenuation (continental fog) are combined with the achieved results in **Chapter 6** for atmospheric turbulence-induced fading based on Radiosonde Observation (RAOB) data. Their join influence is observed and evaluated in terms of 2.7 km FSO link. The applied GoC Multilink 155F system relies on multi-link transmission based on four VCSEL operating in Near Infrared (NIR) spectrum at 840 nm wavelength with maximum 155 Mbps data throughput ***[33]***. This Multiple Input Single Output (MISO) approach allows high resistance to atmospheric turbulence. In accordance with ***[123]***, it leads to 2 – 7 dB gain, which successfully mitigated atmospheric turbulence-induced fading. Consequently, the 12-months measurement campaign carried out in Graz, Austria is solely focused on the evaluation of Mie scattering (continental fog) attenuation ***[84]***. The applied multi-link transmission FSO system is characterized with system power figure of 53 dBm. Moreover, the implemented Si APD detector is distinguished with optical sensitivity of minimum -41 dBm. When the FSO communication link of 2.7 km together with Eq. (2.11) are taken into account, the calculated losses due to channel distance component are ~74 dB. Once the power system figure, optical sensitivity as well as channel losses are calculated, the available link budget for 2.7 km channel distance is figured out based on Eq. (2.13). Its value is 20 dB and which provides ~7 dB/km specific link margin.

In accordance with the International visibility code table in ***[93]*** as well as the measured peak attenuation of 120 dB/km for the location of Graz Austria ***[36]***, the different fog types from light up to dense one are given in ***Table 5.6***.

Parameter		Specific Fog attenuation [dB/km]	Total fog attenuation [dB] – 2.7 km
Fog	Dense	120 dB/km*	324 dB
	Thick	75 dB/km	202 dB
	Moderate	28.9 dB/km	78 dB
Light fog		6 – 18 dB/km	16.2 – 48.6 dB

*In accordance with [36] the maximum fog attenuation for Graz is 120 dB/km.

Table 5.6: Typical measured fog conditions for Graz, Austria

Along with the average attenuation in [dB/km], ***Table 5.6*** provides the attenuation values for the considered scenario with FSO link's distance of 2.7 km. In particular, even the minimum light fog attenuation of 16.2 dB is very close to the available 20 dB link margin, which can easily trigger a weather-induced disruption. On the other hand, the maximum attenuation of light fog is 48.6 dB, which is more than two times the available link margin. The shortage of enough link margin occurs, due to operation range of the applied FSO system, which should not exceed 1 km. In accordance with the link budget calculations, 1 km leads to 28 dB link margin. The later, allows reliable data transmission in the presence

of an average moderate fog event, which attenuation is up to 28.9 dB for distance of 1 km. Nevertheless, the applied Mie scattering (fog) measurements based on the aforementioned long-distance FSO scenario distinguish between only two types of continental fog events including light one as well as moderate up to dense one. Due to restricted link margin, an additional digital camera is applied for validation of the results. Along with the measurements in terms of continental fog for the area of Graz, Austria, also full evaluation of overall system availability is carried out.

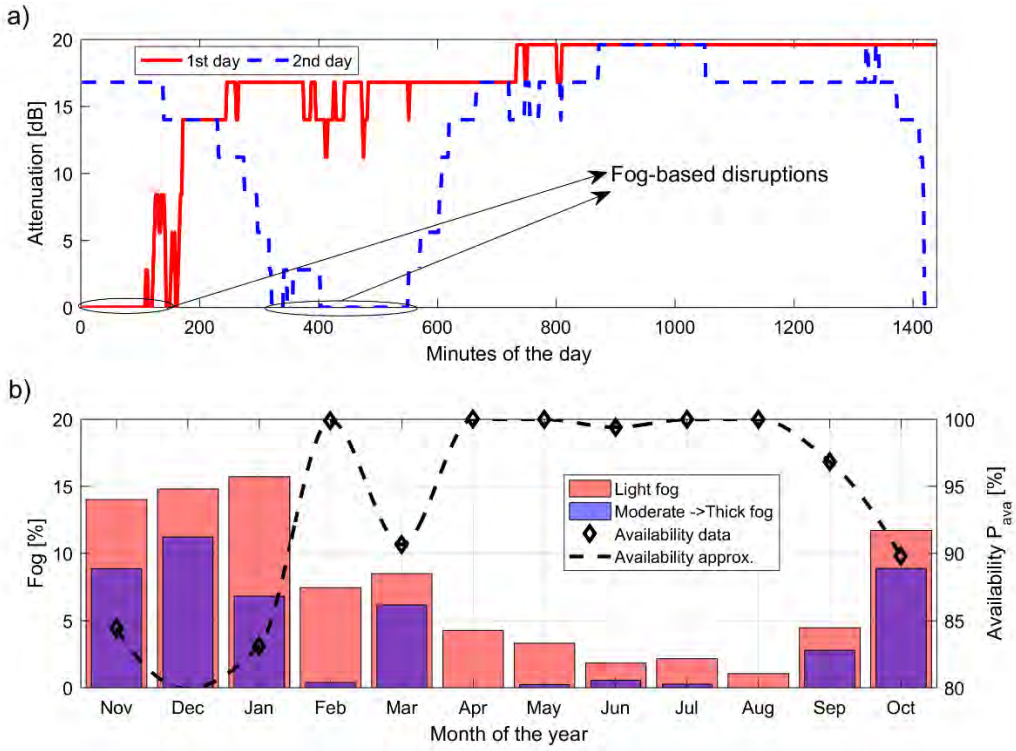

Figure 5.16: Evaluation of 1-year fog measurements performed in Graz, Austria for 2.7 km FSO communication channel and 20 dB link margin: a) fog induced attenuation measurements for two independent days; b) fog statistics in respect to light -> thick fog as well as FSO system availability (Modified figure based on own publication [84])

For better understanding of processed measurements, two independent days during winter season are initially shown in ***Figure 5.16 a)*** for which the fog attenuation values are monitored and stored every two minutes. Although there are numerous insignificant reductions of the optical power, there are two major events during, which the link is fully blocked. Both of them are due to continental fog (Mie scattering) and lead to a significant drop in FSO reliability and availability parameters. Besides, the lower plot ***b)*** of ***Figure 5.16*** provides the statistics concerning the occurrence of fog events in Graz. In detail, the left y-axis represents the monthly rate of light and dense fog events, while the right y-axis gives information about the corresponding availability of the established FSO link. It is visible that the system availability/reliability decreases with an increment of dense fog events. In addition, the light fog events also results in high influence on the established FSO

communication link. This is consequence of the 2.7 km link distance, which exceeds nearly three times the appointed 1 km distance in the system specifications.

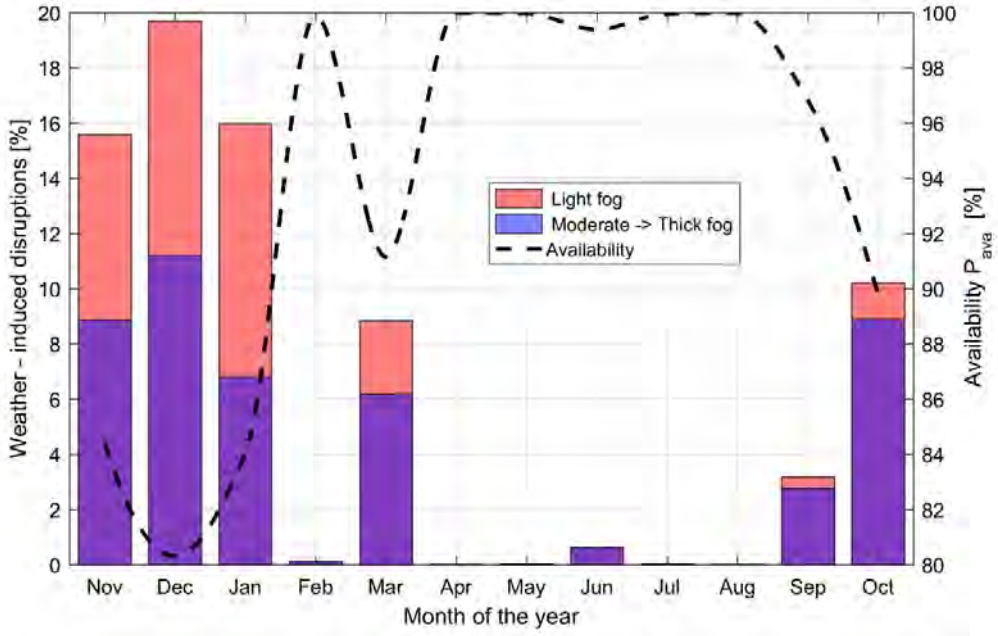

Figure 5.17: Weather-induced disruptions versus month regarding light to thick fog conditions as well as measured FSO system availability (Modified figure based on own publication [84])

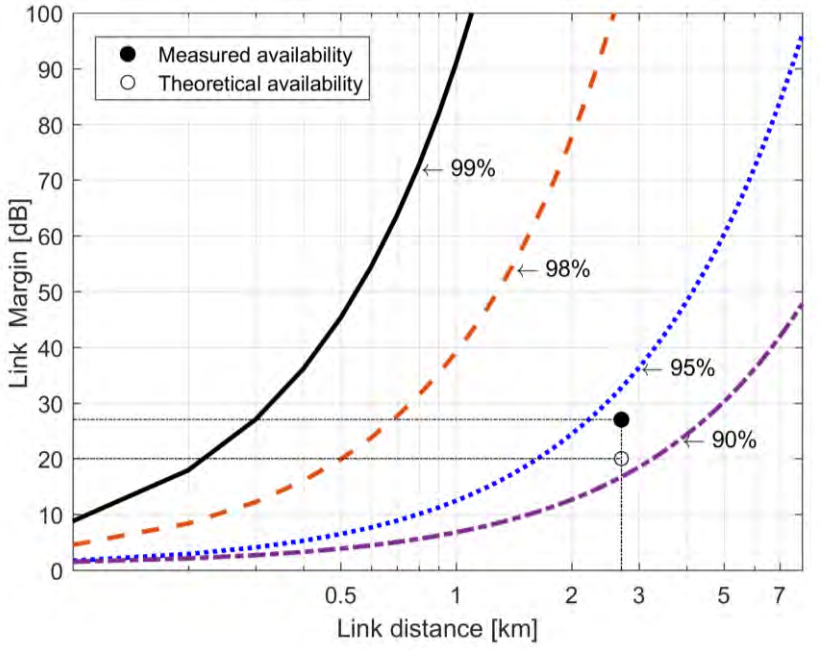

Figure 5.18: FSO link margin versus link distance in respect to four availability settings (90 %, 95%, 98 % and 99 %) allowing comparison between measured and theoretically estimated 1-year FSO system availability (Modified figure based on own publication [84])

Furthermore, the fog-induced disruptions and the availability parameter are depicted in ***Figure 5.17***. It is clear that the main contribution to weather-induced disruptions is due to moderate up to dense fog. Nonetheless, light fog also has a significant impact on the 2.7 km FSO communication link characterized with restricted link margin of 20 dB. In coherence with the previous considerations, only very light fog event up to 7 dB/km cannot trigger a large enough disruption leading to interruption of the long-distance FSO link. Hence, the light fog-induced attenuation is often > 7 dB/km, it contributes together with the other stronger fog events to decreasing of FSO system availability. Based on the calculations and measurements related to the types of fog events, the availability of the considered FSO system is evaluated in ***Figure 5.18***. In particular, once the performance of GoC Multilink 155F FSP system is compared to the measured 93.64 % availability for 12-months period, the calculated link margin is 27 dB. From the perspective of an average performance, the calculated theoretical availability for 20 dB link margin and 2.7 km link distance should be 90.8 %. The tiny difference of 2.84 % is explained with little fluctuations of atmospheric effects during the years ***[84]***.

Chapter 6

6. Atmospheric turbulence losses

Taking into account the introduced and derived theory regarding atmospheric turbulence-induced fading, the refractive index structure parameter C_n^2 is simulated by means of Radiosonde Observation (RAOB) (***[124]***) database provided by Wyoming University, USA ***[82]***, ***[84]***. In particular, the applied data has been collected two times per day during whole year of 2017 from Hohe Warte weather station in Vienna, Austria. Based on the considered RAOB data records for the location of Vienna, an excerpt from the data set containing only the most relevant parameters namely height, pressure, potential temperature, relative humidity, wind speed for one measurement carried out within January 2017 is displayed as an example in ***Table 6.1***. The elevation of Vienna – Hohe Warte station – is 200 m, which is the minimum height in terms of the carried out measurements and it is significantly below the thermal inversion layer located at ~1000 m (898 – 958 m) above sea level.

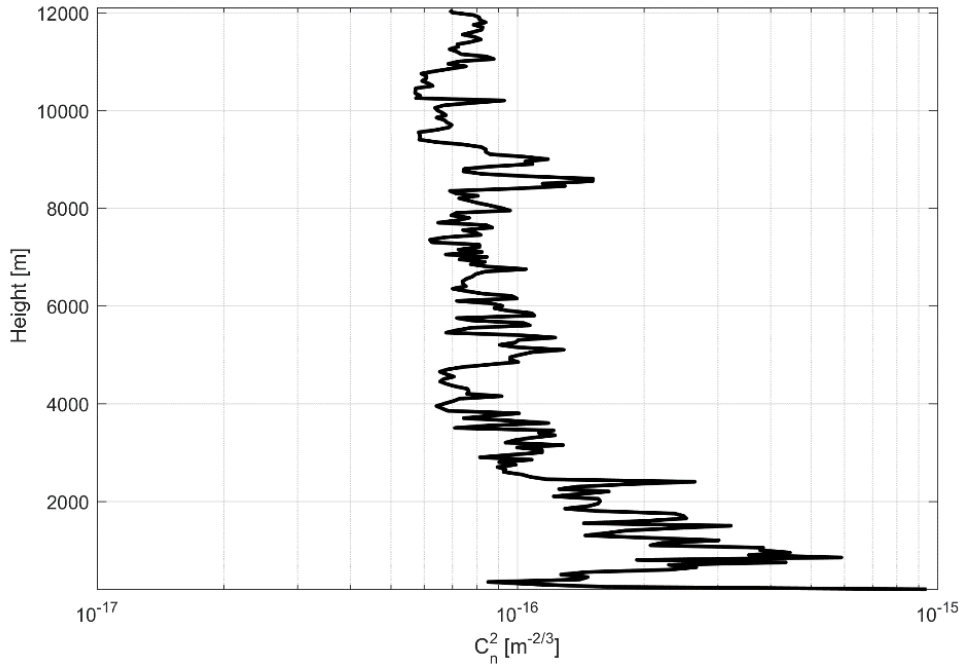

Figure 6.1: Refractive index structure parameter C_n^2 versus height h based on 1-year RAOB measurements accomplsihed by weather station Hohe Warte in Vienna, Austria [82] (Modified figure based on own publication [82])

Height [m]	Pressure [hPa]	Temperature [C]	Potential Temperature [K]	Relative Humidity [%]	Wind speed [knot]
200	1003	-4,7	268,2	84	6
225	1000	-5,1	268,1	89	8
806	928	-9,7	269,1	98	25
831	925	-9,5	269,6	98	25
898	917	-6,7	273,1	79	27
958	910	-5,7	274,8	81	29
1036	901	-4,3	277	83	27
1098	894	-3,7	278,2	58	26
1124	891	-3,9	278,3	36	25
1196	883	-0,9	282,1	19	23
1241	878	2,8	286,4	9	22
1352	866	2,9	287,6	7	19
1494	851	3	289,2	6	21
1503	850	3	289,3	6	21
2821	720	-5,5	294	21	10
3034	701	-6,8	294,8	26	12
3045	700	-6,9	294,8	27	12
3224	684	-8	295,6	24	8
3443	665	-9,3	296,5	22	9
3821	633	-12,5	297	30	11
3918	625	-12,9	297,6	14	11
4037	615	-13,9	297,9	14	12
5498	505	-26,1	300,3	11	21
5570	500	-26,3	300,9	17	21
6209	457	-30,2	303,9	8	25
6910	414	-34,4	307,2	3	25
6928	413	-34,5	307,2	3	25
7150	400	-36,5	307,5	5	23
7202	397	-36,7	307,9	2	23
8522	327	-46,7	311,6	16	27
9090	300	-50,9	313,5	13	29
9980	261	-57,9	315,9	20	29
10126	255	-58,7	316,9	18	29
10250	250	-59,3	317,8	17	29
10689	233	-61,4	321	20	25
10906	225	-62.5	322,6	21	18

Table 6.1: A January measurement representing the used RAOB dataset containing 1-year measured RAOB tropospheric parameters accompished by Hohe Warte weather station, Vienna, Austria

Although the data profile provides atmospheric information for a height up to 30 km, here only the tropospheric layer is considered, which is up to 10 km. The simulated statistical mean of C_n^2 versus height h in respect to all RAOB measurements during 2017 year period is presented in ***Figure 6.1***. The simulations are accomplished in MATLAB with the provided scintillation model in **Chapter 3**. In accordance with ***Figure 6.1***, based on the 1-year RAOB measurements ***(Table 6.1)***, atmospheric turbulence near ground (at 200 m elevation above sea level) is stronger with $C_n^2 = 10^{-15}$ $m^{-2/3}$ and weaker for higher altitudes, i.e. $C_n^2 = 0.2\ 10^{-16}$ $m^{-2/3}$ ***[82]***.

The considered RAOB model in **Chapter 3** provides enhanced resolution (20 times) and significantly improved accuracy in comparison with the most used HV model, which is normally applied together with Buffon wind model and prevails in the most atmospheric turbulence simulations ***[21]***, ***[49]***. In other words, the RAOB model takes into account all specifics of the location based on real performed measurements. Once the vertical profile of C_n^2 is calculated, the next step is finding the Rytov variance, scintillation index as well power scintillation index of the received optical intensity due to turbulence-induced fading for two types of links: the considered in **Subchapter 5.6** long-distance 2.7 km terrestrial link as well as deep space-to-ground FSO downlinks.

6.1 Long-distance terrestrial FSO link

In the context of terrestrial multi-link architecture with 4 transmitters (MISO technique) used for fog characterization in **Subchapter 5.6**, full resistance against atmospheric turbulence is attained. Consequently, the performed simulations regarding atmospheric turbulence-induced fading are examined only in respect to simple terrestrial mono-link case for the same applied FSO scenario. This case also coincides with the investigated space-to-ground downlink whose space borne segment should possess one receiver and one transmitter module due to power and weight considerations ***[18]***, ***[72]***, ***[75]***. The normalized probability histogram of C_n^2 parameter for the considered terrestrial link, which is actually a percent distribution, is shown in ***Figure 6.2***. In order to perform the simulations for horizontal FSO channel operating at ground level, the first layer of the 1-year Hohe Warte RAOB measurements at 200 m above sea level is used.

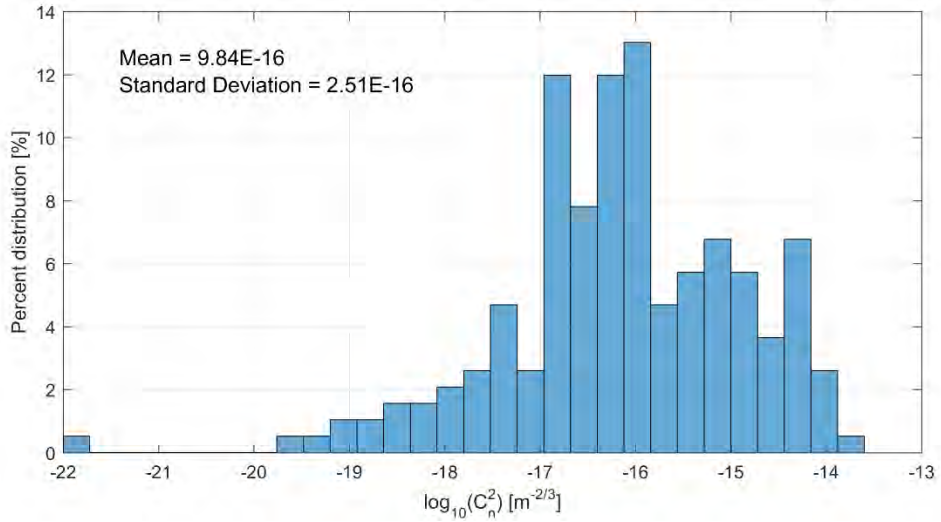

Figure 6.2: Relative frequency histogram of C_n^2 for 2.7 km terrestrial FSO link based on atmospheric data from Vienna, Austria

The spectrum of C_n^2 parameter is between 10^{-13} – 10^{-22} $m^{-2/3}$ with ~10^{-15} $m^{-2/3}$ (9.84E-16) mean and 1.51E-16 Standard Deviation (STD). Furthermore, the 9.84E-16 statistical mean of C_n^2 calculated by means of the probability histogram in ***Figure 6.2***, coincides completely with the provided value in ***Figure 6.1*** for 200 m elevation above sea level. In accordance

with ***Figure 3.6*** in **Subchapter 3.2**, the Rytov variance should be in the range $\sigma_r^2 < 1$ to be considered as a scintillation index, which happens when $C_n^2 \leq \sim 10^{-15}$ for the handled 2.7 km FSO terrestrial link.

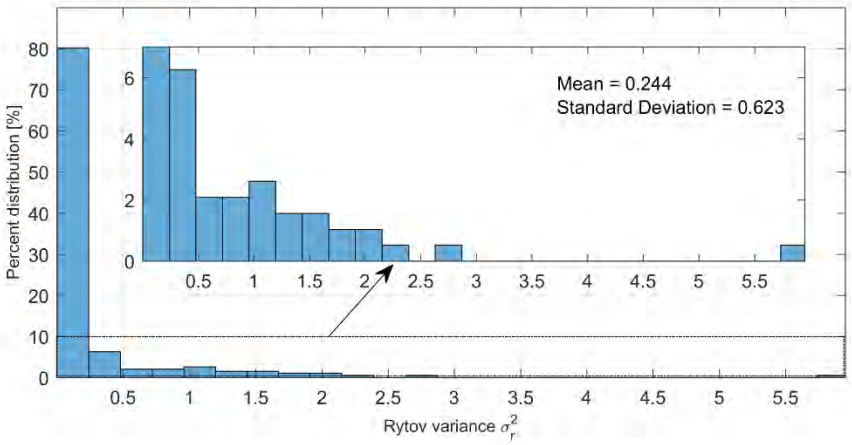

Figure 6.3: Probability histogram of σ_r^2 for near-ground 2.7 km terrestrial FSO link

Consequently, the provided percent distribution for σ_r^2 in ***Figure 6.3***, which reaches values up to 6 cannot be used for direct processing of the atmospheric turbulence attenuation. Instead of Log – Normal distribution, the scintillations follows Gamma – Gamma distribution and they are calculated with Eq. (3.40). As it is shown in ***Figure 6.4***, the probability histogram of the recalculated Gamma – Gamma scintillation index σ_I^2 is featured with σ_I^2 between 0 and 1.2.

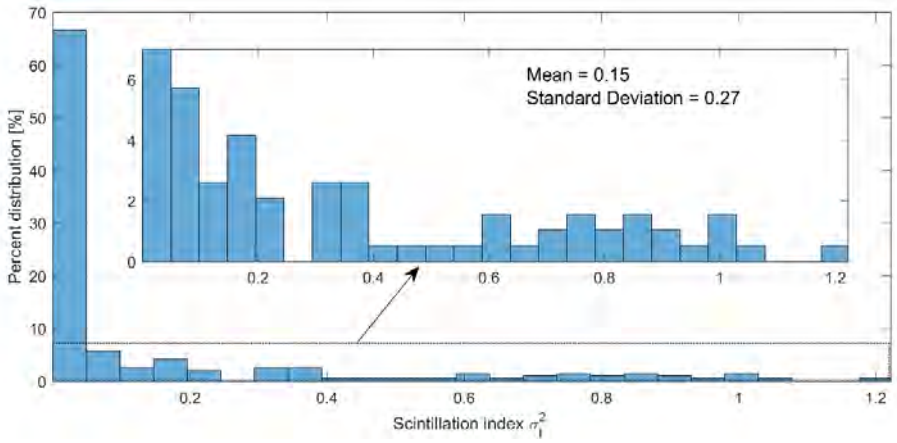

Figure 6.4: Probability histogram of σ_I^2 for near-ground 2.7 km terrestrial FSO link

Nevertheless, the scintillation variance σ_I^2 is valid only for the case of point receiver without considerations of the receiver aperture which for the investigated FSO system is charterized with $R_d = 0.1$ m finite length (**Subchapter 5.6**). Consequently, the power scintillation index σ_p^2, which is calculated in respect to finite receiver aperture diameter, is introduced (***Figure 6.5***). As expected, the aperture averaging technique significantly mitigates the atmospheric

turbulence-induced fading leading to σ_p^2 between 0 and 0.148, which further facilitates the simulations.

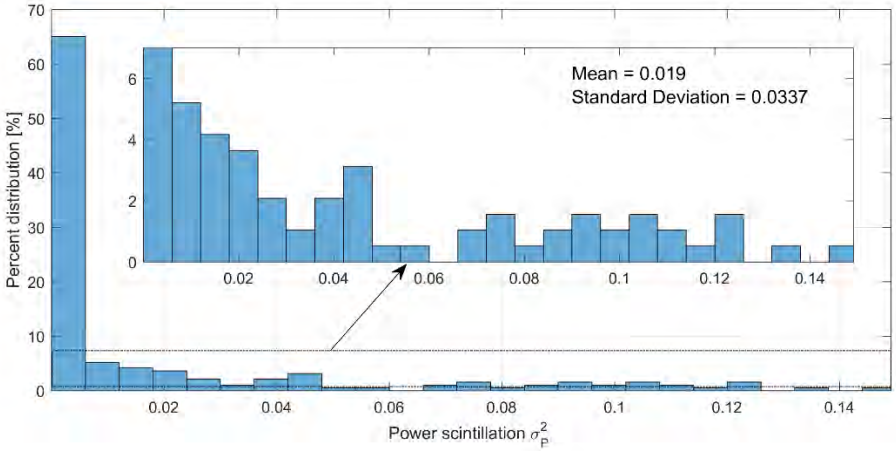

Figure 6.5: Probability histogram of σ_p^2 for near-ground 2.7 km terrestrial FSO link

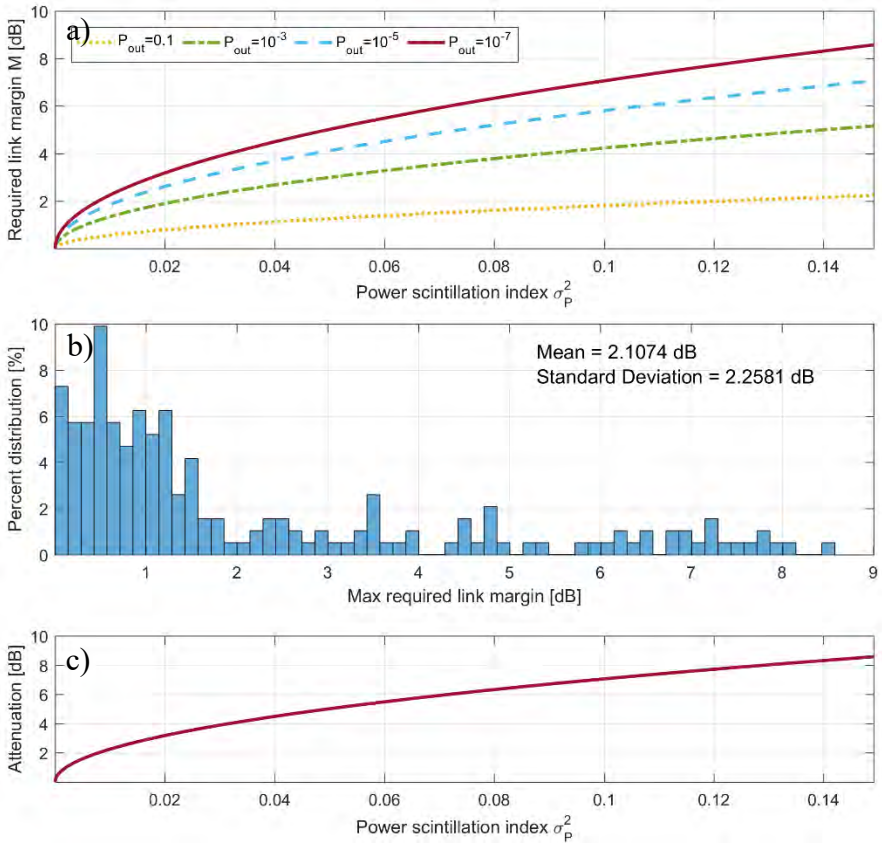

Figure 6.6: Atmospheric turbulence attenuation for 2.7 km terrestrial FSO link : a) attenuation versus σ_p^2 for P_{out} = 0.1, 10^{-3}, 10^{-7}; b) probability histogram of the simulated attenuation for P_{out} = 10^{-7}; c) Optical attenuation versus σ_p^2 graph (Modified figure based on own publication [84])

The achieved condition $\sigma_p^2 << 1$, results in scintillations of the received optical intensity again obeying Log – Normal distribution. In order to calculate the optical attenuation for power scintillation index σ_p^2 and an appropriate outage probability P_{out}, the derived Eq. (3.46) and Eq. (3.47) are applied. In particular, the required FSO link margin, namely optical attenuation versus σ_p^2 for the three outage probabilities $P_{out} = 0.1, 10^{-3}, 10^{-7}$ is presented in ***Figure 6.6 a)***. Nevertheless, the link margin allocated to the outage probability of 10^{-7} corresponds to the maximum possible turbulence attenuation in terms of the investigated near-ground horizontal FSO communication link equal to max ~8.6 dB for 2.7 km ***[84]***. The approximation is possible because this outage probability provides availability of seven nines, which is equal to ~100%. The probability histogram as well as the attenuation graph in ***Figure 6.6 b)*** and ***Figure 6.6 c)*** are performed in terms of Eq. (3.47) for the maximum possible atmospheric turbulence attenuation, namely $P_{out} = 10^{-7}$.

Once the σ_I^2 and σ_p^2 are simulated, the outage probability is evaluated based on the derived Eq. (3.43) in **Appendix B** as well as the equations for α and β parameters of Gamma – Gamma distribution given in Eq. (3.39) ***[111]***. The average link distance and aperture averaging effect make the system invulnerable to turbulence-induced fading. In particular, the statistical mean of atmospheric turbulence attenuation is approximately 2.1 dB (see ***Figure 6.6***). Furthermore, in accordance with Eq. (3.43), the outage probability is at maximum $P_{out} = 10^{-7}$ for γ_n =15 dB. This means that the system is not influenced by the clear-air atmospheric turbulence-induced fading in case of the used $R_d = 0.1$ m aperture and SNR ≥ 15 dB ***[84]***. Consequently, only the scintillation index without applying aperture averaging is considered. P_{out} versus σ_I^2 in terms of a point receiver for three different γ_n is shown in ***Figure 6.7***.

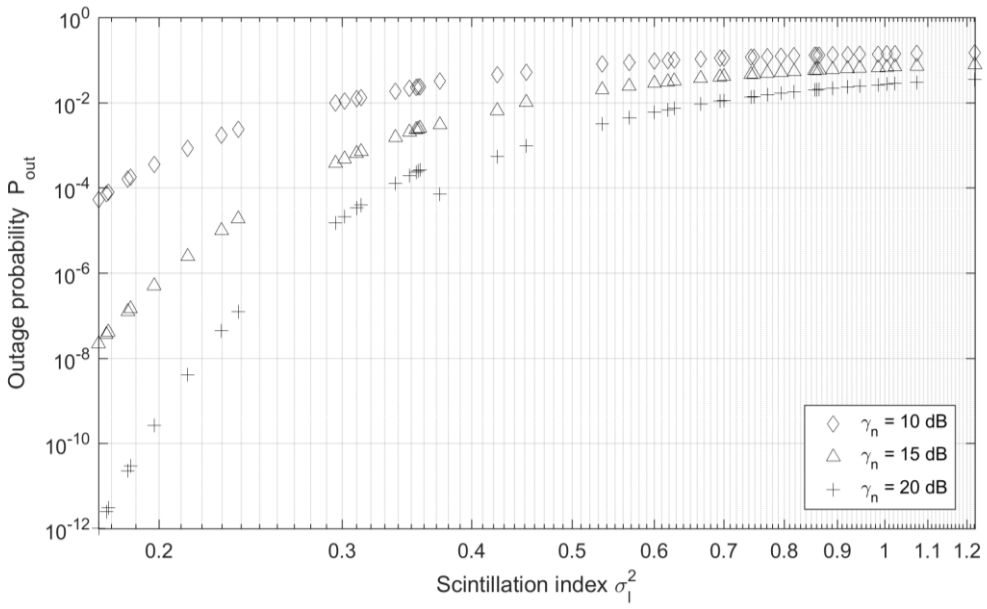

Figure 6.7: Outage probability P_{out} of the investigated 2.7 km terrestrial link versus scintillation index σ_I^2 for γ_n = 10 dB; 15 dB; 20 dB (The figure is obtained from own publication [84])

6.2 Deep space FSO downlink

Having in mind that an ultra-long-distance space-to-ground FSO feeder link is fully asymmetrically located in terms of the Earth atmosphere, there is a clear difference between the influence of atmospheric turbulence-induced fading for an uplink and a downlink. While tropospheric layer surrounds the OGS, the space borne unit is situated in outer space at a significant distance from the troposphere. Apart from scintillations, the uplink is affected by beam wandering that is a result of laser beam size very often comparable or smaller than the calculated Fried parameter ***[43]***, ***[45]***. Nevertheless, the current thesis considers only ultra-long-distance deep space FSO communication downlink (space-to-ground channel), which is subject especially to scintillations. Due to the large beam size reaching the atmosphere, the beam wandering can be neglected in the most cases ***[43]***. Deep space uplink is not considered due its restricted functionality, mainly used as beacon signal and only in special cases as data transmission link ***[70]***. Long-distance terrestrial links easily cope with atmospheric turbulence-induced fading based on simple mitigation techniques, which offer high enough resistance to the issue (**Subchapter 6.1**). On the contrary, ultra-long-distance space-to-ground FSO channels are subject to significantly worsen atmospheric impairments, which even deteriorates further with making the path more slant. In other words, when the elevation angle decreases ($\gamma < 90°$), laser beam travel longer through the troposphere layer leading to more severe optical power penalties.

Although LEO to ground links can handle significantly lower elevation angles γ = ~5° (***[125]***), namely larger amount of air mass, the ultra-long-distance links require $\gamma = 20° < \gamma < 90°$ ***[109]***. Moreover, the basic and the most efficient technique to fight atmospheric turbulence scintillations is based on aperture averaging considering a single or an array of large enough telescopes ***[126]***, ***[127]***. In order this technique to be effective enough, the aperture diameter should be comparable or larger than Fried parameter, which is always valid regarding deep space FSO communication downlinks featured with very large distances as well as large antennas. To observe the resilience to atmospheric scintillations in terms of aperture averaging, three types of diameters are introduced, namely R_d = 1 m ESA's Teide Observatory telescope, R_d = 1.5 m NICT's Tokyo telescope and R_d = 8 m telescope. Similar to the terrestrial horizontal links, the Rytov parameter for a slant FSO downlink regarding the worst case of γ =20° is taken into account (Eq. 3.34). In comparison with horizontal links where C_n^2 is a constant for a given period (***Figure 6.2***), for vertical links, C_n^2 changes with height, which is already shown in Figure 6.1. The Rytov parameter for a space-to-ground downlink with elevation angle γ = 20° and aperture radius R_d = 1 m is provided in ***Figure 6.8 a)***. The mean and the STD values of Rytov parameter are equal to 1.18 and 0.7, which are significantly larger than the ones for the examined 2.7 km terrestrial FSO link. Consequently, the atmospheric turbulence is categorized as a strong one ($\sigma_r^2 > 1$), well-described with Gamma – Gamma distribution, which is evaluated by the given scintillation index σ_I^2 in ***Figure 6.8 b)***. The calculated σ_I^2, that is valid for a point receiver, is with statistical mean = 0.72 and STD = 0.9. Finally, after the aperture averaging is introduced, the power scintillation index σ_p^2 is with *mean* = 0.023 and *STD* = 0.0082 which again obeys Log – Normal distribution (***Figure 6.8 c)***).

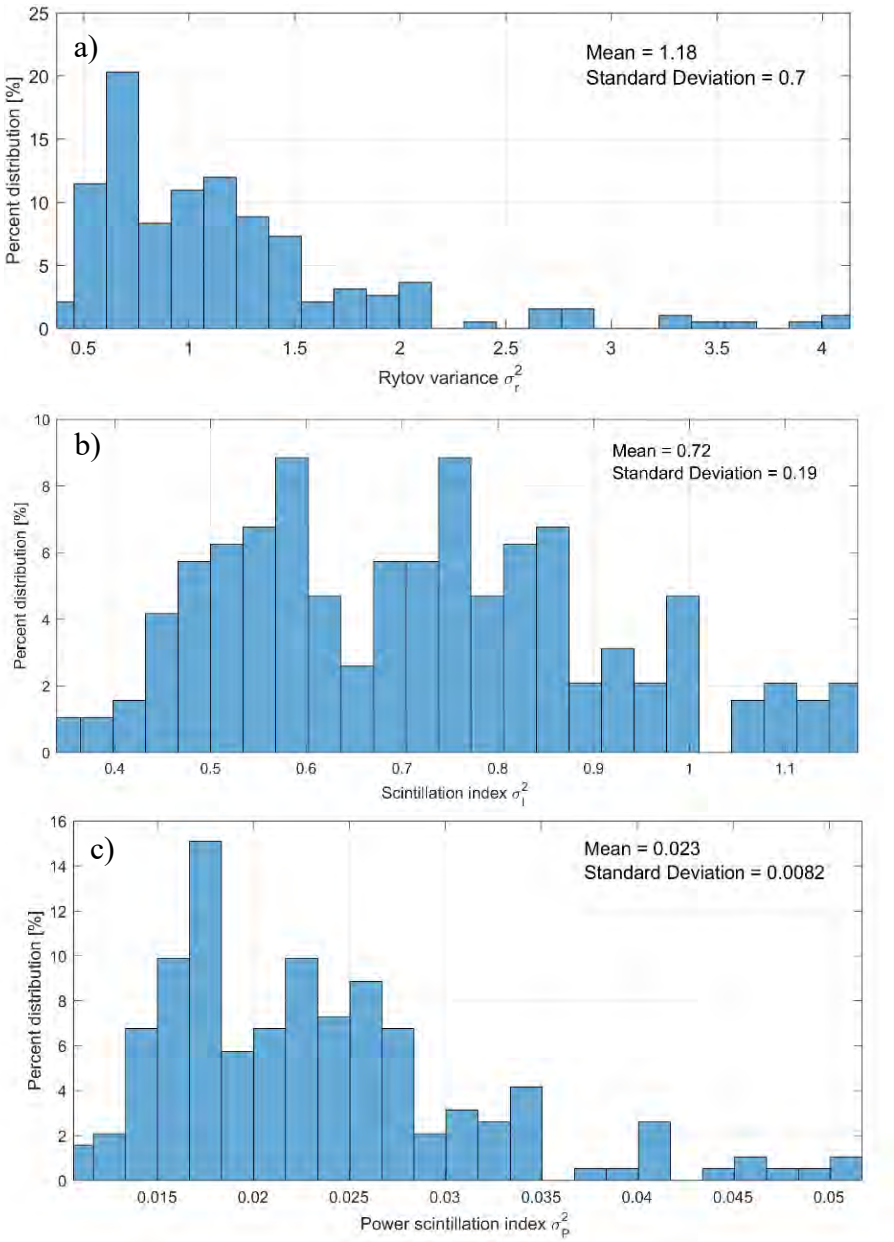

Figure 6.8: Probability histograms of: a) σ_r^2; b) σ_I^2; c) σ_p^2 – regarding space-to-ground FSO downlink for R_d = 1 m and γ =20° based on 1-year ROAB

Having in mind Eq. (3.46) and Eq. (3.47) as well as similar to ***Figure 6.6***, the attenuation histogram due to turbulence scintillations (P_{out} = 10^{-7}) in terms of R_d = 1 m and γ =20° is provided in ***Figure 6.9***. Its mean and STD values are 3.39 dB and 0.57 dB, while the maximum possible attenuation is 5.2 dB. Furthermore, the simulated power scintillation index σ_p^2 is shown in ***Figure 6.10*** for two larger apertures including R_d = 1.5 m and 8 m. The simulations for σ_r^2 and σ_I^2 are provided in **Appendix B**. The attenuation impact over space-to-ground FSO link in provided in ***Figure 6.11*** and ***Figure 6.12*** respectively.

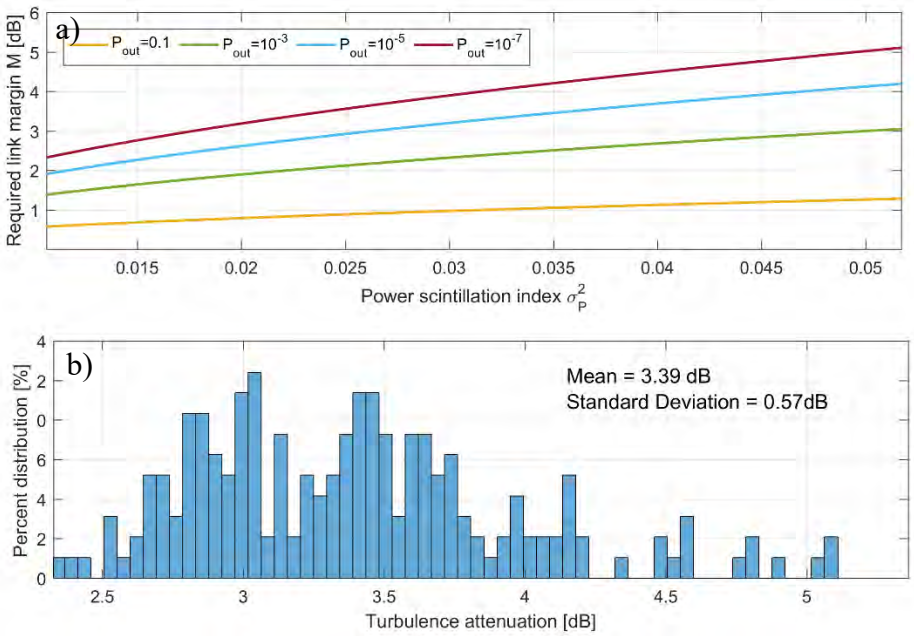

Figure 6.9: Atmospheric turbulence attenuation for R_d = 1 m and γ =20°: a) attenuation versus σ_p^2 for the three outage probabilities P_{out} = 0.1, 10^{-3}, 10^{-7} ;b) probability histogram of the simulated attenuation for P_{out} = 10^{-7} [84]

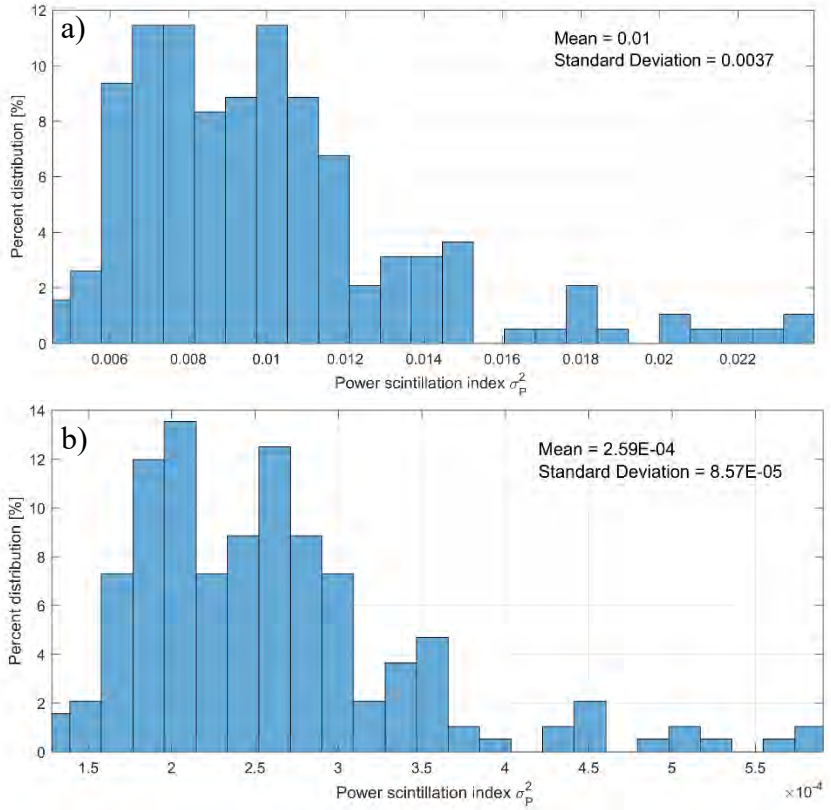

Figure 6.10: Probability histograms of σ_p^2 for R_d = 1.5, 8 m and γ =20° a) R_d = 1.5 m and γ =20°; b) R_d = 8 m and γ =20° based on 1-year ROAB measurements from Vienna Austria

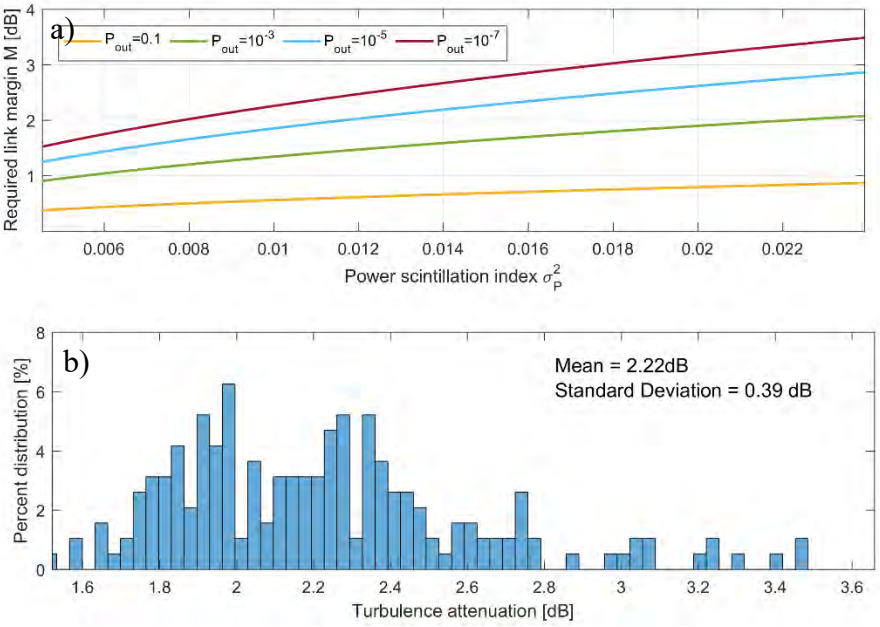

Figure 6.11: Atmospheric turbulence attenuation of space-to-ground FSO link (R_d = 1.5 m and γ =20°): a) optical attenuation versus σ_p^2 for P_{out} = 0.1, 10^{-3}, 10^{-7}; b) probability histogram of the simulated optical attenuation for $P_{out} = 10^{-7}$ [82]

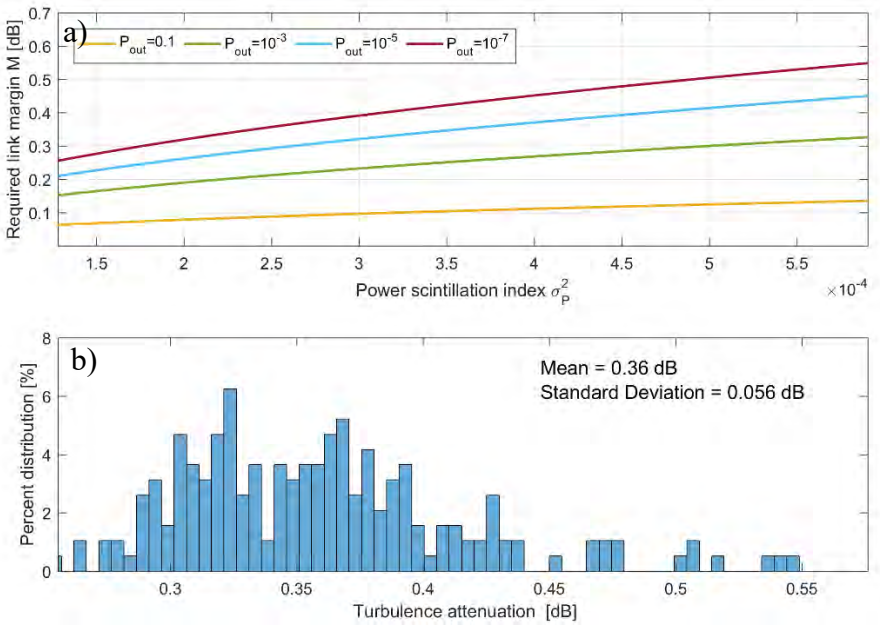

Figure 6.12: Atmospheric turbulence attenuation of space-to-ground FSO link (R_d = 8 m and γ =20°): a) optical attenuation versus σ_p^2 for P_{out} = 0.1, 10^{-3}, 10^{-7}; b) probability histogram of the simulated optical attenuation for $P_{out} = 10^{-7}$ [84]

Chapter 7

7. Deep space FSO downlinks

Due to ultra-long distances (10^3 – 10^8 km), the faced challenges by deep space FSO communication are because of all kind of critical atmospheric impairments together with geometrical losses, which both determine the deep space photon-starved communication regime. The constrains in the context of emerging deep space wireless optical links are fully covered by the scope of current thesis including atmospheric turbulence-induced fading accompanied by Mie scattering (clouds). Nevertheless, before the performance of High Photon Efficiency (HPE) FSO communication link to be assessed in terms of tropospheric perturbation effects, the specifics related to OGS and its Cloud Free Line of Site (CFLOS) availability parameter are introduced with emphasis on the applied location, namely Vienna, Austria. Furthermore, the carried out research fully complies with CCSDS standards.

7.1 Deep space FSO ground stations

The usage of terrestrial (e.g., long-distance) FSO communication systems is normally independent on the choice of a location around the globe. However, the selection of optimal sites with maximum CFLOS probability is an obligatory requirement for deep space FSO links. Having excluded Cirrus clouds, the minimum amount of FSO power penalties in the presence of all other cloud types is higher than 30 dB, which is unbearable in terms of the investigated space-to-ground communication downlinks (**Chapter 5**). Based on satellite images, various studies were performed from ESA, JPL and CNES ***[128]***, ***[129]***. Since, each of the selected sites is subject to limited CFLOS availability, a proper network combining OGSs from various locations is assessed ***[130]***. In particular, OGSs already operates at the first three most favourable locations, namely Izana (***Figure 7.1***), La Palma and Calar Alto.

Figure 7.1: ESA Teide Observatory, Izana, Tenerife, Spain: a) Cirrus clouds [20]; b) Clear sky with lower Cumulus clouds; c) Clear sky

Nevertheless, the selected location for the thesis is Vienna, Austria with 37.5 % availability (P_{out} = 0.625), which normally needs to be combined in a network with other OGS sites.

Location of OGS	Availability [%]	Location of OGS	Availability [%]
Izana	81	Noto	67.5
La Palma	77.8	Gibraltar	57.9
Calar Alto	62.9	Nuoro	59.2
Maspalomas	76.6	Villafranca	61.3
Marseille	66.6	Catania	59
Athens	68.8	Vienna	37.5

Table 7.1: CFLOS probability for different locations (partly based on data from [130])

Considering Earth's weather system, the selected sites should be situated at least several hundreds of kilometres from each other that assures enough low correlation level between them. According to ***[130]***, when European network applies site diversity mitigation technique including OGSs at 12 different locations, the maximum achieved outage probability is 10^{-3} (Availability = 99.9%). In other words, the selected OGS location in Vienna needs to be combined with other 11 sites to reach availability of 99.9%. In case such a network is built in Germany, the outage probability is significantly higher (namely 10^{-1}) even if the OGS number is increased up to 12. Moreover, an international network considering 9 OGSs possesses outage probability reaching 10^{-7} that can be considered as availability of 100 %. In the accomplished research by NASA in ***[108]***, based only on four selected OGS sites including Oldstone, CA; Kitt Peak, AZ; McDonald Observatory, TX and Mama Kea, Hawaii the calculated availability is 96 %.

7.2 CCSDS standards

Consultative Committee for Space Data Systems (CCSDS) is an organization for standards' development, dealing with space borne information equipment as well as data. In accordance with the OSI model, CCSDS provides draft recommendations for the first three most significant OSI layers of bidirectional long-distance deep space FSO photon-communication link, considering Physical, Data and Network layers respectively. Although both uplink and downlink specifications regarding HPE deep FSO channel are provided, only the downlinks are of interest for the current work. Furthermore, only the basic system requirements of the Physical layer standard as well as the coding and synchronization part of Data layer standard are introduced ***[70]***, ***[71]***. Due to lower atmospheric attenuation in C-band, a deep FSO communication downlink operates at λ_0 = 1550 nm central wavelength with a range between 1530.33 and 1564.68 nm. The spectral laser linewidth of the modulated bell-shaped laser beam is accepted to be not larger than 6.26 GHz at $1/e^2$ level. An implementation of a polarized laser beam is a subject to final architecture requirements together with polarization Extinction Ratio (ER), which should be larger than 10 dB. Moreover, the timing jitter of transmitted pulses should be at maximum 10 % of the pulse width T_s, which obtains the following values: T_s = 0.125, 0.25, 0.5, 1, 2, 4, 8, 512 ns. In case of deep FSO uplink, the data transmission is not obligatory and it is accomplished at 1030 nm with laser beam linewidth no larger than 53 GHz ***[70]***.

The second CCSDS standard provides coding and synchronization specifications in terms deep space HPE FSO links ***[71]***. In particular, the downlink synchronization is accomplished in two phases, namely frame and code word synchronization respectively. In addition, the encoding is implemented by means of Serially Concatenated Pulse Position Modulation (SCPPM) involving convolution encoder with 1/3, 1/2, 2/3 code rate, inteleaver and Pulse Position Modulation (PPM) of 4, 8, 16, 32, 64, 128, 256 order. After an additional channel interleaver, spreading operation is applied with a spreading factor between 1 and 32. Beside the challenging downlink, which requires transmission of very high amount of telemetry data, also an uplink beacon communication is foreseen in CCSDS HPE standard. In comparison to the downlink, Low Density Parity Check (LDPC) encoder ((128, 64), (512, 256) or (2048, 1024)) together with a PPM of 2nd order is applied, which is appropriate for the required low data rates.

7.3 SNSPD receiver unit at 1550 nm

A selection of a proper detector with optimal parameters is a crucial task for each FSO communication system. This is especially true in terms of the investigated long-distance space-to-ground FSO communication downlinks ***[77]***, ***[82]***, ***[85]***, ***[86]***. Having addressed the amount of the optical power as well as the type of optical detector, several different channel models are applied including Gaussian, Web, Poisson as well as Polya ones ***[85]***. In the current thesis, ultra-long deep space FSO link scenarios in the presence of weather-induced disruptions, which require single-photon communication, are investigated. In other words, SNSPD receiver unit that is considered as the most state-of-the-art detector regarding deep space FSO communication is applied ***[81]***. Although the operation of this detector is partly demonstrated during LLCD mission of NASA, substantially more investigations are necessary in terms of longer-link distances including Earth – Venus/Mars communication channels subject to adverse tropospheric influences ***[87]***. The current leading-edge work supported by ESA (partly accomplished in frame of ESA's Hybridised Optical/RF Payload Data Transmitter study ***[73]***) is considered as high contribution to this objective ***[77]***. SNSPDs are manufactured as an array of detectors (elements), which number N_r is between 2 and 64. An example of such SNSPD array is provided in ***Figure 7.2 a)***. The operation of each SNSPD element is based on not totally confirmed but well-recognised theory that the copper pairs are broken after interaction with single photons, which causes fixed resistance within the nanowire. Consequently, a detection of a single-photon event happens ***[131]***.

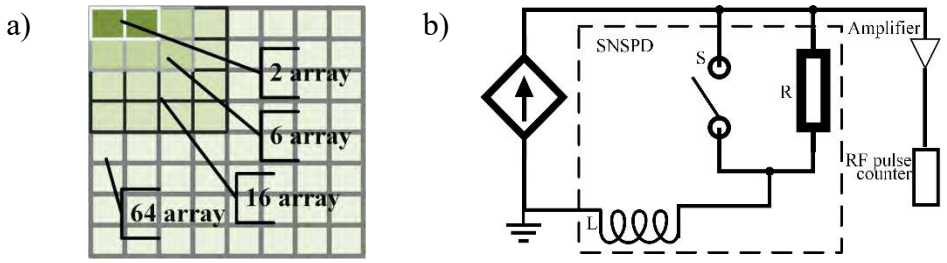

Figure 7.2: N_r-SNSPD array: a) Arrangements of SNSPD elements in different array sizes (The figure is obtained from own publication [82]); b) phenomenological scheme of a single SNSPD element (Modified figure based on publication [131])

The phenomenological scheme of SNSPD is shown in ***Figure 7.2 b)***. In order to describe theoretically a single SNSPD element, a basic electrical circuit with a simple switch, which is either closed when the detector operates in superconducting mode or opened due to fixed resistance caused by detection of a photon event, is applied. Meanwhile, the installed closed-cycle cryostat system, opens the door for cooling down the device near to the absolute zero (~2 K) which makes possible the disappearance of the electrical resistance. In the case of incidence of a single photon, which is absorbed by the nanowire, the superconductivity is broken for certain dead time τ_d. Consequently, part of the detector becomes resistive and the flowing current through the amplifier results in a voltage pulse ***[85]***. The SNSPD device is biased with a direct current I_b that is normally between 7 – 15 μA and it is set up regarding the amount of incoming optical received power P_r, dead time, DCR and quantum efficiency η. The specifications of SNSPD technology embracing the most state-of-the-art version as well as the currently implemented one, subject to sophisticated investigation within the thesis, are provided in ***Table 7.2.*** Serving as a good reference point, the performance of SNSPD receiver unit used during LLCD mission, based on ***[132]***, ***[133]***, is also offered.

Parameter	Ideal SNSPD	SNSPD under test	SNSPD (LLCD) [132]
Operation Wavelength	800 – 1550 nm	1550 nm	1550 nm
Dark count rate	1 – 10 Hz	300 Hz	10 – 30 Hz [133]
Dead time	10 – 15 ns	20 ns	15 ns
Detection efficiency	90 %	~40%	60 %
Time jitter	~20 ps	60 ps	60 ps
Detection channels	64	2	16
Output pulse height	600 – 800 mV	730 mV	588 mV [133]
Rise time of the output pulse	100 ps (300 ps)	100 ps (300 ps)	-

Table 7.2: Specifications of an ideal, the obtained as well as LLCD's SNSPD systems

The core advantages of SNSPD comprising high detection efficiency $\eta \leq 90$ %, low jitter $\geq$ ~20 ps and DCR $\geq$ 1 Hz ***[134]***. In particular, the performance is partly boosted with decreasing the wavelength and especially regarding 800 nm detectors, for which self-performed measurements carried out in Single Quantum Company are shown in ***[81]***. Yet the major constraint for all NIR spectrum is due to dead time τ_d, which is also known as a recovery time of the superconducting nanowire, after a photon energy is absorbed. Although, a commercial versions has τ_d reaching ~20 ns @1550 nm (***[134]***), also a custom made SNSPD can be delivered where the applied superconducting nanowire is shorter which allows faster recovery ~12 ns or even $\leq$ 10 ns in expense of detection efficiency (decreased active area and/or decreased wavelength) ***[131]***. Another possibility to overcome the recovery time issue is by installing a detector with larger number of channels. In accordance with ***Figure 7.2 a)***, for SNSPD array with $N_r = 64$, the recovery time can be decreased up to 64 times, which is a significant optimization in terms of overall FSO system performance. One additional point worth mentioning is the dependence of SNSPD detection efficiency η on the wavelength λ_0. Although the maximum detection efficiency of a 1550 nm SNSPD is for $\lambda_0 = 1550$ nm central wavelength (CCSDS standards), the surrounding wavelengths are also subject to detection. In other words, if the full background noise spectrum is coupled without a suitable filter, the system would be exposed to numerous non-signal photons.

Nevertheless, due to a trade-off between price and detector's capabilities, the currently applied SNSPD offers an average performance (***Table 7.2***). It contains an array of two separated detectors, namely N_r = 2. Regarding the CCSDS specifications for a real deep space FSO link, the SNSPD wavelength is chosen to be λ_0 = 1550 nm. In addition, the measured nominal values are: quantum efficiency η = 40 %; the jitter is 60 ps, DCR = 300 Hz; dead time τ_d is 17 – 20 ns ***[85]***. Considering, that the SNSPD's performance is directly dependent on the incoming optical power, the maximum efficiency is hard to be reached. During normal operation of the selected SNSPD, η = ~35 % (measured in **Subchapter 7.8**). Moreover, τ_d is ~20 ns and dead time reduction by means of higher number of detectors cannot be fulfilled because of the low number of array's elements (N_r = 2). A photograph of the obtained SNSPD system is provided in ***Figure 7.3***.

Figure 7.3: The evaluated SNSPD system obtained from Single Quantum Company containing SNSPD, air-cooled helium compressor and vacuum pump in TU-Graz Lab

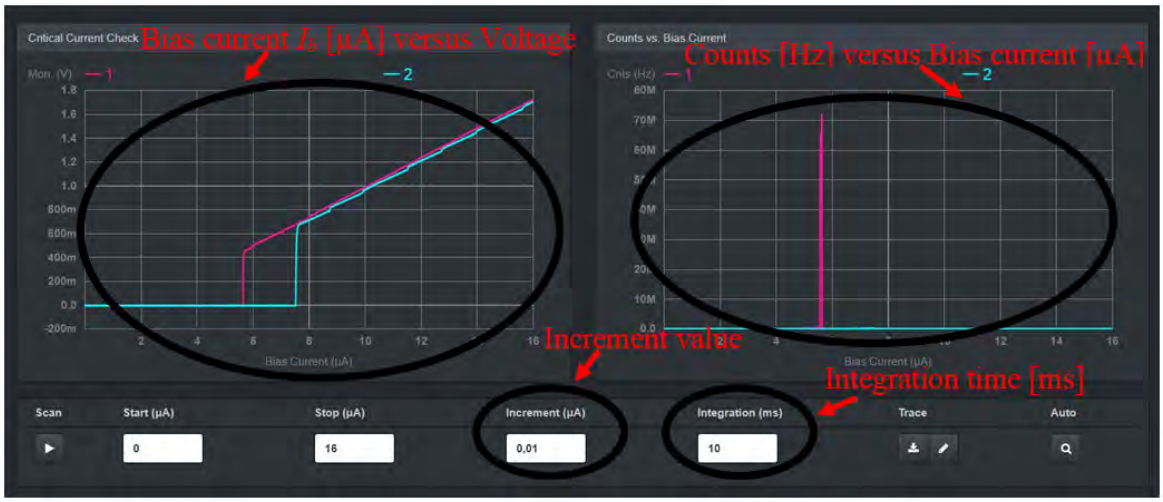

Figure 7.4: Control software for the SNSPD system provided by Single Quantum Company

Similar to the other SNSPD systems, the used module delivered by Single Quantum Company contains three major parts including closed-cycle cryostat, SNSPD array and electronic unit, which is used for information processing as well as full system control. The both SNSPDs are fibre couple based on FC/PC connectors. The SNSPD's ~2 K operation temperature is attained with help of a closed-cycle cryostat, which contains cold head, vacuum shroud, vacuum pump and compressor. In particular, the closed-cycle cryostat operates based on cold head, which is filled with helium gas. The cold head is connected to the air-cooled helium compressor. The cryostat is surrounded by the vacuum shroud, which is connected to the turbo vacuum pump system. The very high vacuum, which is at minimum of 10^7 Pa allows full isolation of the cold head from the room temperature. In addition, the investigated SNSPD system is accompanied by control unit, which is presented in ***Figure 7.4*** and allows precise setup of the biased current I_b between 0 – 20 µA with minimum increment of 0.01 µA for all array elements of the SNSPD system. In order to maximize the SNSPD operation, the I_b is determined based on information for the critical current I_c, namely the provided I_b versus Detected voltage figure as well as DCR. Moreover, the system contains photon counter providing photon counts versus I_b, which is characterized with minimum integration time of 10 ms (100 Hz frequency).

7.3.1 Characterization of the output RF pulses

Once a photon is received, the necessary recovery time of the nanowire to reach again superconductive operation mode is a major drawback of SNSPDs, which lowers the overall FSO communication system's performance. The output SNSPD RF pulse corresponding to a detection of a single-photon event is measured with Keysight 54201D digital oscilloscope. For the purpose of the current measurement, the bias current of the SNSPD has an average value of 11.6 µA. A single SNSPD pulse is shown in ***Figure 7.5***.

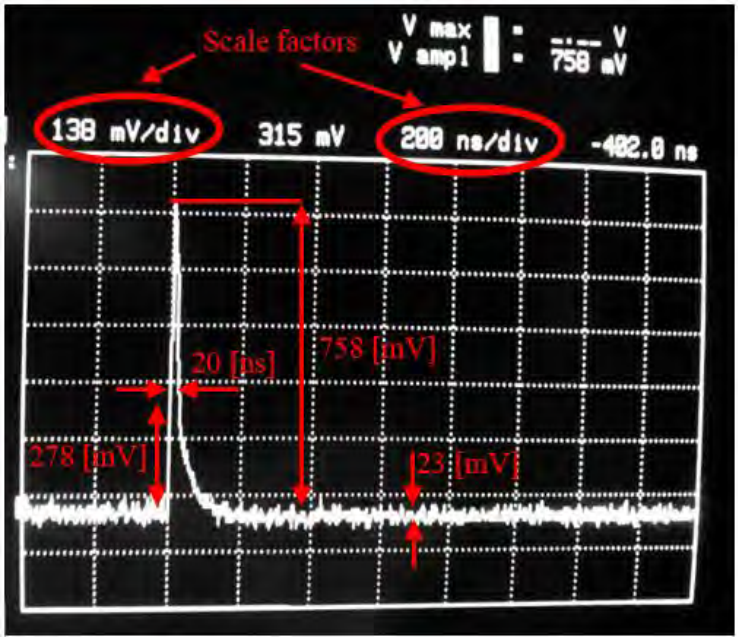

Figure 7.5: Output SNSPD RF pulse in result of a single-photon absorption

The applied oscilloscope grid is characterized with voltage scale factor of 138 mV/div and horizontal time scale factor of 200 ns/div. The measured rise time of the RF SNSPD pulse is 0.1 – 0.3 ns. Due to fact that the pulse has exponentially decaying behaviour (***[82]***), the dead time is equal to the time constant. In other words, when the voltage of a RF pulse is decreased by factor of 1/e, the recovery time is measured. In the case of ***Figure 7.5***, the pulse peak is 758 mV. Applying a decay factor of 1/e leads to 278 mV pulse height, approximately corresponding to τ_d = ~20 ns, which is higher than the minimum measured 17 ns recovery time for I_b = 7 μA.

7.3.2 DCR noise measurements

Along with the finite recovery time, the other limited factor in the context of the applied SNSPD technology is the DCR noise. DCR is measured, when both FC/PC input optical ports of the obtained SNSPD are not connected and fully closed. The DCR measurements in respect to the two channels is provided in ***Figure 7.6***. In accordance with the specifications, the optimal operation of the SNSPD system is within the nominal region of operation featured with DCR noise below 300 Hz, namely DCR < -134.2 dBm (***Table 7.2***). Consequently, the bias current should be below the critical current, which is determined in the context of the provided detected voltage versus bias current graph for each of the channels. Having addressed this constrains, the maximum measured bias current for the two channels is 11.9 μA @300 Hz and 15 μA @300 Hz.

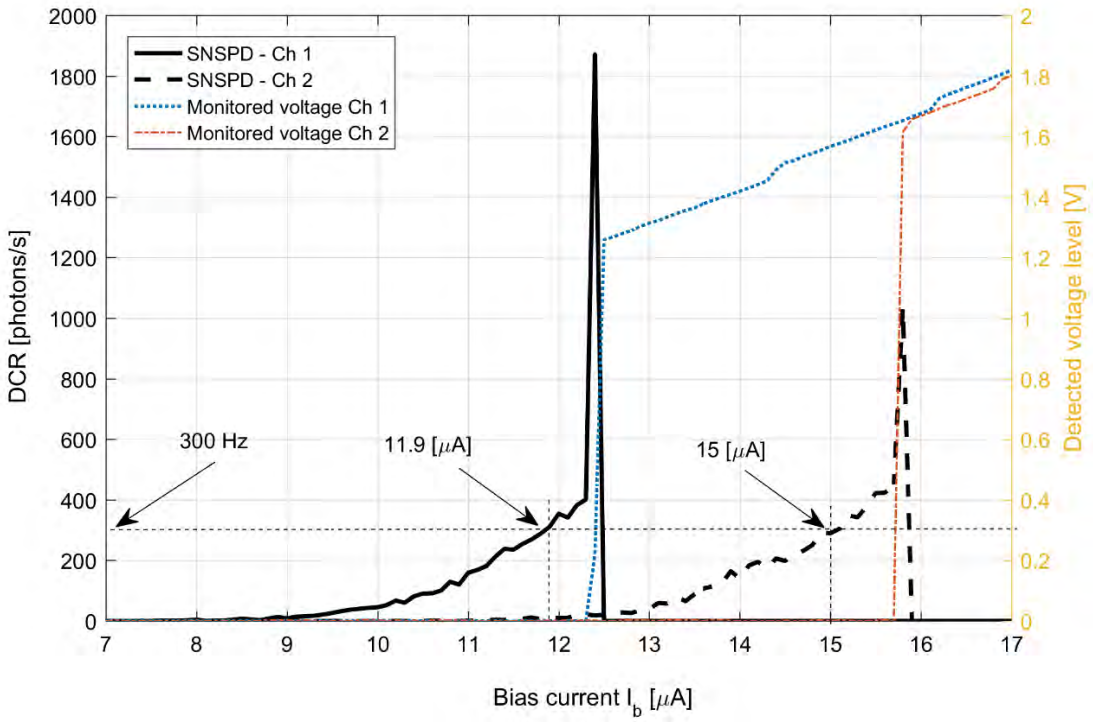

Figure 7.6: DCR measurements for the two different SNSPD channels

7.3.3 Polarization measurements

Having investigated the performance of the applied nanowire by means of the electromagnetic response show clear dependence of detection efficiency on the polarization state of the coupled light. Since the superconducting nanowire is meander-shaped with horizontal orientation, the SNSPD is characterized with a maximum sensitivity when the incoming optical signal is linearly polarized and parallel to the nanowire. Those results are also shown in ***[135]***. In particular, by applying a polarization controller, the polarization state of the signal is altered to a linear one. Although the polarization controller contains three plates, only changes into the first two are introduced during the measurements, while the third one is only tuned when an additional precision is needed. The first plate called $\lambda_0/4$ introduced a phase shift of $\pi/4$ between the two perpendicular slow and fast axis of propagation, while the second $\lambda_0/2$ plate result in π phase shift. In particular, the rotation of the two paddles leads to changes in the proportion between the horizontal and the vertical transmitted waves. The measurements with the approximately vertically oriented linear polarized input light shown in ***Figure 7.7***, significantly favours the usage of the polarizer, which provides gain of up to 4.72 dB that well coincides with the measured 3 – 4 dB polarization losses within LLCD mission ***[132]***. More specifically, having addressed that the input optical power P_r is -88.68 dBm and $\eta = 37.5$, the maximum detected amount of photons for the case of horizontally polarized light is 3.96 Mph/s, which corresponds to -92.95 dBm. In comparison the measurements without tuning the polarization state of the incoming optical signal and consequently not changing the initial nearly perpendicularly polarized light leads to 1.33 Mph/s or -97.67 dBm.

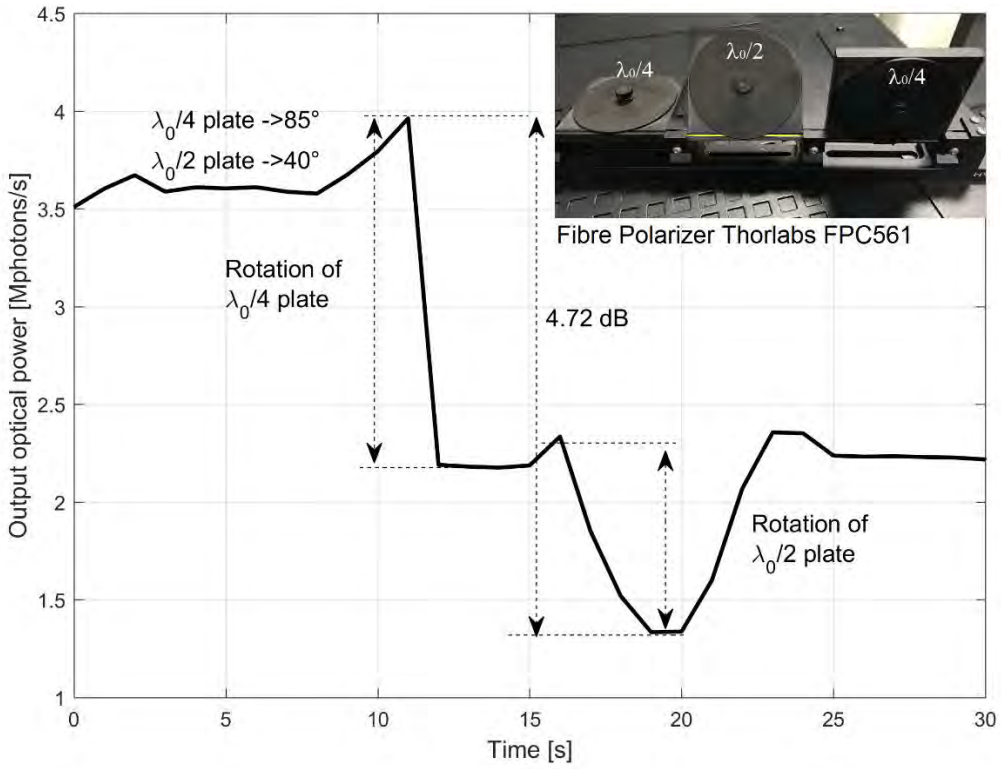

Figure 7.7: Measured polarization dependence for the obtained SNSPD system

In order to reach the objective gain of 4.72 dB in conditions of nearly vertically input polarized light, the $\lambda/4$ plate has a tilt angle of 85°, while the angle between the $\lambda/2$ paddle and X axis is 40°, which guaranties achieving a horizontal linear polarization state leading to maximum η = 37.5 %. The quarter wave plate, which is tilted at 85° angle, turns the slightly elliptically polarized light into linearly polarized one. Moreover, the 40° angle of half-wave plane alters the slightly tilted linearly polarized state to the desired horizontal position. As it is depicted in ***Figure 7.7***, when the tilt angle of $\lambda/4$ paddle is decreased, the polarization state is changed to an elliptical one, which together with additionally rotation of the $\lambda/4$ paddle (angle of 0°) results into backward effect of decreased SNSPD efficiency. Similar to the real atmospheric conditions characterized with random changes in the polarization state, the emulated optical channel includes non-polarization maintaining components. Consequently, the polarization instability induces additional variations of the detected amount of photons that can be mitigated only with an increased number of SNSDP channels, namely $16 \leq N_r \leq 64$.

7.3.4 Instability performance

The internal instability of SNSPD receiver unit for the case of low input optical power P_r = 0.25 Mph/s (-108.5 dBm) is measured and shown in ***Figure 7.8***. While the SNSPD is characterized with uncertainty of 0.63 dB per SNSPD channel, time-to-time anomalous behaviour characterized with sharp optical signal drops (spikes) is also observed. Although the mitigation of the measured instability would favour an SNSPD array with larger number of receiver units ($N_r > 16$), the obtained $N_r = 2$ channel SNSPD array is strongly susceptible to the 0.63 dB uncertainty.

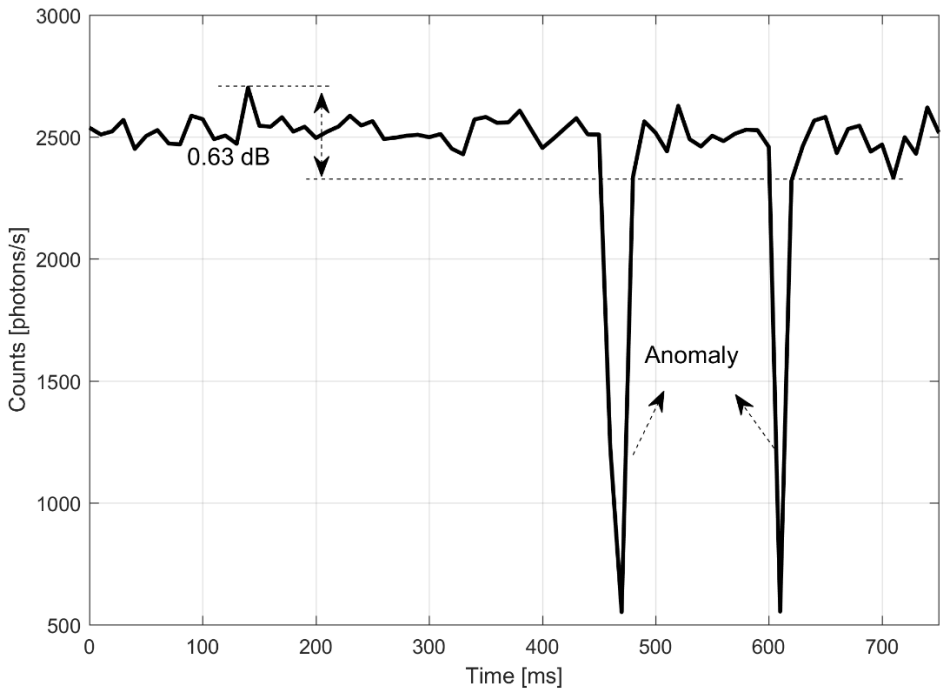

Figure 7.8: Instability characterization of the obtained SNSPD system

7.4 Modelling of deep space Poisson FSO channel with SNSPD

The operation of ultra-long-distance FSO downlink in the presence of atmospheric turbulence-induced fading is modelled based on the introduced theory as well as empirical research findings ***[82]***, ***[84]***, ***[85]***, ***[86]***. The main objective of the developed model is to show the influence of turbulence attenuation over the received optical signal without additional mitigation techniques subject to complex signal processing. For this purpose, the main emphases are put over the proper representation of deep space FSO Poisson channel and emulation of real OGS including very-large-size optical apertures 1 m < R_d < 8 m as well as up to N_r = 64 SNSPD elements. Similar to other areas in optical communication domain, MATLAB is considered as the most suitable programming environment to emulate the behaviour of a real deep space FSO link. The rough state-of-the-art modelling concept of the represented deep space HPE FSO channel is provided in ***Figure 7.9***.

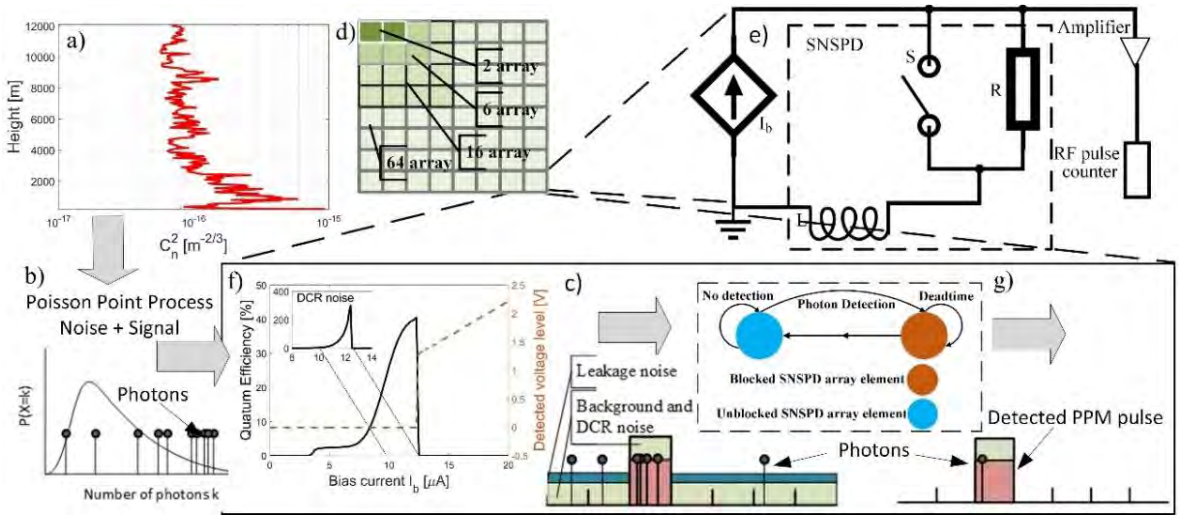

Figure 7.9: Modelling of a deep space FSO Poisson channel in the presence of atmospheric turbulence-induced fading (The figure is obtained from own publication [86])

The model involves the following parts:

1) Implementation of clear-air atmospheric turbulence-induced fading taking into account the simulated atmospheric vertical profile of C_n^2 in terms of real RAOB data for central Europe, namely Vienna, Austria. The simulation results provided in ***Figure 7.9 a)*** are obtained from **Chapter 6**.
2) Modelling of ideal deep space Poisson channel based on the introduced Poisson point processes (PPPs) in **Subchapter 7.4.1** (***Figure 7.9 b)***).
3) In accordance with CCSDS standards, the information is transmitted as M order PPM pulses, which are theoretically defined in **Subchapter 7.4.3**. The average optical power level within an empty slot as well as within a PPM pulse is calculated based on transmitted optical power and additive Poisson noise (leakage noise, background noise, DCR) (***Figure 7.9 c)***).

4) Addressing the behaviour of a real SNSPD receiver unit, which is manufactured in variety of configurations (***Table 7.2***). In particular, the model provided in ***Figure 7.9*** is optimized to represent all deep FSO scenarios with spatial focus on $N_r = 2$ SNSPD.
   - A matrix of 1 – 64 single-photon elements is considered with emphasis on the most common designs comprising $N_r = 2, 8, 16, 64$ (***Figure 7.9 d)***).
   - Each element is described by its phenomenological scheme (basic electrical circuit), provided in ***Figure 7.9 e)***, which generates train of exponentially decreasing output RF pulses that number corresponds to the amount of detected single-photon events.
   - A special emphasis is put on the SNSPD's quantum efficiency η and DCR versus bias current I_b. The self-measured results with the obtained SNSPD shown in ***Figure 7.9 f)*** corresponds to an ideal bias-current operation point I_b = 11.6 μA, which delivered the assumed nominal η = 40 % in the detector's specification (***Table 7.2***). Nevertheless, this is in expense to low input optical power, a well-examined challenge during the accomplished breadboard real measurements.
   - Having addressed the measured recovery time τ_d of the SNSPD's nanowire, a dead time model for each element of SNSPD matrix is introduced. Moreover, ***Figure 7.9 g)*** includes the detected PPM symbol based on absorption of a single-photon event.

The nowadays technological advances allows ground-to-deep-space FSO links to be established between Earth and nearby planets in the solar system including possible future missions to Mars, Venus, etc. In order to address broad variety of such scenarios reaching distances of up to ~10^9 km (6.7 A.U.), simulations for wide range of transmitted optical power are performed in the current thesis. Moreover, the applied parameters are fully complied with the introduced ones in CCSDS standards (**Chapter 7.2**). For representing a real deep space FSO communication link, the simulations are based on IM/DD architecture, which is simpler and cheaper than the coherent one. In particular, the coherent scheme suffers from lack of capabilities to provide sufficient photon starved sensitivity in the presence of atmospheric turbulence. The reason for this is the small coherence length of the atmosphere (turbulence-induced fading), which leads to imperfection of the matching between incoming signal and the local oscillator ***[136]***. The idea behind the IM/DD is transmitting the information on the instantaneous power of optical carrier signals operating on 1550 nm wavelength. Moreover, a photon starved Poisson channel and PPM modulation with soft decision decoding, which relies on extracting soft information based on Euclidian distance is addressed ***[137]***, ***[138]***. In other words, PPM optical pulse train is processed based on soft decision decoding scheme, which is a superior scheme in comparison to the hard decision decoding one ***[136]***. Although CCSDS standards recommend LDPC or SCPPM coding, the current thesis model does not consider forward error correction codes. In particular, the goal of the current work is to investigate and show the effect of atmospheric turbulence-induced attenuation over deep space Poisson channel without consideration of further high demanding mitigation techniques. However, direct-sequence spread spectrum (DSSS) technique, well known as Pseudo Noise (PN)-spreading is implemented. Regarding this method, the processed uncoded PPM frame is used to modulate PN pulse train characterized with considerably reduced pulse length. This technique is successfully used to

fight the consequences of very low data throughput (< 10 Mbps) which leads to low peak to average PPM power ratio *[71]*.

On the contrary of conventional deep space FSO communication systems operating with high enough optical power measured in [mW] and more specifically in [dBm] units, photon-starved FSO links rely on ultra-low received optical power measured in photon counts. Respectively, the applied units are photons per nanosecond in [dB] ((ph/ns) [dB]) and photons per PPM slot in [dB] ((ph/sl) [dB]). For example, it is visible that 10 (ph/s) [dB] correspondence to 10 ph/s. In accordance with Planck – Einstein relation, the energy of a single photon, which depends on the selected wavelength λ_0, is given in Eq. (7.1).

$$E\ [J] = \frac{hc}{\lambda_0} \qquad (7.1)$$

Where h = 6.62 10^{-34} m^2 kg/s is the Planck constant and c = 3 10^8 m/s is the light speed in vacuum. The self-derived forward calculations of [dBm] in respect to (ph/s) [dB] and (ph/sl) [dB] are provided in Eq. (7.2) and Eq. (7.3).

$$P\ [dBm] = 10lg\frac{E[J]10^{\frac{P\ (ph/s)[dB]}{10}}}{1\ mW} \qquad (7.2) \qquad P\ [dBm] = 10lg\frac{E[J]\frac{10^{\frac{P\ (ph/sl)[dB]}{10}}}{T_{slot}\ [s]}}{1\ mW} \qquad (7.3)$$

The self-derived backward calculation of (ph/s) [dB] and (ph/sl) [dB] in respect to [dBm] is given in Eq. (7.4) and Eq. (7.5).

$$P\ (ph/s)[dB] = 10lg\frac{10^{\frac{P\ dBm}{10}}1mW}{E[J]} \qquad (7.4)$$

$$P\ (ph/sl)[dB] = 10lg\frac{10^{\frac{P\ dBm}{10}}1mW}{E[J]}T_{slot}\ [s] \qquad (7.5)$$

Despite the complexity at first site, the equations results from the simple [dBm] to [mW] conversation principal given in Eq. (2.7), the famous Planck – Einstein relation (7.1) as well as the knowledge that the P [W] is equal to E [J] multiplied by the number of photons per second (P [W] = E [J] * P [ph/s]).

7.4.1 Poisson point processes based model

The current subchapter is partly obtained from own publication *[81]*, *[85]*. Taking into account theory and practice, FSO communication link is statistically represented with a few well-known channel models. Along with terrestrial channels, shorter space-to-ground FSO links utilizing PIN/APD are accurately demonstrated by Gaussian channel modelling *[61]*, *[139]*. In these conditions of high enough received FSO optical power accompanied by AWGN, the photon stream and thereof generated electrical signal, is approximated by Gaussian distribution *[42]*.

$$p(i) = \frac{1}{\sqrt{2\pi(\sigma_s^2 + \sigma_b^2)}}exp\left\{-\frac{(i-<i>)^2}{2(\sigma_s^2 + \sigma_b^2)}\right\} \qquad (7.6)$$

While i is the electrical current, σ_s and σ_b are shot noise and background noise variances. Due to extremely high number of received photons, these FSO systems are featured with high optical power measured in [dBm] units and more specifically, the number of detected photons is not taken into account. In particular, APD has 5 – 10 dB better receiver sensitivity in comparison with PIN ***[140]***. Considering the dependence of sensitivity parameter on data rates, an APD sensitivity of -30.2 dBm @1550 nm for 10 Gbps data throughput is demonstrated in ***[141]***. Moreover, a commercially available reverse-biased PIN with built-in transimpedance amplifier reaching sensitivity of -50 dBm @1064 nm, which supports low data rates, is applied during the experimental campaign between ESA's OGS and the installed TESAT LCT-135 at EDRS-A GEO satellite ***[20]***. In case of ultra-long ground-to-deep-space FSO communication links, the received optical power is lower than ~-60 dBm. In frame of LLCD, the considered FSO communication link to the Earth's closest celestial body, namely Moon, is characterized with an average downlink optical power of ~ -70 dBm @1550 nm at maximum data rate of 622 Mbps ***[72]***. Consequently, a ground-to-deep-space FSO link in terms of further-distances celestial objects (e.g., Mars or Venus) faces even lower received optical power. Taking into account above very stringent restrictions regarding sensitivity, single-photon detectors for which the very low number of received photons leads to other distribution models than Gaussian one are used.

Although InGaAs GM-APD technology that allows detection of single-photon events was significantly upgraded recently, still the extremely high 1 Hz – 10 kHz DCR and $\tau_d < 1$ µs dead time, prevent its use in real deep space FSO scenarios. Furthermore, Photo Multiplier Tube (PMT) single-photon detector, which operates based on dynodes chain including stages with different gains, is mathematically modelled with Polya distribution ***[142]***. The PMT technology is characterized with high gain and allows generation of high number of photoelectrons (10^5 – 10^6) in terms of absorbing one single photon. The simplest form of Polya distribution in case of single dynode stage is provided in Eq. (7.7).

$$p(n) = \frac{\mu^n}{n!}(1 + b\mu)^{-n-(1/b)\prod_{i=1}^{n-1}(1*ib)} \qquad (7.7)$$

Where n is the number of the generated photoelectrons, b is a shaping graph parameter and μ is the main gain. Unfortunately, this technology is characterized with detection efficiency only up to 6 % and 200 kHz DCR, which is the major cause for lack of performance. Although commercially available PMT by Hamamatsu is used for additional validation of ultra-long FSO downlink between LADEE unit of NASA and ESA's OGS in Tenerife, the transferred data amount is considerably low, namely 38 Mbps @1550 nm wavelength ***[143]***. In order to achieve evidently improved results, the originally established downlink between LADEE and Earth in frame of LLCD (carried out by NASA) is based on still state-of-the-art SNSPD technology attaining the remarkable 622 Mbps @1550 nm ***[72]***. Consequently, SNSPD is the detector of choice for the future ultra-long-distance FSO links, which suffer from lack of enough investigation in terms of atmospheric effects. In comparison to PMT, a deep space FSO communication link applying SNSPD receiver unit is modelled as a Poisson channel, where the well-known Poisson point processes PPPs are applied ***[144]***.

For large number of photons k, the limiting form of the Poisson distribution is Gaussian distribution. Nonetheless, when the number of photons k is low, which is the case for the investigated deep space FSO link based on SNSPD receiver unit, only the genuine Poisson channel is introduced. Although SNSPD detectors have still limitations in terms of τ_d (see ***Table 7.2***), the very low amount of received photons allow such a deep space link to be enough accurately modelled by PPPs. In particular, direct-detection deep space FSO link with a SNSPD that obeys the concept for photon-counting detection is modelled by Poisson channel, which was already well considered back in 1981 in the famous work ***[69]*** of J. Pierce. Taking into account an additive noise channel model, the output $y(t)$, which is sum of received signal $x(t)*h(t)$ and noise $n(t)$, is provided in Eq. (7.8).

$$y(t) = x(t)*h(t)+ n(t) \qquad (7.8)$$

Both, the transmitted signal $x(t)$, which propagates through a FSO communication link with an impulse response $h(t)$ as well as the Poisson noise $n(t)$ obey Poisson point processes (PPPs). Considering an additive noise channel as well as the well-known superposition theorem, the channel output $y(t)$ is also a Poisson point process. In general, the introduced impulse response $h(t)$ characterizes fully a deep space FSO link. It includes mainly, propagation path losses and pointing errors (**Chapter 2**) as well as atmospheric-induced fading (**Chapter 3**) ***[136]***. The Poisson distribution characterizing both the transmitted signal and noises is given in Eq. (7.9) ***[69]***.

$$P(k,\lambda) = \frac{\lambda^k e^{-\lambda}}{k!} \qquad (7.9)$$

Where $P(k, \lambda)$ is the probability that k number of photons will be detected when the investigated Poisson channel has arrival rate (intensity) equal to λ. In theory, an analogue continuous transmitted optical signal, which is categorised as a PPP with a certain continuous time-varying intensity is assumed to be inhomogeneous. On contrary, FSO technology is manly based on digital pulse modulation schemes (e.g, OOK, PPM) where identical pulses are utilized, which result in homogeneous PPP with constant average intensity per pulse λ_p. Furthermore, the photon noise whose mean rate per empty slot λ_n is superposition of several noises characterized with Poisson distribution is also homogeneous PPP. In particular, the main three types of noise, having a significant influence on a deep space FSO communication system, are DCR noise of the SNSPD with intensity λ_{dcr}, background noise having rate λ_b and leakage noise with λ_{ln} ***[82]***. The background noise is mainly due to sun irradiance (***[42]***) whose mean arrival photon rate per T_s slot λ_b is calculated based on the average background noise power P_b including sky irradiance as well as reflected sunlight from the observed planets (***Figure 1.1***) given in self-derived Eq. (7.10) ***[85]***.

$$\lambda_b = \eta T_s \frac{P_b \lambda_0}{hC} \qquad (7.10)$$

Where λ_0 is the operational wavelength, h= 6.62 10^{-34} m^2 kg/s is the Planck constant, c = 3 10^8 m/s is light velocity, T_s is the PPM slot width, η is the detection efficiency of the selected single-photon detector. In comparison, with the other two noises, the leakage noise, which is defined in **Subchapter 7.4.4,** is due to On-Off ER of the external MZM used for

modulation of a CW laser source at 1550 nm wavelength. The conditional probability mass functions of both, the transmitted optical signal (pulse slot) and noise (empty slot) PPPs are provided in Eq. (7.11) and Eq. (7.12), which are based on ***[144]*** and the research in ***[82]***.

$$P_{\lambda_p}(k) = \frac{(\lambda_s + \lambda_b + \lambda_{dcr})^k e^{-(\lambda_s+\lambda_b+\lambda_{dcr})}}{k!} \quad (7.11)$$

$$P_{\lambda_n}(k) = \frac{(\lambda_{ln} + \lambda_b + \lambda_{dcr})^k e^{(\lambda_{ln}+\lambda_b+\lambda_{dcr})}}{k!} \quad (7.12)$$

Where $P_{\lambda p}$ is the probability that k number of photons will be detected during a pulse slot and $P_{\lambda n}$ is the probability that k number of noise photons will be detected in an empty slot.

7.4.2 Pulse position modulation with guard slots

The most common modulation techniques are PPM and OOK modulations, while Pulse Interval Modulation (PIM) is rarely used ***[42]***. All three are accompanied by a direct detection receiver, which is part of the IM\DD architecture. In the OOK scheme, the '1' bit is represented by an optical pulse that occupies part or the full bit duration while the '0' bit indicates the absence of an optical pulse. One of the biggest advantages of this method is its simplicity. Nevertheless, in accordance with the introduced CCSDS standards, PPM is the selected optical modulation for long-distance deep space FSO communication. The most distinguishable characteristic of this modulation is that each optical pulse can be used to represent L bits of information by its position in frame of an M-slots symbol. The notation for a PPM slot duration is T_s. When L is increased, the related slots M will be also increased. Consequently, the duration of our optical pulse will get smaller with respect to duration of one bit. This means that PPM has higher bandwidth requirements than OOK and as a result, its bandwidth efficiency decreases ***[42]***. Theoretically, this cannot be a major hurdle because optical bandwidth is mainly limited by the current technology level. The most important advantage here is that PPM has really better power efficiency than OOK. In the case of infinity ER, the peak power of 1 PPM pulse is M times the average optical power P_r, which is substantially higher in comparison with the $2P_r$ peak power for OOK ***[84]***.

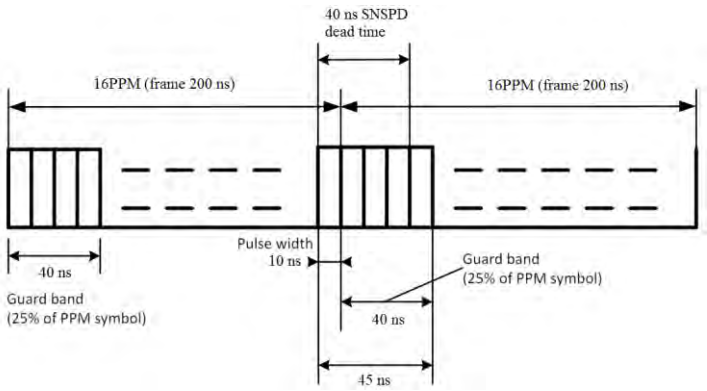

Figure 7.10: The arrangement of 16-PPM frame including 25 % guard slots and T_s = 10 ns preventing the adverse influence of SNSPD's dead time parameter (Modified figure based on own publication [84])

In addition, CCSDS standards require Guard Slots (GS) that are 25 % of the generated PPM frame to be inserted. The PPM modulation together with the applied GS is assumed as a decent mitigation technique, which reduces the influence of SNSPD dead time while providing the required resilience against multiple symbol errors. In respect to a selected scenario with 16-PPM (LLCD mission) and T_s = 10 ns (CCSDS standards) as well as measured τ_d = 20 ns (***Figure 7.5***), a detailed illustration is provided in ***Figure 7.10***. In particular, the 25% GS for 16 PPM are 4 and hence, the PPM frame duration is 20 slots or 200 ns. The worst-case scenario, given in ***Figure 7.10***, occur when there is 4 times "1" bit or the pulse of PPM modulation is in the last slot neighbouring to the next frame. Considering the current case with τ = 20 ns and T_s = 10 ns, the detector will be blind for a considerable amount of time when the next frame arrives, leading to very high information losses and low SNR. Nevertheless, the remaining 10 ns in which the detector is not available will be part of the 40 ns guard band of the next frame (taken from own publication ***[84]***).

To sum up, the guard band has a restriction of minimum 20 ns, which is equal to the DT of the detector. Consequently, the dead time has to be observed together with the requirement for 25 % GS. Although the Poisson distributed incoming noise photons still cause serious blockage, GS at least relax the dead time limitations.
Taking into account the conditional probability mass functions in Eq. (7.11) and Eq. (7.12) as well as the selected PPM technique with soft decision decoding, the obtained equation for the capacity of noiseless Poisson channel is given in Eq. (7.13) ***[144]***.

$$C_{ppm}(M, \lambda_s, \lambda_n = 0) = \frac{\log_2 M}{M}\left(1 - e^{\eta \lambda_{s\_ns} M T_s}\right) \qquad (7.13)$$

Where, λ_{s_ns} is the photon rate per [ns], while $\eta\lambda_{s\_ns}MT_s = \lambda_s$ corresponds to the average signal-photon rate per PPM slot. Nonetheless, the channel capacity needs to be reconsidered for the common case when photon noise is also headed into the receiver's FoV. Although coping with the general C_{ppm} (M, λ_s, $\lambda_n > 0$) equation is tricky and demanding task, having the knowledge for $\lambda_{s\_ns} \rightarrow 0$, allows Taylor series for a single point $\lambda_{s\_ns} = 0$ to be applied ***[144]***. The approximation for deep space Poisson channel operating in the presence of photon noise which is based on a third degree Taylor polynomial is given in Eq. (7.14).

$$C_{ppm}(M, \lambda_s, \lambda_n) = \left(\frac{M-1}{2ln2}\right)\frac{\eta\lambda_{s\_ns}^2}{\lambda_{n\_ns}} \qquad (7.14)$$

Where λ_{n_ns} is the mean noise photon rate per [ns], which characterizes the Poisson point process of the photon noise. In particular, similar to Eq. (7.10), the final amount of all noise photons per slot is $\lambda_n = \eta T_s \lambda_{n\_ns}$.Without limiting the generality, the ideal case of noiseless Poisson channel for M =16, 64, 256 PPM with soft decision decoding is plotted in ***Figure 7.11***.

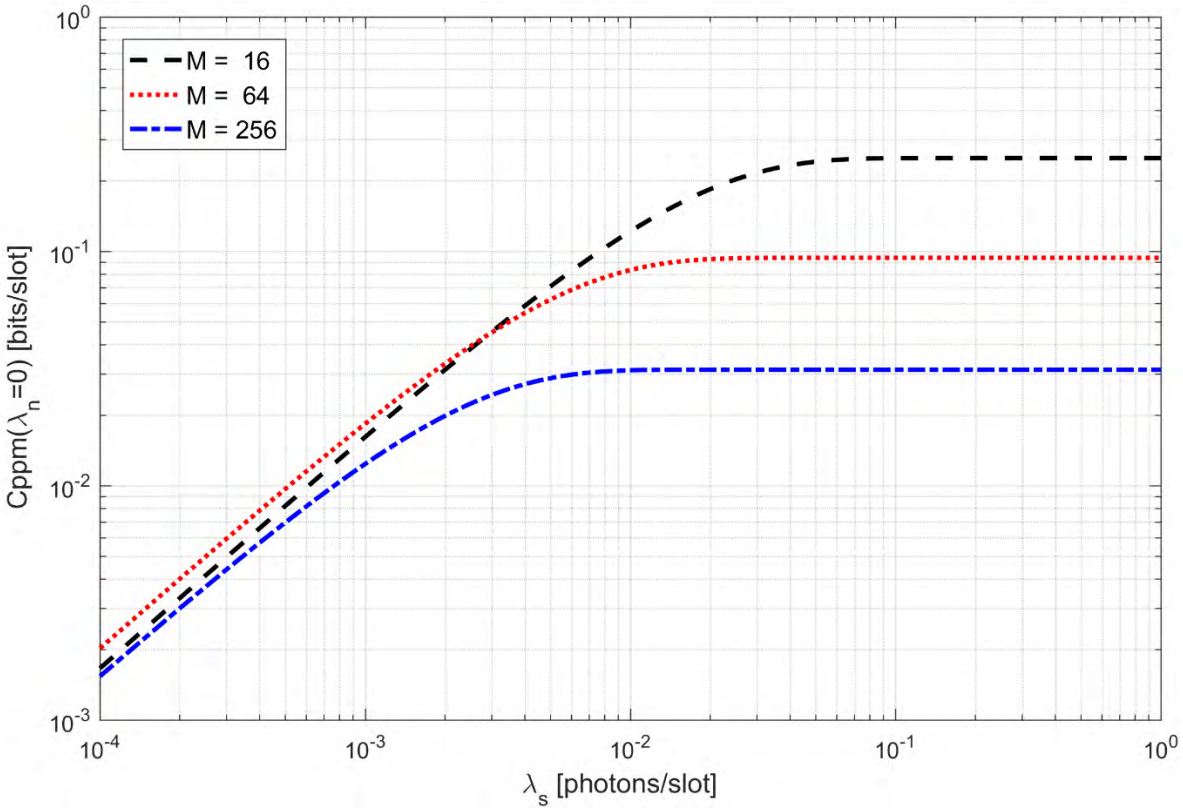

Figure 7.11: Channel capacity versus λ_s for ideal case of noiseless Poisson channel in terms of PPM order M = 16, 64, 256 (The figure is obtained from own publication [81])

The selected order M, which is well-complied with the CCSDS standards is in the typical min-max range of an interplanetary deep space mission. Furthermore, the detection efficiency η = 90 % corresponds to a SNSPD receiver unit with the highest possible performance. As expected, when the average optical power measured in photons per slot λ_s is high enough, the channel capacity is independent on the amount of the received photons. However, for low enough optical power levels, due to quantum-limited performance in respect to the nature of light, the capacity of a deep space Poisson channel decreases sharply. Moreover, The PPM with higher M order offers better channel capacity for the same average optical power levels. Nevertheless, the higher power-efficiency is attained in expense of lower bandwidth efficiency. In order to highlight the importance of quantum efficiency η, which plays role of a major limitation factor for the defined capacity in Eq. (7.13) and Eq. (7.14), the SNSPD is compared with the performance of two other aforementioned single-photon detectors comprising GM-APD ($\eta_{gm\text{-}apd}$ = 30 %) and PMT (η_{pmt} = 6 %) . The simulation results are provided in ***Figure 7.12 [81]***.

The simulations in ***Figure 7.12*** are performed for the selected 16-PPM based on NASA's LLCD and CCSDS standards as well as ***Figure 7.11***. The dependence on quantum efficiency is evident and well explained by the fact of its direct influence over received optical power. The boosted performance in the case of SNSPD, which is capable to operate very near to C_{ppm} information capacity limit, results in further implementation of the evaluated SNSPD

in the carried out simulations and breadboarding. On the contrary to the shown curve for η = 90 %, the implemented SNSPD is lower class which is charterized with η = 40 %.

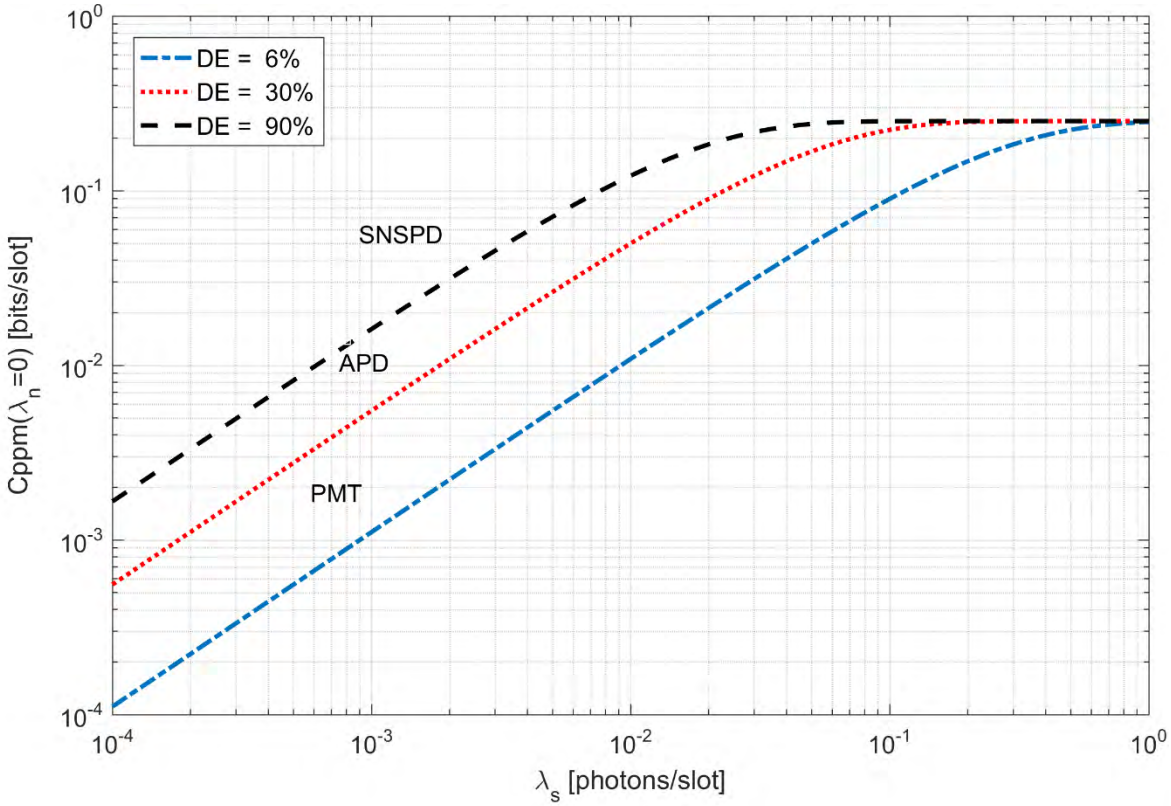

Figure 7.12: Channel capacity versus λ_s for noiseless Poisson channel and 16-PPM in terms of SNSPD, InGaAs GM-APD and PMT receiver units (The figure is obtained from own publication [81])

7.4.3 Extinction ratio of Mach – Zehnder modulator

One of the major technological limitations of applied Master Oscillator Power Amplifier (MOPA) architecture part of the space borne FSO transmitter's equipment is related to finite Extinction Ratio (ER) of Mach – Zehnder modulator (MZM). It substantially increases the noise and the related BER, which is direct challenge to deep space FSO downlinks operating in HPE regime.

In particular, ER is defined as a proportion between the optical power levels corresponding to pulse 'on' ('1') and pulse 'off' ('0') that with the latest technological advances, introducing silicon photonic chips based on Mach-Zehnder interferometers, can reach value up to 60 dB @1550 nm wavelength ***[21]***, ***[146]***. Nonetheless, this achievement is non-applicable to space missions due to strict standards for space qualification and design. Since the near and deep space FSO distinguishes with limited performance due to severe space conditions, the imposed requirements in ***[143]*** for minimum uplink ER regarding LLCD are ER > 13 dB while an ordinary downlink demands ER ≥ duty cycle +15 dB ***[147]***. Having in mind the asymmetric data transmission, only long-distance LEO/GEO-to-ground and ultra-long-

distance deep space (e.g., Mars/Venus-to-ground) FSO communication downlinks are of importance that are charterized with ER ≥ 23 dB. Due to harsh operating environment, even with the most state-of-the-art space-qualified MZMs implementing $LiNbO_3$ and GaAs crystals, the reached ER values are in a range of 23 – 30 dB. (e.g., iXblue Company and More Photonics Company). Taking into account the specifics of SNSPD-based HPE optical communication link, the leakage noise due to finite ER is a main limitation factor. The applied PPM modulation featured with duty cycle of $1/(L+GS)$ has Peak to Average Ratio (PAR) given in Eq. (7.15) ***[21]***. Addressing PAR, the mean photon rate in terms of finite ER for pulse slot is derived in Eq. (7.16).

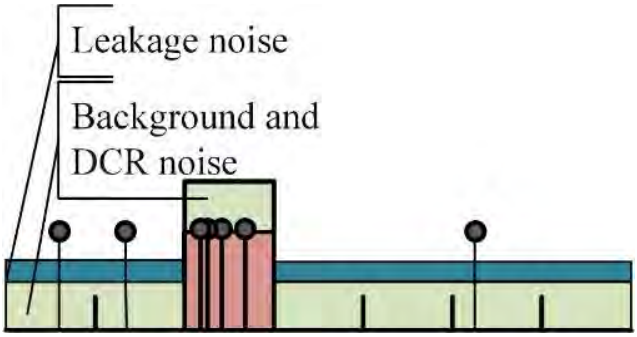

Figure 7.13: PPM frame depicting the Poisson channel's noises (λ_b, λ_{DCR}, λ_{ln}) [82]

$$PAR = \frac{(L+GS)\,ER}{1+(L+GS)} \quad (7.15) \qquad \lambda_s = PAR * \frac{P_r \lambda_0}{hc} T_s \quad (7.16)$$

Taking into account the above definition for ER, the average residual noise ratio N_{PAR} is given in Eq. (7.17). Moreover, the mean photon rate of leakage noise in respect to an empty slot is derived and shown in Eq. (7.18).

$$N_{PAR} = \frac{(L+GS)}{1+(L+GS)} \quad (7.17) \qquad \lambda_{ln} = N_{PAR} * \frac{P_r \lambda_0}{hc} T_s \quad (7.18)$$

A PPM symbol, comprising a frame with a transmitted pulse together with a number of empty slots that operates in background, DCR and leakage noise is given in ***Figure 7.13***.

7.4.4 Detection of a PPM symbol based on SNSPD receiver unit

In order to simulate SNSPD-based photon-starved FSO communication link in MATLAB, the developed Poisson channel model in **Subchapter 7.4.1** is modified in respect to the special features of SNSPD receiver technology. A SNSPD system contains an array with up to $N_r = 64$ separated channels ***[86]***. Taking into account the superposition principle of a linear system, the incoming single photons are equally divided among the N_r-SNSPD's elements. The recalculated mean arrival photon rates in accordance with N_r value and in respect to both PPPs regarding a pulse slot (received optical signal + noise) as well as empty slot (namely only noise: background noise, leakage noise and DCR) is provided in Eq. (7.19) and Eq. (7.20) ***[82]***.

$$\lambda_{pn} = \frac{\lambda_s + \lambda_b + \lambda_{dcr}}{N_r} \quad (7.19) \qquad \lambda_{nn} = \frac{\lambda_{ln} + \lambda_b + \lambda_{dcr}}{N_r} \quad (7.20)$$

An example for redistribution of the received optical power in respect to Poisson channel modelling as well as the obtained SNSPD, which has an array of two elements ($N_r = 2$) is given in ***Figure 7.14***.

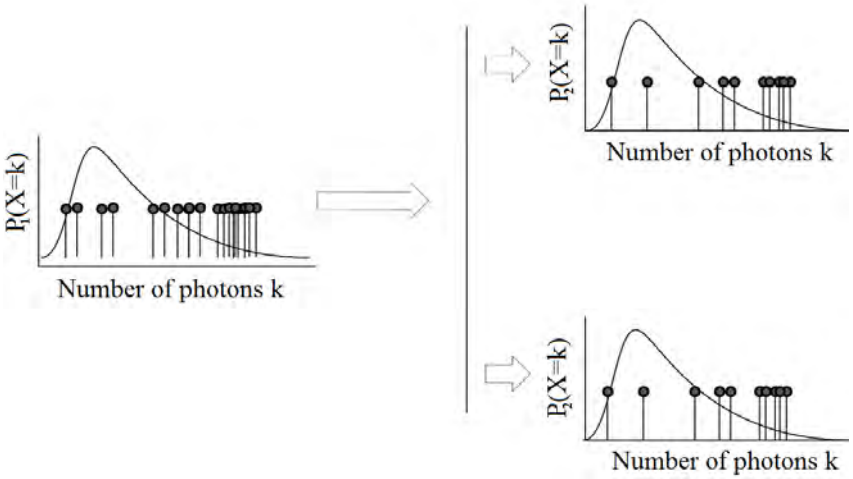

Figure 7.14: PPP in terms of a SNSPD array with $N_r = 2$ (Modified figure based on own publication [82])

Applying the results form Eq. (7.19) and Eq. (7.20) in the provided $P_{\lambda_p}(k)$ (Eq. (7.11)) and $P_{\lambda_n}(k)$ (Eq. (7.12)), leads to correction in the context of detection probability for a single-photon event during a pulse and an empty slot. Both equations valid for a single element of the SNSPD array are derived and shown in Eq. (7.21) and Eq. (7.22).

$$P_{\lambda_{pn}} = \frac{\lambda_s + \lambda_b + \lambda_{dcr}}{N_r} e^{-\left(\frac{\lambda_s+\lambda_b+\lambda_{dcr}}{N_r}\right)} \qquad (7.21)$$

$$P_{\lambda_{nn}} = \frac{\lambda_{ln} + \lambda_b + \lambda_{dcr}}{N_r} e^{-\frac{\lambda_{ln}+\lambda_b+\lambda_{dcr}}{N_r}} \qquad (7.22)$$

Once a single-photon event arrives at an SNSPD's element, the measured dead time τ_d parameter, which is ~20 ns, should be also considered. Consequently, the train of SNSPD's output RF pulses corresponding to detection of single-photon events cannot be described exactly with PPPs. However, depending on the requirements of a specific scenario, a higher number of SNSPD channels ($N_r > 2$) significantly decreases the influence of DT parameter. In other words, the Poisson distribution is considered as good enough approximation for the generated RF-pulse waveform. Nevertheless, the exact theoretical distribution of RF pulses is not an objective in the context of the accomplished simulations and it is not necessary to be further taken into account. In particular, the most crucial part is the modelling of SNSPD receiver unit including blocking model based on two states Markov chain processes showed in ***Figure 7.15***. On the one hand, the state "0" corresponds to a non-detected single-photon event, namely unblocked SNSPD channel. On the other hand, state "1" corresponds to an already detected single-photon event and consequently a blocked SNSPD element for the duration of the dead time. In accordance

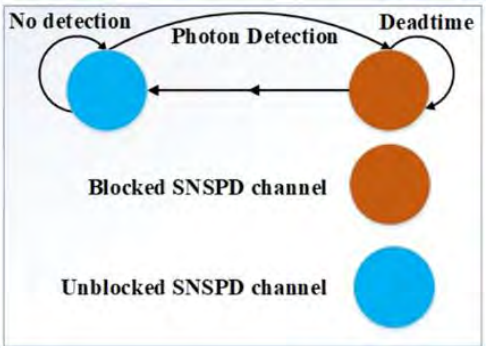

Figure 7.15: Blocking model of a SNSPD element [82]

with PPPs, the probability to stay in unblocked state is μ_0=e$^{-\lambda/Nr}$, which is calculated for k = 0. In case τ_d of SNSPD receiver as well as its non-blocked RF pulse rate l are considered, the probability for unblocked state is calculated with Eq. (7.23) ***[148]***.

$$\mu_0 = \frac{1}{1+\tau_d l} \quad (7.23)$$

Regarding the current simulations, this theoretical representation of the SNSPD blocking behaviour is based on timers. Once the SNSPD behaviour is treated with Markov processes and PPM symbol is detected in respect to a single photon (***Figure 7.16***), the specific shape of an output RF SNSPD's pulse is mathematically modelled with an empirically based Eq. (7.24) ***[148]***. Its features are fully dependent on the provided model in ***Figure 7.2 b)***, which describes the basic operation of one SNSPD element.

Figure 7.16: PPM frame after SNSPD detection [82]

$$w(t) = \begin{cases} 0 & t < 0 \\ \dfrac{V_p}{1-\frac{1}{e}}\left(1 - e^{-\frac{t}{\tau_1}}\right) & 0 < t < \tau_1 \\ V_p e^{\left(-\frac{t-\tau_1}{\tau_2}\right)} & t > \tau_1 \end{cases} \quad (7.24)$$

In order to model the exponential RF pulses, the maximum voltage peak V_p is assumed to be equal to 740 mV. Moreover, τ_1 and τ_2 are two time constants of decay, which sum $\tau_1 + \tau_2 = \tau_d$ is equal to the 20 ns dead time analogous with the performance of the selected SNSPD receiver unit. In accordance with SNSPD phenomenological model (***Figure 7.2 b)***), the waveform of SNSPD's RF pulse is determined in terms of load impedance R_0 = 50 Ω, a self-calculated inductance L and a resistive impedance R = 500 Ω when the switch is opened. Having introduced these three parameters, the time constants τ_1 and τ_2 are calculated by the following two equations: $\tau_1 = L/(R+R_0)$ and $\tau_2 = L/R_0$ (***[131]***). The simulation result based on Eq. (7.24) of a single RF pulse for all introduced parameters is shown in ***Figure 7.17***, while the generated pulse train before and after the antialiasing low-pass filter is given in ***Figure 7.18 a)*** and ***b)***. In addition, a single output pulse after the convolution operation between the impulse response of the initializing filter and simulated waveform of a single RF pulse (***Figure 7.17***) is given in ***Figure 7.18 c)***.

In order to address the developed model, simulations are performed. The applied parameters of the simulated deep space FSO communication scenario are provided in ***Figure 7.19***. Their values are carefully selected in respect to all previous considerations. An exception is made with τ_d = 4 ns, which is given only for a comparison. In accordance with LLCD and ***[11]***, the output optical power is assumed to be 0.5 – 10 W. Moreover, typical daytime measured value for background noise at ESA Teide Observatory is 150 pW (***[149]***) corresponding to P_b = 0.68 (ph/ns) [dB] (~0 (ph/ns) [dB]), which is clear objective to the obtained low-performance SNSPD. For this purpose, P_b = -15 (ph/ns) [dB] is also considered. This value is suited to Mars-Earth link with minimum -28 (pn/ns) [dB] noise given in ***[62]***.

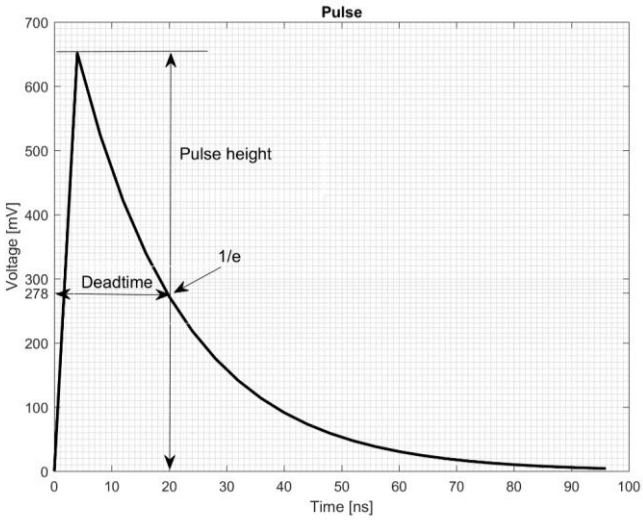

Figure 7.17: Simulations of an output SNSPD RF pulse based on τ_d = 20 ns (Modified figure based on own publication [82])

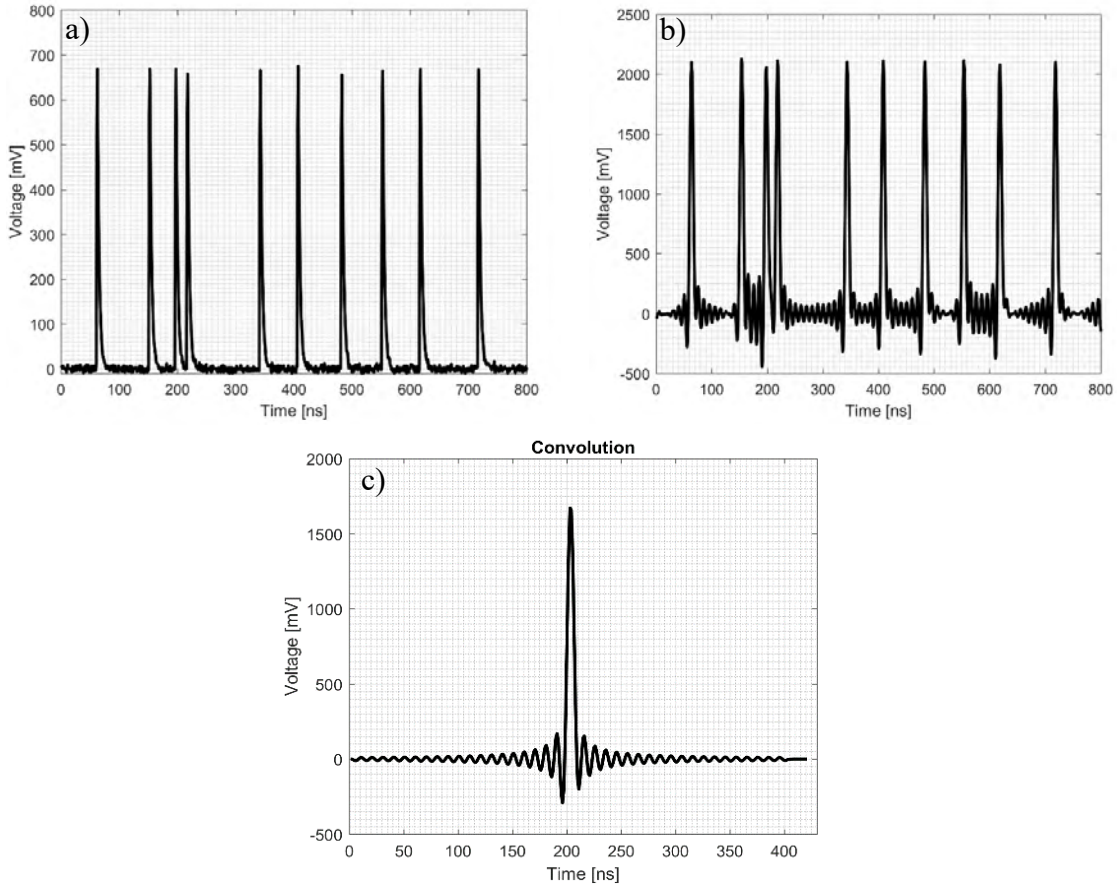

Figure 7.18: Simulations of an output SNSPD RF waveform: a) Output pulse sequence before the antialiasing low-pass filter; b) Output pulse train after the antialiasing low-pass filter (Figures a) and b) are obtained from own publication[82]); c) A single RF pulse waveform after the antialiasing low-pass filter

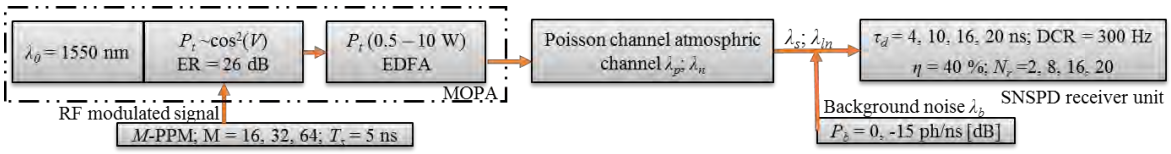

Figure 7.19: Block scheme of the modelled HPE deep space FSO downlink

The simulation results based on the proposed system parameterization in ***Figure 7.19***, are shown in ***Figure 7.20***. The assumed default values corresponding to the obtained SNSPD are $N_r = 2$, $\tau_d = 20$ ns and $P_b = -15$ (ph/ns) [dB] as well as $M = 16$ with $T_s = 5$ ns. It is evident that the system performance improves with increasing the PPM order M and SNSPD's N_r as well as reducing τ_d and P_b.

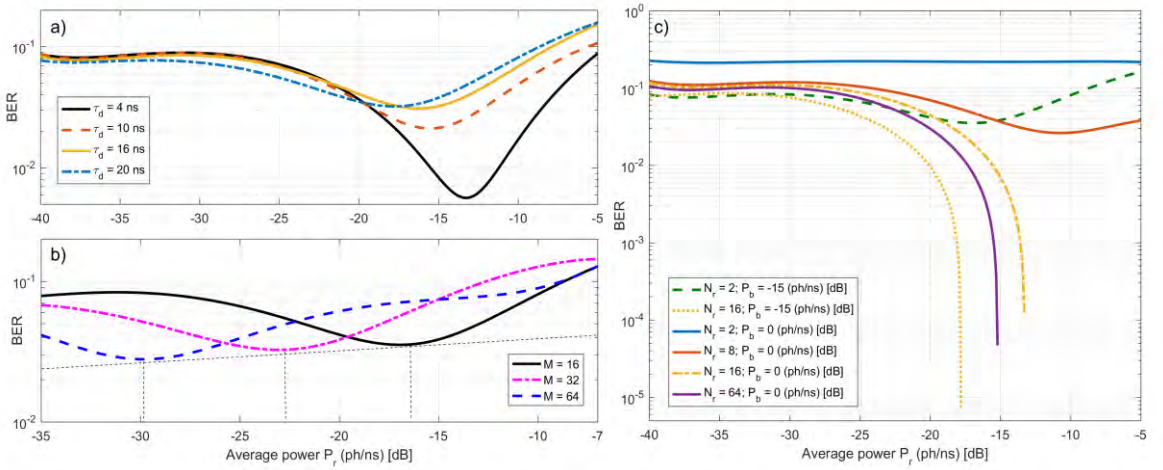

Figure 7.20: BER performance of the modelled deep space FSO communication link in terms of a) dead time τ_d b) PPM order M c) number of SNSPD elements N_r and background noise P_b

In conclusion, the obtained low-performance SNSPD system is greatly vulnerable to background noise and to all kind of stochastic influences. In order to reach better BER values, the assumed background noise in the simulated scenario in **7.4.6** is -15 (ph/ns) [dB], while the PPM slot width T_s is increased from 5 ns to 10 ns. The proposed T_s in ***[62]*** is between 0.5 – 8 ns which well coincide with the selected values. Nevertheless, the signalling parameter set for the simulated deep space FSO communication scenario is given in **7.4.6**.

7.4.5 Simulation-parameter set complied with LLCD mission

In order to keep the main emphasis on atmospheric turbulence-induced fading along with the chosen SNSPD receiver unit, a signalling parameter set is selected to provide only the basic performance of a real deep space FSO communication system. Both the successful demonstration of an optical link between Moon and Earth (LLCD) as well as CCSDS standards are taken into account during the made assumptions. In accordance with CCSDS standards (**Subchapter 7.2**) and similar to the verified deep space FSO link during LLCD,

the selected modulation technique is M = 16 PPM *[72]*. Due to considerably shorter distances, the time duration of a PPM slot for LLCD mission nearly reaches the absolute minimum of the recommended values in the CCSDS standards, namely T_s = 0.2 ns. In expense of data rate, the maximum time duration of a PPM slot for LLCD is T_s = 3.2 ns. Since the current thesis aims to test deep space FSO communication links based on the obtained low-performance 2-array SNSPD as well as no additional coding and interleaving, the selected PPM time slot width T_s is 10 ns. In particular, this is a direct result from the conclusions in respect to ***Figure 7.20***. While T_s = 10 ns still allows sufficient data rate of 20 Mbps, this parameter completely complies with the main task for evaluation of space-to-ground FSO downlinks beyond Moon distance (e.g., Mars/Venus-to-Earth at $z_d > 10^7$ km), which operate in the presence of atmospheric turbulence-induced fading.

Having addressed the aforementioned considerations, coding, interleaving and synchronization are not applied in the current work. In other words, the parameters including code rate r, rows N_u and shift register length increment B_u of the channel interleaver are omitted. In addition, PN-spreading technique is implemented but due to concerns for unnecessary complexity, the PN-spreading factor F_{pn} obtains the lowest possible value, namely 1. Finally, the recommended 25 % Guard Slots (GS) in CCSDS standards from the selected PPM order M, which are of high importance in terms of combating SNSPD dead time restrictions, are inserted.

CCSDS standards – simulation parameters	
Order of PPM modulation	16
PPM slot width	10 ns
PN-spreading factor	1
Shift register length increment B_u	N/A
Rows N_u	N/A
Code rate	N/A

Table 7.3: Simulation parameter set complied with CCSDS standards

The applied system parameters are provided in ***Table 7.4***. Having in mind the MOPA architecture, the utilized CW laser is featured with λ_0 =1550 nm and the ER of the intensity MZM is 26 dB, which is an average value within the defined range of 23 – 30 dB (**Subchapter 7.4.4**). Furthermore, the FSO system's limitations shown in ***Figure 7.20*** results in background noise with P_b = -15 (ph/ns) [dB]. Atmospheric turbulence-induced fading is implemented based on the performed analysis in **Chapter 6** offering scintillation data for the location of Vienna, Austria featured with $10^{-15} < C_n^2 < 10^{-16}$. In addition, aperture diameters R_d of most space-to-ground optical telescopes used mainly for GEO-satellite feeder links are between 27 cm to 1.5 m *[125]*. Nevertheless, a deep space FSO communication downlink requires optical antennas with larger apertures, which exceed 7 m *[126]*. In accordance with *[126]*, the optimal telescope diameter for ultra-long-distances is 8 m < R_d < 10 m. Consequently, two different aperture types are implemented: R_d = 1.5 m corresponding to OGS of NICT, Tokyo, Japan as well as deep space communication telescope with R_d = 8 m. In accordance with *[109]* and **Chapter 6**, the elevation angle of ground-to-deep-space link should be greater than 20°, which prevents the link to propagate

through large amount of tropospheric air mass allowing smaller fraction fade time parameter. Consequently, the elevation angle is selected to be between 20° and 30°.

Simulation – parameters	
SNSPD's DT	20 ns
SNSPD's DCR	300 Hz
SNSPD output pulse height	650 – 750 mV
SNSPD array	2, 6, 16
MZM – ER	26 dB
Data rate	20 Mbps
Turbulence attenuation	Up to 3.5 dB
Refractive index structure parameter C_n^2	10^{-15} – 10^{-16}
Elevation angle	20°, 30°
Receiver aperture	1.5, 8 m
Background noise	-15 (ph/ns) [dB]

Table 7.4: Simulation parameters including SNSPD, MZM, atmospheric turbulence-induced fading as well as OGS specifications

Finally, taking into account both the general SNSPD specifications and the measurements with the obtained SNSPD from Single Quantum Company, the applied characteristics of the considered single-photon receiver in the simulations are also provided.

7.4.6 Simulation of deep space FSO downlink – Results

The quantized nature of photons, which are the building elements of light leads to inherited uncertainty during transition, transmission and detection of the optical signal. Consequently, on the assumption of an ideal communication system with no noise, the system performance is again limited due to quantum noise and more specifically the light itself. Only at first sight, fluctuations within the amount of arrival photons are a random process. In particular, this behaviour is well described with PPPs, which are already introduced and defined in **Subchapter 7.4.1**. Although the investigation of the fundamental quantum noise limits is not of crucial importance for conventional FSO systems, it leads to restrictions in deep space HPE FSO communication. This means that each received photon matters for establishing a reliable photon starved communication link. While a certain quantum limit cannot be influenced in the name of having improved SNR (BER) performance, the utilized background noise (P_b = -15 (ph/ns) dB), leakage noise (ER = 26 dB) as well as DCR (DCR = 300 Hz) are optimized in terms of the drawn technological limits. In order to evaluate a deep space HPE FSO communication downlink including quantized nature of photons as well as accompanied noises, the developed SNSPD-based Poisson channel model summarized in ***Figure 7.9*** is applied. The simulations shown in ***Figure 7.21*** and ***Figure 7.22*** incorporates the findings in respect to the characterized SNSPD receiver, MZM performance, CCSDS standards, background noise as well as OGS parameters all provided in ***Table 7.3*** and ***Table 7.4***. Both figures prove the decent HPE FSO system performance until the leakage noise is raised, which is direct result from the increased average transmitted optical power P_t (average received optical power P_r) ***[82]***, ***[86]***. In this case, the graphs are curved in forward BER direction and the performance significantly degrades.

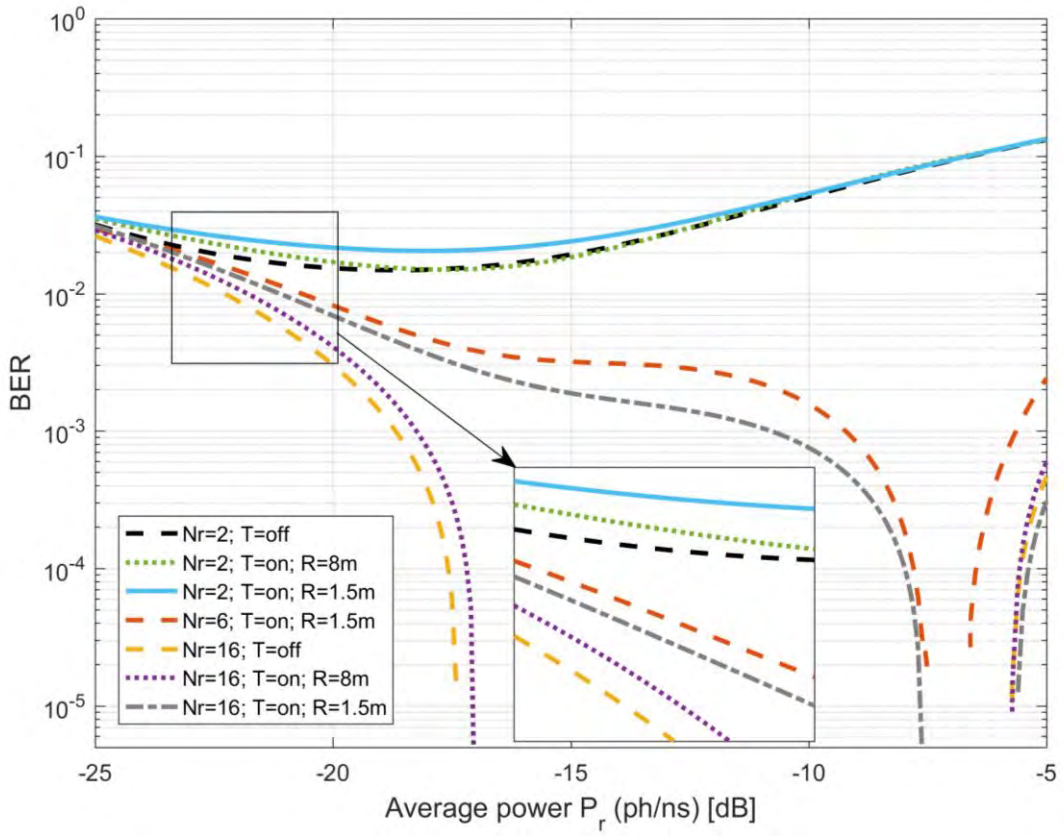

Figure 7.21: BER versus average received optical power for R_d = 1.5, 8 m and γ = 20° as well as SNSPD with Nr =2, 6, 16 (Modified figure based on own publication [86])

Nevertheless, the most significant emphasis regarding the carried out modelling is placed on the simulated clear-air atmospheric turbulence-induced fading (parameter T) in respect to space-to-ground FSO channels (**Chapter 6.2**). The self-simulated turbulence attenuation for minimum outage probability $P_{out} = 10^{-7}$ considering to OGS's apertures R_d = 1.5 m and R_d = 8 as well as an elevation angle γ = 20° is incorporated. For each iteration is selected a turbulence attenuation data sample based on its probability of occurrence, which is given by the created normalized attenuation histograms (Gamma – Gamma PDFs) in ***Figure 6.11*** and ***Figure 6.12***. Once this operation is accomplished and statistical averaging is performed, the results are shown in ***Figure 7.21***. It is evident that BER of the evaluated real N_r = 2 SNSPD cannot be decreased more than ~10^{-2}, which determines it is weakly dependence on the aperture averaging (R_d = 1.5 m R_d = 8 m) namely atmospheric turbulence scintillation strength. However, deep space downlink with N_r = 16 SNSPD elements already has an improved performance (BER = 10^{-5}) which for low noise and no atmospheric turbulence is assumed to be very near to the quantum limit. Having introduced atmospheric turbulence, the R_d = 8 m OGS offers high resilience to scintillations characterized with attenuation < 0.55 dB, which shifts the required average received optical power P_r from -17.7 (ph/ns) [dB] to -17.2 (ph/ns) [dB]. In case R_d = 1.5 m, the shift is already significant requiring instead -17.7 (ph/ns) [dB], P_r = -6 (ph/ns) [dB]. Besides, the dependence of atmospheric turbulence on two elevation angles (γ = 20° and γ = 30°) for R_d = 1.5 m is shown in ***Figure 7.22***.

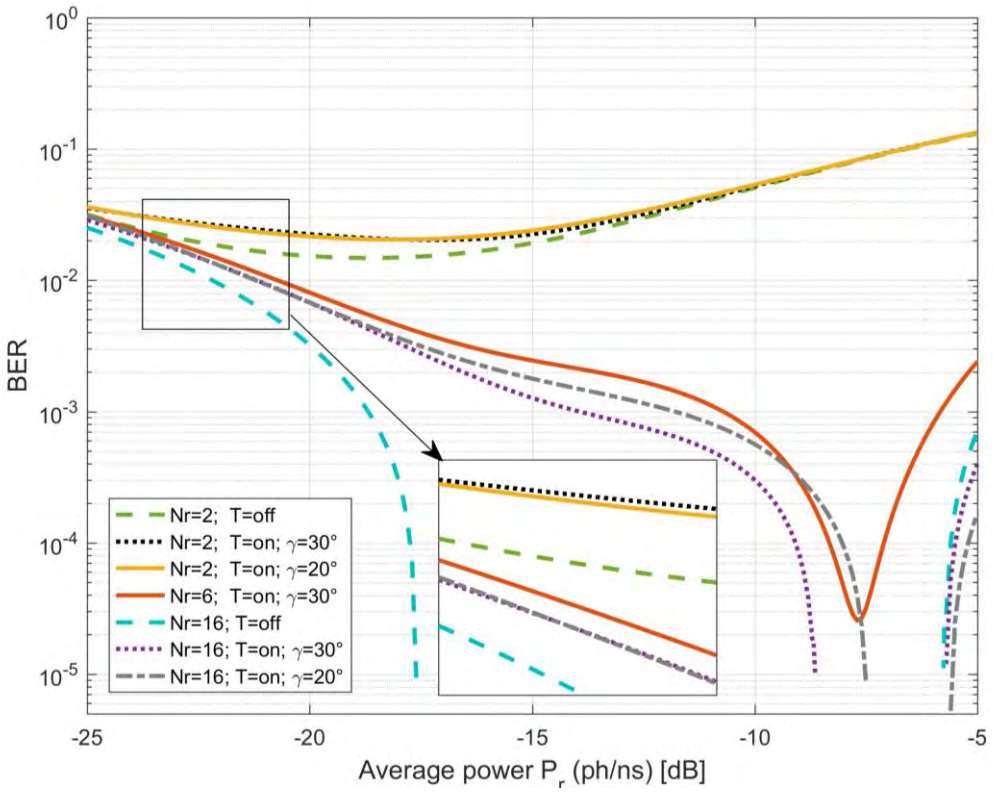

Figure 7.22: BER versus average received optical power for γ = 20, 30°and R_d = 1.5 m as well as SNSPD receiver unit with Nr =2, 6, 16 (Modified figure based on own publication [86])

When the elevation angle is increased from γ = 20° to γ = 30°, it is already noted significant difference in space-to-ground FSO downlink performance. While the behaviour for saturated N_r = 2 SNSPD is similar to ***Figure 7.21*** (without difference between γ = 20° and γ = 30°), increasing γ = 20° to γ = 30° in terms of N_r = 16 SNSPD leads to optical power gain of 2 (ph/ns) [dB]. In particular, the required received optical power for γ = 30° is -8 (ph/ns) [dB] and for the worst FSO communication case of γ = 20°, it is already needed -6 (ph/ns) [dB].

In order to have better evaluation of the achieved simulation results shown in ***Figure 7.21*** and ***Figure 7.22*** with maximum BER =10^{-6}, it is worth showing the quantum limits regarding photon-starved space-to-ground downlinks. The calculation of quantum noise requires assumption of perfect no other noise conditions. In other words, an error only occurs when no photons are detected during transmitted pulse slot. Taking into account PPPs (Eq. 7.9) for the case of NRZ OOK modulation, the probability for an error during an optical pulse is:

$$P(0) = \frac{{n_s}^0 e^{n_s}}{0!} = e^{n_s} \qquad (7.25)$$

Where n_s is another way to express λ_s, which corresponds to the average number of photons in an optical pulse slot. Considering (7.25) for NRZ OOK and a predefined BER value, the applied quantum limit regarding the minimum required number of photons n_{s_min} within an

optical pulse slot is calculated. The factor ½ in Eq. (7.26) is due to possibility for an error occurrence only during a pulse slot.

$$P(0/n_s) = BER = \frac{1}{2}e^{n_s} \quad \rightarrow \quad n_{s\_min} = \ln\left(\frac{BER^{-1}}{2}\right) \qquad (7.26)$$

Having in mind, the observed results in ***Figure 7.21*** regarding the carried out simulations for $N_r = 2$ SNSPD channels without atmospheric turbulence (T = off) and using uncoded 16-PPM signalling, the minimum achieved BER is 10^{-2}. In accordance with Eq. (7.26), the minimum required number of photons in terms of BER = ~10^{-2} for NRZ OOK is ~ 3.91 photons. Nevertheless, recalculations for the lowest allowed optical power is necessary due to applied PPM modulation of order M = 16. Taking into account the minimum distance between two symbols in terms of NRZ OOK and M-PPM, the increased optical power gain G_{ppm_soft} for PPM is calculated based on formula (7.27) ***[42]***.

$$G_{ppm\_soft} = \sqrt{\frac{M \log_2 M}{2}} \qquad (7.27)$$

Eq. (7.27) is derived for the current applied case of soft decision decoding leading to ~1.5 dB power gain in comparison with hard decision one ***[42]***. Taking into account the selected 16 PPM modulation technique, the $G_{16\text{-}ppm\_soft} = 5.65$. Consequently, the required minimum optical power for the applied soft decision 16-PPM modulation technique is $n_{s\_min} \log_2 M / 2G_{ppm_{soft}} = 1.38$ photon per transmitted PPM pulse and more specifically 0.34 photons per bit (PPB).

Having in mind Eq. (7.27), when the order M of PPM modulation is growing, the amount of PPB decreases without any noticeable limitation. Nonetheless, the Shannon capacity for photon-starved Poisson link is limited due to thermal noise. In particular, the constraint is defined based on ratio between thermal noise and energy of a single photon given in Eq. (7.28) ***[15]***.

$$n_{s\_min} = \frac{k_B T ln(2)}{h\lambda} = \frac{1.38\ 10^{-23} J/K\ 300\ K \ln(2)}{6.63\ 10^{-34} 1550\ nm} = 0.02\ PPB \qquad (7.28)$$

In the case of room temperature of ~300 K and optical wavelength of 1550 nm, the applied limit is 0.02 PPB. This limit is considerably lower for SNSPD systems, which is super-cooled and is operated at ~2 K cryogenic temperature. Moreover, the receiver telescope is pointed directly into the deep space lowering additionally the thermal background radiation, which for perfect conditions could be of ~ 4 K. Consequently, this allows Shannon limit to be additionally decreased hundreds of times. Nevertheless, for the investigated scenarios including 16 PPM, the calculated value 0.34 PPB is considerably larger.

In addition to the addressed power efficient 16 PPM modulation with soft decision decoding, the SNSPD array containing N_r detectors significantly lowers the influence of background as well as leakage noise. Since it is considered a case with multiple detectors, the system can be described as Single Input Multiple Output (SIMO) photon starved FSO link. Nonetheless,

for the firsts considered scenario with 2-channels SNSPD, the benefit of SIMO technique is considerably low. In other words, the established high noise floor due to background radiation as well as optical power leakage of MZM cannot be handled, which is the reason for the high BER value of at minimum 10^{-2}.

The carried out theoretical analysis complies completely with the simulation results, according to which the minimum attained BER for the 2 channel SNSPD require an average optical power of -18 pn/ns [dB] (-86.93 dBm) or ~4 photons per PPM pulse (-74.87 dBm). Considering the quantum efficiency of the available SNSPD (η = 40 %), the necessary photons per pulse decrease to 2 ph/pulse or in other words 0.5 PPB. The negligible difference with the observed theoretical calculations (0.34 PPB) is due background noise, which cannot be still handled by the N_{arr} = 2 SNSPD array. In the current case, dead time is not from significant importance due to the slot duration of T_s = 10 ns, which is half of the recovery time of SNSPD's nanowire.

To facilitate the analysis, the observed results for 2-array SNSPD are compared with a detector with 16 separated channels. Taking into account the quantum limit for the second scenario characterized with minimum BER = 10^{-5}, the lowest required number of photons for NRZ OOK modulation is 10.81. In particular, for 16 PPM combined with soft decision decoding, the optical power should be equal or higher than 3.83 photons per PPM pulse, which corresponds to 1 PPB. Addressing further the same case in the carried out simulations (***Figure 7.21***), namely deep space FSO channel with 16-array SNSPD without atmospheric turbulence (T = off), involves an average optical power of -17.7 (ph/ns) [dB]. After recalculation including 40 % efficiency of the obtained SNSPD, the system requires ~ 2 photons per PPM pulse. This result is twice lower than the quantum limit for BER = 10^{-5} provided in the theoretical analysis. The explanation is in the applied SIMO mitigation technique in the face of 16-array SNSPD. In comparison with 2-array SNSPD, the one with 16 channels lower the noise nearly to minimum. Nonetheless, this is not the case for a real deep space FSO link, which operates in the presence of atmospheric turbulence-induced fading. The simulations show that for a typical average aperture diameter R_d = 1.5 m and γ = 20°, the clear-air atmospheric turbulence ≤ 3.5 dB leads to penalties of -9.4 dB, which increases the optical power requirements to -7.8 (ph/ns) [dB] and corresponds to 34 photons per PPM pulse. The requirements for significant boost of the received (transmitted) optical power are due to package nature of the single photon communication combined with leakage noise. In case of an optimum aperture of 8 m diameter, the effect of atmospheric turbulence attenuation is negligible (0.5 dB).

Once the simulations for the considered deep space FSO scenario enclosing atmospheric turbulence fading (up to 3.5 dB) are verified based on quantum theory of light, a laboratory prototype of a real space-to-ground photon starved link is developed. In particular, the self-built breadboard in the frame of the current work has the objective to prove the operation of the obtained SNSPD detector in terms of the emulated real deep space FSO communication link in the present of adverse atmospheric conditions.

7.5 Deep space FSO laboratory testbed

The chapter is partly obtained from two own contributions ***[77]***, ***[85]***. The main objective of the breadboard, which is built within the thesis as a partial support to ESA's Hybridised Optical/RF Payload Data Transmitter study ***[77]***, is to emulate the performance of a real deep space HPE FSO downlink in the presence of impairments including Mie scattering, atmospheric turbulence as well as background noise. In particular, the testbed is built as close as possible hardware representation of a real deep space FSO downlink, simulated in **Subchapter 7.4**, which always has the core task to transmit as high as possible amount of telemetry data. The uplink, which in accordance with ***[71]***, consists of beacon used in Pointing, Acquisition and Tracking (PAT) systems as well as optional synchronization and control data transmission, is not considered. In order to achieve the aforementioned task, the breadboard partly reuses elements from the basic concept of two already carried out space-to-ground demonstrations, namely TESAT LCT space borne transceiver and the successful LLCD mission (***Figure 1.1*** and ***Table 1.1***). In addition, the breadboard implements the verified CCSDS standards from **Subchapter 7.2**.

In accordance with the CCSDS standards and the considered modelling in **Subchapter 7.4**, IM/DD technique is preferred instead the coherent one. The implemented detector is based on SNSPD technology, which was already well proven within the aforementioned LLCD mission incorporating photon counting receiver with N_r = 16, η = 60%, τ_d = 15 ns ***[132]***, ***[150]*** (***Table 7.2***). In order to represent a photon-starved optical channel, the testbed incorporates the developed deep space FSO downlink emulator operating based on fibre optics. In general, one channel of a commercial SNSPD is characterized with diameter less than 10 – 14 µm @1550 nm, which is best suited to Single Mode Fibre (SMF) with Mode Field Dimeter (MFD) of ~10 µm @1550 nm ***[131]***, ***[151]***. Comparing the results from ***[133]***, ***[151]*** and ***[152]*** for 1550 nm wavelength, there is an evident restriction for changing the diameter of the SNSPD's active area (nanowire's length) due to either deterioration of recovery time (10 – 16 ns) (increased nanowire) or efficiency (<< 90 %) (decreased nanowire). On the other hand, in ***[151]*** is reported an implementation of several-mode fibre solution with 20 µm MFD, which allows higher amount of optical power to be coupled into SNSPD receiver, estimated to 5.5 dB gain. Paralleling this method to previous attempts for multimode fibre coupling with 50 µm core in ***[152]***, shows ~30 % improvement in terms of SNSPD efficiency. However, the both methods are in expense of substantial technological complications, which required also custom modifications in SNSPD systems. Moreover, the dead time in ***[151]*** is τ_d = 12 ns at 1/e (25 ns at 90 %/10 %), which is an improvement in contrast to the SMF-coupled SNSPD with τ_d = 16 ns at 1/e (35 ns at 90 %/10 %) given in the previous NASA Glenn research centre work ***[133]***. Moreover, SNSPD receiver units produced by Single Quantum Company and characterized with larger 20 – 50 µm active areas are tested based MMF coupling in ***[153]***. While for the visible part of the spectrum it is characterized with η = 80 %, the 1550 nm NIR SNSPD has already only η = 50 %, which causes serious power penalties in contrast to η = 90 % with a SMF. Moreover, as it was discussed, a larger active area leads to deteriorated performance due to increased dead time parameter. In ***Figure 7.23 a)***, ***b)*** and ***c)*** are given the active areas of Single Quantum SNSPD with 20 µm and 50 µm diameter measured by Optics Research Group, Delft University of

Technology, while in ***d)*** is provided the photograph of the currently obtained Single Quantum SNSPD.

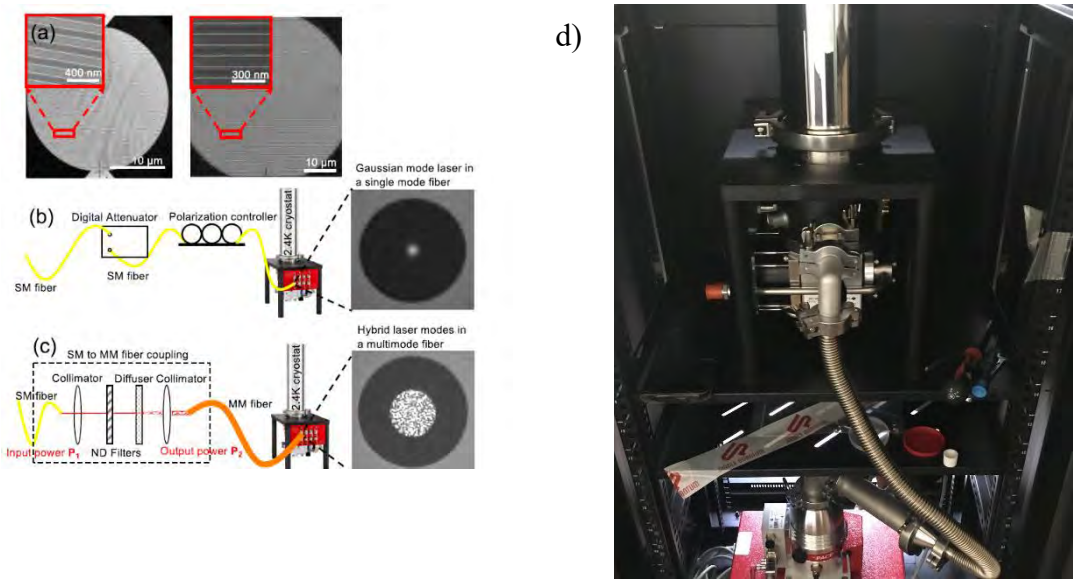

Figure 7.23: SNSPDs of Single Quantum Company: a) b) c) are taken from [153], which shows the active area of two types of SNSPD receiver units with diameter of 20 µm and 50 µm; d) Photograph of the obtained and investigated SNSPD

Taking into account the complexity of MMF, the self-developed breadboard design is based on SMF-28 fibre with 8.2 µm core diameter and *MFD* = 10.4 µm. This type of fibre supports better emulation of the genuine photon starved optical channel, which operates at 1550 nm wavelength. The reason is that FSO system functions in fundamental transverse TEM_{00} mode, which in the optical fibre is supported as linearly polarized LP_{01} mode. In other words, the laser beam of SMF system does not have fully Gaussian shape. However, based on appropriate coupling between laser and fibre, the fundamental Gaussian mode is launched into SMF with a η = 80% efficiency, which is a decent approximation of the real wireless optical channel ***[80]***.

Furthermore, a major objective of the current thesis in respect to selection of a SMF is the considered atmospheric effects (i.e. clear-air tropospheric turbulence). In a real deep space communication link, a small part of the optical energy, which is contained in TEM_{00} mode, is redistributed in higher-order modes due to atmospheric turbulence-induced fading. In other words, higher-order modes, which are larger than LP_{01}, appear in the optical fibre and require MFD up to 17 µm ***[151]***. In comparison with a MMF, these modes are normally not supported by selected SMF with MFD = ~10.4 µm. Nevertheless, due to limitations of the currently applied low-performance SNSPD receiver unit, an approximation that all power is concentrated in LP_{01} mode is assumed. This is completely satisfactory solution because the applied turbulence attenuation is simulated without considerations in terms of optical energy modes and it is directly applied on the transmitted optical power as a relevant attenuation value in [dB]. The block scheme of the developed breadboard is shown in ***Figure 7.24***, which is followed by a description of the testbed operation.

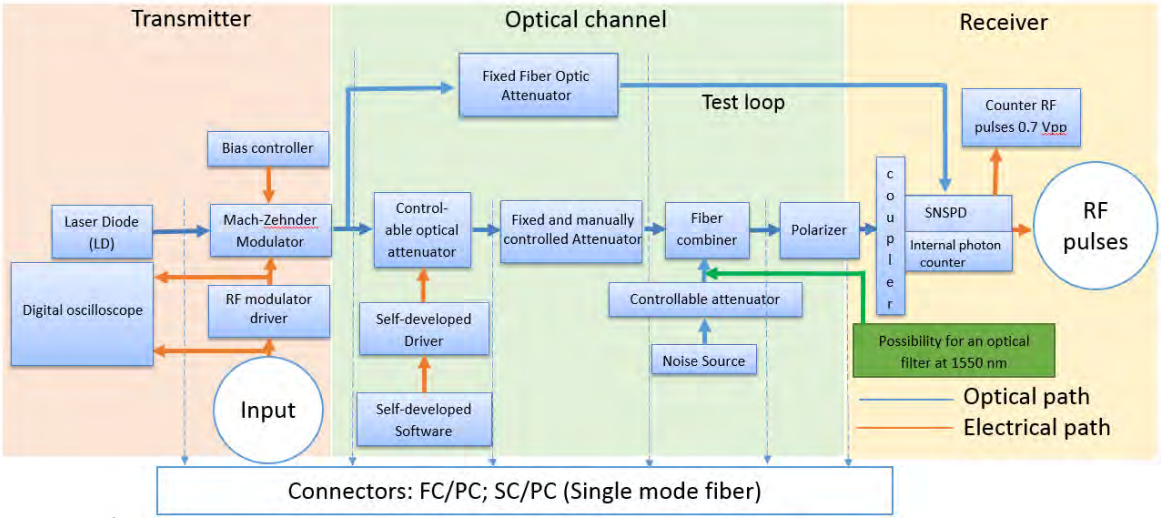

Figure 7.24: Architecture of the self-developed breadboard used for evaluation of real deep space HPE FSO communication links in laboratory conditions (The figure is obtained from own published report [77])

The main modules of the current breadboard include transmitter part, channel emulator and receiver part. In accordance with the performed simulations in **Subchapter 7.4**, the architecture of the transmitter is based on built-in external MZM setup comprising CW laser source, $LiNbO_3$ MZM, RF driver and Bias controller. In comparison with the applied external intensity modulation supporting up to 10 Gbps data throughput, the internally modulated lasers operate at no more than 2.5 Gbps. While, the maximum achieved data rates are not of key importance for the breadboard, the deep space FSO communication is based on very short PPM pulses leading to low bandwidth efficiency, which welcomes the offered performance by MZM. The CW laser is selected in terms of its wavelength (1550 nm) as well as output power. In general, the laser and MZM in a real deep space MOPA architecture is accompanied by EDFA, which for the case of the breadboard is not required. Therefore, the Distributed Feedback Laser (DFB) laser featured with maximum 10 dBm optical power is only chosen to comply with the requirements of the bias controller. Its operating current is 80 mA with threshold of 16 mA and maximum value of 100 mA. In respect to the reliable operation of DFB lasers, the laser unit incorporates a monitor photo diode. Consequently, a laser driver compiling with the N-type architecture of the photo diode and hence providing the required control feedback loop is incorporated. Moreover, the signal-processing unit, which is also part of the transmitter and delivers encoded SCPPM RF signal to the MZM is not part of current work but it is well considered and evaluated in the offered final report document in ***[73]***. The representation of a real FSO link incorporating the developed and tested VOA-based optical power regulator is used for static and dynamic control of the transmitted optical power within 0 – 50 dB range (max 0 – 60 dB). On the one hand, the later can play role of a channel emulator representing different static and dynamic atmospheric attenuation changes such as atmospheric turbulence-induced fading as well as Mie scattering (fog and clouds). On the other hand, the VOA together with the control driver is used as an optical power control as well as very slow optical modulator for testing the limitations and

tuning the selected SNSPD system. A polarizer, narrowband splitter together with SNSPD unit are the main building blocks of the receiver. The three paddles polarizer converts the random polarized light into linear one with the required orientation, which is already introduced in **Subchapter 7.3.3**. The narrowband ±15 nm 1x2 fibre splitter that offers splitting ratio of 50:50, divides equally the transmitted optical power into two linear polarized signals headed to the aforementioned $N_r = 2$ SNSPD (**Subchapter 7.3**).

Moreover, in order to emulate the real deep space FSO Poisson channel, only low amount of single photons should reach the photon-counting detector. In other words, up to three fixed attenuators, each characterized with 25 dB optical attenuation, are installed between the VOA and the SNSPD decreasing the transmitted optical power to a desired level. The last installed unit is an optical source representing the full Power Spectral Density (PSDen) of background noise including the influence of sun irradiance over the established HPE FSO link. The emulated noise by means of Tungsten-Halogen lamp with 2796 K colour temperature is mixed with the transmitted and attenuated optical signal in terms of ±15 nm 2x1 fibre combiner.

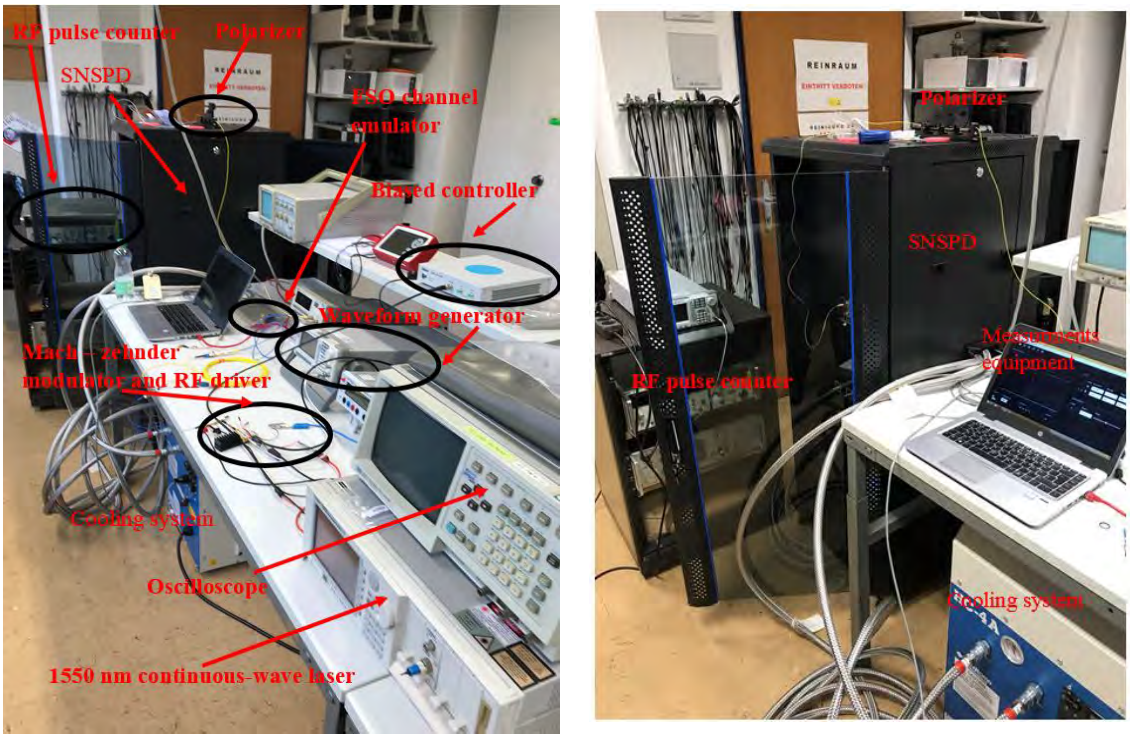

Figure 7.25: Photographs of the self-developed deep space FSO breadboard setup based on the architecture provided in Figure 7.24 (TU-Graz Optikom Lab)

7.5.1 1550 nm external Mach-Zehnder modulator

The standard fabrication materials of MZM are Lithium Niobat ($LiNbO_3$) and GaAs, which are especially well suited to space applications (both are considered in **Subchapter 7.4.4** in terms of ER parameter**)**. Although GaAs material is characterized with very high engineering tolerance in terms harsh deep space environment, its intrinsic features lead in most of the cases to ER < 26 dB (e.g., iXblue Company and More Photonics Company). In other words,

$LiNbO_3$ is applied in space borne FSO communication as a trade-off between stability and ER. Moreover, a new trend led to building MZMs based on concept utilizing a silicon (Si) photonics platform. The main advantages of a silicon photonic MZM are related to the increased integration density along with a low half-voltage length-product but their modulation depth is very low (3 to 5.5 dB), which makes them inappropriate for space applications ***[154]***, ***[155]***. This is the reason that research based on heterogeneous platforms including the advantages of Si and $LiNbO_3$ technologies emerged in the last years ***[156]***. The most important advantages of $LiNbO_3$ modulator are the high data rates allowing microwave signal up to 100 GHz modulation bandwidth, as well as a high modulation depth. The only disadvantage is the lower dependence of the $LiNbO_3$ refractive index on the applied voltage. In comparison with a Si MZM, larger half-wave voltage lengths are required. The other important parameters of $LiNbO_3$ MZMs are optical loss, switching voltage, modulator chirp, bias stability and microwave/RF scattering parameters such S11 and S21.

The $LiNbO_3$ MZM can be produced and set up in several configurations. Since the goal of the thesis is to determine one optimal solution for the specified testbed, all of them will be discussed. The topology of a MZM is either dual drive or single drive. In particular, $LiNbO_3$ crystal axes can have a different orientation in terms of MZM waveguides and electrodes. Based on these remarks, the main $LiNbO_3$ MZM configurations are dual drive z-cut, single drive x-cut and single drive z-cut. The key difference between the listed configurations are related to the overlapping between RF and optical field, which leads to different half-wave voltage and chirp values ***[157], [158]***. In the case for the developed breadboard, only the chirp characteristic will be considered as an important one in terms of the testbed architecture. When the system exhibits chirp in addition to the desired intensity modulation, then also a phase or frequency modulation will be available. In some cases, the induced chirp is used to decrease the dispersion effect in long haul fibre links. Although, the chirp is mainly of importance for larger distances and pulses < 100 ns, to assure enough high stability, the unchipped MZM is obtained, which is well-known practice in space (e.g., iXblue Company's MZM). In other words, since a deep space wireless optical link is tested in the context of the current work, only intensity PPM modulation is taken into account ***[77]***.

In case of the z-cut configuration, only the dual drive version can be chirp free. The requirements for this are: the applied voltages over the two arms should have equal amplitudes and be π (180°) out of phase. If these two conditions are changed, a chirp can be induced in the communication link. On the other hand, the single drive z-cut configuration will always exhibit chirp due to unsymmetrical overlapping between the two waveguides and the electrodes. This type of modulator has a chirp parameter equal to approximately 0.7. The latest version of the MZM, which will be mentioned is the x-cut single drive one. This configuration is intrinsically balanced meaning that both arms of MZM are fully symmetric ***[157]***, ***[158]***.

Although the dual drive z-cut configuration is a more sophisticated version in terms of possible adjustments, it is difficult to be stably configured as well as to be obtained an unchirped signal, since the operation of two drivers has to be very precisely synchronized. Regarding this fact, a single drive x-cut MZM is applied for the proposed testbed used for characterization of long-distance HPE FSO space-to-ground downlinks. In this way, better stability as well as chirp parameter equal to zero is implemented.

Based on the discussion above, the chosen MZM has to be with single drive *x*-cut configuration and to allow data rates up to 10 Gbps. This type of modulators are offered by company Thorlabs, namely Thorlabs LN81S ***[159]***. The operation wavelength is 1550 nm and the measured On-Off ER is up to 30 dB. While the bias voltage is between -8 V and 8 V, the RF driver voltage is in the range of 3 – 8 V. In addition, the maximum allowed input optical power is 20 dBm, which is double than the output optical power of the selected laser source (10 dBm). Typical for the MZM is that the electro-optics effect is characterized with $cos^2(V)$ function, which is defined based on driven voltage V_π for having the two arms of MZM in phase 0. Consequently, while phase shift of π corresponds to destructive interface, namely "off" state, the phase shift of 0 between the two arms leads to constructive interface featured with maximum transmitted optical power ("on" state). Moreover, the quadrature point in the middle of linear region of cos^2 shape curve is $V_p/2$. In particular for the case of PPM modulation, which is characterized with transmission of rectangular RF pulses, the required input switching RF voltage is between 0 V and V_p. Regarding the selected MZM, the chosen value is $V_p = 5.57$ V. Moreover, in order to operate the modulator in the linear region of cos^2 curve, the bias voltage has value corresponding to the introduced quadrature point. Having accomplished both requirements, it is guaranteed maximum ER, which according to the MZM specifications is 30 dB. The last important parameter is the optical insertion losses of a MZM, which for the LN81S is 4 dB. The MZM setup including CW 1550 nm laser, MZM, RF driver and Bias controller is provided in ***Figure 7.27***.

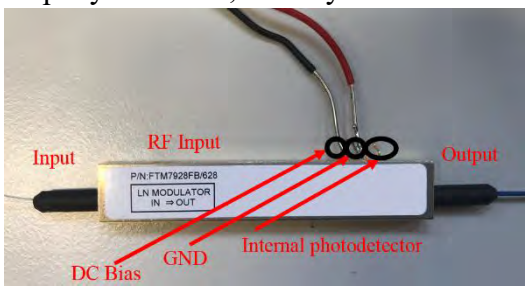

Figure 7.26: Thorlabs LN81S MZM [159]

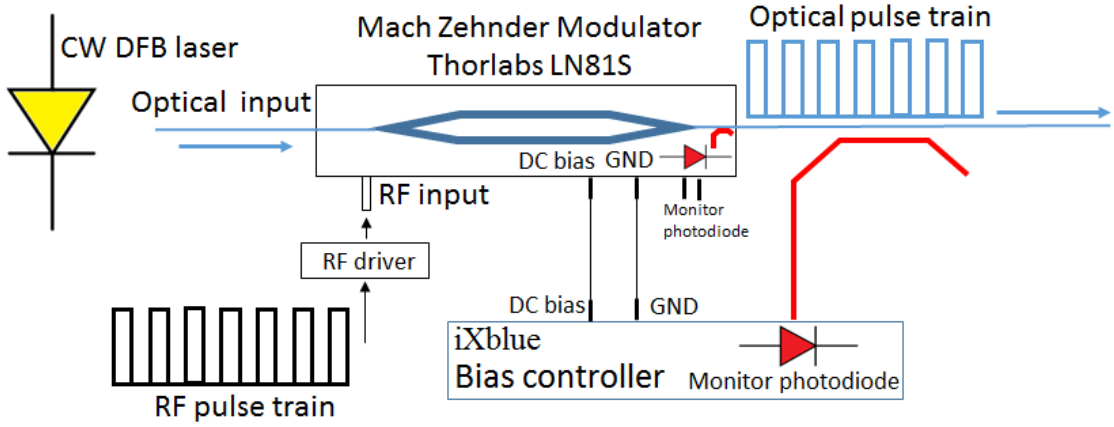

Figure 7.27: Configurtion of the Mach-Zehnder modulator setup icluding iXblue bias controller, Thorlabs LN81S MZM and iXblue RF driver (Self-drawn based on design of iXblue company)

In general, MZMs are produced to work for high data rates, which is also valid for the selected Thorlabs LN81S modulator. In according with **Subchapter 7.4**, the 2-array SNSPD

with dead time τ_d = 20 ns does not support data throughput more than 20 Mbps in normal operation conditions. Nevertheless, the PPM with its short pulses is a bandwidth inefficient modulation with significantly enlarged bandwidth requirements. To address, these considerations, the performance of MZM should be properly evaluated. In the following part, the main parameters and properties of the LN81S modulator are given:

1) In order to carry out preliminary evaluation of Thorlabs LN81S MZM for the required 20 Mbps data rates, the microwave/RF scattering parameters S11 and S21 are considered. As visible in ***Figure 7.28***, the two scattering parameters depend on the data frequency. According to the graphs, the modulator has a good performance for low frequencies (data rates) which is an important point in terms of the breadboard. The S11 graph shows that the reflected power is very low amount for frequencies around 50 MHz. On the other hand, the losses in terms of low data rates (S21 parameter) are less than 1 dB at 50 MHz.

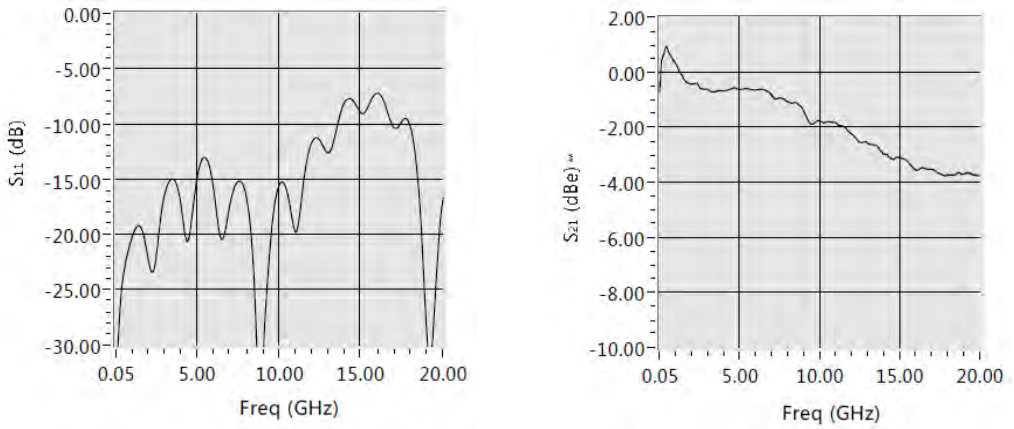

Figure 7.28: Measurements of S11 and S12 parameters of Thorlabs LN81S MZM (The figures are obtained from the device datasheet document [159])

2) In respect to the selected MZM, the ER is equal to 30 dB, which is also well-aligned with the used ER = 26 dB in the developed MATLAB model in **Subchapter 7.4**.
3) The selected Thorlabs LN81S modulator includes an equalizer, which acts like a high-pass filter with low frequency cut-off equal to 30 kHz. Generally, this is not a problem when the MZM operates at high data rates. In respect to low data frequency (related to data rates) under 30 kHz. This issue can be overcome by removing the equalizer which will eliminate the low frequency cut-off and the possible phase delay. However, this will lead to a larger difference in the drive voltage between 1 to 10 GHz.
4) In order to setup a precise value for the bias voltage, applied to the MZM, an appropriate bias controller from iXblue Company is used (***Figure 7.27***). Hence, the specific electrical-bias quadrature point on the modulator's transfer function graph, which is temperature-dependent, is maintained. In this way, the problem related to the voltage drift over time, which leads to performance issues, is solved. The selected

controller operates based on incorporated feedback loop including photodiode, which maintains locking stability featured with STD of 0.1. The supported bias voltage range between ±10 V completely complies with the selected MZM. Moreover, the maintained input optical power is between 0 dBm and 18 dBm.

The **subchapter 7.5.1** "1550 nm external Mach-Zehnder modulator" is partly obtained from the published within the current doctoral research own Report ***[77]***.

7.5.2 Representation of background noise due to solar irradiance

An important feature of the breadboard is representation of the background noise of a real deep space optical communication channel, which includes blue sky brightness as well as reflected irradiance from the observed celestial bodies. In particular, the noise is emulated based on two different optical sources namely Tungsten – Halogen lamp and a CW laser diode at 1550 nm. Both of them include controllable attenuators, which provide the possibility for tuning the output optical power. After a precise amount of background noise is set up, ±15 nm 2x1 optical coupler combines the background noise and the modulated communication signal and coupled them into the SNSPD. In case that a Tungsten – Halogen lamp with broad power spectrum is applied, optical filter with bandwidth < 0.1 nm before SNSPD is considered.

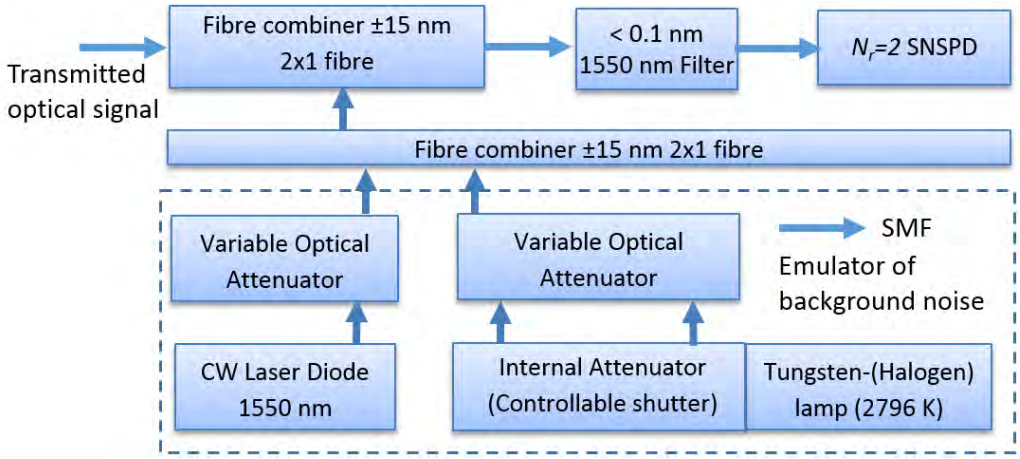

Figure 7.29: Self-accomplished design of solar background simulator

In order to emulate the Sun and the related blue-sky irradiance, the task should be theoretically evaluated. From a scientific point of view, the Sun is described with the properties of a black body as its surface temperature is 5500K with electromagnetic spectrum provided in Eq. (7.29).

$$B_\upsilon(T) = \frac{2h\nu^3}{c^2}\frac{1}{e^{\frac{h\nu}{kT}} - 1} \qquad (7.29)$$

Where the parameter υ is the frequency of the electromagnetic radiation. In accordance with Eq. (7.29) if the temperature of a blackbody is raising, the emitted PSDen increases. This leads to moving the overall emitted energy along with the radiation peak to shorter

wavelengths. In other words to represent the Sun in terms of Planck´s law, a light source with a proper spectrum and colour temperature has to be chosen. Consequently, its power spectrum density should overlap the blackbody energy spectrum as tightly as possible for the given temperature. However, the temperature has to have value closer to the sun colour temperature of 5500K.

The American Society for Testing and Materials (ASTM) published several standards related to sun radiation which reach planet Earth, namely standards for Air Mass (AM) 0, 1, 1.5, 2 etc. (***Figure 7.30***). The difference between them is in the terms of the zenith angle during the measurements, which leads to a different amount of air mass (atmosphere). The AM0 describes the sun spectrum outside Earth's atmosphere, which is important for most devices launched into space (e.g., satellites). However, for representing the sky irradiance, which is part of the accomplished work, also the influence of Earth's atmosphere is included. The later is taken into account in all solar spectral ASTM irradiance standards for an air mass equal or higher than 1. For instance AM1, is for zenith angle 0 characterizing the equatorial and tropical regions which are considered as a good option for the deep space link. On the other hand, AM1.5 provides the solar irradiance for zenith angle 48.2 degrees. Moreover, the measured spectrum can include Direct sunlight (D) as well as both direct and diffused sunlight (Global (G)). Both of them (Direct and Global) are influenced by molecules and particles in the Earth atmosphere. In other words, the atmospheric absorption and scattering effects lead to changing the AM0 spectrum to a modified AM1 and AM1.5 spectrums, including also the diffused light (sky radiance) in case of a Global standard (AM1G and AM1.5G) ***[161]***.

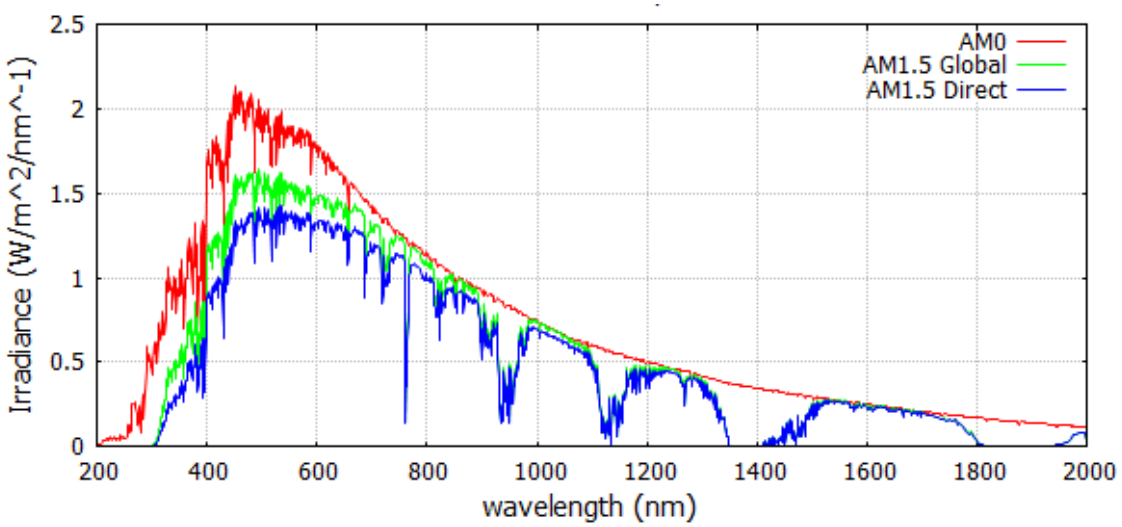

Figure 7.30: ASTM standards is respect to AM0, AM1.5 Global and AM1.5 Direct solar spectral irradiance (The figure is obtained from [160])

Together with the sky irradiance, the second factor, which significantly contributes to the background noise, is the false light coming from a specifically observed planet in the Solar system. In this work, a deep space HPE FSO communication link to two planets of highest interest during last decade namely Mars and Venus is considered. In particular, the surface

temperature of Venus is 744 K and Mars is 288 K. However, both Mars and Venus PSDen is roughly approximated by a black body with 277 K and 213 K temperature. Regarding Venus, the main reason for this enormous difference is the very high amount of CO_2 in the atmosphere. Similar to Venus, the atmosphere of Mars also conation mainly CO_2 gas. Nevertheless, the Mars atmosphere is extremely thin, which is the reason for the small difference between surface and effective temperature. In accordance with ***[162]*** the large amount of CO_2 for the both planets contributes to the strong absorption features in the middle infrared part of the spectrum.

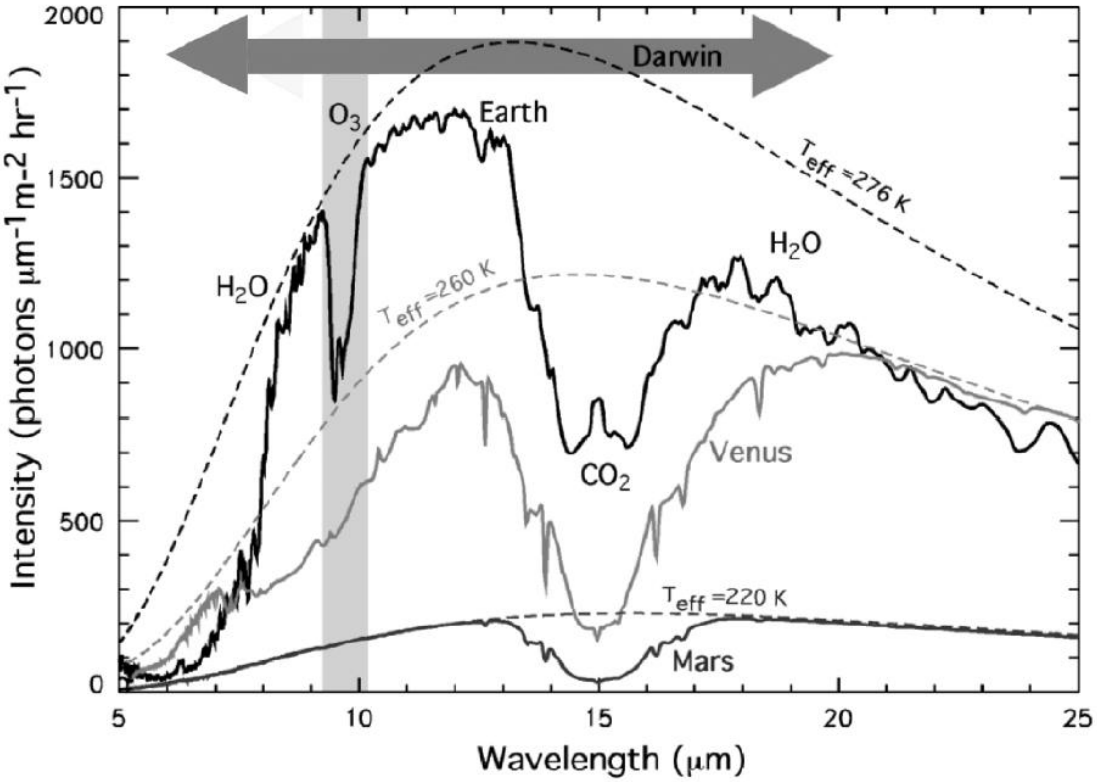

Figure 7.31: Mars and Venus spectral irradiance, where is indicated the spectrum of interest during DARWIN mission (The figure is obtained from publication [162])

Similar to the performed study by Jet Propulsion Laboratory in ***[163]*** regarding deep space RF communication links, two extreme scenarios in terms of space-to-ground FSO channels are considered. Due to the different position of both planets relative to the Earth, Venus is classified as an inferior and Mars as a superior one. Consequently, when Venus is in inferior conjunction, its contribution to the background noise can be neglected and only sky irradiance should be implemented. However, Mars is a superior planet and in times of inferior conjunction, the only contribution to the background noise is due reflected sun irradiance. Indeed, during inferior conjunction, Mars is situated on the opposite site of the Earth and the deep space FSO communication link is established in the presence of night sky when the sun influence is kept at minimum. On the other hand, when a superior conjunction happens, together with the sky irradiance, also reflected sun irradiance from both planets Mars and Venus should be considered. Furthermore, the reflected irradiance

values are higher than the sky irradiance due to the fact that false light reflected from Mars and Venus is directly entering the FoV of the detector.

There are different artificial light sources, which partly represent the power spectrum density of the sun. Unfortunately, the most utilized LED technology is not suitable for representing NIR part of the spectrum over 1000 nm. Nevertheless, Tungsten – Halogen lights, which accurately represent the AM0 NIR part of the spectrum over 900 nm is the source of interest for current work. The most significant advantages concern the property of Tungsten, which operates very close to its 3380 °C melting point. In other words, the ordinary Tungsten lamps typically have 2700 °C filament temperature.

Although Tungsten – Halogen light is well suited to the NIR spectrum, it cannot represent the visible spectrum adequately. This is due to the low melting point of the Tungsten, which delivers a colour temperature of about 3350 K. However, the Sun is considered as a black body with colour temperature of around 5500 K. Consequently, according to Eq. (7.29), this low value of the Tungsten-Halogen lamps is the reason that the overall spectrum is moved to the longer (NIR) wavelengths. Hence, different combinations between the sources are used. The authors in ***[164]*** construct a simulator, which has to match the visible portion of the global solar spectrum in terms of the AM1.5G standard. The simulator is based on a LED-array configuration, which includes six different light sources operating on different wavelengths. The spectrum is controlled by a self-developed GUI and a digital signal processor which applies the desired current values related to the required AM1.5G solar spectrum specifications. Another solar simulator is presented in ***[165]***, where the terrestrial spectrum of AM1.5G is supplied by 6 LEDs for the visible part of the spectrum and Halogen lamp for the NIR one. The main advantage here is related to the Halogen lamps. Their intensity radiation can easily cover the NIR AM1.5G spectrum up to around 950 nm, which is not a simple task for LEDs.

Having in mind that the current breadboard operating at 1550 nm wavelength, the chosen solar simulator has to deliver a well-suited NIR spectrum below and around 1550 nm respectively. In addition, the influence of the visible spectrum in terms of the current model should be excluded due to the selected 1550 nm wavelength. However, the main goal of the two solar simulators described above is to cover the spectrum range around 300 – 1000 nm. Although they delivered a spectrum, which is a good approximation of the AM1.5G standard, their performance beyond 920 nm decreases. One reason is the impossibility LEDs, which match precisely enough the AM1.5G NIR spectrum, to be produced. On the other hand, the Halogen lamps with their continuous blackbody NIR radiation are very suitable for the solar range around 950 nm. However, AM1.5G NIR solar radiation over 950 nm must also represent the scattering and absorption processes in the atmosphere, which cannot be cover by a normal Halogen lamp. In other words instead of AM1.5G, AM0 solar spectral irradiance defined in ASTM E490 standard (***Figure 7.30***) is provided which allows breadboard to be tested under more extreme conditions in terms of the full sunlight spectrum. Similar solar simulator representing the AM0 NIR spectrum is provided in paper ***[166]***. In comparison with the previous ones (AM1.5G solar simulator), it simulates the AM0 spectrum, which does not include the atmospheric influences. This simulator is again based on LEDs for the visible part and Tungsten – Halogen for the NIR part of the spectrum. The Mars and Venus NIR spectrum are already completely included in the simulated AM0 NIR spectrum with the proposed Tungsten – Halogen lamp. ***Figure 7.31*** also proves this fact, where it is evident that the Mars and Venus spectrum can be represented by a black body

with 213 K and 277 K temperatures, which are considerably lower than the sun temperature of 5500 K.

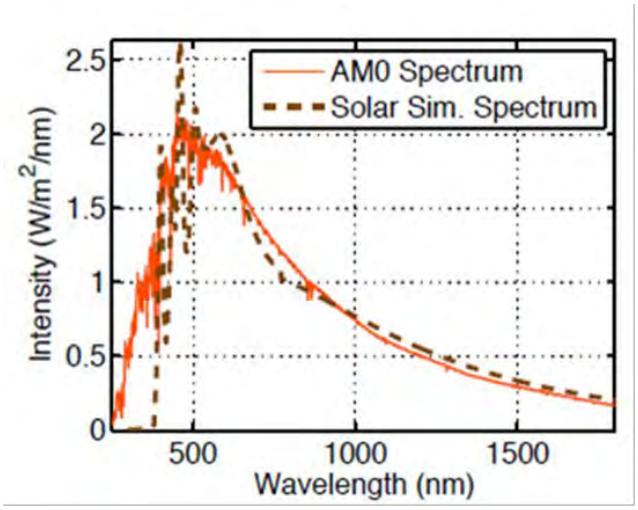

Figure 7.32: AM0 solar simulator based on Tungsten – Halogen lamp (The figure is obtained from publication [166])

The chosen light sources is Quartz Tungsten – Halogen from Thorlabs (SLS201L) (***[167]***), which operates at 2796K colour temperature with deviation of ±15 K. Although this temperature is lower than the sun colour temperature of 5500K, this is a good representation of the NIR spectrum up to 2600 nm with peak wavelength of 1000 nm. This device includes a special housing in which the Tungsten – Halogen is installed. The light from the bulb is directed towards a collimator and coupled into multimode fibre-optics patch cables, which have a large core diameter of around 400 µm (***[167]***). This characteristic allows the transmission of multi wavelength optical signals corresponding to the Tungsten – Halogen lamp's output broad spectrum. In addition, this fibre provides enough optical power. Nevertheless, the design of the current testbed requires SMF-28 fibre instead of a multimode optical patch cable. This substitution leads to significant penalties calculated with Eq. (7.30).

$$P_2 = P_1 \left(\frac{d_{c2} NA_2}{d_{c1} NA_1} \right)^2 \quad (7.30)$$

While P_1 is the coupled optical background noise in terms of a multimode fibre optic patch cable, the P_2 is the coupled optical background noise for SMF. In particular, the measured value for P_1 is equal to 10 dBm for the entire wavelength range and -22.54 dBm for operation wavelength of 1550 nm (***[167]***). In addition, d_{c1} and NA_1 are the core diameter and the numerical aperture which for the used multimode fibre optic patch cable are equal to d_{c1} = 400 µm and NA = 0.39. The numerical aperture is related to the acceptance angle of the fibre and it is dependent on the index of refraction and the maximum half angle of an incident beam. Respectively d_{c2} and NA_2 corresponding to the newly applied single mode 1550 nm fibre. The NA and d_c characteristics of two different single mode fibres together with a multimode fibre optic patch cable are provided in ***Table 7.5***. Based on them, the available total received background noise is calculated. Moreover, its value for the wavelength of interest (1550 nm) is also given.

Fiber type	d_c	NA	Coupled background noise power	Coupled background noise power for 1550nm
Fiber optic patch cable	400 µm	0.39	10 dBm (P_1)	-22.54 dBm
Single mode 1550 nm fibers	10 µm	0.1	-33.86 dBm (P_2)	-66.4 dBm
	8.5 µm	0.13	-32.99 dBm (P_2)	-65.53 dBm

Table 7.5: SMF-coupled background noise power based on SLS201L Tungsten – Halogen lamp at 1550 nm wavelength (The table is obtained from own report [77])

This restriction significantly decreases the applied optical power. It is important to be mentioned that in case of the provided breadboard, the background noise power should be precisely controlled for 1550 nm wavelength. In other words, a second laser source with 1550 nm in combination with a Tungsten – Halogen lamp operating at 10 dBm optical power is provided.

The **subchapter 7.5.2** "Representation of background noise due to solar irradiance" is partly obtained from the published within the current doctoral research own Report ***[77]***.

7.6 Link budget estimation for deep space FSO downlink

Given LLCD parameters	Value	Recalculated LLCD parameters	Value
Average transmitted optical power P_t	0.5 W	Transmitted power (EDFA) P_t	1 W
FWHM divergence angle θ_{FWHM}	16.2 µrad	Divergence angle θ_t (at $1/e^2$)	13.72
Aperture diameter R_d	4 x 0.4 m	Aggregate aperture diameter R_d	0.8 m
Link distance Earth -> Moon	400000 km		
Downlink wavelength λ_0	1550 nm		
SNSPD efficiency (LLCD mission) $\eta_{60\%}$	60 %		
SNSPD efficiency (Single Quantum Company) $\eta_{40\%}$	40 %		

Table 7.6: LLCD parameters of the established HPE FSO communication link

Having addressed the hardware representation of space-to-ground HPE FSO channel in laboratory conditions, a closure investigation of the link budget is required. Taking into account that the implemented OGS detector unit is the state-of-the-art SNSPD, the findings within LLCD are considered. Furthermore, scenarios including larger communication distances, which pose higher limitations regarding received optical power, are examined. This includes the foreseen in near future Mars-to-Earth and especially Venus-to-Earth communication links. In particular, similar to the previous considerations, the uplink is excluded and only the downlink budget is calculated. Unfortunately, the available literature does not provide full data regarding the downlink budget of LLCD, which requires a self-made analysis to be performed based on available parameters values from several well-known references ***[72]***, ***[74]***, ***[75]*** and ***[143]*** (***Table 7.6***), the most important of which were already introduced in ***Table 1.1***. Having in mind ***[72]***, the ground receiver has 4 identical

apertures with diameter of R_d = 0.4 m. In accordance with the aggregate aperture rule in ***[127]***, which is especially applied in deep space FSO communication, the aggregate diameter for such an array with negligible number of relatively large antennas is sum of all antennas, namely R_d = 0.8 m. Furthermore, the provided value for FWHM divergence angle in ***[74]*** is 16.2 μrad. Nevertheless, the link budget calculations require the half divergence angle to be determined for Gaussian beam radius at $1/e^2$ point. Having applied $\theta_t = \theta_{FWHM} / 1.18$ law, its value for the LLCD's space borne unit is 13.72 μrad. Moreover, the generated optical signal based on an external MZM modulator and the following amplification in EDFA unit is characterized with average power of 0.5 W at 1550 nm operational wavelength ***[72]***. Considering the already introduced doubling in case of Gaussian beam, the transmitted power is 1 W, which corresponds to 30 dBm power. Last but not least, the considered average communication distance between Earth and Moon is 400000 km.

Parameter – Moon -> Earth	Value	Parameter – Mars -> Earth	Value
Transmitted power P_t (EDFA)	30 dBm	Transmitted power P_t (EDFA)	43 dBm
Transmitted antenna gain G_t	103.1 dB	Transmitted antenna gain G_t	106 dB
Receiver antenna gain G_r	124.2 dB	Receiver antenna gain G_r	144.2 dB
Free-space losses L_{path}	-310.2 dB	Free-space losses L_{path}	-370.2 dB
Scintillations – mean value	-4.23 dB	Scintillations – mean value	-0.36 dB
Cirrus clouds	-2.56 dB	Cirrus clouds	-2.56 dB
Transmitter losses T_{th}	-4.5 dB	Transmitter losses T_{th}	-4.5 dB
Receiver losses T_r	-3.2 dB	Receiver losses T_r	-4 dB
Antenna R_d = 0.8 m	-1 dB	Antenna R_d = 8 m	-1 dB
Polarization	-4 dB	Polarization	-4 dB
Average optical power at OGS	-72.39 dBm	Average optical power at OGS	-93.42 dBm
Beam splitting (2-SNSPD array) and SMF insertion loss	-0.8 dB	Beam splitting (2-SNSPD array) and SMF insertion loss	-0.8 dB
SNSPD with N_r = 2	-3.01 dB	SNSPD with N_r = 2	-3.01 dB
Average optical power at SNSPD	-76.2 dBm	Average optical power at SNSPD	-97.23 dBm
SNSPD efficiency (60 %)	-2.21 dB	SNSPD efficiency (60 %)	-2.21 dB
SNSPD efficiency (40 %)	-3.97 dB	SNSPD efficiency (40 %)	-3.97 dB
Received optical power with η = 60 % SNSPD element	-78.41 dBm	Received optical power with η = 60 % SNSPD element	-99.44 dBm
Received optical power with η = 40 % SNSPD element	-80.17 dBm	Received optical power with η = 40 % SNSPD element	-101.2 dBm

Table 7.7: Link budget calculations for shorter Moon to Earth as well as longer-distances Mars to Earth HPE FSO communication link

Having in mind the available LLCD specifications in the literature as well as the above self-performed analysis, the final necessary parameters for the calculation of the link budget are also provided in ***Table 7.6***. This allows all parameters including transmitter gain, receiver gain and path losses to be estimated with the derived link budget in **Chapter 2** (***Table 7.7***). Moreover, in accordance with ***[143]***, also system losses incorporating optical power penalties in the transmitter (~4.5 dB) and receiver (~3.2 dB) as well as a loss due to optical fibre coupling (1 x 2 beam splitter = 0.6 dB) and an insertion loss of SMF fibre (2 x 0.1 dB) are implemented. The average mean attenuation due to Mie scattering (Cirrus clouds) is

obtained from the simulations in **Subchapter 5.1.1**, which is 2.6 dB. Moreover, the simulated mean attenuation value regarding clear-air atmospheric turbulence scintillations for R_d = 0.8 m in respect to the used model in **Chapter 3** is 4.23 dB. Nonetheless, one of the main objectives regarding current thesis is to consider deep space communication scenarios characterized with larger distances than LLCD mission, namely Mars-to-Earth and Venus-to-Earth FSO downlinks. While the maximum deep space channel distance for Venus is 1.73 A.U. (~260 000 000 km), in the case of Mars the distance is~2.67 A.U. (~400 000 000 km). Consequently, for such extremely long-path HPE FSO communication links, a significant improvement of the aforementioned LLCD specifications should be carried out. Taking into account the specifics of long-distance mission to Venus ***[68]***, the half width divergence angle is decreased to 10 μrad. In addition, the average transmitted optical power at output of EDFA is increased to 10 W namely 40 dBm. When the optical beam is with Gaussian amplitude profile, the transmitted average optical power for perfectly alighted deep space FSO link is 20W or 43 dBm. The simulated transmitter and receiver antenna gains as well as free-space loss parameters are shown in ***Figure 7.33***. Each of them is investigated between the drawn limits of the shorter Moon-to-Earth and larger Mars-to-Earth link distances. In particular, transmitter antenna gain G_t versus divergence angle θ_t (10 – 14 μrad) is shown in ***Figure 7.33 a)***; the free-space path losses versus link distance z_d (1.73 – 2.67 AU) are depicted in ***Figure 7.33 b)***; and finally the receiver antenna gain G_r versus ground aperture diameter R_d (0.8 – 8 m) is given in ***Figure 7.33 c)***.

Parameters – Moon -> Earth	Value	Parameters – Mars -> Earth	Value
Incoming power at OGS Table 7.7	-72.39 dBm	Incoming power at OGS Table 7.7	-93.42 dBm
Beam splitting (16-SNSPD array) and SMF insertion loss	-3.1 dB	Beam splitting (16-SNSPD array) and SMF insertion loss	-3.1 dB
SNSPD with N_r = 16	-12.04 dB	SNSPD with N_r = 16	-12.04 dB
Average optical power at SNSPD	-87.53 dBm	Average optical power at SNSPD	-108.56 dBm
SNSPD efficiency (40 %)	-3.97 dB	SNSPD efficiency (40 %)	-3.97 dB
Average received optical power at SNSPD	-91.5 dBm	Average optical power at SNSPD	-112.53 dBm
16-PPM gain	12.04 dB	64-PPM gain	18.06 dB
Received optical power per PPM pulse	-79.46 dBm	Received optical power per PPM pulse	-94.47dBm

Table 7.8: Calculations of peak received power regarding 16 PPM and N_r = 16 for both scenarios given in Table 7.7

Although the average optical power is of importance, the peak PPM pulse power should be introduced if real data are fed into the testbed, which are subject to signalling pre-processing described in CCSDS standards. The applied 16 PPM modulation technique results in an additional gain which is calculated based on simple equation $G_{ppm} = 10\log_{10}M$ [dB] = 12 dB for M = 16 (***Table 7.8***). For the maximum given PPM order M = 256 in CCSDS standards G_{ppm} = 24 dB. If instead of N_r = 2, an SNSPD unit with a larger N_r =16 array (e.g., LLCD mission; simulations in ***Figure 7.20***) is incorporated, power loss per photon detector element raise from 3.01 dB to 12.04 dB accompanied by increased losses from 0.8 dB to 3.1 dB.

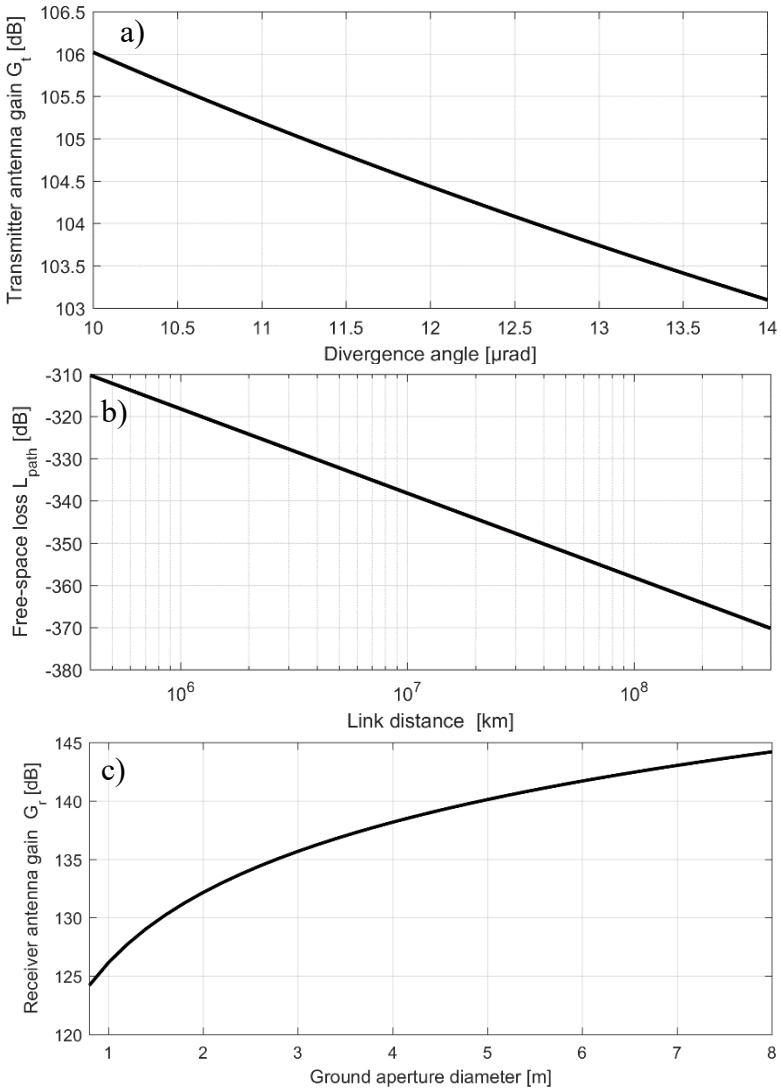

Figure 7.33: Simulations of deep space FSO link budget including: a) transmitter antenna gain; c) free-space loss; b) receiver antenna gain

Once the self-made link budget calculations regarding LLCD as well as the foreseen long-distance deep space FSO between Earth and Mars are performed, a general conclusion for the lower as well as upper limit of the received optical power can be drawn. In other words, the required average received optical power values in respect to which the developed breadboard is evaluated are within a range -76.2 dBm (Moon) – -97.23 dBm (Mars) (***Table 7.7***).

7.7 Testbed evaluation of a FSO link in static loss regime

The current subchapter is partly obtained from own publication ***[85]***. The obtained downlink budged for modest-distance space-to-ground FSO links imposes strict requirements for the operation diapason of the ground receiver unit. Since the range of the estimated received irradiance is between ~-75 dBm and ~-100 dBm, which is equivalent to detection of single-photon events, the applied architecture significantly favours the incorporation of still state-of-the-art SNSPD technology. Nevertheless, the quite low performance of the applied η = 40 % SNSPD unit should involve a verification strategy in order to be proven its possibility to emulate ground-to-deep-space FSO links in laboratory conditions. Although, the real (long-distance) optical wireless links are subject to perturbation effects including mainly Mie scattering as well as clear-air atmospheric turbulences, the time changes of the induced optical attenuation is considerably longer than duration of the transmitted bits ***[145]***. While the CCSDS-standardized transmitted-pulse waveform which is characterised with a downlink's PPM slot width between 0,125 – 512 ns (~0.2 – 3.2 ns for LLCD), the fastest Mie scattering attenuation is up to ~1 Hz and atmospheric turbulence scintillations interval are up to 200 Hz within a 95 % confidence interval ***[15]***, which is equivalent to a slow fading Poisson channel. The applied aperture averaging technique in **Chapter 6** significantly mitigates the influence of clear-air atmospheric turbulence in terms of optical signal losses as well as fading fluctuation frequency. Moreover, the robustness to any possible burst errors is increased to a new level by means of channel interleaving accompanying the SCPPM coding technique, which according to the described the CCSDS standards allows formation of encoded PPM symbols and their large-scale permutation based on interleaving process in the time domain. Since the recommendation in the CCSDS standards proposes the use of a channel convolutional interleaver with N_u rows where each row is presented by gradually increasing shift register nB_u with n between [1, N_u-1], the interleaver can handle N_u (N_u -1)/2B_u number of PPM symbols. Considering the channel interleaver rule given in ***[71]***, that B_u*N_u = multiple of 128, the selected values are N_u = 84 and B_u = 6048 ***[125]***. This leads to internal memory of 21083328 PPM symbols. Having addressed again LLCD with 16-PPM, 25 % GS and slot width between ~0.2 – 3.2 ns, the self-performed calculations show that the channel interleaver can handle atmospheric-induced fading between 0.168 – 1.35 s which corresponds to 0.74 – 5.95 Hz fluctuation frequency. Nevertheless, such a large convolution interleavers result in high initial delays of N_u(N_u-1)B_u (for LLCD this is between 337 ms – 2.7 s) which is often unacceptable for high data speed communications and consequently the related interleaving depth should be adjusted appropriately. In addition, the implementation of this complex processing is still impractical for the very slow fading conditions ***[42]***. Despite the mentioned constraints, the quasi-dynamic deep space FSO channel implementing an interleaver can be described as fading-free one, which allows the breadboard (i.e. SNSPD) to be initially tested by means of FSO link operating in the presence of static losses. This assumption coincide with the taken mean Mie scattering (clouds) and scintillation attenuation values in the estimated link budget calculations for Moon/Mars-to-Earth FSO downlink. In other words, the breadboard is evaluated in terms of the calculated average received optical power at the input of the SNSPD receiver system, which is between

-76.2 dBm (Moon) – -97.23 dBm (Mars). In addition, the breadboard design includes also a solution regarding evaluation of deep space FSO communication system in terms of encoded SCPPM signal on the presence of dynamic losses and without an interleaver. Since the detailed breadboard architecture is already provided in **Subchapter 7.5** and the design of channel emulator is given in **Chapter 4**, only the facilitated schematic showing the setup in terms of dynamic as well as static atmospheric losses is shown in ***Figure 7.34***. While the dotted line corresponds to evaluation of the breadboard in terms of the accomplished link budget in **Subchapter 7.6**, considering transmitted average optical power and static losses, the solid line depicts transmission of PPM processed (or SCPPM encoded) optical signal facing dynamic attenuation losses.

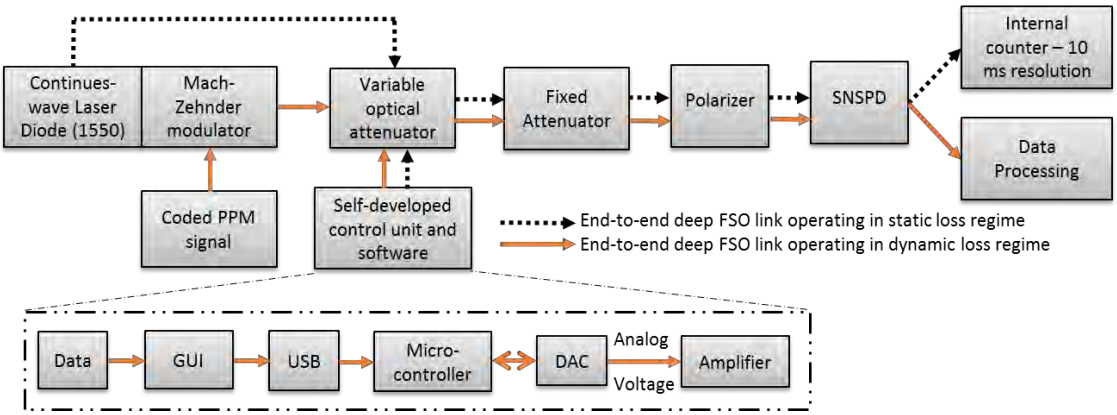

Figure 7.34: Testbed for evaluation of end-to-end deep space FSO link in respect to static and dynamic atmospheric losses (Modified figure based on own publication [85])

In particular, in case of dynamic loss mode, the 1550 nm laser source is externally modulated based on the selected MZM and PPM processed (or SCPPM encoded) RF signal, which allows evaluation of the end-to-end real deep space FSO communication system. Nonetheless, when the testbed is used in static loss mode, the external modulator is omitted and the CW laser is directly coupled into VOA, yielding results especially regarding the SNSPD performance, which is evaluated, based on internal photon counter. Beyond the considered differences, the most emblematic unit well presented into two operation regimes is the VOA together with a self-developed control driver and software used for static/dynamic control of the transmitted optical power. On the one hand, the later plays role of a channel emulator representing different atmospheric effects such as Mie scattering (fog and clouds) as well as turbulence-induced fading. On the other hand, the VOA is used as a very slow optical modulator for testing the On-Off ER (stability) limitations of the selected SNSPD system.

Addressing the evaluation capabilities of the first breadboard regime given in ***Figure 7.34***, the performance and the operation of the SNSPD by means of average optical power including static losses is examined. In particular, the breadboard is utilized as a test setup for the obtained SNSPD, which is the main component representing the Poisson channel. The tests are conducted by applying different attenuation patterns and values to the SMF link of

the breadboard. The static attenuation changes are implemented based on the already introduced voltage-controlled VOA, which attenuation is set up between 0 and 50 dB. In particular, within the static loss regime of the testbed, VOA is used as a precise instrument for controlling the transmitted optical power. In this way, measurements of the SNSPD's efficiency and detection intensity versus bias current are performed. While this provides significant information for the SNSPD limitations in terms of the input optical signal, an additional investigation of supported On-Off ER (modulation depth) is carried out. VOA unit is utilized as a very slow OOK optical modulator, which is well suited for investigation of the SNSPD's On-Off ER limitations. A basic scheme of this experiment is shown in ***Figure 7.35***.

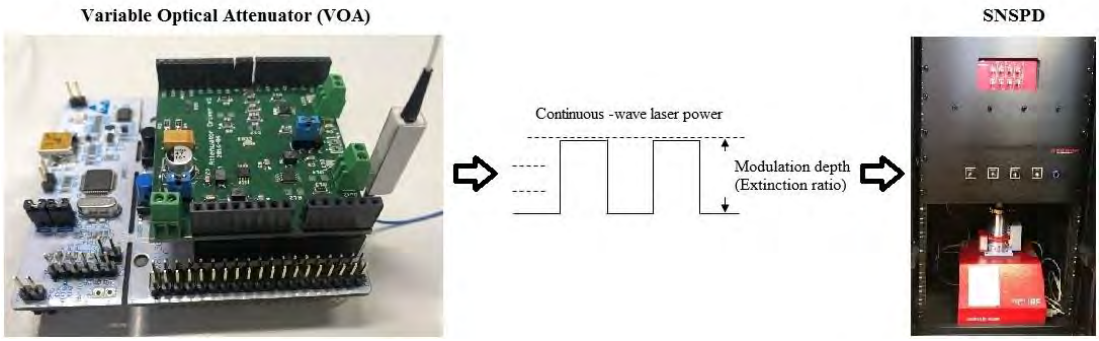

Figure 7.35: VOA unit, controlled by the provided driver and software, used as a slow OOK optical modulator, which characterises the stability of SNSPD (The figure is obtained from own publication [85])

Based on the self-developed software, an attenuation lookup table corresponding to OOK optical signal is loaded. Having the possibility to set up the period of time between the attenuation values (response time) the data rate is easily controlled.

The main reason to use VOA instead of MZM accompanied with bias voltage controller and RF modulator driver is the support of very slow data rates. While the cut-off frequency of MZM system is 50 kHz, the response time of VOA is at ~10 ms, which corresponds to OOK data rates at maximum 0.1 kHz. In particular, the internal SNSPD photon counter has minimum integration time of 10 ms, which means that the pulses should be at maximum 0.1 kHz (10 ms). In addition, the very low data rate allows measurements of the On-Off ER nearly at DC point data frequency, or constant input optical power. This is highly welcome when a SNSPD operating point should be evaluated in respect to its stable operation.

During the SNSPD tests in the breadboard's evaluation mode, the estimated received optical power -76.2 – -97.23 dBm in respect to the link budget, coincide nearly with optical-power upper bound (-75 dBm) of the detector. Consequently, the test is performed within -75 – -100 dBm. The optical power of the selected contentious-wave LD is 6 dBm. Moreover, in accordance with CCSDS standards, it operates in near infrared spectrum, namely 1550 nm wavelength. In order to decrease the laser power up to levels of single photons, three 25 dB fixed attenuators are applied. In addition, the components have additional internal

attenuation of 6 dB. Consequently, the laser signal power arriving at the input port of SNSPD is at minimum -75 dBm. The necessary additional attenuation between 0 – 25 dB is imposed by the implemented VOA unit, which can reach up 50 dB. Consequently, for the selected 1550 nm wavelength, the minimum setup optical power of -75 dBm corresponds to ~10^8 photons.

The measured performance of the selected SNSPD was provided in the **Chapter 7.3**. As already was well explained, one of the most crucial parameters in terms of Poisson channel's capacity is the SNSPD quantum efficiency. Having possibility for precise changes of the input optical power with the applied VOA, the relevant maximum optical output power corresponding to an exact SNSPD's bias value is measured. Once the measurements are available, the SNSPD maximum obtainable quantum efficiency versus bias current is calculated. The results are shown in ***Figure 7.36***.

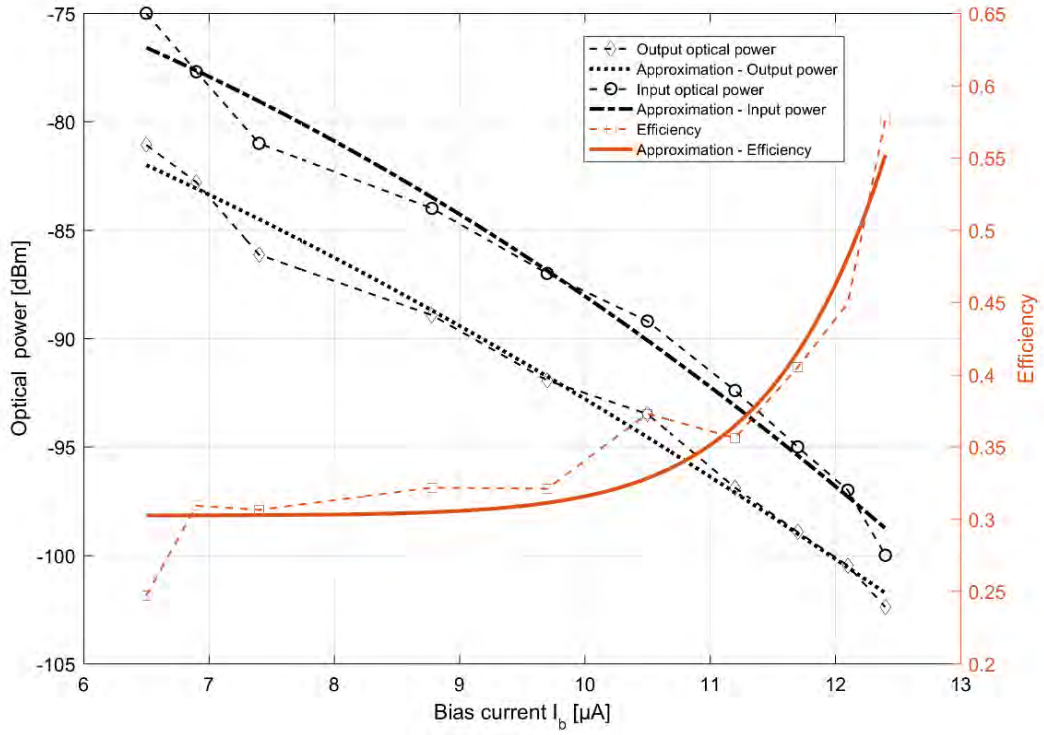

Figure 7.36: Measurements of SNSPD's efficiency, input and output optical power versus bias current I_b (The figure is obtained from own publication [85])

It is clearly visible that the efficiency decreases with having a higher amount of optical power, which corresponds to a reduced SNSPD bias current I_b. In the case of the following measurements, the selected optical input power is -91 dBm (6.2 Mph/s) supporting quantum efficiency $\eta = 0.36$ (36%). Taking into account the provided SNSPD specifications in ***Table 7.2***, $\eta = 36$ % is located within the nominal operating region of the SNSPD, very closed to the optimal nominal value of $\eta = 40$ %. According to ***Figure 7.36***, in case the input optical power is increased over -91 dBm, the quantum efficiency η decreases under 35 %, which is accompanied with increased instability, well investigated in the following part of the section.

Once the maximum obtainable quantum efficiency corresponding to an exact input optical power value is chosen in ***Figure 7.36***, an additional calibration is performed. In particular, the calibration process should take into account both, the value of critical bias current I_c together with the detector internal noise. In the context of this considerations, each selected operating point within ***Figure 7.36*** should be solely evaluated. ***Figure 7.37*** shows the above presented concept of defining the value of I_b together with measurements in respect to selected nominal input optical power of -91 dBm and the obtained DCR noise.

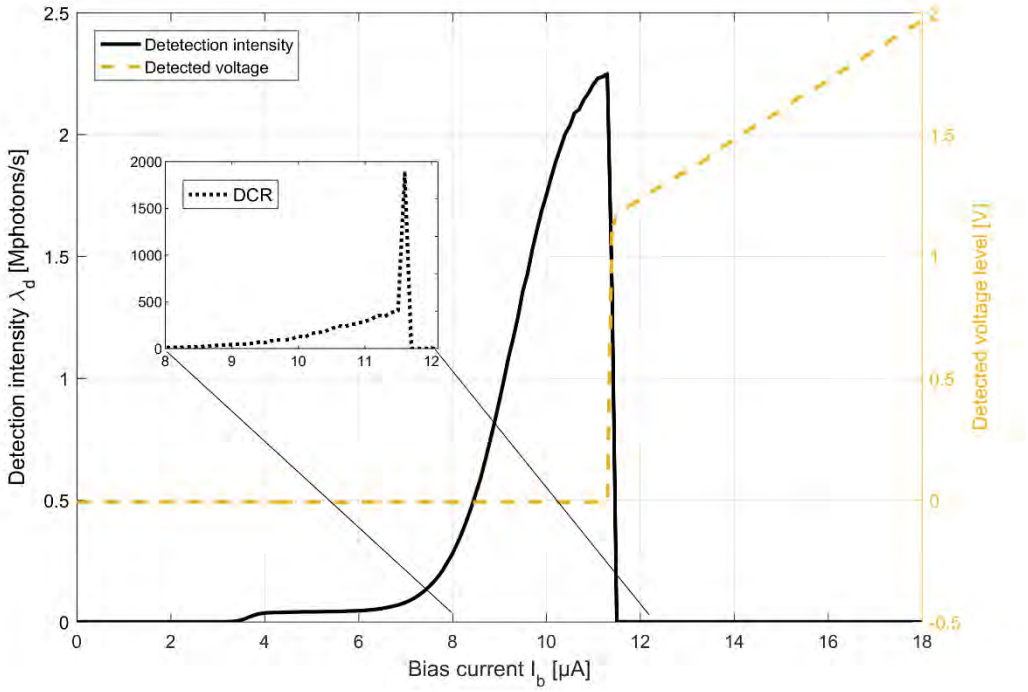

Figure 7.37: Measured detection intensity λ_d, detected voltage level and DCR noise versus bias current I_b for a single SNSPD element (The figure is obtained from own publication [85])

In ***Figure 7.37***, the dependence of detection intensity λ_d [Mph/s] on bias current I_b is evaluated, which strictly follows the phenomenological model provided in ***Figure 7.2*** . For a given fixed input power, the increase of I_b leads to growth in detection efficiency that allows larger amount of photons per second to be absorbed by each SNSPD channel. Nevertheless, the explained process is possible until the saturation point (critical current I_c) is reached, which happens at 11.3 μA. For larger values than I_c = 11.3 μA, the fragile superconductive mode is not supported and the photon detection is interrupted until I_b is decreased. The condition $I_b > I_c$ is accompanied by a rapid voltage growth that is well visible in the provided detected voltage figure. In order to determine the operation point of the detector, limitations due to Dark Count Rate (DCR) noise, which was already evaluated in **Subchapter 7.3.2** should be also observed. Having in mind that the intensity peak of DCR noise λ_{dcr_s} [ph/s] coincides with the detection intensity of the input optical signal λ_d, the bias current I_b should be additionally decreased. While DCR for an operation point I_b = 11.3 μm is λ_{dcr_s} = 1800 ph/s, the nominal noise value of 300 ph/s (300 Hz) (***Figure 7.6***) is attained

when I_b = 10.8 μA. In particular, this operating point of SNSPD system for the selected -91 dBm fixed input optical power offers optimal trade-off between high-enough quantum efficiency and SNR.

Furthermore, in accordance with the given results, it is worth investigating the quantum efficiency η of the SNSPD versus I_b for a fixed optical power. Having in mind the selected -91 dBm input optical power located within the observed nominal operating region of the evaluated SNSPD, the maximum detection efficiency shown in ***Figure 7.38*** is η = 0.36 (36 %). In other words, from the received 6.2 Mph/s (-91 dBm) only 2.5 Mph/s are absorbed, which coincides with the findings in ***Figure 7.36***. Nevertheless, in to order to mitigate the influence of DCR noise over SNR parameter, an additional drop in the biased current is required, namely I_b = 10.8 μA. Therefore η is decreased with 1%, namely η = 35% which is considered to be the operating value for the built-in breadboard.

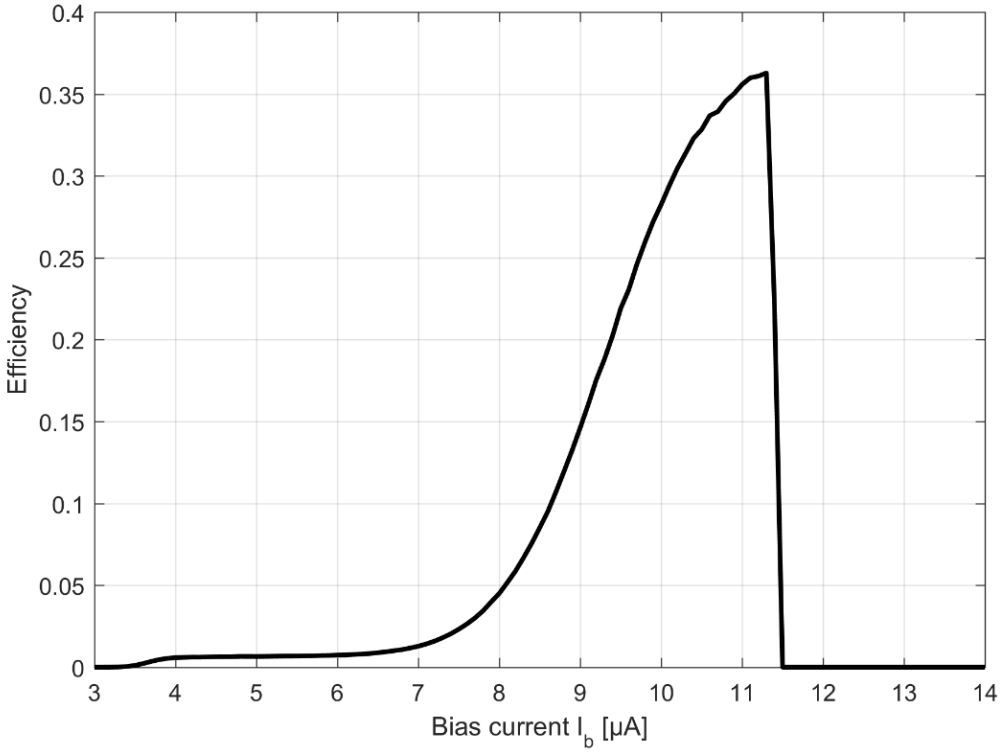

Figure 7.38: SNSPD detection efficiency versus bias current I_b (The figure is obtained from own publication [85])

Besides the accomplished calibration in terms of the examined quantum efficiency parameter, there are also SNSPD constrains link to the maximum allowed modulation depth of the transmitted optical pulses. Similar to quantum efficiency, the On-Off ER parameter is dependent on the input optical power and related to SNSPD bias current. This can be explained with the fact that SNSPD has completely different performance, when the input power is increased. This is well shown in ***Figure 7.39***.

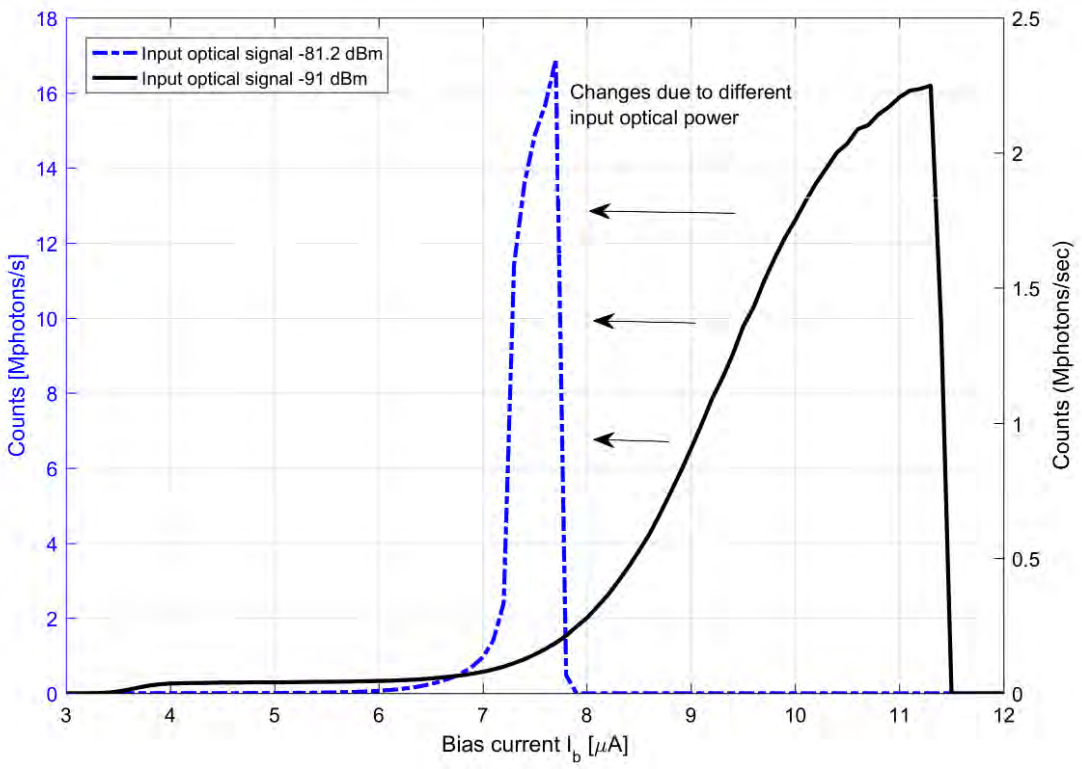

Figure 7.39: Comparison between SNSPD systems' performance in terms of two different input optical signals (The figure is obtained from own publication [85])

According to ***Figure 7.39*** the bias current versus detection efficiency graph is changing with increasing the input optical power. Apart that SNSPD architecture requires less current due to higher amount of photons and corresponding RF pulses, the graph becomes narrower with a sharper peak. The consequence of this is higher instability, which leads to lower On-Off ER. High On-Off ER requires broaden graphs similar to the one based on -91 dBm input optical power. To address this unstable and non-linear performance the self-developed breadboard allows full investigation of the relation between On-Off ER and bias current (maximum allowed input optical power). For this purpose, the already considered VOA unit is applied. In particular, VOA is used as a very slow OOK modulator with 125 ms pulse duration, which is well suited to the pulse counter specifications (minimum 10 ms integration time). The breadboard measurements are accomplished in terms of different optical pulses distinguished by peak power as well as On-Off ER. The ***Figure 7.40*** provides information regarding the maximum and minimum detected amount of photons versus bias current when an OOK optical signal is coupled into the SNSPD. This concept provides the rough information for the On-Off ER, which is the difference between the two described power levels.

The full investigation of the On-Off ER is provided in ***Figure 7.41***. In particular, the exact value of the On-Off ER versus SNSPD bias current is provided. According to the results, On-Off ER exponentially increases with rising the bias current or reducing the average

optical input/output power. Consequently, the On-Off ER for bias current under 11 μA is less than 25 dB, which is insufficient for real deep space optical communication.

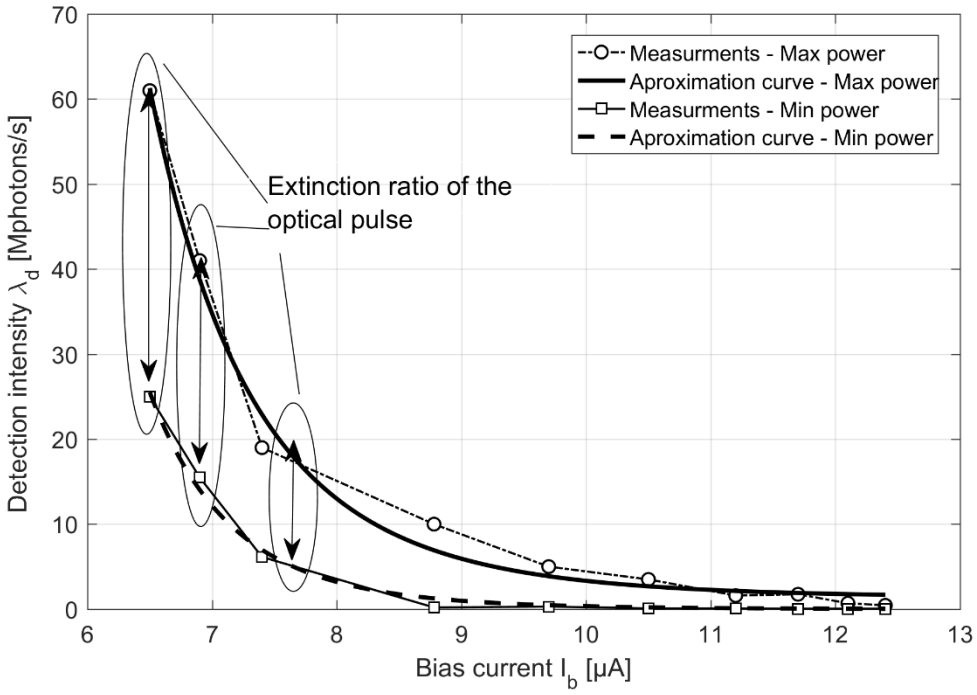

Figure 7.40: SNSPD minimum and maximum detection intensity λ_d related to 'On' and 'Off' states of a OOK optical signal, versus bias current I_b (The figure is obtained from own publication [85])

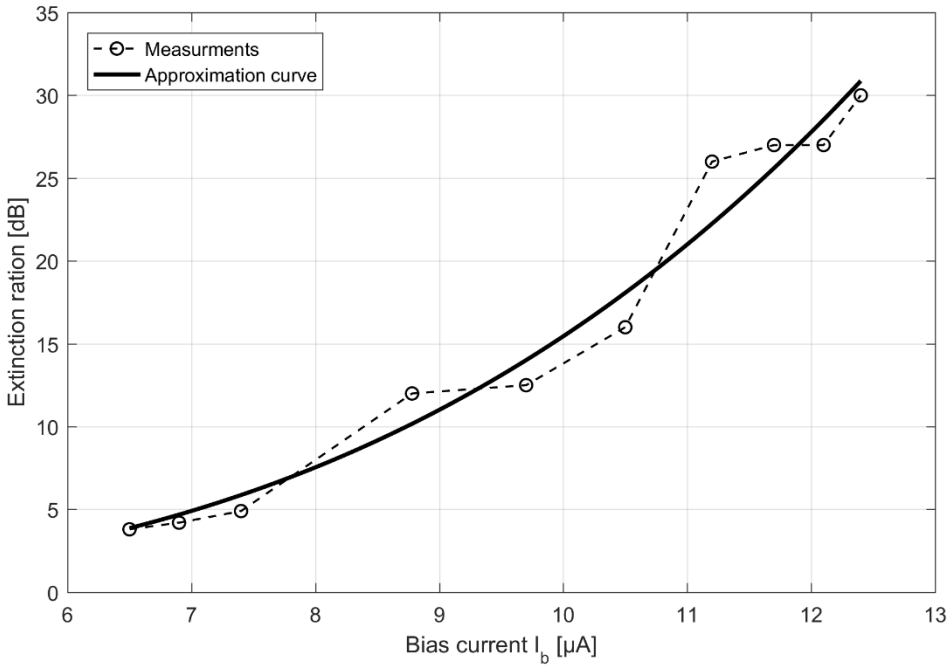

Figure 7.41: On-Off ER limitations of a single SNSPD element in terms of different bias current I_b (The figure is obtained from own publication [85])

7.8 Channel emulator measurements based on atmospheric turbulence fading

The measured low performance of the obtained $N_r = 2$ SNSPD receiver unit together with its strict polarization dependence leads to significant instability, which poses limitations on implementation of a dynamic-loss scenario. The reach conclusions in results of the carried out assessments in **Subchapter 7.3** and **Subchapter 7.8** are:

1) The obtained and measured SNSPD ($N_r = 2$) supports $\eta > 36$ % and ER > 25 dB when the received optical power is less than -91 dBm. Nevertheless, the shorter downlink between Moon and Earth requires the incoming average optical power to be -76.2 dBm per SNSPD element, which substantially affects the quantum efficiency, dropping from 36 % to 30 %. Moreover, the SNSPD ER parameter describing the overall stability is 4.2 dB, which is not enough to guarantee stable operation. On the other hand, the received average optical power for longer-distance mission to Mars decreases even further to -97.23 dBm. While the first scenario can be handled if only the power is redistributed to larger SNSPD array ($16 < N_r < 64$) at minimum corresponding to -87.53 dBm per SNSPD channel for $N_r = 16$, the second case requires more SNSPD channel due to introduced quantum, background, leakage, DCR noise limitations.
2) A non-optimized polarization state before optical signal to be coupled into SNSPD leads to penalties up to 4.72 dB. Even when the optical signal is horizontally oriented in terms of the superconducting nanowire, the non-polarization maintaining VOA, which represent the adverse atmospheric effects, causes 0.87 dB fluctuation. Moreover, the recorded internal instability of the SNSPD receiver unit is 0.63 dB.

Having in mind 1) and 2) together with the mean and STD values of the simulated atmospheric turbulence attenuation that for $R_d = 1$ m, 1.5 m, 8 m are 0.36 dB – 3.39 dB and 0.056 dB – 0.57 dB, the setup suffers from lack of capabilities to emulate a real dynamic atmospheric channel. Since this issue, the breadboard is only enough to evaluate the signal processing part of the space-to-ground downlink. The relevant findings are given in ***[73]*** document, where the obtained SNSPD operation is experimentally proved based on real CCSDS signalling parameter sets. In other words sophisticated signal processing considering SCPPM encoded data with additional spreading, interleaving and synchronization technique are applied. Nevertheless, the compatibility of the channel emulator with the requirements to represent dynamic atmospheric fading due to clear-air atmospheric turbulence is evaluated independently. For the purpose, both the characterized 1550 nm channel emulator in **Chapter 4** with the simulated atmospheric turbulence-induced fading in **Chapter 6** are combined in respect to emulation of scintillation impact over space-to-ground downlink. At first, the RAOB-based simulations of turbulence scintillations for $R_d = 8$ m and $\gamma = 20°$ are applied to VOA driver, whose response time is set up to 5 ms, while in **Appendix C**, ***Appendix Figure 3*** measurements with 1 ms, 2 ms, 10 ms and 100 ms are provided. This initially selected 5 ms response time corresponds exactly to 200 Hz atmospheric turbulence fluctuations, which is the maximum value regarding defined 0.1 – 200 Hz interval of normal scintillation's occurrence. In accordance with ***Figure 6.12***, the

percent distribution of the attenuation is in the range between 0.27 dB and 0.55 dB with *mean* = 0.36 dB and *STD* = 0.056 dB. Taking into account the scale of the provided plots, the amount of attenuation samples is equal to 190. Once the measurement is accomplished, the comparison between real turbulence attenuation data and based on them simulated ones with the proposed testbed in terms of time is provided in ***Figure 7.42***.

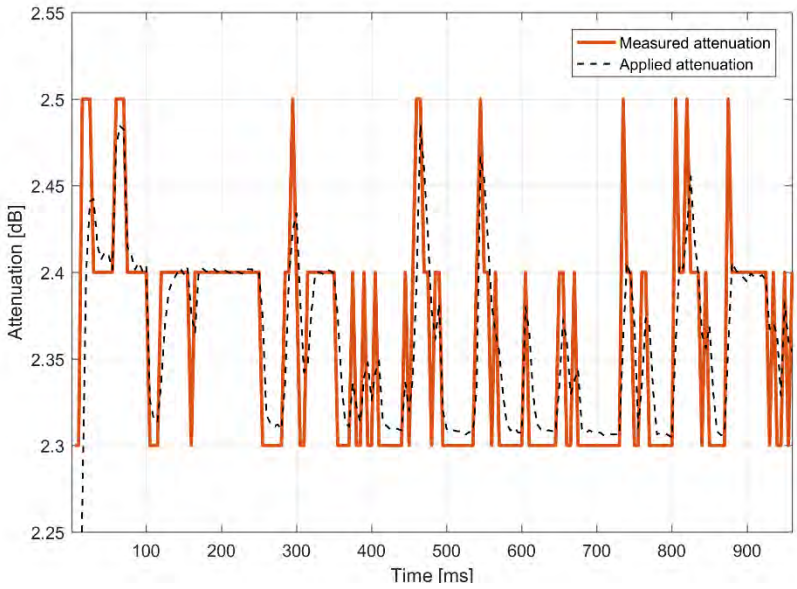

Figure 7.42: Comparison between simulated and measured turbulence attenuation data with the proposed testbed in terms of time

In order to increase the operation stability (working into defined linear region – ***Figure 4.15***), the lower limit is set up to 1 dB, which together with the considered attenuator design (1 dB losses) is sum up to 2 dB. Moreover, the SM – VOA shows clear limitation in terms of its precession due fast scintillation frequency as well as VOA technology. While the used DAC resolution is 65536 providing precision 5, the VOA can cope only with decimal fixed-point numbers with numeric scale 1, which leads to rounding the all applied attenuation samples. Nevertheless, the impact of such low atmospheric turbulence-induced attenuation over space-to-ground FSO system is minimum, which is also well shown in the simulation results in ***Figure 7.21***. In other words the low numeric scale of 1, which leads to 3 levels of change within 0.3 dB and 0.5 dB, offers enough accuracy in the representation of the scintillations. Having in mind the accuracy regarding the used approach, an absolute error statics is applied. Both, the absolute error between real turbulence attenuation data and based on them simulated ones as well as its probability histogram are given in ***Figure 7.43***.

The absolute error between real turbulence attenuation data and based on them simulated ones is at maximum 0.15 dB, which is quite large. However a closer look at the given PDF statics in ***Figure 7.43***, the mean and STD values of the absolute error are quite small with mean = 0.025 dB and STD = 0.028 dB. In particular, 60 % confident interval is featured with absolute error of up to 0.02 dB while the absolute error is up to 0.07 dB for 90 % confident interval, which is significantly lower compared to the 0.15 dB maximum. The error floor is

dependent on various factors, including laser and receiver source stability as well as VOA technology. Moreover the absolute error is partly influenced by the non-perfect linearization (calibration) of electro-optical transfer function provided in ***Figure 4.13***, which for the selected operation interval leads to nearly static absolute error of ~0.012. Nevertheless, this error was easily overcame based on modification in the link budget of the setup.

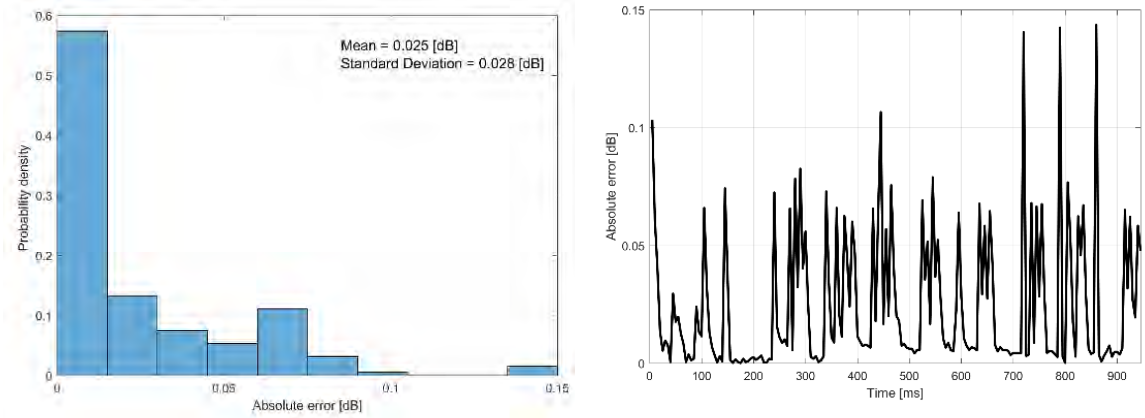

Figure 7.43: Absolute error statistics of the VOA-based FSO channel emulator fed with simulated turbulence date regarding scenarios with R_d = 8 m, γ = 20° and VOA response time 5 ms

Although the current analysis is performed for 5 ms (200 Hz), the VOA-based channel emulator setup covers implementation of other scenarios with more extreme or slower scintillation frequencies. Considering ***Figure 4.15***, the forward response time to attain 0 dB -> 37 dB is ~155 ms and the reverse response time to reach 37 dB -> 0 dB is ~13 ms respectively. Consequently, an attenuation spike leads to 168 ms (5.95 Hz) response time. Nonetheless, for the applied case with upper attenuation limit of 0.55 dB, the determined minimum response time is 1 ms (1 kHz) (**Appendix C**).

Chapter 8

8. Conclusions and future aspects

In order to have facilitated characterization of long and ultra-long FSO communication links operating in Mie scattering and atmospheric turbulence-induced fading, the current thesis proposes pioneering approaches based on prototyping and simulations. While this leads to clear and comprehensive conclusions listed in **Subchapter 8.1**, the broad scope of the thesis allows to be set up various future aspects provided in **Subchapter 8.2.**

8.1 Conclusions

The main outcomes of the accomplished work, which strictly correspond to the listed thesis's objectives and contributions given in **Chapter 1**, are provided in the conclusion part. Both optical attenuation due to Mie scattering as well as atmospheric turbulences are theoretically modelled at first, which provides the required results for the further prototyping task.

1) The characterization of Mie scattering effect benefits from well-established theoretical and empirical approaches, merging into a novel way Mie theory, fog and clouds microphysics, models dealing with atmospheric visibility parameter as well as real data. Rarely considered in the literature, cloud atmospheric effect is introduced in the current work regarding deep space FSO communication downlink. In comparison with ***[64]***, where the simulations are based on r = 0.1 μm resolution, the current approach uses the well-defined in Mie theory size parameter x – that implements the inherent dependence on the wavelength – with step size equal to 0.1. The largest self-simulated scattering coefficient β_{sca} = 130.73 km^{-1} is for Cumulus clouds. Based on the made assumption that mainly ballistic photons reach the OGS in respect to deep space FSO communication downlink, the generated attenuation is 567 dB/km. Nevertheless, the clouds of the highest interest for deep space communication are Cirrus ones. Their self-generated β_{sca} (0.087 – 0.92 km^{-1}) has values in the range of atmospheric light fog leading to attenuation between 0.4 – 12 dB/km. The characterization of real and artificial fog attenuation considerably benefits from the well-calibrated simulations in respect to clouds. The simulated β_{sca} = 16 km^{-1} regarding moderate continental fog leads to ~70 dB/km attenuation well corresponding to the values in International visibility code table given in ***[88]***.
2) Contrary to the normally applied HV and Buffon modesl in ***[21]*** and ***[49]***, the current work operates with vertical profile of atmospheric measurements from Vienna, Austria based on RAOB. The atmospheric turbulence-induced fading due to scintillations is

defined in respect to probability theory applying Log – Normal as well as Gamma – Gamma PDFs, which provides accurate information in respect to power scintillation index. The investigated long distance 2.7 km terrestrial link is characterized with typical C_n^2 mean value equal to ~10^{-15}, which causes scintillations featured with $\sigma_p^2 \leq 0.148$ (attenuation ≤ 8.6 dB) for 0.1 m receiver aperture. In respect to a space-to-ground feeder link, the statistical mean outcomes for C_n^2 (10^{-15} – 10^{-16}) completely adhere to the offered measurements in ***[22]*** and ***[49]***. Moreover, the optical attenuation in dependence on R_d =1, 1.5, 8 m and γ = 20°, 30° is evaluated based on generated relative frequency histograms having value ≤ 5.2 dB. Similar to Mie scattering, the outcomes are incorporated into two developed simulation models and testbed.

Along with theoretical representation of atmospheric effects supported by real RAOB and ECMWF measurements, the pioneering VOA-based channel emulator is provided and implemented within the current work. The generated high-attractiveness of this novel technique is due to facilitated verification of (ultra) long-distance FSO links, which is a substantial alternative to the expensive and demanding real measurement approaches. Although other research groups ***[60]*** developed similar approaches through years, according to my knowledge the idea was officially presented for first time in media in ***[78]***. In contrast to the applied lookup tables in ***[60]***, both selected 850 nm MM – VOA and 1550 nm SM – VOA are subject to self-performed linearization process in respect to VOA's electro-optical transfer function. Their state-of-the-art characterization, which substantially benefits from the simulated atmospheric-turbulence induced fading together with Mie scattering attenuation, proves the required performance. In particular, the attained attenuation range in respect to the represented high-demanding space to ground FSO downlinks is between 0 – 50 dB for 1550 nm SM – VOA, while the response time is up to 1 kHz, which strongly depends on the induced-fading properties. The FSO channel emulator is part of two self-developed state-of-the-art prototypes, which offer emulation of terrestrial and space-to-ground FSO communication links:

1) Although the major contribution of the current work is in respect to deep space FSO downlinks operating at 1550 nm wavelength, (long-distance) terrestrial channels are considered using a self-built testbed containing SFP module, which is well-integrated in the most low-cost FSO systems. Even though the prototype with 1.25 Gbps SFP @850 nm aimed to emulate real horizontal FSO links near ground, its main benefit translates into overall verification of the feasibility of FSO channel emulator to introduce adverse atmospheric conditions. Having in mind the target BER = 10^{-12} of SFP-based porotype with 27 dB link margin, the measured BER curve continuously degrades for the applied optical attenuation between 27 dB and 31 dB, which completely complies with the theoretical performance of a FSO system integrating maximum likelihood receiver with hard decision decoding. Along with the prototyping, the processed real atmospheric measurements in terms of 2.7 km long-distance FSO link prove that terrestrial links are prone to decreased availability due to fog effect while atmospheric scintillations do not play an important role. This is especially true when MISO with an aperture averaging technique is applied leading to availability of 93.64 %. This conclusion is supported by

the simulated outage probability results for 2.7 km FSO link in the presence of atmospheric turbulence-induced fading. The simulated outcomes shows that SISO FSO system is featured with $P_{out} < 10^{-7}$ for an average normalized SNR of γ_n= 15 dB, R_d = 0.1 m and typical continental conditions. Furthermore, another alternative to the VOA-based terrestrial channel emulator is proposed in the face of 50 m artificial fog channel, which aims to represent Mie scattering based on two artificial fog sources. Having addressed real LDS measurements of PSD together with the well-tuned Mie scattering approach, there is only ~7 dB difference between the simulated optical attenuation is respect to measurements and theoretically defined continental fog. The results proves not only the validity of this complicated approach but also the advantages of VOA-based channel emulator offering facilitated representation of fog as well as atmosphere turbulence.

2) It can be concluded that the main thesis contribution comprises the performed ultra-long-distance deep space FSO downlink characterization. While the carried out analysis significantly benefits from the accomplished Mie scattering (clouds) and atmospheric turbulence assessment accompanied by integration of VOA-based FSO channel emulator, also the concept of Poisson point processes describing HPE deep space FSO link needed to be introduced. The model integrates N_r = 2 channels SNSPD receiver distinguished with following measured nominal parameters: ~40 % quantum efficiency, ~300 Hz DCR and DT= ~20 ns. Although deep space HPE FSO link is simulated in ***[62]***, the atmospheric effects were neglected, which are the main focus of the current work. Having simulated the worst downlink scenario with uncoded FSO signal, atmospheric turbulence fading and γ = 20° proves that a satisfactory performance is possible when an OGS has 8 m diameter aperture and SNSPD receiver is with $N_{arr} \geq 16$. In particular, the required received optical power for BER = 10^{-5} is -17.7 (pn/ns) [dB], which is comparable with the simulation outcome in ***[62]*** for SCPPM encoded FSO signal. The proposed pioneering testbed implements the most significant elements from the carried out simulations together with the VOA-based channel emulator and the SNSPD with N_{arr} = 2. The emulated end-to-end deep space communication downlink is assessed in the presence of static atmospheric losses (scintillations and Mie scattering) in the calculated received optical power range between -76.2 – -97.23 dBm. Due to the low performance of the obtained SNSPD, dynamic atmospheric losses cannot be investigated in the current work. Nevertheless, the performance of the VOA-based channel emulator is solely investigated with the simulated atmospheric turbulence fading, which can reach up to 1 Hz in case of proposed 8 m aperture diameter. These final results fully proved the investigated methodology for characterization of long-distance links in laboratory conditions.

The reached concussions by means of theoretical modelling together with prototyping prove the importance of the used approaches in the current thesis. Based on them **Subchapter 8.2** offers comprehensive outlook of the possible future work.

8.2 Future work

The accomplished analyses within the current work aim to evaluate all-important aspects of the atmospheric influences related to terrestrial as well as deep space-to-ground FSO

downlinks. Nevertheless, the large scope of the current thesis left the door open not only to one future task. From theoretical point of view, the current work (**Chapter 3**) deals with single-scattering atmospheric medium that is a decent approximation for terrestrial and deep space FSO communication links. Nevertheless, the introduction of multiple scattering medium would allow more accurate evaluation of Mie scattering optical attenuation due to atmospheric events with larger optical thickness such as very dense fog and Cumulus clouds that is especially important for near-Earth (e.g., LEO/GEO satellites) FSO feeder links. Furthermore, the carried out validation in **Chapter 4** of the developed hardware FSO channel emulator based on 850 nm SFP module would welcome implementation of other scenarios comprising 1550 nm SFPs and up to 10 Gbps data rates. Apart from those topics, an important future contribution to the investigated adverse atmospheric effects in **Chapter 5** and **Chapter 6** would be evaluation of atmospheric turbulence-induced beam-wandering effect, which is of crucial significance for reliability of ground-to-space FSO communication uplinks. In other words, a future aspect of comprehensive research well related to **Chapter 7** that currently evaluates in detail space-to-ground downlinks, is investigation of FSO uplinks based on simulations and breadboarding. While the emphasis of the current MATLAB simulations is solely placed over representation of space-to-ground downlinks in the presence of atmospheric turbulences without forward error correction codes, future work regarding such a mitigation technique would be also of high interest. In particular, forward error correction codding techniques comprising LDPC and SCPPM will be implemented in the already simulated photon starved FSO Poisson channel. Nonetheless, the most important goal is improvement of the developed testbed used for emulation of real deep space FSO downlinks in **Chapter 7**. In accordance with the measurements and the simulations, an obtaining a higher-class SNSPD detector with $N_{arr} \geq 16$ would allow tests in the presence of dynamic scintillation losses. Moreover, this would contribute to the task, VOA-based channel emulator to be tested with the SCPPM encoded data.

Own publications

Contributions and published materials: The section summarizes the authors' contributions published in Journals, Book chapters, Conference proceedings and Project reports based on the accomplished research in frame of the current thesis. Consequently, they comprise part of the used novel approaches, carried out research as well as thesis content. All **own publication materials** used in the thesis are referred to the **Bibliography**.

Journal papers:

- **H. Ivanov**, E. Leitgeb, P. Pezzei, and G. Freiberger, "Experimental characterization of SNSPD receiver technology for deep space FSO under laboratory testbed conditions," Optik journal, Volume 195, October 2019. **(See Bibliography [85])**
- M. Głąbowski, **H. Ivanov**, E. Leitgeb, M. Sobieraj, and M. Stasiak, "Simulation studies of elastic optical networks based on 3-stage Clos switching fabric," Optical Switching and Networking journal, vol. 36, February 2020. **(See Bibliography [6])**
- G.D. Roumelas, H.E. Nistazakis, E. Leitgeb, **H.D. Ivanov**, and C.K. Volos, "Serially DF Relayed Hybrid FSO/MMW Links with Weibull Fading, M-Turbulence and Pointing Errors," Optik journal, vol. 216, August 2020.

Book chapters

- **H. Ivanov**, E. Leitgeb, D. Kraus, F. Marzano, A. Jurado-Navas, S. Dorenbos, R. Perez-Jimenez; and G. Freiberger, "Free Space Optics System Reliability in Presence of Weather-induced Disruptions," In: J. Rak, D. Hutchison (eds.) Guide to Disaster-Resilient Communication Networks, **ISBN 978-3-030-44684-0**, Computer Communications and Networks, Springer, July 2020. **(See Bibliography [84])**
- R. Bruzgiene, L. Narbutaite, T. Adomkus, P. Pocta, P. Brida, J. Machaj, E. Leitgeb, P. Pezzei, **H. Ivanov**, N. Kunicina, A. Zabasta, J. Caiko, and A. Patlins, "Environmental Conditions Mitigation by Application of Quality-driven Techniques to Improve Wireless Communications Resilience," In: J. Rak, D. Hutchison (eds.) Guide to Disaster-Resilient Communication Networks, **ISBN 978-3-030-44684-0**, Computer Communications and Networks, Springer, July 2020. **(See Bibliography [31])**

Conference proceedings

- **H. Ivanov**, P. Pocta, F. Marzano, E. Leitgeb, and G. Freiberger, "**Resilience of** Deep Space FSO Communication Scenario Involving SNSPD Receiver to Atmospheric Turbulence," IEEE, 14th International Conference on Advanced Technologies, Systems and Services in Telecommunications (TELSIKS 2019), pp. 235-240, Nis, Serbia, October, 2019. **(See Bibliography [82])**

- D. Kraus, **H. Ivanov**, and E. Leitgeb, "Novel Optical Network Design for Automotive Applications using ROADMs," 2019 15th International Conference on Telecommunications (ConTEL), pp. 1-6, Graz, Austria, 3rd – 5th July, 2019.
- D. Kraus, **H. Ivanov**, and E. Leitgeb, "Approach for an Optical Network Design for Autonomous Vehicles," 2019 21st International Conference on Transparent Optical Networks (ICTON), pp. 1-6, Angers, France, 9th – 13th July, 2019.
- **H. Ivanov**, E. Leitgeb, T. Plank, and D. Kraus, "Evaluation of FSO-technology as a Candidate for Reliable Long-distance Communication Links for Deep Space Applications," IEEE, PhotonIcs &Electromagnetics Research Symposium - Spring (PIERS), Rome, Italy, June, 2019. **Invited paper (See Bibliography [87])**
- **H. Ivanov**, E. Leitgeb, and G. Freiberger, "Modelling of a deep space FSO-link with a SNSPD receiver unit under turbulence-induced fading conditions," OSA Conference on Lasers and Electro-Optics (CLEO 2019), San Jose, California, USA, 5th – 10th May, 2019. **(See Bibliography [86])**
- P. Bekhrad, **H. Ivanov**, and E. Leitgeb, "Car to X Communication with Optical Wireless as Support and Alternative to RF-Technologies for Roads and Future Transportation," 24th International Conference on Software, Telecommunications and Computer Networks (SoftCOM 2016), Supetar, Croatia, 13th – 15th September, 2018.
- **H. Ivanov**, T. Plank, E. Leitgeb, L. Mustafa, and E. Cerncic, "Estimation of Mie scattering influence for the FSO channel under artificially simulated fog conditions," SPIE Remote Sensing (ERS18), Berlin, Germany, 10th – 13th September, 2018. **(See Bibliography [83])**
- **H. Ivanov**, E. Leitgeb, and G. Freiberger, "Characterization of Poisson Channel for Deep Space FSO Based on SNSPD Technology by Experimental Demonstration," 11th International Symposium on Communication Systems, Networks and Digital Signal Processing, CSNDSP18 Budapest, Hungary, July 18th – 20th July, 2018.
- E. Leitgeb, T. Plank, P. Pezzei, **H. Ivanov**, and R. Perez, "Optical Wireless Communications and Optical Sensing and Detection Technologies for Increasing the Reliability and Safety in Autonomous Driving Scenarios," 20th International Conference on Transparent Optical Networks (ICTON 2018), Bucharest, Romania, 1st – 5th July, 2018.
- **H. Ivanov**, S. Dorenbos, E. Leitgeb, G. Freiberger, and P. Bekhrad, "Design of an evaluation breadboard with SNSPD for testing various deep space optical communication applications," SPIE Photonics Europe (EPE18), Strasbourg, France, 22th – 26th April, 2018. (**See Bibliography [81])**
- P. Bekhrad, E. Leitgeb, and **H. Ivanov**, "Benefits of visible light communication in car-to-car communication," SPIE Photonics Europe (EPE18), Strasbourg, France, 22th – 26th April, 2018.
- **H. Ivanov**, T. Plank, C. Pock, and E. Leitgeb, "FSO System Performance Evaluation Based on Calibrated Atmospheric Channel Emulation," 14th International Conference on Telecommunications (ConTEL 2017), Zagreb, Croatia, 28th – 30th June, 2017. **(See Bibliography [80])**

- E. Leitgeb, **H. Ivanov**, T. Plank, P. Pezzei, and C. Pock, "Implementation of a Testbed with a Hardware Channel Emulator for Simulating the Different Atmospheric Conditions to Verify the Transmitter and Receiver of Optical Wireless Systems," 19th International Conference on Transparent Optical Networks (ICTON 2017), Girona, Spain, 2nd – 6th July, 2017.
- **H. Ivanov**, P. Pezzei, T. Plank, C. Pock, and E. Leitgeb, "Design of a Hardware Channel Emulator as Lab Demonstrator for Detailed Verification of Long-Distance FSO Systems," International Conference on Broadband Communications (CoBCom'2016), Graz, Austria, 14th – 16th September, 2016. **(See Bibliography [78])**
- P. Bekhrad, **H. Ivanov**, E. Leitgeb, and B. Mikac, "Simulation of Fiber Taper for Both Forward and Reverse Cases," 10th International Symposium on Communication Systems, Networks and Digital Signal Processing, CSNDSP16 Prague, Czech Rep., July 20th-22nd, 2016.
- D. Krstic, M. Stefanovic, V. Milenkovic, D. Radenkovic, **H. Ivanov**, and E. Leitgeb, "Performance of Wireless Communication System in the Presence of Rician Short Term Fading, Gamma Long Term Fading and Cochannel Interference," IEICE Information and Communication Technology Forum (ICTF) 2016, Patras, Greece, July 6th - 8th, 2016.
- D. Krstic, M. Stefanovic, V. Milenkovic, D. Radenkovic, **H. Ivanov**, and E. Leitgeb, "Performance of Wireless System in the Presence of κ-μ Multipath Fading, Gamma Shadowing and κ-μ Cochannel Interference," IEICE Information and Communication Technology Forum (ICTF) 2016, Patras, Greece, July 6th - 8th, 2016.
- **H. Ivanov**, E. Leitgeb, P. Bekhrad, T. Plank, and T. Mitsev, "Link Budget Optimization of Free Space Optical Systems in Relation to the Beam Diverging Angle," 13th International Conference on Telecommunications (ConTEL 2015), Graz, Austria, July 13th – 15th, 2015. **(See Bibliography [79])**

Published project reports (Technical notes)

- **H. Ivanov**, "Breadboard Detailed Design," System Study of Optical Communications with a Hybridised Optical/RF Payload Data Transmitter, Report (Technical Note 3), ESA Contract No. 4000115256/15/NL/FE, January 2018. **(See Bibliography [77])**
- H. Schlemmer, B. Ferenczi, I. Stamenic. J. Widmer, E Leitgeb, **H. Ivanov**, N. Metzger-Fragnol, J. Johansson, and M. Schönhuber, "System Study of Optical Communications with a Hybridised Optical/RF Payload Data Transmitter," Final report, ESA Contract No. 4000115256/15/NL/FE, 2020. **(See Bibliography [73])**

Bibliography/References

[1] World record in free-space optical communications, [online]. Available: https://www.dlr.de/content/en/articles/news/2016/20161103_world-record-in-free-space-optical-communications_19914.html, DLR news, 2016.

[2] F. E. Goodwin, "A review of operational laser communication systems," in Proc. of the IEEE, vol. 58, no. 10, pp. 1746-1752, Oct. 1970.

[3] M. A. Khalighi and M. Uysal, "Survey on Free Space Optical Communication: A Communication Theory Perspective," in IEEE Communications Surveys & Tutorials, vol. 16, no. 4, pp. 2231-2258, 2014.

[4] A. S. Hamza, J. S. Deogun, and D. R. Alexander, "Classification Framework for Free Space Optical Communication Links and Systems," in IEEE Communications Surveys & Tutorials, vol. 21, no. 2, pp. 1346-1382, 2019.

[5] M. Curran, M. S. Rahman, H. Gupta, K. Zheng, J. Longtin, S. R. Das, and T. Mohamed, "FSONet: A Wireless Backhaul for Multi-Gigabit Picocells Using Steerable Free Space Optics," In Proceedings of the 23rd Annual International Conference on Mobile Computing and Networking (MobiCom '17). ACM, pp. 154-166, New York, NY, USA, 2017.

[6] M. Głąbowski, **H. Ivanov**, E. Leitgeb, M. Sobieraj, and M. Stasiak, "Simulation studies of elastic optical networks based on 3-stage Clos switching fabric," Optical Switching and Networking journal, vol. 36, February 2020.

[7] M. M. Abadi, Z. Ghassemlooy, N. Mohan, S. Zvanovec, M. R. Bhatnagar, and R. Hudson, "Implementation and Evaluation of a Gigabit Ethernet FSO Link for 'The Last Metre and Last Mile Access Network'," 2019 IEEE International Conference on Communications Workshops (ICC Workshops), Shanghai, China, pp. 1-6, 2019.

[8] M. Uysal, C. Capsoni, Z. Ghassemlooy, A. Boucouvalas, and E. Udvary, "Optical Wireless Communications: An Emerging Technology," Signals and Communication Technologies, Springer, 2016.

[9] Franz Fidler, Markus Knapek, Joachim Horwath, and Walter R. Leeb, "Optical Communications for High-Altitude Platforms," IEEE Journal Of Selected Topics In Quantum Electronics, vol. 16, no. 5pp. 1058 – 1070, September/October 2010.

[10] E. Leitgeb et al., "Reliable Optical Wireless Links used as feeder links between earth and satellite," 2009 11th International Conference on Transparent Optical Networks, Azores, pp. 1-7, 2009.

[11] H. Hemmati, A. Biswas, and I. B. Djordjevic, "Deep-Space Optical Communications: Future Perspectives and Applications," in Proc. of the IEEE, vol. 99, no. 11, pp. 2020-2039, Nov. 2011.

[12] National Aeronautics and Space Administration Space, "Technology Game Changing Development Deep Space Optical Communications (DSOC)," Jet Propusion Laboratory Pasadena, CA 91109, July 2015.

[13] D. M. Boroson, J. J. Scozzafava, D. V. Murphy, B. S. Robinson, and M. I. T. Lincoln, "The Lunar Laser Communications Demonstration (LLCD)," 2009 Third IEEE

International Conference on Space Mission Challenges for Information Technology, pp. 23-28, Pasadena, CA, 2009.

[14] D. J. T. Heatley, D. R. Wisely, I. Neild, and P. Cochrane, "Optical wireless: the story so far," in IEEE Communications Magazine, vol. 36, no. 12, pp. 72-74, Dec. 1998.

[15] A. K. Majumdar, "Advanced free space optics (FSO): A systems approach," Springer Science+Business Media, New York, 2015.

[16] J. Poliak, D. Giggenbach, F. Moll, F. Rein, C. Fuchs, and R. M. Calvo, "Terabit-throughput GEO satellite optical feeder link testbed," 2015 13th International Conference on Telecommunications (ConTEL), pp. 1-5, Graz, 2015.

[17] J. R. Lesh, L. J. Deutsch, and W. J. Weber, "A Plan for the Development and Demonstration of Optical Communications for Deep Space," Progress Report JPL-TDA-PR-42-103, Jet Propulsion Laboratory, USA, 1990.

[18] H. Zech, F. Heine, D. Troendle, P. M. Pimentel, K. Panzlaff, M. Motzigemba, R. Meyer, and S. Philipp-May "LCTS on ALPHASAT and Sentinel 1a: in orbit status of the LEO to geo data relay system," Proc. SPIE 10563, International Conference on Space Optics — ICSO 2014, 105630W, November 2017.

[19] G. Muehlnikel, H. Kämpfner, F. Heine, H. Zech, and D. Troendle, "The Alphasat GEO Laser Communication Terminal Flight Acceptance Tests," Proc. International Conference on Space Optical Systems and Applications (ICSOS) 2012, pp. 13-1, Ajaccio, Corsica, France, October 2012.

[20] J. M. Perdigues, Z. Sodnik, H. Hauschildt, P. Sarasa, F. Porte-Proust, M. Wiegand, C. Rochow, D. Troendle, and F. Heine "The ESA's optical ground station for the EDRS-A LCT in-orbit test campaign: upgrades and test results," Proc. SPIE 10562, International Conference on Space Optics — ICSO 2016, 105622V, September 2017.

[21] A. K. Majumdar and J. C. Ricklin, "Free-Space Laser Communications Principles and Advances," Springer Science+Business Media, LLC, 2008.

[22] A. Alonso, M. Reyes, and Z. Sodnik, "Performance of satellite-to-ground communications link between ARTEMIS and the Optical Ground Station," Proc. SPIE 5572, Optics in Atmospheric Propagation and Adaptive Systems VII, Nov. 2004.

[23] E. Leitgeb, S. Sheikh Muhammad, B. Flecker, C. Chlestil, M. Gebhart, and T. Javornik, "The influence of dense fog on optical wireless systems, analysed by measurements in Graz for improving the link-reliability," in Proceedings of 2006 International Conference on Transparent Optical Networks, Nottingham, United Kingdom, June 2006.

[24] W. Hergert and T. Wriedt, "The Mie Theory Basics and Applications," Springer, Springer Series in Optical Sciences 169, 2012.

[25] C. F. Bohren and D. R. Huffman, "Absorption and scattering of light by small particles," John Wiley and sons, New York, 1983.

[26] R. Nebuloni and C. Capsoni, "Effects of Adverse Weather on Free Space Optics," In: Uysal M., Capsoni C., Ghassemlooy Z., Boucouvalas A., Udvary E. (eds) Optical Wireless Communications. Signals and Communication Technology. Springer, 2016.

[27] D. Harris, "The attenuation of electromagnetic waves due to atmospheric fog, International journal of infrared and millimeter waves," vol. 16, no. 6, pp. 1091-1108, 1995.

[28] E. P. Shettle, "Models of aerosols, clouds and precipitation for atmospheric propagation studies," AGARD conference, vol. 454, no. 15, pp. 1-13, 1989.

[29] S. S. Muhammad, M. S. Awan, and A. Rehman, "PDF Estimation and Liquid Water Content Based Attenuation Modeling for Fog in Terrestrial FSO Links," Radioengineering [online]. Společnost pro radioelektronické inženýrství, vol. 19, no. 2, pp. 228-236, 2010.

[30] I. I. Kim, B. McArthur, and E. J. Korevaar "Comparison of laser beam propagation at 785 nm and 1550 nm in fog and haze for optical wireless communications," Proc. SPIE 4214, Optical Wireless Communications III, February 2001.

[31] R. Bruzgiene, L. Narbutaite, T. Adomkus, P. Pocta, P. Brida, J. Machaj, E. Leitgeb, P. Pezzei, **H. Ivanov**, N. Kunicina, A. Zabasta, J. Caiko, and A. Patlins, "Environmental Conditions Mitigation by Application of Quality-driven Techniques to Improve Wireless Communications Resilience," In: J. Rak, D. Hutchison (eds.) Guide to Disaster-Resilient Communication Networks, Computer Communications and Networks, Springer, July 2020.

[32] M. C. Al Naboulsi, H. Sizun, and F. de Fornel, "Fog attenuation prediction for optical and infrared waves," Optical Engineering, vol. 43, no. 2, pp. 319–329, 2004.

[33] E. Leitgeb, M. Gebhart, P. Fasser, J. Bregenzer, and J. Tanczos, "Impact of atmospheric effects in free-space optics transmission systems," Proc. SPIE 4976, Atmospheric Propagation, April 2003.

[34] M. Gebhart, E. Leitgeb, S. Sheikh Muhammad, B. Flecker, C. Chlestil, M. Al Naboulsi, F. de Fornel, and H. Sizun, "Measurement of Light attenuation in dense fog conditions for FSO applications," Proc. SPIE 5891, Atmospheric Optical Modeling, Measurement, and Simulation, 58910K, August 2005.

[35] B. Flecker, M. Gebhart, E. Leitgeb, S. Sheikh Muhammad, and C. Chlestil "Results of attenuation measurements for optical wireless channels under dense fog conditions regarding different wavelengths," Proc. SPIE 6303, Atmospheric Optical Modeling, Measurement, and Simulation II, 63030P, September 2006.

[36] M. S. Awan, E. Leitgeb, C. Capsoni, R. Nebuloni ; Marzuki, F. Nadeem, and M. S. Khan, "Attenuation Analysis for Optical Wireless Link Measurements under Moderate Continental Fog Conditions at Milan and Graz," 2008 IEEE 68th Vehicular Technology Conference, pp. 1-5, Calgary, BC, 2008.

[37] M. S. Awan, L. C. Horwath, S. S. Muhammad, E. Leitgeb, F. Nadeem, and M. S. Khan, "Characterization of fog and snow attenuations for Free-Space Optical propagation," Journal of Communications, vol. 4, no. 8, pp. 533-545, September 2009.

[38] M. S. Awan, Marzuki, E. Leitgeb, B. Hillbrand, F. Nadeem, and M. S. Khan, "Cloud attenuations for free-space optical links," 2009 International Workshop on Satellite and Space Communications, pp. 274-278, Tuscany, 2009.

[39] M. Kavehrad, "Equalization and Markov chains in cloud channel," In: S. Arnon et al. (edc.) Advanced Optical Wireless Communication Systems, Cambridge University Press, 2012.

[40] L. Andrews and R. Phillips, "Laser Beam propagation trough Random Media," Second edition, SPIE Press, Washington, USA, 2005.

[41] J. Jiménez, "The Contributions of A. N. Kolmogorov to the theory of turbulence," Arbor, vol. 178, no. 704, August 2004.

[42] Z. Ghassemlooy, W. Popoola, and S. Rajbhandari, "Optical wireless communications system and channel modelling with MATLAB," CRC Press, Taylor & Francis Group, 2013.

[43] L. C. Andrews, "Field Guide to Atmospheric Optics," Second Edition

[44] R. S. Lawrence and J. W. Strohbehn, "A survey of clear-air propagation effects relevant to optical communications," in Proceedings of the IEEE, vol. 58, no. 10, pp. 1523-1545, Oct. 1970.

[45] D. L. Fried, "Scintillation of a ground-to-space laser illuminator," J. Opt. Soc. Am., vol. 57, no. 8, pp. 980–983, 1967.

[46] T. Morio, K. Toshiaki, K. Werner, T. Masahiro, T. Hideki, S. Yozo, T. Yoshihisa, K. Yoshisada, K. Hiroo, J. Takashi, Y. Shiro, and A. Katsuyoshi, "Overview of the Laser Communication System for the NICT Optical Ground Station and Laser Communication Experiments on Ground-to-Satellite Links," Journal of the National Institute of Information and Communications Technology, vol. 59, no. 1, March 2012.

[47] R. Mata Calvo, P. Becker, D. Giggenbach, F. Moll, M. Schwarzer, M. Hinz, and Z. Sodnik, "Transmitter diversity verification on ARTEMIS geostationary satellite," Proc. SPIE 8971, Free-Space Laser Communication and Atmospheric Propagation XXVI, 897104, March 2014.

[48] N. Perlot, M. Knapek, D. Giggenbach, J. Horwath, M. Brechtelsbauer, Y. Takayama, and T. Jono, "Results of the optical downlink experiment KIODO from OICETS satellite to optical ground station Oberpfaffenhofen (OGS-OP)," Proc. SPIE 6457, Free-Space Laser Communication Technologies XIX and Atmospheric Propagation of Electromagnetic Waves, 645704, February 2007.

[49] F. Moll, "Channel Characterization and Modeling for LEO-Ground Links," In: Uysal M., Capsoni C., Ghassemlooy Z., Boucouvalas A., Udvary E. (eds) Optical Wireless Communications. Signals and Communication Technology. Springer, 2016.

[50] H. Takenaka, D. Kolev, Y. Koyama, M. Akioka, Y. Munemasa, H. Kunimori, and M. Toyoshima, "Experimental results of satellite-to-ground laser communications link through atmospheric turbulence using SOTA," Proc. SPIE 10562, International Conference on Space Optics — ICSO 2016, 105624A, September 2017.

[51] D. R. Kolev and M. Toyoshima, "Received-Power Fluctuation Analysis for LEO Satellite-to-Ground Laser Links," in Journal of Lightwave Technology, vol. 35, no. 1, pp. 103-112, Jan. 2017.

[52] F. S. Marzano and G. d'Auria, "Model-based prediction of amplitude scintillation variance due to clear-air tropospheric turbulence on Earth-satellite microwave links," in

IEEE Transactions on Antennas and Propagation, vol. 46, no. 10, pp. 1506-1518, Oct. 1998.

[53] G. d'Auria, F. S. Marzano, and U. Merlo, "Model for estimating the refractive-index structure constant in clear-air intermittent turbulence," Appl. Opt. vol. 32, no. 15, pp. 2674-2680, 1993.

[54] F.S. Marzano, D. Carrozzo, S. Mori, and F. Moll, "Clear-air turbulence effects modeling on terrestrial and satellite free-space optical channels," IEEE 15649659, 4th International Workshop on Optical Wireless Communications (IWOW) Istanbul, Turkey, 2015.

[55] National Aeronautics and Space Administration, Technology Readiness Level Definitions," [online]. Available: https://www.nasa.gov/pdf/458490main_TRL_ Definitions.pdf

[56] J. Pesek, M. Ijaz, Z. Ghassemlooy, O. Fiser, and S. Rajbhandari, "Measuring the fog attenuation in an indoor free space optical laboratory chamber," IEEE, Applied Electronics (AE), Pilsen, Czech Republic, October 2012.

[57] M. Ijaz, Z. Ghassemlooy, H. Le-minh, S. Zvanovec, J. Perez, J. Pesek, and O. Fiser, "Experimental validation of fog models for FSO under laboratory controlled conditions," IEEE, 24th Annual International Symposium on Personal, Indoor, and Mobile Radio Communications (PIMRC), London, United Kingdom, September 2013.

[58] L. Mustafa, E. Černčič, and B. Thomsen, "FSO artificial low-cost fog attenuation experiment design," IEEE, Communication Systems, Networks and Digital Signal Processing (CSNDSP), Prague, Czech Republic, September 2016.

[59] S. Hippler, T Henning, F. Hormuth, D. Butler, and W. Brandner, "Generation of atmosphere-like optical turbulence," SPIE newsroom, 2007.

[60] A. Shrestha, D. Giggenbach, A. Mustafa, J. Pacheco-Labrador, J. Ramirez, and Fabian Rein "Fading testbed for free-space optical communications," Proc. SPIE 9991, Advanced Free-Space Optical Communication Techniques and Applications II, 999105, October 2016.

[61] A. Burton, Z. Ghassemlooy, and P. Arapoglou, "Physical layer solutions for optical communications in space," 2016 10th International Symposium on Communication Systems, Networks and Digital Signal Processing (CSNDSP), pp. 1-6, Prague, 2016.

[62] M. Srinivasan, R. Rogalin, N. Lay, M. Shaw, and A. Tkacenko, "Downlink receiver algorithms for deep space optical communications," Proc. SPIE 10096, Free-Space Laser Communication and Atmospheric Propagation XXIX, 100960A, February 2017.

[63] T. Plank, E. Leitgeb, and M. Loeschnigg, "Recent developments on free space optical links and wavelength analysis," 2011 International Conference on Space Optical Systems and Applications (ICSOS), Santa Monica, CA, pp. 14-20, 2011.

[64] M. S. Awan, R. Nebuloni, C. Capsoni, L. Csurgai-Horváth, S.S. Muhammad, F. Nadeem, M. S. Khan, and E. Leitgeb, "Prediction of drop size distribution parameters for optical wireless communications through moderate continental fog," Int. J. Satell. Commun. Network, vol. 29, no. 1, pp. 97-116, 2011.

[65] A. Burton, Z. Ghassemlooy, and P. Arapoglou, "Physical layer solutions for optical communications in space," 2016 10th International Symposium on Communication Systems, Networks and Digital Signal Processing (CSNDSP), Prague, pp. 1-6, 2016.

[66] M. Toyoshima, W. R. Leeb, H. Kunimori, and T. Takano, "Comparison of microwave and light wave communication systems in space applications," OE vol. 46, no. 1, 015003, 2007.

[67] R. E. Hodges, N. E. Chahat, D. J. Hoppe and J. D. Vacchione, "The Mars Cube One deployable high gain antenna," 2016 IEEE International Symposium on Antennas and Propagation (APSURSI), Fajardo, pp. 1533-1534, 2016.

[68] R. C. Ghail1, C. F. Wilson, and T. Widemann, "EnVision M5 Venus Orbiter Proposal: Opportunities and Challenges," LPSC 2016, The Woodlands, USA, 2016.

[69] J. Pierce, E. Posner, and E. Rodemich, "The capacity of the photon counting channel," in IEEE Transactions on Information Theory, vol. 27, no. 1, pp. 61-77, 1981.

[70] CCSDS Draft Recommendation for Space Data System Standards, "Optical Communications Physical Layer," CCSDS 141.0-R-1, Red Book, URL: https://public.ccsds.org/Lists/CCSDS%201410R1/141x0r1.pdf, November 2017.

[71] CCSDS Draft Recommendation for Space Data System Standards, "Optical Communications Coding & Synchronization," CCSDS 142.0-R-1, Red Book, https://public.ccsds.org/Lists/CCSDS%201420R1/142x0r1.pdf, June 2018.

[72] D. M. Boroson and B. S. Robinson, "The Lunar Laser Communication Demonstration: NASA's First Step Toward Very High Data Rate Support of Science and Exploration Missions," Space Sci Rev, vol. 185, no. 1–4, pp. 115–128, December 2014.

[73] H. Schlemmer, B. Ferenczi, I. Stamenic. J. Widmer, E Leitgeb, **H. Ivanov**, N. Metzger-Fragnol, J. Johansson and M. Schönhuber, "System Study of Optical Communications with a Hybridised Optical/RF Payload Data Transmitter," Final report, ESA Contract No. 4000115256/15/NL/FE, 2020.

[74] C. E. DeVoe, A. D. Pillsbury, F. Khatri, J. M. Burnside, A. C. Raudenbush, L. J. Petrilli, and T. Williams, "Optical overview and qualification of the LLCD space terminal," Proc. SPIE 10563, International Conference on Space Optics — ICSO 2014, 105630F, 17 November 2017.

[75] S. Constantine, L. E. Elgin, M. L. Stevens, J. A. Greco, K. Aquino, D. D. Alves, and B. S. Robinson, "Design of a high-speed space modem for the lunar laser communications demonstration," Proc. of SPIE, vol. 7923, Free-Space Laser Communication Technologies XXIII, San Francisco, CA, USA, Jan. 2011.

[76] H. Hemmati, G. G. Ortiz, W. T. Roberts, M. W. Wright, and S. Lee, "Flight Transceiver," In: H. Hemmati (edc.) Deep Space Optical Communications, Jet Propulsion Laboratory California Institute of Technology, Wiley, June 2006.

[77] **H. Ivanov**, "Breadboard Detailed Design", System Study of Optical Communications with a Hybridised Optical/RF Payload Data Transmitter, Report (Technical Note 3), ESA Contract No. 4000115256/15/NL/FE, January 2018.

[78] **H. Ivanov**, P. Pezzei, T. Plank, C. Pock, and E. Leitgeb, "Design of a Hardware Channel Emulator as Lab Demonstrator for Detailed Verification of Long-Distance FSO

Systems," International Conference on Broadband Communications (CoBCom'2016), Graz, Austria, September 2016.

[79] **H. Ivanov**, E. Leitgeb, P. Bekhrad, T. Plank, and T. Mitsev, "Link Budget Optimization of Free Space Optical Systems in Relation to the Beam Diverging Angle," 13th International Conference on Telecommunications (ConTEL 2015), Graz, Austria, July 2015.

[80] **H. Ivanov**, T. Plank, C. Pock, and E. Leitgeb, "FSO system performance evaluation based on calibrated atmospheric channel emulation," IEEE, 14th International Conference on Telecommunications (ConTEL), Zagreb, Croatia, 2017.

[81] **H. Ivanov**, S. Dorenbos, E. Leitgeb, G. Freiberger, and P. Bekhrad, "Design of an evaluation breadboard with SNSPD for testing various deep space optical communication applications," SPIE Photonics Europe (EPE18), Strasbourg, France, April 2018.

[82] **H. Ivanov**, P. Pocta, F. Marzano, E. Leitgeb, and G. Freiberger, "Resilience of Deep Space FSO Communication Scenario Involving SNSPD Receiver to Atmospheric Turbulence," IEEE, 14th International Conference on Advanced Technologies, Systems and Services in Telecommunications (TELSIKS 2019), pp. 235-240, Nis, Serbia, October, 2019.

[83] **H. Ivanov**, T. Plank, E. Leitgeb, L. Mustafa, and E. Cerncic, "Estimation of Mie scattering influence for the FSO channel under artificially simulated fog conditions," SPIE Remote Sensing (ERS18), Berlin, Germany, September, 2018.

[84] **H. Ivanov**, E. Leitgeb, D. Kraus, F. Marzano, A. Jurado-Navas, S. Dorenbos, R. Perez-Jimenez, and G. Freiberger, "Free Space Optics System Reliability in Presence of Weather-induced Disruptions," In: J. Rak, D. Hutchison (eds.) Guide to Disaster-Resilient Communication Networks, Computer Communications and Networks, Springer, July 2020.

[85] **H. Ivanov**, E. Leitgeb, P. Pezzei, and G. Freiberger, "Experimental characterization of SNSPD receiver technology for deep space FSO under laboratory testbed conditions," Optik Journal, vol. 195, October 2019.

[86] **H. Ivanov**, E. Leitgeb, and G. Freiberger, "Modelling of a deep space FSO-link with a SNSPD receiver unit under turbulence-induced fading conditions," OSA Conference on Lasers and Electro-Optics (CLEO 2019), San Jose, California, USA, May 2019.

[87] **H. Ivanov**, E. Leitgeb, T. Plank, and D. Kraus, "Evaluation of FSO-technology as a Candidate for Reliable Long-distance Communication Links for Deep Space Applications," IEEE, PhotonIcs &Electromagnetics Research Symposium - Spring (PIERS, Rome, Italy June, 2019, **Invited paper**.

[88] I. I. Kim and E. J. Korevaar "Availability of free-space optics (FSO) and hybrid FSO/RF systems," Proc. SPIE 4530, Optical Wireless Communications IV, November 2001.

[89] T. Mitsev, K. Dimitrov, H. Ivanov, and N. Kolev, "Optimum divergence of laser radiation in FSO systems" 7th International Conference on "Communications, Electromagnetics and Medical Applications" (CEMA'12), Athens, Greece, November 2012.

[90] S. V. Kartalopoulos, "Free Space Optical Networks for Ultra-Broad Band Services," Wiley-IEEE Press, ISBN: 978-0-470-64775-2, August 2011.
[91] R. D. Hudson, "Atmospheric transmittance measured over 1820m path at sea level," Journal Infrared System Engineering, vol. 115, Wiley & Sons, 1969.
[92] O. Bouchet, H. Sizun, C. Boisrobert, F. de Fornel, and P.-N. Favennec, "Free-Space Optics: Propagation and Communication," Wiley - ISTE Ltd, ISBN: 978-1-905-20902-6, 2006.
[93] I. I. Kim, B. McArthur, and E. J. Korevaar, "Comparison of laser beam propagation at 785 nm and 1550 nm in fog and haze for optical wireless communications," Proc. SPIE 4214, Optical Wireless Communications III, February 2001.
[94] S. S. Muhammad, B. Flecker, E. Leitgeb, and M. Gebhart, "Characterization of fog attenuation in terrestrial free space optical links," Optical Engineering vol. 46, no. 6, 066001, June 2007.
[95] B. Y. Hamzeh, "Multi-rate wireless optical communications in cloud obscured channels," Ph.D. Thesis, Pennsylvania State University, December 2005.
[96] C. Mätzler, "MATLAB Functions for Mie Scattering and Absorption Research Report," No. 2002-11, Institut für Angewandte Physik Mikrowellenabteilung, University of Bern, August 2002.
[97] F. Tampieri and C. Tomasi, "Size distribution models of fog and cloud droplets in terms of the modified gamma function," Tellus, Pages 333-347, vol. 28, no. 4, 1976 | Accepted 14 Oct 1975, Published online: Feb 2017.
[98] A.J. Heymsfield, M. Krämer, A. Luebke, P. Brown, D.J. Cziczo, C. Franklin, P. Lawson, U. Lohmann, G. McFarquhar, Z. Ulanowski, and K. Van Tricht, "Cirrus Clouds," Meteorological Monographs, vol. 58, pp. 2.1–2.26, 2017.
[99] S. Arnon and N. S. Kopeika, "Adaptive optical transmitter and receiver for space communication through thin clouds," Appl. Opt., vol. 36, no. 9, pp. 1987-1993, 1997.
[100] S. Mori and S. F. Marzano, "Microphysical characterization of free space optical link due to hydrometeor and fog effects," Applied optics, vol. 54, no. 22, pp. 6787-6803, 2015.
[101] C. Tomasi and F. Tampieri, "Features of the proportionality coefficient in the relationship between visibility and liquid water content in haze and fog," Atmosphere, vol. 14, no. 2, pp. 61-76, 1976.
[102] I. Gultepe, R. Tardif, S. C. Michaelides, J. Cermak, A. Bott, J. Bendix, M. D. Müller, M. Pagowski, B. Hansen, G. Ellrod, W. Jacobs, G. Toth, S. G. Cober, et al., "Fog Research: A Review of Past Achievements and Future Perspectives," Pure appl. geophys., vol. 164, no. 6–7, pp 1121–1159, June 2007.
[103] R.G Eldridge, "Electromagnetic scattering on spherical polydispersions," Elsevier, Haze and fog aerosol distributions. J. Atmos. Sci., vol. 23, pp. 75-119 New York, 1966.
[104] N. Blaunstein, S. Arnon, A. Zilberman, N. Kopeika, "Applied aspects of optical communication and LIDAR," SRS Press, Taylor and Francis Group, U.S., 2010.
[105] V. I. Tatarski, "The effects of the turbulent atmosphere on wave propagation," Jerusalem: Israel Program for Scientific Translations, 1971.

[106] E. M. Dewan, R. E. Good, R. Beland, and J. Brown, "Model For C_n^2 (Optical Turbulence) Profiles Using Radiosonde Data," PL-TR-93-2043, AD-A279 399, Environmental Research Papers, no. 1121, 1 March 1993.

[107] T. Cherubini and S. Businger, "Another Look at the Refractive Index Structure Function," Journal of Applied Meteorology and Climatology vol.52, no. 2, pp. 498-506, February 2013.

[108] A. Biswas, K. E. Wilson, S. Piazzolla, J. P. Wu, and W. H. Farr, "Deep-space optical communications link availability and data volume," Proc. SPIE 5338, Free-Space Laser Communication Technologies XVI, June 2004.

[109] A. Biswas and S. Piazzolla, "The Atmospheric Channel," In: H. Hemmati (edc.) Deep Space Optical Communications, Jet Propulsion Laboratory California Institute of Technology, Wiley, June 2006.

[110] M. C. Al Naboulsi, H. Sizun, and F. de Fornel, "Fog attenuation prediction for optical and infrared waves," Optical Engineering vol. 43, no. 2, February 2004.

[111] W. O. Popoola, Z. Ghassemlooy, and E Leitgeb, "Free-space Optical communication using subcarrier modulation in gamma gamma atmospheric turbulence," IEEE, 9th International Conference on Transparent Optical Networks, pp. 156–160, 2007.

[112] D. Giggenbach and H. Henniger, "Errata: Fading-loss assessment in atmospheric free-space optical communication links with on-off keying," Optical Engineering vol. 47, no. 6, 069801, June 2008.

[113] T. Fahey, "Snowfall Rate Thresholds for Light, Moderate and Heavy" Aerodrome Meteorological Observation and Forecast Study Group (AMOFSG), Seventh Meeting, Montréal, September 2008.

[114] S. S. Muhammad, P. Kohldorfer, and E. Leitgeb, "Channel modeling for terrestrial free space optical links," Proceedings of 2005 7th International Conference Transparent Optical Networks, 2005., Barcelona, Catalonia, vol. 1, pp. 407-410, 2005.

[115] L. Mustafa and B. Thomsen, "Reintroducing Free-space Optical technology to Community Wireless Networks," Proceedings of the Nineteenth Americas Conference on Information Systems AMCIS, Chicago, Illinois, August 2013.

[116] L. Amaral, J. Troska, A. Pacheco, S, Dris, D. Ricci, C. Sigaud, and F. Vasey, "Evaluation of Multi-Gbps Optical Transceivers for Use in Future HEP Experiments," Topical Workshop on Electronics for Particle Physics, pp.151-155 (CERN-2008-008) , Naxos, Greece, Sep 2008.

[117] E. Säckinger, "Broadband Circuits for Optical Fiber Communication,", John Wiley & Sons, Inc., January 2005.

[118] F. Moll and M. Knapek, "Wavelength selection criteria and link availability due to cloud coverage statistics and attenuation affecting satellite, aerial, and downlink scenarios," Proc. SPIE 6709, Free-Space Laser Communications VII, 670916, September 2007.

[119] A. Thomas, and et al., "In situ measurements of background aerosol and subvisible cirrus in the tropical tropopause region," J. Geophys. Res., vol 107, no. D24, 4763, 2002.

[120] K. N. Liou, Y. Takano, S. C. Ou, and M. W. Johnson, "Laser transmission through thin cirrus clouds," Appl. Opt., vol. 39, no. 27, pp. 4886-4894, 2000.

[121] R. Meerkötter, G. Gesell, V. Grewe, C. König, S. Lohmann, and H. Mannstein, "A High Resolution European Cloud Climatology from 15 Years of Noaa/Avhrr Data," January 2004.

[122] T. T. Chiao and A. R. Thompson, "Densities and Refractive Indices for Glycol-Water Solutions...Triethylene Glycol, Dipropylene Glycol and Hexylene Glycol," Anal. Chem. vol. 29, no. 11, pp. 1678-1681, 1957.

[123] R. Boluda-Ruiz, A, García-Zambrana, B, Castillo-Vázquez, and C. Castillo-Vázquez, "On the capacity of MISO FSO systems over gamma-gamma and misalignment fading channels," Opt. Express vol. 23, pp. 22371-22385, 2015.

[124] Atmospheric Soundings (RAOB), [online]. Available: http://weather.uwyo.edu/upperair/sounding.html, Department of Atmospheric Science, University of Wyoming, USA, 2020.

[125] D. Giggenbach, A. Shrestha, C. Fuchs, C. Schmidt, and F. Moll "System aspects of optical LEO-to-ground links," Proc. SPIE 10562, International Conference on Space Optics — ICSO 2016, 105625N, 25 September 2017.

[126] M. R. Garcia-Talavera, C. Rivera, G. Murga, I. Montilla, and A. Alonso, "Analysis of large optical ground stations for deep-space optical communications," Proc. SPIE 10563, International Conference on Space Optics — ICSO 2014, 105630Z, November 2017.

[127] A. J. Hashmi, A. A. Eftekhar, A. Adibi, and F. Amoozegar, "Analysis of telescope array receivers for deep-space inter-planetary optical communication link between Earth and Mars," Optics Communications, vol. 283, no. 10, pp 2032-2042, 2010.

[128] R J. Alliss, and B. Felton, "The mitigation of cloud impacts on free-space optical communications," Proc. SPIE 8380, Atmospheric Propagation IX, 83800S, May 2012.

[129] A. Guérin, F. Lacoste, A. Laurens, G. Azéma, C. Périard, and D. Grimal, "Optical Links Capacity for LEO Satellites Over European Ground Networks," International Telemetering Conference Proceedings, 2010.

[130] C. Fuchs and F. Moll, "Ground station network optimization for space-to-ground optical communication links," in IEEE/OSA Journal of Optical Communications and Networking, vol. 7, no. 12, pp. 1148-1159, Dec. 2015.

[131] S. N. Dorenbos, E. M. Reiger, U. Perinetti, V. Zwiller, T. Zijlstra, and T. M. Klapwijk, "Low noise superconducting single photon detectors on silicon," Applied Physics Letters, vol, 93, id. 131101, 2008.

[132] M. M. Willis, A. J. Kerman, M. E. Grein, J. Kansky, B. R. Romkey, E. A. Dauler, D. Rosenberg, B. S. Robinson, D. V. Murphy, and D. M. Boroson, "Performance of a Multimode Photon-Counting Optical Receiver for the NASA Lunar Laser Communications Demonstration,"Proc. International Conference on Space Optical Systems and Applications (ICSOS) 2012, pp. 4-3, France, October 2012.

[133] B. E. Vyhnalek, S. A. Tedder, and J. M. Nappier, "Performance and characterization of a modular superconducting nanowire single photon detector system for space-to-Earth optical communications links," Proc. SPIE 10524, Free-Space Laser Communication and Atmospheric Propagation XXX, 1052419, February 2018.

[134] Single Quantum Company, "SNSPD Closed-Cycle System," [online]. Available: https://singlequantum.com/wp-content/uploads/2019/05/Single-Quantum-Eos.pdf, May 2019.

[135] F. Zheng, R. Xu, G. Zhu, B. Jin, L. Kang, W. Xu, J. Chen, and P. Wu, "Design of a polarization-insensitive superconducting nanowire single photon detector with high detection efficiency," Sci Rep vol. 6, 22710, 2016.

[136] S. J. Dolinar, J. Hamkins, B. E. Moision, and V. A. Vilnrotter, "Optical Modulation and Coding," In: H. Hemmati (edc.) Deep Space Optical Communications, Jet Propulsion Laboratory California Institute of Technology, Wiley, June 2006.

[137] S.S. Muhammad, T. Javornik, I. Jelovčan, Z. Ghassemlooy, and E. Leitgeb, "Comparison of hard-decision and soft-decision channel coded M-ary PPM performance over free space optical links," Eur. Trans. Telecomm., vol. 20, pp. 746-757, 2009.

[138] M. Tomlinson, C. J. Tjhai, M. A. Ambroze, M. Ahmed, and M. Jibril, "Soft and Hard Decision Decoding Performance," In: M. Tomlison (edc.) Error-Correction Coding and Decoding. Signals and Communication Technology, pp 25-41, Springer, Cham, 2017.

[139] S. Dolinar, D. Divsalar, J. Hamkins, and F. Pollara, "Capacity of PPM on APD-detected optical channels," IEEE, MILCOM 2000 Proceedings, Los Angeles, CA, USA, Oct. 2000.

[140] J. C. Campbell, "Recent Advances in Telecommunications Avalanche Photodiodes," in Journal of Lightwave Technology, vol. 25, no. 1, pp. 109-121, Jan. 2007.

[141] K. Shiba, T. Nakata, T. Takeuchi, T. Sasaki and K. Makita "10 Gbit/s asymmetric waveguide APD with high sensitivity of 30 dBm," in Electronics Letters, vol. 42, no. 20, pp. 1177-1178, September 2006.

[142] A. Biswas, and W. Farr, "Laboratory Characterization and Modeling of a Near-Infrared Enhanced Photomultiplier Tube," IPN Progress Report 42-152, Jet Propulsion Laboratory, pp. 1–14, USA, 2003.

[143] Z. Sodnik, H. Smit, M. A. Sans, D. Giggenbach, P. Becker, R. Mata Calvo, C. Fuchs, I. Zayer, M. Lanucara, K.-J. Schulz, J. Widmer, F. Arnold, A. Alonso, and I. Montilla, "Results from a Lunar Laser Communication Experiment between NASA's LADEE Satellite and ESA's Optical Ground Station," Proc. International Conference on Space Optical Systems and Applications (ICSOS) 2014, S2-1, Kobe, Japan, May 2014.

[144] B. Moision and J. Hamkins, "Deep-space optical communications downlink budget: modulation and coding," IPN Progress Report 42-154, Jet Propulsion Laboratory, pp. 1-28, USA, 2003.

[145] A. A. Farid and S. Hranilovic, "Outage Capacity Optimization for Free-Space Optical Links With Pointing Errors," Journal of Lightwave Technology, vol. 25, no. 7, pp. 1702 – 1710, July 2007.

[146] C. M. Wilkes, X. Qiang, J. Wang, R. Santagati, S. Paesani et al., "60 dB high-extinction auto-configured Mach–Zehnder interferometer," OSA, Optics Letters vol. 41, no. 22, pp. 5318-5321, 2016.

[147] D.O. Caplan, J.P. Wang, M.L. Stevens, C.D. Burton, J.J. Carney, and et al., "Next-generation Free-space Optical Transceivers for Highcapacity Space-based

Communications," IEEE 2017 Conference on Lasers and Electro-Optics (CLEO), pp. 1-2, San Jose, CA, 2017.

[148] C. Roth, "Physical Layer Solutions for Deep Space Hybrid Optical / RF PDT," System Study of Optical Communications with a Hybridised Optical/RF Payload Data Transmitter, Report (Technical Note 2), ESA Contract No. 4000115256/15/NL/FE, July 2017.

[149] Z. Sodnik and G. Baister, "Alphasat's (TDP) Technical Description: Alphasat Optel Terminal," Technical Note, EUI-ESRIN/0511/020, no 1, Dec. 2015.

[150] A. J. Kerman, E. A. Dauler, B. S. Robinson, R. Barron, D. O. Caplan, M. L. Stevens, J. J. Carney, S. A. Hamilton, W. E. Keicher, J. K. W. Yang, K. Rosfjord, V. Anant, and K. K. Berggren, "Superconduct-ing nanowire photon-counting detectors for optical communications," Lincoln Laboratory Journal vol. 16, no. 1, pp. 217-224, 2006.

[151] B. E. Vyhnalek, S. A. Tedder, E. J. Katz, and J. M. Nappier, "Few-mode fiber coupled superconducting nanowire single-photon detectors for photon efficient optical communications," Proc. SPIE 10910, Free-Space Laser Communications XXXI, 109100D, February 2019.

[152] L. Zhang, M. Gu, T. Jia, R. Xu, C. Wan, L. Kang, and J. Chen, P. Wu, "Multimode Fiber Coupled Superconductor Nanowire Single-Photon Detector," in IEEE Photonics Journal, vol. 6, no. 5, pp. 1-8, Oct. 2014.

[153] J. Chang, I. E. Zadeh, J. W. N. Los, J. Zichi, A. Fognini, M. Gevers, S. Dorenbos, S. F. Pereira, P. Urbach, and V. Zwiller, "Multimode-fiber-coupled superconducting nanowire single-photon detectors with high detection efficiency and time resolution," Appl. Opt. vol. 58, pp. 9803-9807, 2019.

[154] H. Zwickel et al., "120 Gbit/s PAM-4 Signaling Using a Silicon-Organic Hybrid (SOH) Mach-Zehnder Modulator," ECOC 2016, 42nd European Conference on Optical Communication, pp. 1-3, Dusseldorf, Germany, 2016.

[155] Z. Yong et al., "A 44Gbps high extinction ratio silicon Mach-Zehnder modulator with a 3D-integrated 28nm FD-SOI CMOS driver," 2017 Optical Fiber Communications Conference and Exhibition (OFC), pp. 1-3., Los Angeles, USA, 2017.

[156] S. Fathpour et al., "Heterogeneous integration of compact lithium niobate microring and Mach-Zehnder modulator on silicon," 2016 IEEE Photonics Conference (IPC), pp. 3-4. Waikoloa, HI, 2016.

[157] P. Bravetti, G. Ghislotti, and S. Balsamo, "Chirp-inducing mechanisms in Mach-Zehnder modulators and their effect on 10 Gb/s NRZ transmission studied using tunable-chirp single drive devices," in Journal of Lightwave Technology, vol. 22, no. 2, pp. 605-611, Feb. 2004.

[158] L. Mollenauer and J. Gordon, "Solitons in Optical Fibers: Fundamentals and Applications," Elsevier Academic Press, 2016.

[159] Mach-Zehnder Modulator, "Thorlabs LN81S," zero (x-cut), device data, 2016.

[160] TS-Space Systems "ASTM Spectral Distribution of Irradiance Performance Requirements," Solar Simulator - Spectral Match, [online]. Available: https://www.solar-simulator.info/solar-simulator-match.html, 2015

[161] A. T. Mecherikunnel et al., "Spectral Distribution of Solar Radiation," NASA Technical Memorandum 82021, 1980.

[162] C. S. Cockell, J. A. Raven, L. Kaltenegger, and R. C. Logan, "Planetary targets in the search for extrasolar oxygenic photosynthesis," Plant Ecology & Diversity, vol.2, no. 2, pp. 207-219, 2009.

[163] D. Morabito, and R. Hastrup, "Communications with Mars During Periods of Solar Conjunction: Initial Study Results," The Interplanetary Network Progress Report, IPN PR 42-147, pp. 1-16, July-September 2001.

[164] A. M. Bazzi, Z. Klein, M. Sweeney, K. P. Kroeger, P. S. Shenoy, and P. T. Krein, "Solid-State Solar Simulator," in IEEE Transactions on Industry Applications, vol. 48, no. 4, pp. 1195-1202, July-Aug. 2012.

[165] G. Grandi, A. Ienina, and M. Bardhi, "Effective Low-Cost Hybrid LED-Halogen Solar Simulator," in IEEE Transactions on Industry Applications, vol. 50, no. 5, pp. 3055-3064, Sept.-Oct. 2014.

[166] K. A. Kim et al., "Low-cost solar simulator design for multi-junction solar cells in space applications, " 2014 Power and Energy Conference at Illinois (PECI), pp. 1-6., Champaign, IL, 2014.

[167] Thorlabs Company, "Stabilized Tungsten Light Sources, SLS201L," User Guide document, Rev D, Jan. 2020.

[168] J. M. Garrido-Balsells, A. Jurado-Navas, J. F. Paris, M. Castillo-Vazquez, and A. Puerta-Notario, "On the capacity of M distributed atmospheric optical channels," Optics Letters, vol. 39, no. 3, pp. 653–653, 2014.

Appendix A: Outage probability of FSO system

In order to estimate the outage probability of a FSO system operating in atmospheric turbulence fading, knowledge of FSO receiver sensitivity S_r in terms of threshold irradiance I_{th} and received optical irradiance I_r are required. The outage probability $P_{out}(I_r < I_{th})$ is the CDF of the normalized irradiance, which is calculated based on integration of Gamma – Gamma PDF provided in Eq. (3.38).

$$F(I_t) = P_{out}(I_r < I_{th}) = \int_0^{I_{th}} \frac{2(\alpha\beta)^{\frac{\alpha+\beta}{2}-1}}{\Gamma(\alpha)\Gamma(\beta)} I_r^{\frac{\alpha+\beta}{2}-1} K_{\alpha-\beta}\left(2\sqrt{\alpha\beta I_r}\right) dI_r \quad A(1)$$

Although there are different methodology for solving the Eq. A(1), the solution in the current work is based on Meijer-G and Hypergeometric functions. At first, the modified Bessel function of second kind is considered. Addressing the Eq. (03.04.26.0009.01), the special Bessel K function is converted into Meijer-G function (Eq. A(2)).

$$P_{out}(I_r < I_{th}) = \int_0^{I_{th}} \frac{2(\alpha\beta)^{\frac{\alpha+\beta}{2}-1}}{\Gamma(\alpha)\Gamma(\beta)} I_r^{\frac{\alpha+\beta}{2}-1} \frac{1}{2} G_{0,2}^{2,0}\left(\alpha\beta I_r \middle| \frac{\alpha-\beta}{2}, \frac{\beta-\alpha}{2}\right) dI_r \quad A(2)$$

Taking into account the type of the integral, involving a product of a simpler function together with the already applied Meijer-G function, an additional transformation based on Eq. (07.34.21.0002.01) is applied. Moreover, to be addressed Eq. (07.34.21.0002.01), an integration by substitution ($z=I_r\alpha\beta$) is used. The final closed form expression for the outage probability is given in Eq. A(3).

$$P_{out}(z) = \frac{1}{\Gamma(\alpha)\Gamma(\beta)} G_{1,3}^{2,1}\left(z \middle| \begin{matrix} 1 \\ \alpha\ \beta\ 0 \end{matrix}\right) \quad A(3)$$

Moreover, Eq. A(2) also can be written based on Hypergeometrical functions, which are more robust against numerical inconsistencies. The derived equation based on Hypergeometrical functions is provided in Eq. A(4).

$$P_{out}(z) = \pi \csc\left(\pi(\beta-\alpha)\right) \Gamma(\alpha) z^{\Gamma(\alpha)} F_2(\alpha, \alpha-\beta+1\ \alpha+1, z) - \Gamma(\beta) z^{z^{\Gamma(\beta)}} F_2(\beta, \beta-\alpha+1\ \beta+1, z) \quad A(4)$$

Nevertheless, Meijer-G is the function of choice for calculating the outage probability of a long-distance FSO link operating in atmospheric turbulence fading. In particular, these general functions cover large amount of special functions including also Hypergeometrical ones. To simplify its application and in parallel with the accomplished work in ***[168]***, instead of intensity, the normalized SNR in lack of atmospheric turbulence is applied . Addressing the normalized Gamma – Gamma distribution and more specifically the Eq. A(1), the $P_{out}(I_r < I_{th})$ in terms of SNR is equal to:

$$P_{out}\left(I_r < \sqrt{\frac{I_{th}^2}{I_0^2}}\right) = P_{out}\left(I_r < \sqrt{\frac{\gamma_{th}}{\gamma_0}}\right) = P_{out}\left(I_r < \sqrt{\frac{1}{\gamma_n}}\right) \quad A(5)$$

Where I_{th} and I_0 are the threshold of the optical irradiance and the target optical irradiance in lack of atmospheric turbulence. Based on this assumptions, γ_n is defined as the normalized intensity, which value is equal to the desired intensity above the established threshold γ_{th}, namely $\gamma_n=\gamma_0 - \gamma_{th}$ [dB]. After substitution of Eq. A(5) in Eq. A(4), the final derived closed-form expression for the outage probability in terms of Gamma – Gamma turbulence Eq. (3.38) is given in Eq. A(6). The equation is published in own publication ***[84]***.

$$\mathrm{P_{out}}(\gamma_n) = \frac{1}{\Gamma(\alpha)\Gamma(\beta)} \mathrm{G}_{1,3}^{2,1}\left(\alpha\beta \frac{1}{\sqrt{\gamma_n}} \middle| \begin{matrix} 1 \\ \alpha\ \beta\ 0 \end{matrix}\right) \qquad A(6)$$

Appendix B: Scintillation histograms

Along with the full characterization of atmospheric turbulence induced-fading regarding space-to-ground FSO link with R_d = 1 m and γ = 20° considering σ_r^2, σ_I^2, σ_p^2 parameters, **Appendix B** provides the same analysis in respect to the two other R_d = 1.5; 8 m scenarios. In order to address the full picture, σ_r^2, σ_I^2, σ_p^2 for scintillation cases of R_d = 1.5, 8 m and γ = 20° are given.

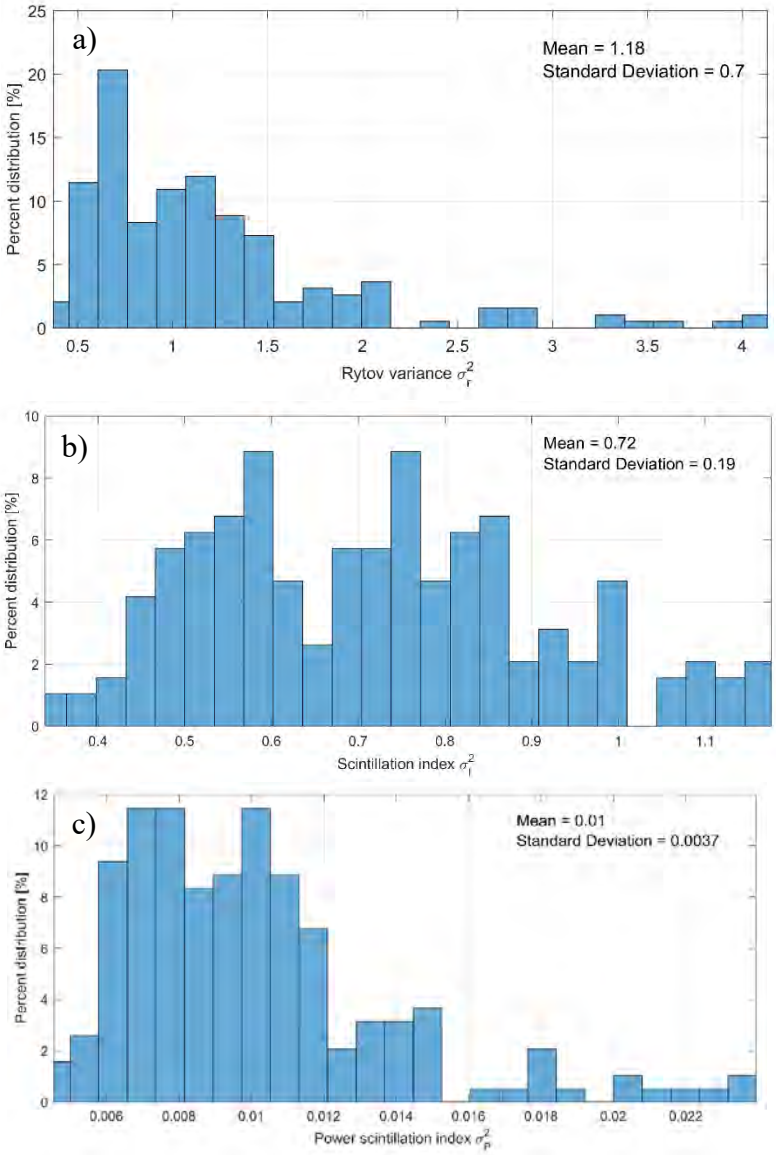

Appendix Figure 1: Probability histograms of a) σ_r^2; b) σ_I^2; c) σ_p^2 – regarding space-to-ground FSO downlink for R_d = 1.5 m and γ =20° based on 1-year ROAB measurements from Vienna, Austria

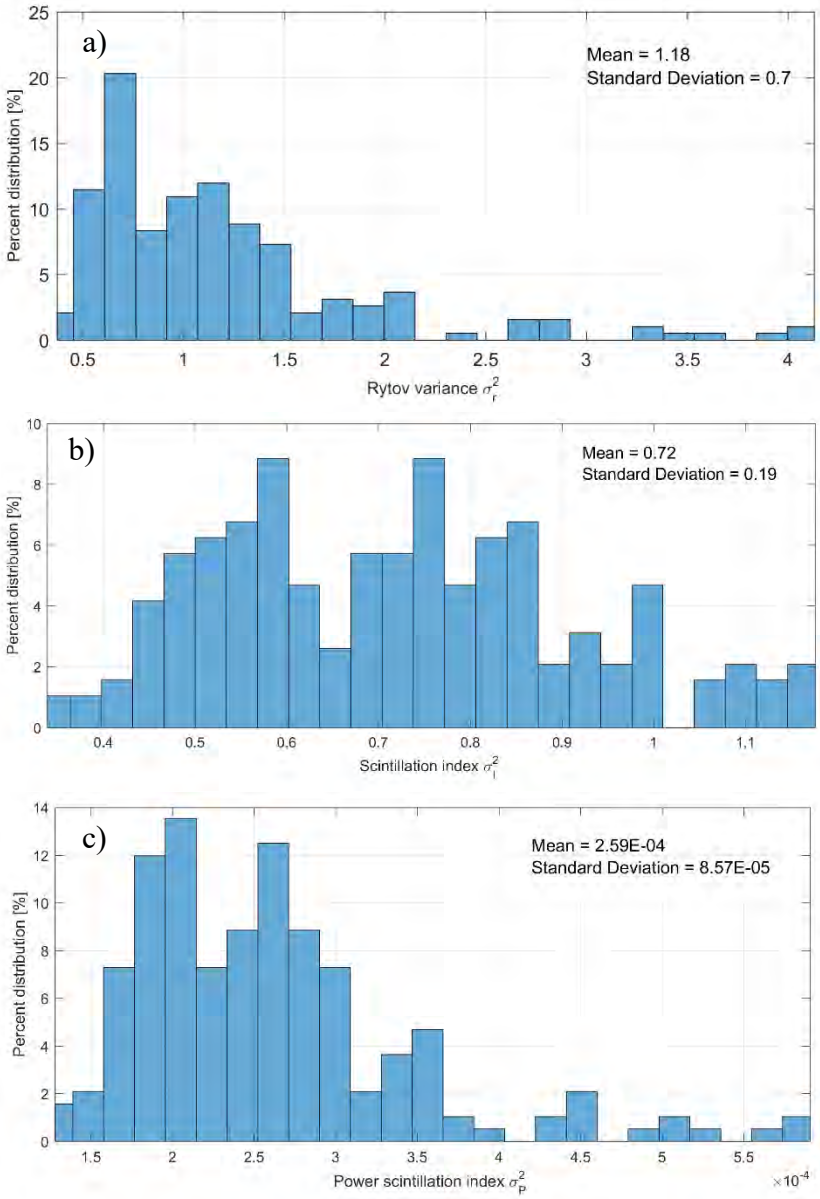

Appendix Figure 2: Probability histograms of a) σ_r^2; b) σ_I^2; c) σ_p^2 – regarding space-to-ground FSO downlink for R_d = 8 m and γ =20° based on 1-year ROAB measurements from Vienna, Austria

Appendix C: VOA-emulator measurements

In **Appendix C** an additional contribution to the accomplished and discussed measurements in **Subchapter 7.8** is provided. Along with the carried out test of the hardware FSO channel emulator based on R_d = 8, γ = 20° and fading frequency 200 Hz (5 ms response time), measurements with 1 kHz (1 ms), 500 Hz (2 ms), 100Hz (10 ms) and 10 Hz (100 ms) scintillations are provided. Moreover, two more scenarios involving assessment of atmospheric turbulence conditions in respect to R_d = 1, 1.5 m and γ = 20° are implemented. Taking into account the first scenario with 0.55 dB maximum optical attenuation, the improvement with increasing the response time in terms of average absolute error is evident and leads to ~22 times higher accuracy. Nevertheless, for other two scenarios the difference is only ~10 and ~3 times, comparing the average absolute errors for the case of 500 Hz (2 ms) and 10 Hz (100 ms).

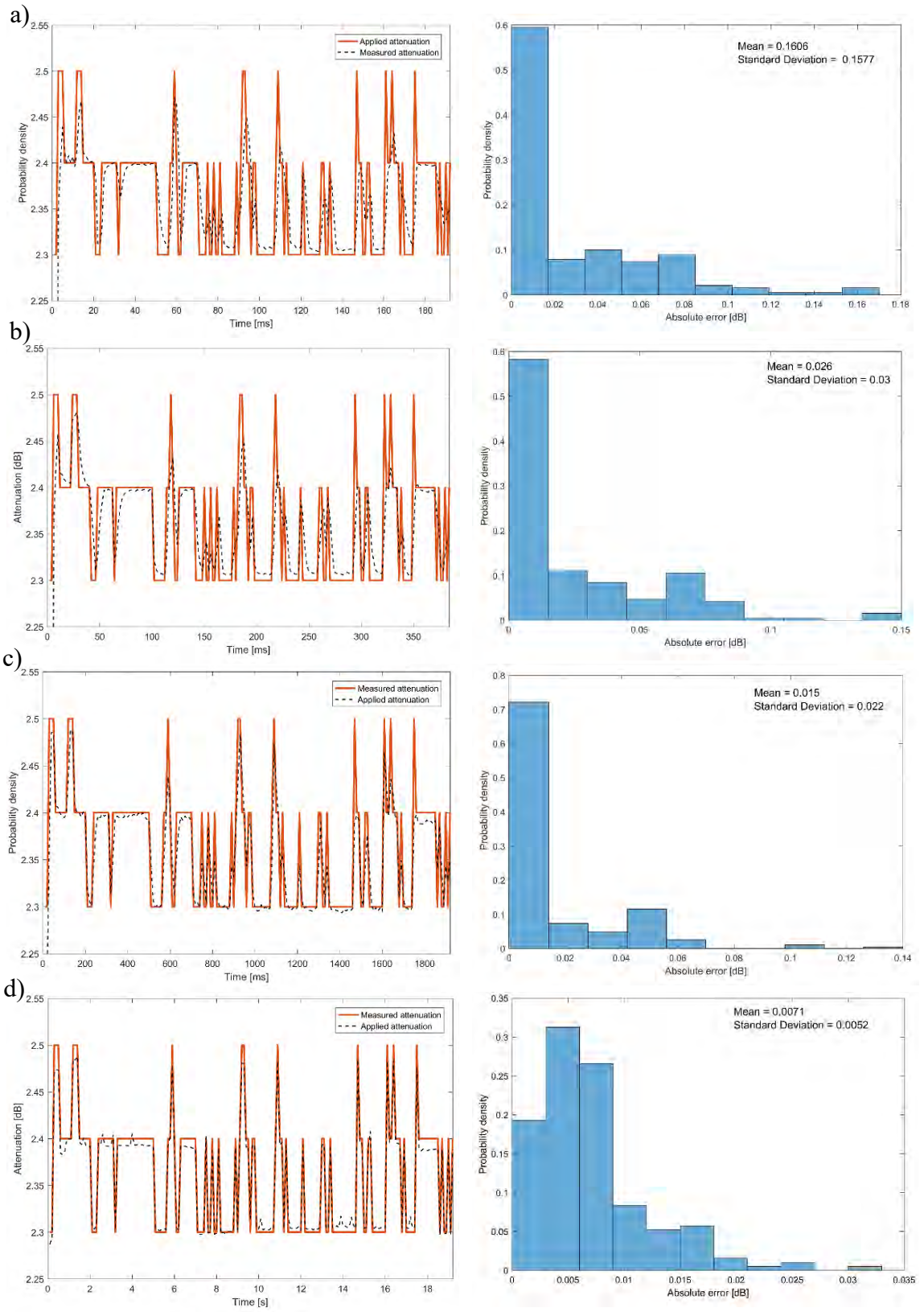

Appendix Figure 3: Comparison between applied scintillation for $R_d = 8$ m, $\gamma = 20°$ and measured data with the VOA-based FSO channel emulator in respect to response time: a) 1 ms (1 Hz); b) 2 ms (500 Hz); c) 10 ms (100 Hz); d) 100 ms (10 Hz)

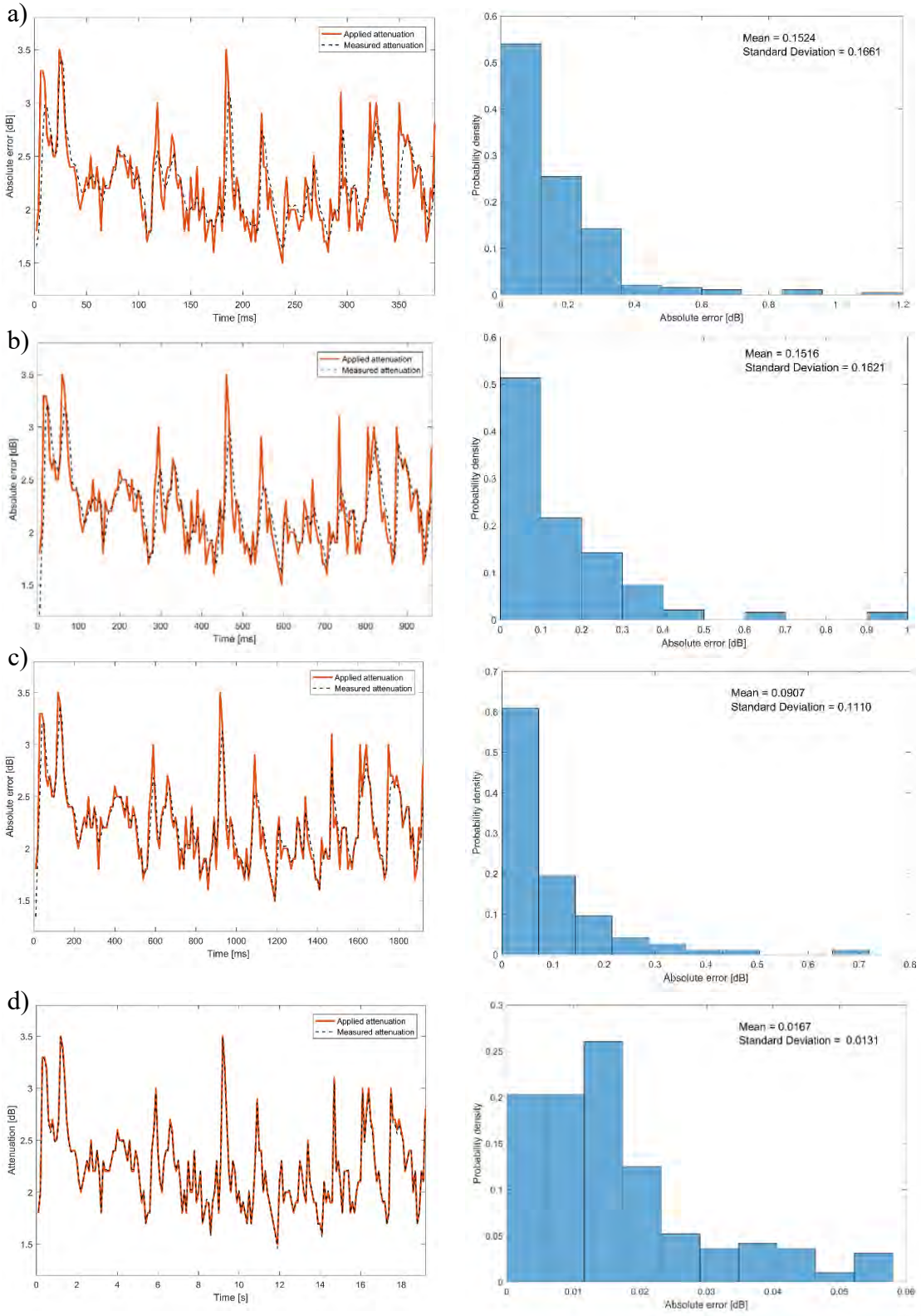

Appendix Figure 4: Comparison between applied scintillation for R_d = 1.5 m, γ = 20° and measured data with the VOA-based FSO channel emulator in respect to response time: a) 2 ms (500 Hz); b) 5 ms (200 Hz); c) 10 ms (100 Hz); d) 100 ms (10 Hz)

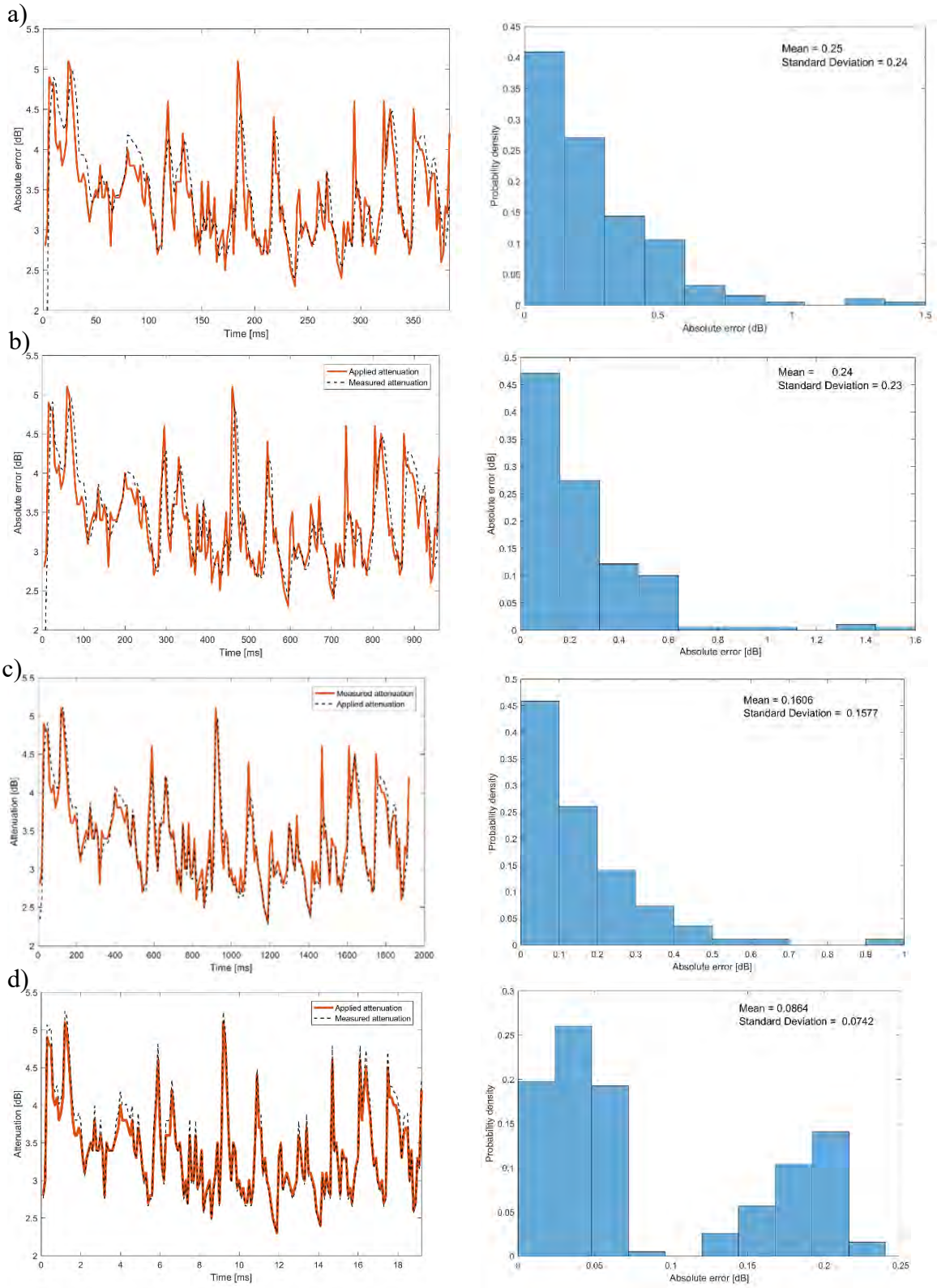

Appendix Figure 5: Comparison between applied scintillation for $R_d = 1$ m $\gamma = 20°$ and measured data with the VOA-based FSO channel emulator in respect to response time: a) 2 ms (500 Hz); b) 5 ms (200 Hz); c) 10 ms (100 Hz); d) 100 ms (10 Hz)